An integrated computational methodology for coupling in-crack physics with the adjacent environment

With an application on Solid-State Batteries

Timothy Raue

Delft University of Technology

TU Delft

An integrated computational methodology for coupling in-crack physics with the adjacent environment

With an application on Solid-State Batteries

by

Timothy Raue

to obtain the degree of Master of Science
at the Delft University of Technology,
to be defended publicly on Tuesday May 28, 2024 at 09:00 AM.

Student number:	5268052	
Project duration:	September, 2023 – May, 2024	
Thesis committee:	Dr. B. Giovanardi,	TU Delft, supervisor
	Dr. S.R. Turteltaub,	TU Delft, chair
	Dr. M. Gerritsma,	TU Delft, external member

Cover:	Overview of a Solid State Battery [1] (Modified)
Style:	TU Delft Report Style, with modifications by Daan Zwaneveld

An electronic version of this thesis is available at `http://repository.tudelft.nl/`.

TU Delft

Preface

This thesis is the last part of my journey to obtain a master's degree at the faculty of Aerospace Engineering of Delft University of Technology. I am very thankful for the invaluable supervison of Bianca Giovanardi during the entire project. I also owe many thanks to my family, who supported me throughout all the years I have studied. Finally, I want to thank my friends who were part of the journey.

Timothy Raue
Delft, May 2024

Executive Summary

One of the most well-known innovations for reducing emissions in aviation is the introduction of the electric airplane, but significant improvements are still required before these airplanes can be used for large-scale commercial flights. The crucial component to improve is the batteries. The biggest challenge at this moment is the improvement of energy density and specific energy. This could be achieved through the introduction of solid-state batteries. However, the limited lifespan is a massive disadvantage of solid-state batteries due to new failure modes resulting from the introduction of solid electrolytes. Dendrites, small needle-like lithium structures growing in the solid electrolyte, are an example of such a failure mode. The lifespan can be significantly improved if the effect of dendrites can be reduced. To achieve this, it is crucial to have a model that can predict this phenomenon.

An approach to determine dendrite propagation is through discrete modeling methods. These methods introduce the crack as a discontinuity in the mesh, dividing the cracked and uncracked parts into two different domains. This work aims to formulate a computational model that couples the physics of the internal crack with the adjacent environment. The methodology can be applied to all discrete approaches, but this work specifically considers Discontinuous Galerkin Cohesive Zone Modeling. In the new method, the governing equations of the two-dimensional crack domain are projected in the tangential direction of the crack to obtain a hybrid-dimensional formulation of the weak form. Because the fracture is reduced to a lower dimensional domain, this methodology leads to a discontinuity in the primal solution field. Therefore, a discontinuous Galerkin approach is employed in the discretization of the equations.

An analytical model is derived to verify the results obtained by the numerical model. The analytical and numerical models are compared for several combinations of the ratio between the conductivity inside the crack and the solid electrolyte. All these combinations demonstrate perfect alignment between both models. Secondly, the results are compared with the phase-field model developed by Bistri and Leo. Both models yield similar results, with the only discrepancy being that the crack opening is smaller in the newly developed model. This variation arises from the distinct natures of the two models. The phase field models cracks as smoothed volumetric phenomena, whereas the new method employs sharp edges. Validation against experiments would be necessary to assess which solution is more predictive.

The new methodology for solving partial differential equations has proven successful in computing the electric potential. To extend this approach to modeling dendrite propagation, it is necessary to also rewrite the chemical governing equations in this hybrid formulation form and add the coupling with fracture mechanics. This will enable the development of a coupled model combining all three areas of physics. When the fully coupled model is achieved, the model can be used to develop further promising solutions to improve the lifespan of solid-state batteries. An example of such a solution is dendrite deflection, which occurs when a load is applied to the solid electrolyte, which delays or even prevents the dendrites from growing to the other side of the solid electrolyte.

Contents

Nomenclature

Glossary

Definition	Description
Active material	The parts that undergo chemical reactions
Anions	Negative charged ions
Anode	The electrode where oxidation occurs
Cathode	The electrode where reduction occurs
Cations	Positive charged ions
Composite electrodes	Active particles that are embedded in the solid electrolyte
Concentration gradient	The difference in concentration between two points in space
Current density	Normalizing the current by dividing through the electrode area
Critical current density	The maximum current density without negative side reactions
Deintercalation	Loss of particles that were intercalated before
Dendrites	Small needle-like lithium structures that grow through the solid electrolyte
Diffusion	Movement of cations due to a concentration gradient
Displacement jump	The difference between the two sides of the cohesive zone
Electropotential	Potential difference between two points in an electrochemical system
Energy density	The amount of energy in a given volume
Favorable propagation angle	The angle at which the mode I stress intensity factor becomes maximum
Intercalation	Reversible reaction of the cations with the electrode
Interphase layer	An irreversible layer at the interface between the electrode and solid electrolyte
Migration	Movement of cations due to the presence of an electric field
Half-cell reaction	The chemical reaction at one of the electrodes
Oxidation	A chemical process resulting in the loss of electrons by a substance
Plating	Depositing of lithium at the electrode due to a reduction reaction of the lithium ions of the solid electrolyte
Redox reaction	Simultaneous occurrence of reduction and oxidation reactions
Reduction	A chemical process resulting in the gain of electrons by a substance
Specific energy	The amount of energy per unit mass
Stripping	Desolving of lithium in the solid electrolyte due to an oxidation reaction
Viscoplasticity	The time-dependent irreversible strain of solids

Abbreviations

Abbreviation	Definition
ASSB	All Solid-State Batteries
CZM	Cohesive Zone Model
DG	Discontinuous Galerkin
DG-CZM	Discontinuous Galerkin Cohesive Zone Model
MIEC	Mixed ionic-electronic conductor
PFM	Phase-Field model

Abbreviation	Definition
SE	Solid Electrolyte
TSL	Traction-Separation Law

Symbols

Symbol	Definition
c	Number of moles of the mobile ionic species per unit reference volume
$\boldsymbol{C}$	Right Cauchy-Green strain tensor
d	Electric displacement
$\mathcal{D}$	Dissipation
$\boldsymbol{D}^c$	Chemical stretching tensor
$\boldsymbol{D}^r$	Stretching induced by electrodeposition
e	Referential electric field
e^-	electrons
$\boldsymbol{E}$	Logarithmic elastic strain
F	Faraday's constant
$\mathcal{F}$	Thermodynamic driving force
$\boldsymbol{F}$	Deformation gradient
$\boldsymbol{F}^c$	Chemical distortion
$\boldsymbol{F}^e$	Elastic distortion
$\mathcal{G}$	Free energy
$\boldsymbol{G}$	Left Cauchy-Green strain tensor
$\mathcal{H}$	Electromagnetic energy flux
i	Current density
$\mathcal{I}$	Internal energy
J	Jacobian
J^c	Chemical part of the Jacobian
J^e	Elastic part of the Jacobian
$\mathcal{K}$	Kinetic energy
L	Crack length
$\boldsymbol{L}$	Velocity gradient
$\boldsymbol{L}^c$	Chemical velocity gradient
M	M-atoms
$\boldsymbol{M}^e$	Elastic Mandel stress
$\boldsymbol{M}_{mob}$	Mobility tensor
M^{n+}	Cations
$\mathbf{n}^+$	Outwards normal of Ω_{SE} on Γ^+
$\mathbf{n}^-$	Outwards normal of Ω_{SE} on Γ^-
$\mathbf{n}_\gamma$	Outwards normal of Ω_{SE} on $\Gamma^+ \cup \Gamma^-$
$\boldsymbol{P}$	First Piola stress tensor
q	Quadrature point
$\mathcal{R}$	Reference body
$\boldsymbol{Q}$	Rotation tensor
$\boldsymbol{S}^e$	Second elastic Piola stress tensor
$\mathcal{T}$	The energy carried by species transport
$\boldsymbol{T}$	Cauchy stress tensor
$\mathbf{t}^+$	Tangent of Ω_{SE} on Γ^+
$\mathbf{t}^-$	Tangent of Ω_{SE} on Γ^-
$\boldsymbol{U}$	Right stretch tensor
v	velocity or material time derivative of the deformation
$\boldsymbol{V}$	Left stretch tensor
w	Crack opening
$\mathcal{W}$	External power

Symbol	Definition
$\hat{y}$	Deformation mapping
α	interface status parameter
β	Stabilization parameter
Γ	Centerline of Ω_m
Γ^+	Upper crack surface
Γ^-	Lower crack surface
$\dot{\epsilon}^r$	Volumetric strain rate
η	Shape function
$\delta\eta$	Discontinuous test function
Θ	Thermal production of energy
ξ	Electrodeposition of the electric compound
$\dot{\xi}$	Reaction rate
κ_m	Conductivity of the crack domain
κ_{SE}	Conductivity of the solid electrolyte
μ	Chemical potential
μ^e	Electrochemical potential
ϕ_m	Electric potential of the crack domain
ϕ_m^-	Electric potential at the crack at the lower crack boundary
ϕ_m^+	Electric potential at the crack at the upper crack boundary
$\tilde{\phi}_m$	Average electric potential of the crack domain
ϕ_{SE}	Electric potential of the solid electrolyte
ϕ_{SE}^-	Electric potential at the solid electrolyte at the lower crack boundary
ϕ_{SE}^+	Electric potential at the solid electrolyte at the upper crack boundary
ϕ_{SE}^1	Lower Dirichlet boundary condition
ϕ_{SE}^2	Upper Dirichlet boundary condition
ψ	Free energy density
Ω	Complete domain
Ω_{SE}	Domain of the solid electrolyte
Ω_m	Domain of the electrodeposited crack

List of Figures

List of Tables

1

Introduction

Climate change has become an increasingly important topic over the years, and it has become clear that emissions must be significantly reduced. Aviation is a major industry that has a significant influence on pollution. Only aviation contributes 2.4% to CO_2 emissions and 5% to total non-CO_2 emissions [4]. Many innovations are being developed to reduce aviation emissions. One of the most well-known innovations is the introduction of the electric airplane, but significant improvements are still required before these airplanes can be used for large-scale commercial flights. The crucial component to improve is the batteries. The biggest challenge at this moment is the improvement of the *energy density* (the amount of energy in a given volume) and the *specific energy* (the amount of energy per unit mass) because the values for these quantities are much lower than for liquid fuel [5], resulting in a heavier airplane which is highly undesirable. A solution that has great potential is solid-state batteries, also called All Solid-State Batteries (ASSB). In Figure 1.1, solid-state batteries are compared with Li-ion batteries, which are currently the most commonly used type of batteries. This figure shows that the specific energy and energy density that can be reached with solid-state batteries are significantly higher than for the classical Li-ion batteries. Additionally, solid-state batteries improve safety because the batteries no longer consist of flammable liquids. This is a major advantage in an industry where safety is so important. Therefore, solid-state batteries can make an important contribution to the realization of large-scale electric airplanes. Besides aviation, many other sectors, like the car industry, can greatly benefit from the advantages of solid-state batteries. The most striking advantage is the improved range due to the better battery properties.

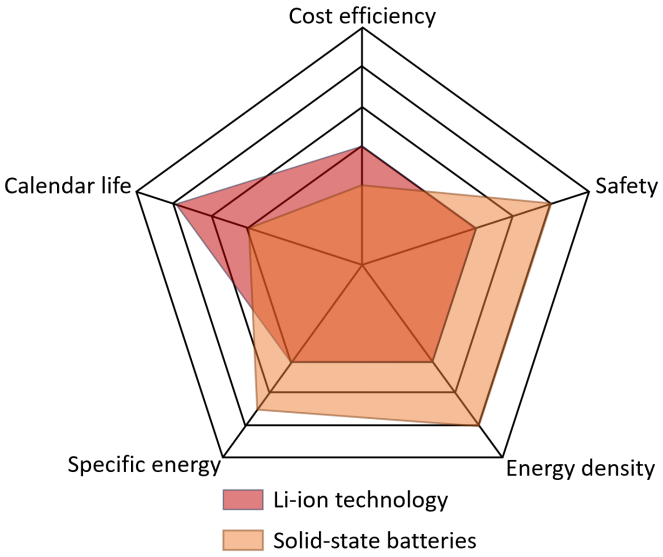

Figure 1.1: Comparison between classical Li-ion batteries and solid-state batteries reveals the significant potential of the latter. The main benefits include high specific energy and energy density. Another crucial improvement point is the battery's lifespan, which is impacted by new failure modes arising from the solid electrolyte. Safety and costs are also important considerations for solid-state batteries. While the safety of solid-state batteries is superior due to the absence of flammable liquids, their costs remain considerably higher. (figure adjusted from [3])

Besides the many advantages, Figure 1.1 also shows the main challenges for the current solid-state batteries. The lifespan stands out the most and is significantly lower than that of Li-ion batteries. The reason for this is new engineering challenges due to the new setup of this battery type. Originally, lithium-ion batteries consist of two electrodes, a liquid electrolyte to allow the movement of lithium

ions between the electrodes and to block the electrons from moving directly from one side to the other, and finally, a separator to prevent contact between the two electrodes. In the case of a solid-state battery, the liquid electrolyte and the separator are combined into a solid electrolyte. The solid configuration of the solid electrolyte results in new challenges at the interface between the electrode and solid electrolyte, such as contact loss and voids. Another major challenge in solid-state batteries is *dendrites*. These small needle-like lithium structures grow through the solid electrolyte, resulting in a short circuit when they reach the other side of the solid electrolyte. Dendrites are also a failure mode in lithium batteries, but the mechanisms of dendrite propagation in solid-state batteries differ fundamentally due to the solid nature of the electrolyte, which introduces the contribution of the microstructure of the solid electrolyte in terms of imperfections. This presents a new problem that must be considered from scratch.

The detrimental effects of dendrite propagation resulting in short circuits are first observed in experimental results when a critical current density is reached [6–8]. Prior to these experimental findings, modeling predictions by Monroe and Newman [9] suggested that dendrite propagation could be suppressed by solid electrolytes if the shear modulus of the solid electrolyte is at least twice as large as that of lithium. However, during the charging cycle of a battery, lithium can electrodeposit into already existing imperfections such as cracks, filling it with lithium and resulting in the formation of dendrites. When the crack is fully filled, the stress on the crack walls increases until the fracture toughness of the solid electrolyte is exceeded, and the crack propagates. Since the model of Monroe and Newman did not capture the described behavior of dendrite propagation, it is crucial to develop new models with this capability. Alternative methods besides experimental results are necessary due to the high costs and time required for experiments.

Reliable models are also essential for finding solutions to increase the lifespan of solid-state batteries. For example, one potential solution to increase the lifespan of solid-state batteries is to deflect the dendrite propagation trajectory by adding a preload, which extends the distance the dendrite must grow before reaching the other side of the electrolyte [10]. The development of such innovations can be significantly accelerated if the propagation behavior can be accurately and consistently modeled to align with experimental results, reducing the need for slow and expensive experiments.

Recently, new methods have been developed to model dendrite propagation in solid-state batteries, always using a form of Phase Field Modeling (PFM). An important reason is that the crack path has no restrictions, allowing the crack to grow in any direction by minimizing the total potential energy. These models define the crack indirectly by a crack zone that diffuses in the surrounding area, meaning that cracks are modeled as a smoothed volumetric phenomenon rather than as the formation and propagation of a sharp discontinuity. Furthermore, due to the lithium deposition inside the crack, the physics within and outside the crack differs and is characterized by different material properties. Inside the crack, the properties of lithium are considered, and outside the crack, the properties of the solid electrolyte material are used. However, this modeling method has the consequence that the cracked and uncracked parts are treated as a single material despite the significant differences in material properties between them. Interpolation functions are used to compensate for the difference in material properties between the two parts. However, these functions are arbitrary and strongly influence the description of the physics inside the crack. In conclusion, while this method can accurately determine the crack path using a mathematical approach, some crack characteristics are neglected, and the arbitrary interpolation functions influence the modeling of the physics inside the crack.

An alternative approach to determine dendrite propagation is through discrete modeling methods. These methods introduce the crack as a discontinuity in the mesh, naturally splitting the cracked and uncracked parts into two different domains. This eliminates the need for interpolation functions and enables the possibility of formulating a computational model that couples the physics of the internal crack with the adjacent environment. The methodology can be applied to all discrete approaches, but this work specifically considers Discontinuous Galerkin Cohesive Zone Modeling (DG-CZM).

The methodology is applied to dendrite propagation, a highly coupled problem that combines three areas of physics: chemistry, electronics, and mechanics. Specifically, this work applies the new methodology to the electronic governing equations, which will be verified using an analytical model of a

simplified configuration and through a quantitative comparison with one of the phase field models.

As discussed above, this research aims to develop a new discrete model for dendrite propagation in solid-state batteries, focusing on the electro-mechanical coupling. This leads to the following main question:

Research question (RQ)

Is it possible to formulate a computational model that accurately and efficiently captures the coupling of in-crack physics with the adjacent environment, while explicitly describing the crack as a sharp discontinuity?

The report's structure is as follows: Chapter 2 contains a literature overview of previous work and consists of two parts. The first part focuses on the physics occurring in solid-state batteries, while the second part discusses in more detail the modeling methods previously used to model dendrite propagation. Chapter 3 gives an overview of the governing equations used to model solid-state batteries. Chapter 4 shows the derivation to obtain the new model, verified in Chapter 5, which consists of the derivation of an analytical model used in combination with the work of Bistri and Leo to verify the results. Chapter 6 discusses the conclusions and provides recommendations. The appendices are used to show a more detailed derivation of the governing equations.

2

Literature study

This chapter reviews the literature concerning previously conducted research on modeling phenomena in solid-state batteries, with a primary focus on dendrite propagation. Three modeling methods are introduced, which are either used or could be used to capture this phenomenon. The previous work on modeling dendrite propagation or similar examples is discussed for all these models, aiming to define the research gaps for modeling dendrite propagation in solid electrolytes.

2.1. Physics of solid-state batteries

This chapter describes the physics occurring in solid-state batteries and is divided into two main parts. The first part introduces the processes that occur in batteries and are the foundations for the phenomena described in the second part of this chapter.

2.1.1. Electrochemical background of batteries

The main components of a battery include the positive and negative electrodes and the electrolyte. The electrolyte, which functions as an ion conductor and electronic insulator, contains a mixture of negatively charged ions (*anions*) and positively charged ions (*cations*). The negative electrode, commonly referred to as the *anode*, and the positive electrode, known as the *cathode*, must not come into contact with each other to prevent an uncontrollable chemical reaction leading to a short circuit. Therefore, a physical separator is placed between the electrodes. In the case of a solid-state battery, the separator and the electrolyte are combined into a solid electrolyte.

Generally, two types of solid electrolytes can be distinguished: organic and inorganic. Organic electrolytes are composed of polymers, offering lower ionic conductivity but flexibility. On the other hand, inorganic electrolytes are made from ceramics or glasses, generally providing higher ionic conductivity, mechanical strength, and resistance against chemical degradation compared to organic ones. However, these electrolytes are brittle and have poor interfacial contact with the electrode, increasing the likelihood of voids [11]. The detrimental effects of voids are discussed later when a closer look is taken at the phenomena occurring in solid-state batteries.

Another innovation closely related to solid-state batteries is the *composite electrode*. This innovation goes even further by combining the solid electrode with the *active materials* (the parts that undergo chemical reactions) through embedding these particles in the solid electrolyte. This not only improves ionic conduction but also reduces the impact of one of the new challenges arising from the introduction of the solid electrolyte. Volume changes of the electrode during the chemical reactions result in increased stress and strain in the solid electrolyte, a phenomenon not encountered with liquid electrolytes [12].
When a battery is connected to an external circuit, a *redox reaction*, which involves the simultaneous occurrence of reduction and oxidation reactions, takes place. At the negative electrode, the first *half-cell reaction* occurs, resulting in the loss of an electron to the external circuit and the formation of cations. This loss of electrons is called oxidation. The second half-cell reaction takes place at the positive electrode, where the electrons move through the external circuit to the positive electrode and are accepted

by it, a process known as reduction. Additionally, the cations transfer from the negative to the positive electrode and react with the electrode, a process called *intercalation*. During intercalation, ions are reversibly included in the available sites of the host material due to the redox reaction occurring at the electrode interface, ensuring that electroneutrality is maintained. *Deintercalation*, the opposite process, occurs at the negative electrode. When the battery is recharged, an external load is applied, reversing the process. This means that electrons and ions move back from the positive to the negative electrode [13].

Referring to the positive and negative electrodes as the anode and cathode can be confusing because the anode is where oxidation occurs, while the cathode is where reduction occurs. This holds during battery discharge, but the process reverses during charging. Thus, oxidation occurs at the positive electrode, and reduction occurs at the negative electrode. Therefore, to avoid confusion, the terms 'negative' and 'positive' electrodes will be used to denote the anode and cathode, respectively.

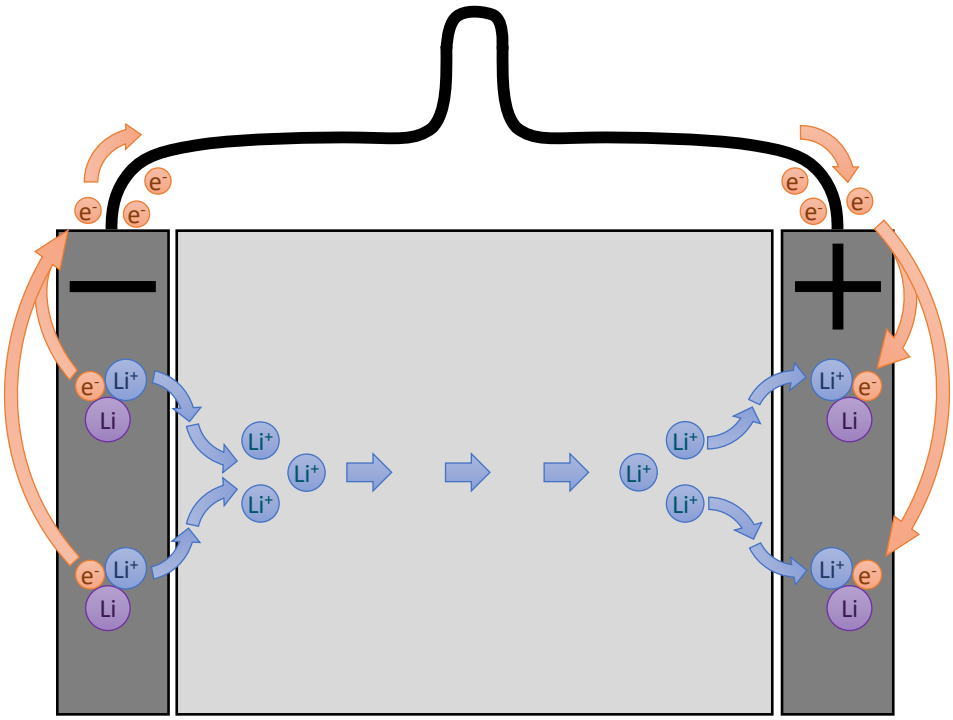

Figure 2.1: A schematic picture of a solid-state battery's electrodes and solid electrolyte connected to an external circuit. At the negative electrode, the oxidation process occurs, resulting in the formation of electrons and cations. The electrons are lost to the external circuit, while the cations migrate to the solid electrolyte, where they begin moving toward the positive electrode. The electrons and cations recombine at the positive electrode, leading to a second chemical reaction called reduction, which forms lithium atoms.

Mass transfer in electrochemical systems comprises three components: migration, diffusion, and convection [14]. However, it is generally assumed that convection is absent [15]. Consequently, mass transfer in batteries is described by *migration* and *diffusion*. Migration is driven by the presence of an electric field, which leads to the transfer of cations from the negative to the positive electrode. The electric field is generated by the *electropotential*, the potential difference between two points in an electrochemical system established between the positive and negative electrodes. Conversely, diffusion is driven by the *concentration gradient*, the difference in concentration between two points in space, causing ions to move from high to low-concentration areas. Consequently, ions move from the negative to the positive electrode [14].

When the battery is uncharged, the electropotential and concentration gradient between the positive and negative electrodes decrease until the battery is empty. At this point, the driving forces for the movement of the electrodes and ion transfer become too low.

In the half-cell reaction at the negative electrode, the active material releases electrons, producing cations. The amount of current provided by this reaction is determined by Faraday's law, which relates the current flowing through the external system to the number of moles of active material involved in the half-cell reaction using Faraday's constant. This constant represents the electric charge of one mole of electrons during the half-cell reaction [14].

The current requirements for various applications vary significantly. For instance, batteries used in smartphones are much smaller than those used in cars. Therefore, current is normalized by introducing the concept of *current density*, which is calculated by dividing the current by the electrode area. This normalization is chosen because electrochemical reactions primarily occur at the surface of the electrode [14].

2.1.2. Electrochemical phenomena in solid-state batteries

This section describes the most important phenomena occurring in solid-state batteries, which influence the modeling of dendrite propagation in solid electrolytes or similar problems. The following phenomena will be discussed:

1. **Active materials:** The effect of active materials is not directly connected to the modeling of dendrite propagation in the solid electrolyte. However, due to the limited amount of research performed on modeling dendrite propagation, crack propagation of the electrode is considered as inspiration for modeling dendrite propagation in solid electrolytes.
2. **Interphase layers:** Interphase layers influence the electrode volume. An increase in volume results in stress on the solid electrolyte and coupling between the mechanical and chemical behavior of the solid-state battery.
3. **Dendrite growth:** Dendrite growth is the main phenomenon considered in this thesis and discussed in more detail.
4. **Voids**: Voids are closely related to dendrites, which significantly influence the formation of dendrites.

Active materials

The active materials in a battery are the components that undergo chemical reactions during the charging and discharging processes. Generally, these materials are located in the electrodes. The insertion or extraction of lithium into/from the active materials of the electrode causes deformations and volume changes, which can be as high as 10% for batteries with a liquid electrolyte [16]. This type of electrolyte allows the swelling of the electrode, which reduces mechanical stress and does not result in destructive failure. However, in solid-state batteries, the solid electrolyte prevents the swelling of active materials, leading to high stresses in the electrode and solid electrolyte, which may cause fracture in these components [17].

Crack propagation in the active parts or electrodes of the battery shares many similarities with modeling cracks in the solid electrolyte. The main differences lie in the driving forces. For electrodes, these are the diffusion of particles and stresses arising from chemical reactions. In contrast, for the solid electrolyte, the driving forces are ionic diffusion, migration, and the formation of dendrites in defects. Despite these differences, crack models of active parts can still inspire fracture models for the solid electrolyte [18].

Interphase layer

Solid electrolytes that conduct lithium ions are generally chemically unstable when in contact with lithium. During charging, this results in a reduction reaction that forms an irreversible *interphase layer* between the negative electrode and solid electrolyte interface, accompanied by volume expansion. However, the solid electrolyte constrains the volume expansion, resulting in internal stresses and possible fracture of the solid electrolyte. Three possible SE/lithium interfaces can occur depending on the solid electrolyte material. The first possibility is a thermodynamically stable interface preventing the formation of an interphase layer. This is the ideal situation but does not exist in currently used solid electrolytes [19]. The second possibility is a thermodynamically unstable interface resulting in an interphase layer isolating electrons and conducting ions. This process is automatically stopped after

the first cycle of the solid-state battery because the interphase layer blocks the electrons, preventing the continuation of the reduction process, as shown schematically in Figure 2.2a. The last possibility is an unstable thermodynamical interface causing the formation of a Mixed Ionic-Electronic Conductor (MIEC). This interphase layer conducts, besides the ions, also the electrons, so the interphase layer never stops the reduction process. This means that the interphase layer keeps growing every cycle, resulting in uncontrolled growth of the interphase layer [19]. A schematic view of this interphase layer is shown in Figure 2.2b.

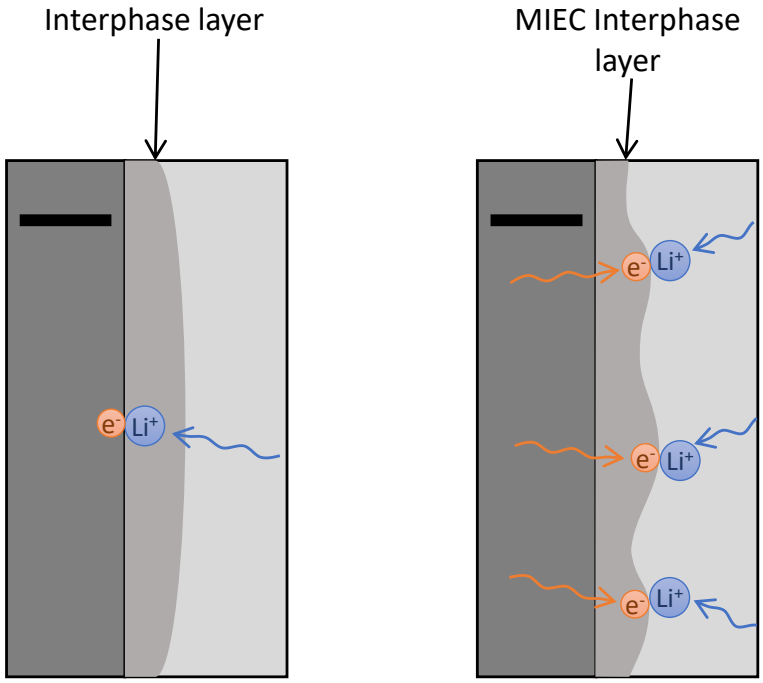

(a) Schematic view of an electronic insulator and ionic conductor interphase layer. The interphase layer blocks the electrons, preventing the reaction at the side of the solid electrolyte, making further growth of the interphase layer impossible. A reaction at the electrode side remains possible because the interphase layer accepts the ions coming from the solid electrolyte.

(b) Schematic view of the MIEC layer, an interphase layer that is both an electronic and ionic conductor. This means that the electrons can still move through the interphase layer and react with the lithium ions, causing an MIEC layer that keeps unstably growing every charging cycle.

Figure 2.2: Possible interphase layers at the electrode solid electrolyte interface

Dendrite growth

Dendrites are needle-like structures consisting of lithium, typically caused by unstable lithium deposition at the interface between the electrode and solid electrolyte [20]. The processes behind lithium deposition at the interface are known as *plating* and *stripping*. During plating, a reversible layer of lithium deposits on the electrode due to a reduction reaction of the lithium ions from the solid electrolyte. Stripping, the opposite reaction, occurs during battery discharge when the lithium layers oxidize and dissolve back into the solid electrolyte [21]. This process results in significant volume changes of the anode, inducing high stresses in the solid electrolyte [22].

Plating and stripping occur independently of the formation of an interphase layer. Despite the presence of the interphase layer, lithium ions, and electrons still react at the interface between the interphase layer and the negative electrode, as illustrated in Figure 2.2a. Consequently, lithium continues to be deposited on the electrode, forming an additional layer [23].

It was initially anticipated that the introduction of solid electrolytes would prevent dendrite formation due to their higher stiffness and toughness compared to lithium. However, experiments have demon-

strated that lithium can still penetrate the solid electrolyte and reach the cathode, leading to a short circuit [17].

There is ongoing discussion and disagreement regarding the failure mechanisms underlying dendrite propagation through inorganic solid electrolytes. Two possible failure mechanisms have been proposed.

The first possibility suggests that dendrite penetration is driven by mechanical failure. Dendrites exhibit a morphology similar to cracks, and the fracture toughness of inorganic solid electrolytes is low [24, 25]. Consequently, during lithium deposition, stress increases at flaws in the interface between the electrode and the solid electrolyte until the fracture strength of the solid electrolyte is exceeded [24]. The size and distribution of surface defects play a significant role in this failure mechanism, although it occurs only above a certain critical current density (the maximum current density without negative side reactions) [24].

The second possibility arises from observations of lithium deposition within the bulk of the solid electrolyte. Over time, chemical processes may increase the electro-conduction of the solid electrolyte, facilitating reduction within the solid electrolyte itself, leading to dendrite growth at this location [26].

Fincher et al. have shown experimentally the relation between the formation of dendrites and crack growth. The authors created a test setup that can induce plating, resulting in a plating pressure in initial flaws. This will drive the dendrite growth. A mechanical compression load is added to balance the increased internal stress due to the plating pressure [10].

The authors developed a fracture mechanics model to support the experiments, assuming that only the plating pressure does not change the trajectory of the dendrite propagation. The dendrite propagation can be deflected when an additional load is applied. The stress state at the crack tip becomes a superposition of both loads. The angle at which the mode I stress intensity factor becomes maximum is called the favorable propagation angle.

This model can determine if experimental results are in agreement with mechanical or chemically driven dendrite growth. If the plating pressure matches the fracture stress of the solid electrolyte, the failure is mechanically driven. However, if the plating pressure is far below the fracture stress of the solid electrolyte, the dendrite growth is due to the chemical processes. The experimental results show a plating pressure that is close to the fracture stress of the solid electrolyte, which indicates that dendrite propagation is a fracture process.

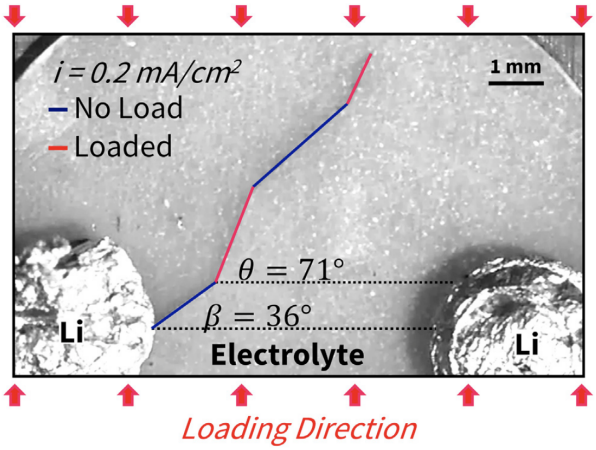

Figure 2.3: Effect of applied load on propagation angle (Propagation angle of 0° results in the fastest trajectory to a short circuit). In the first instance, no load is applied, resulting in a propagation angle of 36° (blue line in the figure), but when the load is applied, the propagation angle is increased to 72° (red line in the figure), making the distance to the other side of the solid electrolyte longer. When the load is removed, the propagation angle decreases again to 36°, and when the load is applied for a second time the propagation angle increases again to 72° [10]

The second part of their research focused on the effect of the compression load on the trajectory of dendrite propagation. If the load can be deflected so that the dendrites no longer grow in the direction of the positive electrode, a short circuit in the batteries can be delayed or even prevented. This can be achieved with a compression load that changes the favorable propagation angle. During the experiments, a mechanical load is applied to achieve this effect. Such loads can arise in solid-state batteries due to thermal or chemically induced stresses, for example, from thermal expansion mismatches of components in the battery. The experiments demonstrate that an in-plane stress of 150 MPa is sufficient

to align dendrite propagation with the loading direction and deflect it away from the electrode. This holds true regardless of the original direction of dendrite propagation. Results of dendrite trajectory deflection are shown in Figure 2.3 and Figure 2.4.

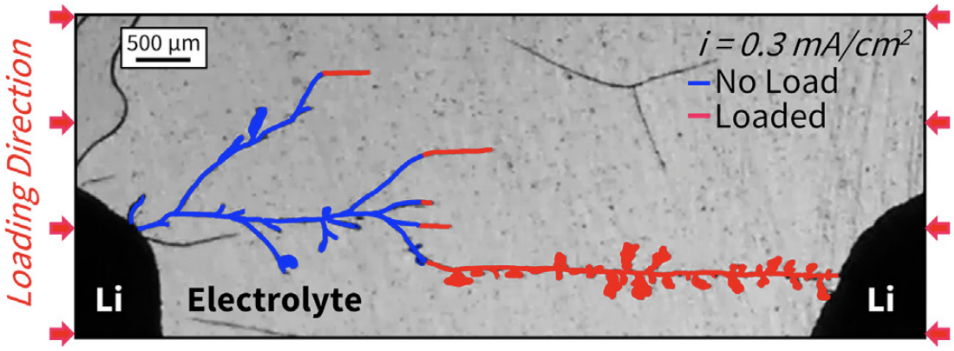

Figure 2.4: Response of dendrite growth on the applied load. The blue parts show the initial growth before applying the load, while the red parts show the propagation after the load is applied, resulting in the deflection of the dendrite trajectory in the direction of the applied load. [10]

The final important note of the paper concerns the stack pressure applied to solid-state batteries. The stack pressure enhances the critical current density and promotes uniform deposition of lithium. However, this pressure is directed toward the electrodes, which reduces the propagation angle, shortening the distance between both electrodes and accelerating the occurrence of a short circuit. This is illustrated schematically in Figure 2.5.

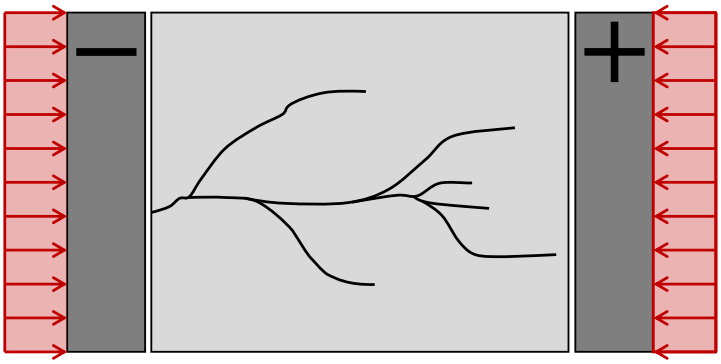

Figure 2.5: Schematic view of dendrite propagation in the solid electrolyte due to the stack pressure. The dendrite trajectory is deflected toward the stacking load, representing the shortest path to the opposite side of the solid electrolyte, thereby reducing the time until a short circuit occurs.

Voids

Voids and contact loss between the electrode and solid electrolyte are newly arising challenges introduced by solid-state batteries. Classical liquid electrolyte batteries do not face these issues due to the excellent wetting properties of the liquid electrolyte. However, the plating and stripping cycle in solid electrolytes leads to the formation of voids and contact loss [18].

The nucleation of voids depends on vacancy diffusion and stripping mechanisms. As long as the current density is not sufficiently high, the stripping rate remains lower than the vacancy diffusion. In this situation, vacancy diffusion can compensate for the stripping, and the interface remains structurally stable. When the current density reaches a certain value, the stripping rate becomes too high, and the vacancy diffusion can no longer compensate for the stripping. This results in the nucleation of voids and contact loss, as shown in Figure 2.6b. When the process is reversed, and plating occurs (Figure 2.6d), the voids can be reversed, improving the surface contact. In most situations, the voids do not disappear completely, but an occluded void remains after the plating process, as shown in Figure 2.6e [20, 27].

Another possibility to reduce void formation is applying pressure on the electrode, which can result from the stacking pressure. This leads to the viscoplastic flow (the time-dependent irreversible strain of solids) and creep of the lithium, which can partially compensate for the empty area resulting from stripping. This is illustrated in Figure 2.6c [20, 27].

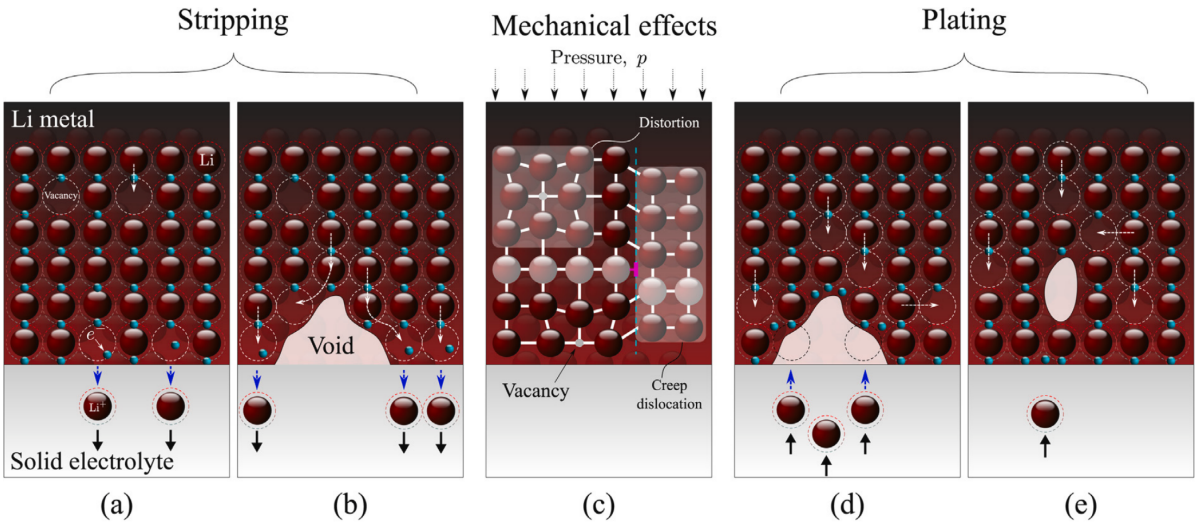

Figure 2.6: (a) Initially, no voids are present in the electrode during the first stripping cycle. (b) As the stripping rates increase beyond what vacancy diffusion can fully compensate for, voids begin to form. (c) Applying pressure can suppress void formation by causing void closure through the creep and viscoplastic behavior of the lithium. (d) The void formation is reversed during the plating process. (e) The voids are only partially undone, resulting in their occlusion [20].

Voids also have a local effect on the current density, resulting in current hot spots at the corners of the voids (see Figure Figure 2.7b) [27]. Current hot spots have a similar effect as mechanical stress concentrations and locally result in high current values. Kasemchainan et al. have shown that dendrite formation and propagation are sensitive to the stripping and plating current [28], and as already mentioned in section 2.1.2, dendrite growth only occurs above a minimal current density. Therefore, the current hot spots are critical locations where dendrites can arise, as shown schematically in Figure Figure 2.7c. Another effect of the current hot spots is the nucleation of dendrites below the general threshold current density because the threshold value of the current density can be exceeded locally. At these locations, dendrite nucleation is still possible [28]. This illustrates the close relationship between voids and dendrites.

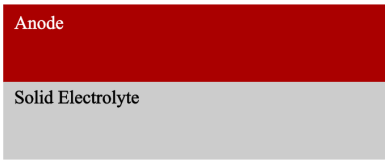

(a) The initial interface between the electrode and solid electrolyte before the occurrence of voids and dendrites

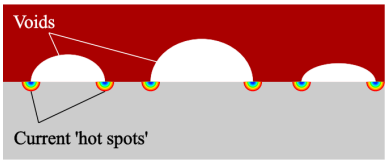

(b) The plating and stripping resulted in the formation of voids with current "hot spots" at the corners of the voids.

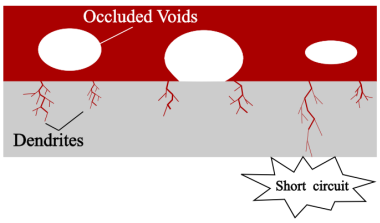

(c) The current "hot spots" have contributed to the formation of dendrites at these locations, eventually resulting in a short circuit.

Figure 2.7: The interplay between voids and dendrite formation and growth.[20]

2.2. Modeling of dendrites in solid-state batteries

This chapter describes previous work on fracture modeling in solid-state batteries. The fracture modeling methods can be roughly divided into discrete and continuum damage models. On the one hand, the discrete models introduce the crack as a discontinuity in the mesh. On the other hand, in continuum damage models, the crack is represented by damage variables describing the material's damage status [29]. In the case of solid-state batteries, the damage is mainly modeled by the cohesive zone model and phase-field models, and recent work has also combined the two models. Cohesive zone modeling can be categorized as a discrete model, while phase-field modeling is in the direction of continuum damage models.

2.2.1. Phase field modeling

Phase-field modeling is the most commonly used method for modeling crack propagation and dendrite growth in solid-state batteries. In this method, the phase-field variable defines the crack and diffuses into the surrounding area. This variable is obtained by minimizing the total potential energy of the computational domain. Therefore, by minimizing the energy, the crack path is determined. This approach ensures that the crack path can be determined without restriction, allowing the crack to grow in any direction. Since the crack is modeled as a diffusive zone within the surrounding area, both the cracked and uncracked parts are represented as a single material. Interpolation functions are employed to address the differences in properties between these parts [2]. However, these functions are purely mathematical and lack physical significance. The variable controlling the width of the diffusive zone is known as the length scale l_0. For a long time, the physical interpretation of the length scale remained unclear [29]. However, Talamini, Mao, and Anand have linked the length scale to the critical energy release rate [30, 31].

Bistri and Leo have formulated a thermodynamically-consistent electro-chemo-mechanical gradient theory to couple electrochemical reactions with mechanical deformations and damage in solids [2]. This theory combines species transport due to diffusion and migration with electrochemical reactions at damaged zones of the host material, resulting in the reduction of ionic species and the formation of new compounds. The theory couples mechanical deformations to electrodeposition. Electrodeposition results in mechanical deformation, stress generation, and damage to the material. On the other hand, mechanical stresses also influence electrodeposition kinetics. The theory combines chemical, electrical, and mechanical effects in a thermodynamically consistent way and defines the contributions of all three mechanisms. The last part of the theory governs the effect of crack growth due to electrodeposition inside the crack.

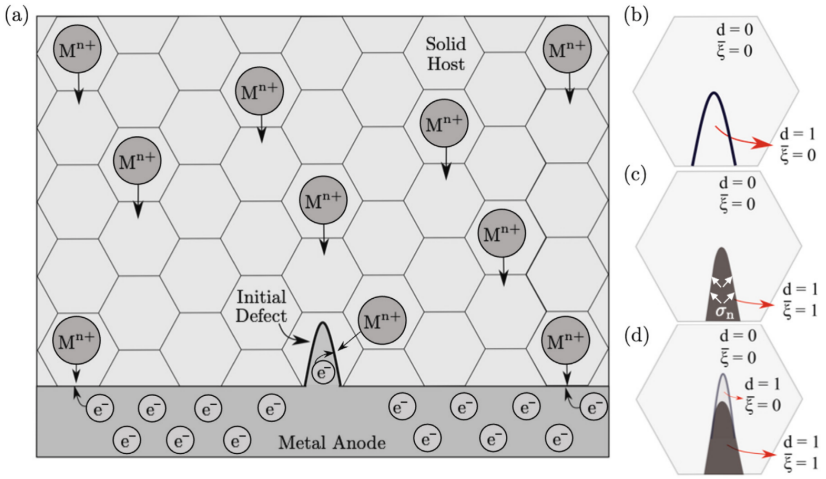

Figure 2.8: (a) A schematic view of a negative electrode and solid electrolyte. (b) A pre-defined crack before lithium is deposited inside of the crack. (c) The lithium is fully deposited inside the crack, and stress increases at the crack surfaces. (d) The stress exceeds the fracture toughness of the solid electrolyte, resulting in the propagation of the crack. [2]

Two phase-field variables are used to model electrodeposition and crack growth: $\bar{\xi}$ for the deposition of lithium and d for the damage state of the solid electrolyte. In the model, electrodeposition occurs only at locations with defects (voids or cracks) because research by Fincher et al. has shown that a defect must be present to ensure vacant space for dendrite growth. At damaged locations, the phase-field parameter $\bar{\xi}$ can vary between 0 and 1. When $\bar{\xi} = 0$, there is no electrodeposition, and when $\bar{\xi} = 1$, the maximum deposition of lithium has been reached. Similarly, the damage state d can vary between 0 and 1, where $d = 0$ indicates no fracture at that location, and $d = 1$ indicates a fracture at the position. Lithium is deposited at this location if there is a defect in the model ($d = 1$), and the crack is filled. When the crack is fully covered by lithium ($\bar{\xi} = 1$), the stress on the crack surface builds up until the fracture toughness is exceeded, and the damage progresses. Lithium can then be deposited at the newly damaged area, and the process will be repeated until the other end of the solid electrolyte is reached, resulting in a short circuit. The constant lithium deposition in defects creates high compressive stress, causing the lithium to flow plastically due to the low yield strength of lithium. This could result in lithium flowing out of the crack along the interphase between the solid electrolyte and the electrode.

The lithium is deposited in defects due to plating, but during discharging, it is resolved back into the solid electrolyte due to the stripping process. However, this only occurs partly because the stripping rate is lower during discharging [32]. Nevertheless, this aspect is neglected in the model proposed by Bistri and Leo as it focuses on dendrite growth. Additionally, plating and stripping are difficult processes to model. The difficulties in modeling this process are twofold. On the one hand, it is challenging from a continuum mechanics perspective because lithium is constantly deposited on the lithium layer, resulting in a reference configuration that is not fixed. On the other hand, it is also challenging from a computational finite element modeling perspective because elements must be constantly inserted at the interface. Narayan and Anand have formulated a mechanical theory to model this process by replacing the electrochemical processes of plating and stripping with an analogous mechanical swelling and deswelling problem of an interphase layer [33].

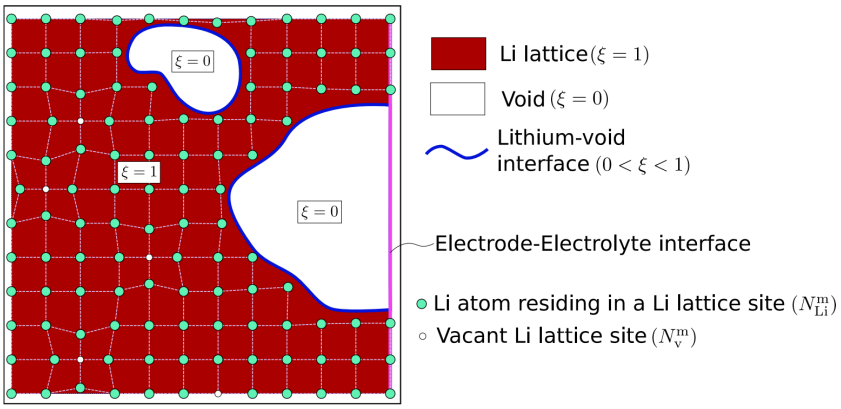

Figure 2.9: A phase field model is employed to describe the formation of voids. This illustration depicts the sites within a volume V of lithium metal. The red portion represents the lithium lattice, corresponding to $\xi = 1$. The white areas denote the voids, where $\xi = 0$. At the interface between the lithium and the void, indicated by the blue line, the value of ξ can vary between 0 and 1. [20]

Contact between the electrode and solid electrolyte interface is assumed to always be perfect. Therefore, voids are not considered in the model. A model for predicting void formation at the electrode and solid electrolyte interface is developed by Zhao, Wang, and Martínez-Pañeda. As mentioned before, stripping is a driving force in the formation of voids, so the phenomena neglected in the work of Bistri and Leo are closely studied in this work. A phase field model is used to describe the evolution of voids in the electrode (see Figure 2.9 for a schematic overview of the model). To achieve this, the phase field parameter ξ is introduced. At void locations, $\xi = 1$, and at lithium sites, $\xi = 0$. The value of ξ can vary between 0 and 1 at the boundary between the void and the lithium. Vacancy diffusion, as well as lithium dissolution and deposition, dominate the evolution of this parameter. Additionally, the mechanical response of lithium is characterized by the elastic-viscoplastic theory proposed by Narayan and Anand. In the final part of this work, the interaction between the electrode and the solid electrolyte is considered to solve the coupled electrochemical mechanical problem in the electrode and solid electrolyte. This enables the determination of local current hot spots, which are important for dendrite nucleation. The simulations focus on void evolution and current hot spots as a function of pressure. The obtained results align with experimental findings [20]. This work focuses in detail on void formation but does not address closely related dendrite propagation.

Returning to the theory proposed by Bistri and Leo, this work is formulated to have general applicability. However, its primary focus is on dendrite growth in solid-state batteries. Consequently, simulations are conducted to address this specific issue. The initial simulations consider the solid electrolyte as a homogeneous material without grain boundaries. In these simulations, the growth of a small initial defect at the interface between the electrode and the solid electrolyte, arising from coupled electro-chemo-mechanical phenomena, is demonstrated. This combines dendrite growth alongside crack propagation. Subsequently, the simulations move to a microstructural level by incorporating the presence of grain boundaries. In these models, the effects of microstructures on dendrite growth resulting from coupled electro-chemo-mechanical interactions are simulated [2].

Yuan et al. formulated another electrochemical and mechanically coupled phase-field model for modeling crack propagation and dendrite growth in solid electrolytes. Important factors in the model include the interfacial defect and stacking pressure. In the initial scenario of the model, a pre-defined defect is present, already fully filled with lithium. The driving forces behind further crack propagation and dendrite growth are the strain energy density caused by stacking pressure and the negative potential resulting from chemical reactions. Additionally, the concentration gradient of lithium ions decreases in the area of dendrite growth due to plating, leading to the formation of dendrites. The phase field parameters govern the evolution of concentration. The results indicate that dendrite and crack growth mainly occur at grain boundaries and cracked areas. The growth of dendrites and cracks depends on the pre-defined defect. A sharp edge or long length of defects promotes the growth of dendrites and cracks. Furthermore, stacking pressure accelerates dendrite and crack growth when it exceeds 10 MPa

[35].

In a second research, Yuan, Lu, and Xu developed a physics-based electrochemical-mechanical coupled model consisting of four parts: a battery model for solving the concentration and potential changes in the electrodes and electrolyte during charging and discharging, a mechanical model to obtain deformations, stresses, and strain, a phase-field model for describing crack and dendrite growth, and a short-circuit model for detecting short-circuits and determining short-circuit resistances. Although this work is closely related to the previous work of Yuan et al. [35] described above, the relation between both works is not discussed in this second work. The model assumes a pre-defined defect at the interface between the negative electrode and electrolyte. Perfect interface contact is also assumed, and no stacking pressure is applied. The results of their work show that a higher charging rate results in a higher overpotential, promoting crack and dendrite growth. Another factor contributing to increased overpotential is the conductivity of the solid electrolyte. Low solid electrolyte conductivity increases the overpotential, accelerating the growth of cracks and dendrites. Another important factor is Young's modulus. It affects both the driving force and resistance of crack and dendrite growth, with crack and dendrite growth being maximally promoted when the modulus is in the range of 40 to 100 GPa. The last factor investigated in this work is fracture toughness. High fracture toughness can suppress dendrite growth [36].

The works of Bistri and Leo and Yuan et al. do not cite each other. One possible reason for this is the difference in research areas between the two authors. Bistri and Leo focuses on continuum modeling of the problem, while Yuan et al. focuses on the material physics aspect of the problem.

2.2.2. Cohesive phase field modeling

As mentioned earlier, the length scale is related to the critical energy release rate. However, chemically induced diffusion also influences fracture properties, such as fracture energy. This means that the length scale becomes a function of concentration, which is undesirable [37]. Therefore, the Cohesive Zone Model and Phase Field Model are combined to formulate a cohesive phase-field (CPF) model, making the formulation almost insensitive to the length scale. Rezaei et al. has formulated a cohesive phase-field model by adding directional dependence of material strength in addition to fracture energy. The length scale becomes a numerical parameter and must be small enough. Cohesive phase-field models have two main advantages: the physics becomes more evident due to the introduction of strength and fracture energy, and the mesh can become coarser because the length scale can be chosen larger. With this method, capturing mode-dependent fracture is not yet possible, and plasticity and large deformation are not included in the formulation [38].

Rezaei et al. applied cohesive phase-field models to determine damage initiation and growth in an electrochemical and mechanically coupled environment [37]. However, this work focuses on crack growth in active parts of solid-state batteries and composite electrodes. The driving forces in these areas are diffusion and reaction-induced stress [18]. Therefore, the electropotential is neglected, resulting in the absence of migration, which is an important driving force for crack growth in solid electrolytes. Additionally, the model does not include the effect of depositing lithium in damaged areas. Hence, dendrite growth is also not considered in this model.

2.2.3. Cohesive zone modeling

Physics is deeply embedded in a cohesive zone model. Tractions $\boldsymbol{t}$ are determined to resist the separation of two interfaces, while the *displacement jump* (the difference between the two sides of the cohesive zone) $\Delta := [\![\boldsymbol{u}]\!]$ is related by a phenomenological traction-separation law (TSL). The tractions in this law are described by a constitutive equation $\boldsymbol{t}(\Delta)$ and gradually decrease to zero. When the traction reaches zero, the two interfaces are no longer influenced by each other. This occurs when the crack displacement jump exceeds the critical crack opening Δ_c [39].

Two modeling approaches can be distinguished in cohesive zone modeling: the intrinsic and extrinsic methods. In the intrinsic method, the cohesive response is initially elastic, which affects the material's effective elastic response until the onset of fracture. In contrast, the extrinsic method initially responds as a rigid material and cohesive elements are only inserted when a predefined fracture criterion is met.

This necessitates changing the mesh topology, which is complicated with parallel computing [40, 41].

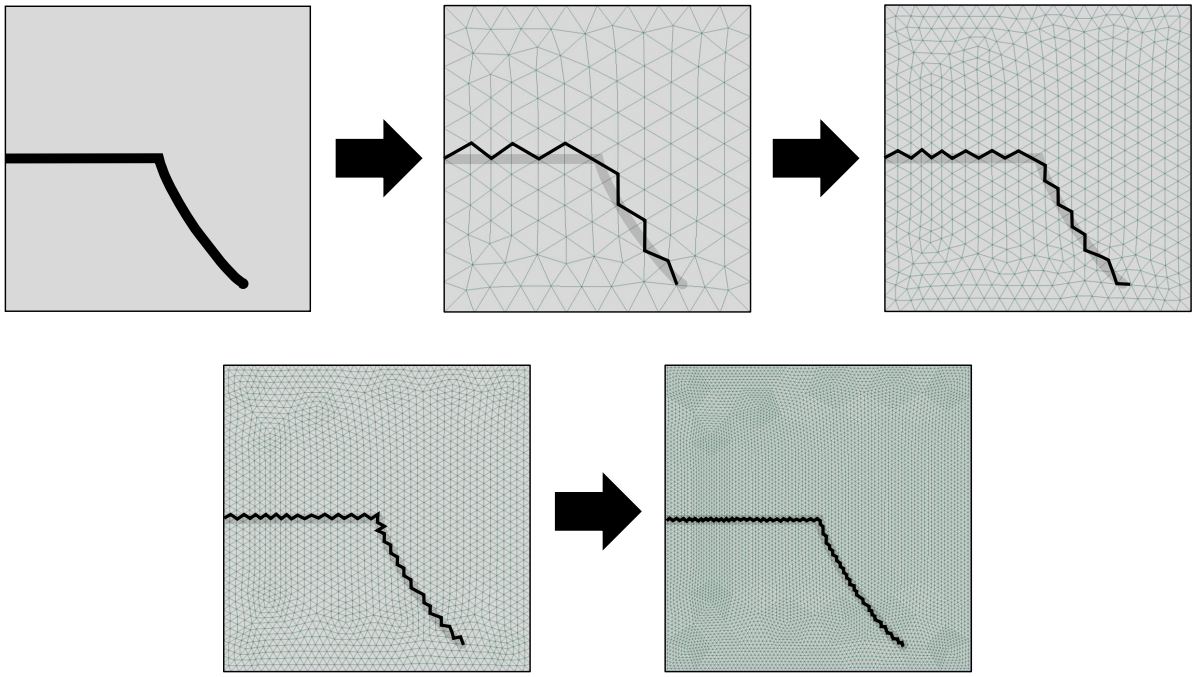

Figure 2.10: Schematic illustration of the effect of mesh refinement on the crack path of an arbitrary crack. The initial image depicts the arbitrary crack, which is subsequently discretized and refined in the following images. With each increment of mesh refinement, the crack path is continuously approximated more closely. Upon reaching the final increment, the crack path can be approached almost perfectly.

The cohesive zone elements are typically implemented at the interface between two elements. Consequently, the element interfaces restrict the crack path, making the method mesh-dependent [39]. Different papers use this as an important reason to use other fracture modeling approaches [18, 37]. R. Radovitzky et al. argued that highly refined meshes can mitigate this limitation, allowing multiple potential failure paths. An example of the effect of mesh refinement is provided in Figure 2.10. Each refinement increment makes the representation of the crack path more accurate. However, this refinement comes at a significant computational cost, necessitating computational schemes that are scalable to accommodate a large number of processors. The Discontinuous Galerkin Cohesive Zone Model (DG/CZM) is a method that guarantees scalability. The parallelization of DG/CZM is easily achieved by employing a parallel Discontinuous Galerkin (DG) model, enabling simulations with highly refined meshes [40].

Due to the challenges mentioned above, cohesive zone modeling is not commonly used in fracture modeling for solid-state batteries. In fact, no complete models are available for fracture modeling in the solid electrolyte. Existing work focuses solely on cohesive zone modeling in (composite) electrodes for solid-state batteries. The main distinctions between fracture modeling of active particles and the solid electrolyte are discussed in Section 2.1.2. Despite the differences in electrode fracture modeling, this research can still serve as inspiration. Consequently, the results obtained from cohesive zone modeling of active components are considered in the subsequent part.

Extensive work on modeling fracture using cohesive zone modeling in composite electrodes has been conducted by Bucci et al. In this work, a composite electrode is modeled, comprising active electrode particles embedded in the surrounding solid electrolyte. The particles are represented as randomly oriented small squares, expanding due to chemical reactions and resulting in high stresses. The composite electrode is modeled in 2D, assuming plane strain to reduce computational costs. The electrochemical-mechanical problem is solved using a Newton-Raphson scheme, considering displacements, lithium concentration, and diffusion potential. The crack propagation aspect of the model is implemented using

intrinsic cohesive zone modeling. The simulations reveal high compression stresses due to expansion. However, small regions around the corners of the particles experience tension, which, depending on the active material and solid electrolyte, can reach levels high enough to initiate cracking. The model predicts that if the fracture energy of the solid electrolyte is sufficiently high ($G_c = 4J/m^2$), the fracture can be suppressed when the expansion of the active material is below 7.5% [41].

Another study using cohesive zone modeling in solid-state batteries is written by Rezaei, Asheri, and Xu. The authors propose a chemo-mechanically coupled cohesive fracture model with mode-dependent cohesive zone damage. The coupling in this formulation involves the mechanical aspect affecting diffusion, while changes in the concentration field alter mechanical properties and damage. The final coupling occurs between the mechanical part and the damage, which influences each other. The traction-separation law used in this study is concentration-dependent, with damage onset in the yield criterion that depends on the concentration. Numerical simulations are conducted to validate the results of diffusion-induced cracks against experimental data. While applicable to solid electrolytes, this model does not incorporate dendrite propagation. Additionally, numerical results of interaction fracture between the solid electrolyte and the electrode are obtained, focusing on the solid electrolyte's impact on crack propagation in the active material [42].

Dendrite-related crack propagation, as discussed previously, results from lithium deposition inside the crack, leading to pressure buildup until the fracture toughness is exceeded. This process exhibits many similarities with fluid-driven crack propagation and could potentially serve as inspiration for modeling dendrite propagation. Giovanardi, Serebrinsky, and Radovitzky has defined a numerical framework for modeling fluid-driven fracture propagation using a hybrid DG/CZM formulation [43]. In this work, a fluid is injected into the crack of a brittle medium at a constant rate. The coupling between the solid and the fluid is two-sided: the fluid applies pressure to the walls of the crack, and the crack geometry of the solid defines the domain of the fluid. The computational framework is verified by comparing the simulations with analytical results of plain-strain and asymmetric cracks, resulting in fluid pressure distributions that align with the analytical models.

2.3. Conclusions from the literature study

The main objective of the literature study was to identify research gaps in modeling dendrite propagation in the solid electrolyte of solid-state batteries. This section provides an overview of these research gaps.

Experiments conducted by Fincher et al. [10] have shown that short circuits caused by dendrite propagation can be delayed or even prevented by applying a load normal to the interface of the electrode and electrolyte. This deflects the propagation trajectory, preventing contact with the opposite electrode. Such a load can be induced by, for example, a thermal expansion mismatch among the different components. However, a dendrite deflection model consistent with these experiments has not yet been developed.

A significant effort in modeling dendrite propagation in the solid electrolyte is demonstrated in the work of Bistri and Leo. This work utilizes a phase-field model to describe dendrite propagation. However, it does not account for the plastic behavior of lithium or the dissolution of lithium during the stripping process. Additionally, it assumes that the contact between the electrode and electrolyte is always perfect.

The work of Zhao, Wang, and Martínez-Pañeda illustrates that dendrite formation and propagation can be significantly influenced by contact loss and the formation of voids. Current hot spots can occur at the corners of the voids, stimulating the plating and stripping processes and facilitating the formation of dendrites. Therefore, combining a dendrite propagation model with a model that predicts void formation can lead to better predictions of dendrite formation and propagation.

The viscoplastic effect of lithium on dendrite propagation remains unclear. One possible effect is that the lithium is pressed outside the crack due to the high pressures at the crack surfaces. However, Klinsmann et al. has argued that this is unlikely to occur. Nonetheless, this does not imply that the viscoplastic behavior of lithium can be entirely neglected, as it may still affect the stress inside the

cracks. Narayan and Anand has developed a model for the large deformation viscoplastic behavior of lithium, which can be used to consider these effects.

Dendrite propagation is solely modeled using phase-field modeling because it allows for the unrestricted representation of the crack path, enabling the crack to grow in any direction. However, this method indirectly models the crack using phase-field variables that diffuse into the surrounding area. The parameter defining the diffusive zone is known as the length scale. The physical interpretation of the length scale remained unclear for a long time, but it has recently been associated with the critical energy release rate. Nonetheless, the length scale remains a challenging parameter, particularly as including chemical reactions in the phase-field model introduces a dependency of the length scale on concentration. Additionally, because of the indirect method of modeling the crack, both the cracked and uncracked parts are treated as a single material. However, since these parts have different material properties, interpolation functions are employed to reconcile these differences. Nevertheless, these interpolation functions are purely mathematical and lack any physical basis. Alternatively, discrete methods offer the potential for more accurate modeling of crack physics, such as cohesive zone modeling (CZM). However, discrete methods have not yet been extensively used to model dendrite propagation, primarily due to their mesh dependence. In CZM, cracks can only initiate at the interface between two elements, necessitating a very fine mesh for arbitrary crack growth, which is computationally expensive. One solution to this challenge is the Discontinuous Galerkin Cohesive Zone Model (DG-CZM), which facilitates parallel computing and thus makes fine meshes feasible.

The following research gaps are identified based on the conclusions outlined above:

1. Developing a discrete modeling method for the modeling of dendrite propagation.
2. Modeling dendrite deflection to prevent short circuits in solid-state batteries.
3. Including large deformation viscoplastic behavior of lithium during dendrite propagation.
4. Combining void formation and dendrite propagation into one model.

The first research gap focuses on a completely different solving method compared to those used in previously developed models. Achieving this research gap could also lead to addressing other research gaps, as they can be integrated into the model seamlessly. The physical basis inside the crack can be exploited by incorporating features such as the large deformation behavior of lithium or by deflecting dendrite propagation. Thus, these additional gaps are well-suited for inclusion in the new model.

3

Governing equations

The governing equations used are derived from the continuum electro-chemical-mechanical theory developed by Bistri and Leo [2], as briefly discussed in Chapter 2. The first part of this chapter summarizes this theory, which applies to a general problem. Secondly, the theory is applied to solid-state batteries, resulting in the applicable governing equations presented in the second part of this chapter. The complete derivation is shown in Appendix B.

3.1. Summary theory

This section summarizes the general theory, covering various aspects such as kinematics and the definition of free energy, stress and force balance, electrochemical and mass balances, electrodeposition kinetics, and electrostatics. The resulting equations for all these topics are presented.

3.1.1. Kinematics and free energy

The deformation gradient is decomposed into the elastic distortion $\boldsymbol{F}^e$ and the chemical distortion $\boldsymbol{F}^m$.

$$\boldsymbol{F} = \boldsymbol{F}^e \boldsymbol{F}^c \tag{3.1}$$

The chemical velocity gradient is given below:

$$\begin{aligned} \boldsymbol{L}^c &= \boldsymbol{F}^c \boldsymbol{F}^{c-1} \\ &= \boldsymbol{D}^c \end{aligned} \tag{3.2}$$

Here, the chemical stretching tensor $\boldsymbol{D}^c$ is defined as follows:

$$\boldsymbol{D}^c = \boldsymbol{D}^r \tag{3.3}$$

The stretching induced by electrodeposition, denoted as $\boldsymbol{D}^r$, is given by:

$$\boldsymbol{D}^r = \dot{\xi} \boldsymbol{N}^r \tag{3.4}$$

Where $\dot{\xi}$ represents the reaction rate, and $\boldsymbol{N}^r$ denotes the direction of the electrodeposition-induced deformations.

Equation 3.5 provides the expression for the free energy:

$$\psi(\Lambda) = \hat{\psi}(\Lambda) \tag{3.5}$$

Here, Λ represents the list of variables:

$$\Lambda = (\boldsymbol{c}, c, \xi, \nabla\xi, \boldsymbol{d}) \tag{3.6}$$

3.1.2. Stress and force balance

The expression for the second Piola stress tensor is obtained in Equation B.120 and repeated below.

$$\boldsymbol{S}^e = \frac{2}{J^c}\frac{\partial \hat{\psi}_x}{\partial \boldsymbol{C}^e} \tag{3.7}$$

The Cauchy stress tensor $\boldsymbol{T}$, the elastic Mantel stress tensor $\boldsymbol{M}^e$, and the first Piola stress tensor P are also defined.

$$\boldsymbol{T} = \frac{1}{J^e}\boldsymbol{F}^e \boldsymbol{S}^e \underline{F}^{eT} \tag{3.8}$$

$$\boldsymbol{M}^e = J^e \boldsymbol{F}^{eT} \boldsymbol{T} \boldsymbol{F}^{e-T} \tag{3.9}$$

$$\boldsymbol{P} = J\boldsymbol{T}\boldsymbol{F}^{-T} \tag{3.10}$$

The stress is governed by the force balance with the corresponding Neumann boundary condition derived in Equation B.62.

$$\begin{aligned} \operatorname{div}(\boldsymbol{P}) + \boldsymbol{f} &= \boldsymbol{0} \\ \boldsymbol{s}(\boldsymbol{n}) &= \boldsymbol{P}\boldsymbol{n} \end{aligned} \tag{3.11}$$

Where $\boldsymbol{s}$ is a prescribed traction.

3.1.3. Electrochemical potential, flux and mass balance

The electrochemical potential is given by Equation B.124:

$$\mu^e = \frac{\partial \hat{\psi}_x}{\partial c} + F\phi \tag{3.12}$$

The referential flux for mobile ionic species is given by Equation B.131.

$$\boldsymbol{h} = -\boldsymbol{M}_{mob} \nabla \mu^e \tag{3.13}$$

Where M_{mob} is a positive semi definite mobility tensor.

The concentration of ionic species transporting the solid host, denoted as c, is governed by the mass balance (Equation B.7), where $\dot{\xi}$ represents the species electrodeposition rate at the reaction site.

$$\dot{c} = -\operatorname{div}(\boldsymbol{h}) - \dot{\xi} \tag{3.14}$$

3.1.4. Reaction driving force: Electrodeposition Kinetics

The electrodeposition driving force is defined in Equation B.129.

$$\mathcal{F} = \mu^{\xi} - \mu^e \tag{3.15}$$

The electrochemical potential of the electrodeposited species is defined in Equation B.127.

$$\mu^{\xi} = \frac{\partial \hat{\psi}_x}{\partial \xi} - E \tag{3.16}$$

The first microforce balance is defined before in Equation B.77

$$\begin{aligned} E - J^c \boldsymbol{M}^e \cdot \boldsymbol{N}^r - \operatorname{div}(\boldsymbol{g}) &= 0 \\ E = J^c \boldsymbol{M}^e \cdot \boldsymbol{N}^r + \operatorname{div}(\boldsymbol{g}) & \end{aligned} \tag{3.17}$$

Equation 3.17 can be substituted in Equation 3.16:

$$\begin{aligned} \mu^{\xi} =& \frac{\partial \hat{\psi}_x}{\partial \xi} - E \\ =& \frac{\partial \hat{\psi}_x}{\partial \xi} - J^c \boldsymbol{M}^e \cdot \boldsymbol{N}^r - \operatorname{div}(\boldsymbol{g}) \end{aligned} \tag{3.18}$$

The vector microstress $\boldsymbol{g}$ is also defined in the derivation by Equation B.122:

$$\boldsymbol{g} = \frac{\partial \hat{\psi}_x}{\partial \nabla \hat{\xi}} \tag{3.19}$$

Equation B.122 can be substituted in Equation 3.18 to obtain the final expression for the electrochemical potential of the electrodeposited species μ^{ξ}:

$$\begin{aligned} \mu^{\xi} =& \frac{\partial \hat{\psi}_x}{\partial \xi} - J^c \boldsymbol{M}^e \cdot \boldsymbol{N}^r - \operatorname{div}(\boldsymbol{g}) \\ =& \frac{\partial \hat{\psi}_x}{\partial \xi} - J^c \boldsymbol{M}^e \cdot \boldsymbol{N}^r - \operatorname{div}\left(\frac{\partial \hat{\psi}_x}{\partial \nabla \hat{\xi}}\right) \end{aligned} \tag{3.20}$$

The reaction kinetics are constrained by the dissipation inequality, as shown in Equation B.133.

$$-\mathcal{F}\dot{\xi} \geq 0 \tag{3.21}$$

3.1.5. Electrostatics

The electropotential is governed by Gauss's law (Equation B.22) and is shown below:

$$\operatorname{div}(\boldsymbol{d}) = q \tag{3.22}$$

In Gauss's law, the expression for the net charge, as defined in the derivation by Equation B.14, can be substituted.

$$\begin{aligned} \operatorname{div}(\boldsymbol{d}) =& q \\ =& F(c - c_0) \end{aligned} \tag{3.23}$$

The electric field is represented by the negative gradient of the electrostatic potential, as given by Equation B.21.

$$\boldsymbol{e} = -\nabla \phi \tag{3.24}$$

The state relations (Equation B.123) are used again to obtain a relation for the electric field:

$$\boldsymbol{e} = \frac{\partial \hat{\psi}_x}{\partial \boldsymbol{d}} \tag{3.25}$$

3.2. Governing partial differential equations

This section presents the full set of governing equations obtained after the complete derivation, which is shown in Appendix B:

1. Force balance defined in Equation B.62.

$$\operatorname{div}(\boldsymbol{P}) + \boldsymbol{f} = \boldsymbol{0} \tag{3.26}$$

   Where the first Piola stress tensor is given in Equation B.191.

2. The local balance for the ionic species is given by Equation 3.27. In this expression, the flux (Equation B.196) is substituted:

$$\begin{aligned} \dot{c} =& -\operatorname{div}(\boldsymbol{h}) - \dot{\xi} \\ =& \operatorname{div}(m \nabla \mu^e) - \dot{\xi} \end{aligned} \tag{3.27}$$

3. The reaction kinetics shown in Equation B.205 is the governing PDE for the reaction coordinate:

$$\dot{\bar{\xi}} = \begin{cases} R_0 \left(e^{\frac{-\alpha \mathcal{F}}{R\theta}} - e^{\frac{(1-\alpha)\mathcal{F}}{R\theta}} \right) & \text{if } 0 < \bar{\xi} < 1 \\ 0, & \text{if } \bar{\xi} = 1 \end{cases} \tag{3.28}$$

   Where the thermodynamic reaction driving force is defined in Equation B.204:

$$\begin{aligned} \mathcal{F} =& \left(\mu_0^{\xi} - \mu_0\right) R\theta \left(\ln \left| \frac{\bar{c}}{1 - \bar{c}} \right| \right) + F\left(\phi_0 - \phi\right) + \frac{\partial}{\partial \xi}\left(W \bar{\xi}^2 (1 - \xi)^2\right) - J^c h(\bar{\xi}) \boldsymbol{M}^e \cdot \boldsymbol{N}^r \\ & - \operatorname{div}(\lambda \xi \nabla \xi) \end{aligned} \tag{3.29}$$

4. The electric potential is governed by Gauss's law (Equation 3.30), and the electric field. The expression of Gauss's law is finalized by substituting the net charge (Equation B.14) into this law.

$$\begin{aligned} \operatorname{div}(\boldsymbol{d}) =& q \\ =& F(c - c_0) \end{aligned} \tag{3.30}$$

Secondly, the electric field (Equation B.21) is substituted in the expression for the electric displacement (Equation B.210):

$$\begin{aligned} \frac{1}{J}\frac{1}{\varepsilon}\boldsymbol{C}\boldsymbol{d} =& \boldsymbol{e} \\ \boldsymbol{d} =& J\varepsilon\boldsymbol{C}^{-1}\boldsymbol{e} \\ \boldsymbol{d} =& -J\varepsilon\boldsymbol{C}^{-1}\nabla\phi \end{aligned} \tag{3.31}$$

Solving ϕ using Equation 3.30 and Equation 3.31 is inconvenient because it requires resolving a boundary layer in the range of a few nanometers, where electroneutral deviations occur. Therefore, in practice, electroneutrality is assumed to solve ϕ, ensuring that the net charge $q = F(c - c_0)$ equals zero. This assumption is used to rewrite Equation B.19.

$$\begin{aligned} \dot{q} =& -\operatorname{div}(\boldsymbol{i}) - F\dot{\xi} \\ 0 =& -\operatorname{div}(\boldsymbol{i}) - F\dot{\xi} \\ \operatorname{div}(\boldsymbol{i}) =& -F\dot{\xi} \end{aligned} \tag{3.32}$$

The referential current density, defined below with κ as the conductivity, is as follows:

$$\boldsymbol{i} = -\kappa\nabla\phi \tag{3.33}$$

Equation 3.32 and Equation 3.33 replaces Equation 3.30 and Equation 3.31.

4

Integrated in-crack formulation with the adjacent environment

This chapter presents the derivation of one of the governing equations into a new hybrid-dimensional formulation, coupling the physics inside the crack with the adjacent environment of the solid electrolyte. This formulation will be discretized using both continuous Galerkin and discontinuous Galerkin methods, resulting in corresponding weak forms. These weak forms are then transformed into local element stiffness matrices.

4.1. Hybrid dimension boundary value problem

The governing equations shown in Equation 3.32 will be written in a hybrid-dimensional formulation proposed by Giovanardi et al.[45]. This formulation allows for the governing equations of both the electrodeposited crack and the bulk of the solid electrolyte to be expressed as a single equation. This is achieved by projecting the governing equations in the tangential direction of the crack, assuming a small crack opening. Specifically, this assumption is represented as $L \gg w$, where L denotes the crack length and w the crack opening.

For convenience, the crack is considered to be horizontal in this derivation, as shown in Figure 4.1. However, in reality, the crack can occur in any direction, which will be accounted for when implementing the model.
Figure 4.1 schematically illustrates a domain Ω that is divided into two subdomains by the crack lips Γ^+ and Γ^-: Ω_m, representing the electrodeposited crack, and Ω_{SE}, the solid electrolyte. The domain Ω can be represented as follows:

$$\Omega = \Omega_m \cup \Omega_{SE} \tag{4.1}$$

At the boundaries of the solid electrolyte subdomain, a Neumann or Dirichlet boundary condition is applied, except for the crack lips. Additionally, the boundary conditions are not allowed to intersect, as shown below:

$$\begin{aligned} &\partial\Omega SE = \partial_N\Omega \cup \partial_D\Omega \cup \Gamma^+ \cup \Gamma^- \\ &\partial_N\Omega \cap \partial_D\Omega \cap \Gamma^+ \cap \Gamma^- = 0 \end{aligned} \tag{4.2}$$

The boundary of the electrodeposited crack subdomain is defined as follows:

$$\partial\Omega_m = \partial\Omega \cap \partial\Omega_{SE} \cup \Gamma^+ \cup \Gamma^- \tag{4.3}$$

The hypothesis of $L \gg w$ facilitates additional assumptions about the normal and tangent vectors depicted in Figure 4.1. Given the significantly longer crack length, it can be inferred that $\mathbf{n}^+ = -\mathbf{n}^-$ and $\mathbf{t}^+ = \mathbf{t}^-$.

Table 4.1: Overview of symbols denoting the domain

Symbol	Meaning
Ω	Complete domain
Ω_{SE}	Domain of the solid electrolyte
Ω_m	Domain of the electrodeposited crack
Γ	Centerline of Ω_m
Γ^+	Upper crack surface
Γ^-	Lower crack surface
$\mathbf{n}^+$	Outwards normal of Ω_{SE} on Γ^+
$\mathbf{n}^-$	Outwards normal of Ω_{SE} on Γ^-
$\mathbf{t}^+$	Tangent of Ω_{SE} on Γ^+
$\mathbf{t}^-$	Tangent of Ω_{SE} on Γ^-
$\mathbf{n}_\gamma$	Outwards normal of Ω_{SE} on $\Gamma^+ \cup \Gamma^-$

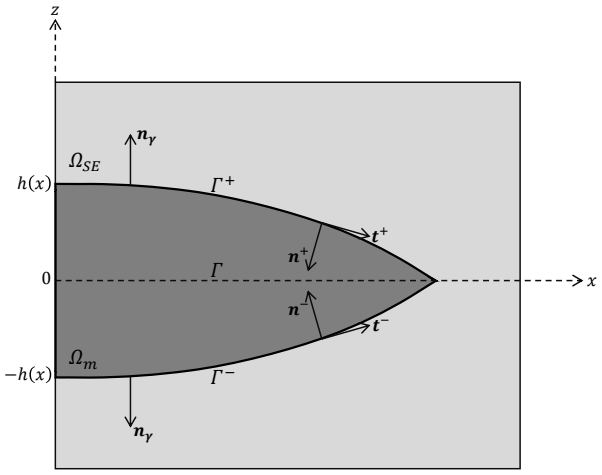

Figure 4.1: Division of the domain into the electrodeposited crack Ω_m and the solid electrolyte Ω_{SE}

The derivation starts with the governing equation for the electric field, which is earlier defined and repeated below:

$$-\text{div}\left(\kappa\nabla\phi\right) = -F\dot{\xi} \tag{4.4}$$

Electrodeposition occurs only in the area with a crack, specifically within the domain Ω_m. Consequently, $\dot{\xi}$ is zero within the solid electrolyte domain Ω_{SE}. Additionally, the boundary conditions between both domains are defined such that the current density is equal at their interface. This leads to the following system defining the electric field of the solid-state battery:

$$\begin{cases} -\text{div}\left(\kappa_{SE}\nabla\phi_{SE}\right) = 0 & \text{in} \quad \Omega_{SE} \\ -\text{div}\left(\kappa_m\nabla\phi_m\right) = -F\dot{\xi} & \text{in} \quad \Omega_m \\ \kappa_{SE}\nabla\phi_{SE}\cdot\mathbf{n}^+ = -\kappa_m\nabla\phi_m\cdot\mathbf{n}_\gamma & \text{on} \quad \Gamma^+ \\ \kappa_{SE}\nabla\phi_{SE}\cdot\mathbf{n}^- = -\kappa_m\nabla\phi_m\cdot\mathbf{n}_\gamma & \text{on} \quad \Gamma^- \end{cases} \tag{4.5}$$

The divergence term of Equation B.21 can be rewritten in the following expression:

$$\begin{aligned} \text{div}\left(\kappa\nabla\phi\right) &= \nabla\kappa\cdot\nabla\phi + \kappa\ \text{div}\left(\nabla\phi\right) \\ &= \nabla\kappa\cdot\nabla\phi + \kappa\Delta\phi \end{aligned} \tag{4.6}$$

The conductivity κ is a constant that depends on the material, and typically, the gradient of this term can be neglected. However, due to the discontinuity in the domain resulting from the presence of two distinct domains, κ will vary over the domain, and thus, it is not possible to remove the term from the expression.

In the first instance, only the domain of the electrodeposited material Ω_m will be considered. The governing equation for this domain (see Equation 4.5) can be written using Equation 4.6. Given that κ is constant in this domain, the gradient term can now be neglected, resulting in only the Laplacian term:

$$\begin{aligned} -\text{div}\left(\kappa_m\nabla\phi_m\right) &= -F\dot{\xi} \\ -\nabla\kappa_m\cdot\nabla\phi_m - \kappa_m\Delta\phi_m &= -F\dot{\xi} \\ \kappa_m\frac{\partial^2\phi_m}{\partial x^2} + \kappa_m\frac{\partial^2\phi_m}{\partial z^2} &= F\dot{\xi} \end{aligned} \tag{4.7}$$

Equation 4.7 will be integrated along z over the domain Ω_m:

$$\begin{aligned}\int_{-h(x)}^{h(x)} \kappa_m \frac{\partial^2 \phi_m}{\partial x^2} + \kappa_m \frac{\partial^2 \phi_m}{\partial z^2}\, dz &= \int_{-h(x)}^{h(x)} F\dot{\xi}\, dz \\ \int_{-h(x)}^{h(x)} \kappa_m \frac{\partial^2 \phi_m}{\partial x^2}\, dz + \int_{-h(x)}^{h(x)} \kappa_m \frac{\partial^2 \phi_m}{\partial z^2}\, dz &= \int_{-h(x)}^{h(x)} F\dot{\xi}\, dz\end{aligned} \tag{4.8}$$

The terms in Equation 4.8 will be evaluated separately for each term. First, the integral of $\kappa_m \frac{\partial^2 \phi_m}{\partial x^2}$ is considered. The boundaries of the integral are dependent on x, making it impossible to switch the partial derivative and the integral. Therefore, a change of variable z is applied:

$$\begin{aligned}\hat{z} &= \frac{z}{h(x)} \quad \in [-1, 1] \\ d\hat{z} &= \frac{dz}{h(x)}\end{aligned} \tag{4.9}$$

The integral can now be rewritten using the change of variables in combination with integration by parts, as follows:

$$\begin{aligned}\int_{-h(x)}^{h(x)} \kappa_m \frac{\partial^2 \phi_m}{\partial x^2}\, dz &= \int_{-1}^{1} \frac{\partial}{\partial x}\left(\kappa_m \frac{\partial \phi_m}{\partial x}\right) h\,(x)\; d\hat{z} \\ &= \int_{-1}^{1} \frac{\partial}{\partial x}\left(\kappa_m \frac{\partial \phi_m}{\partial x} h\,(x)\right) d\hat{z} - \int_{-1}^{1} \kappa_m \frac{\partial \phi_m}{\partial x}\frac{\partial h}{\partial x}\, d\hat{z}\end{aligned} \tag{4.10}$$

Now that the limits of the integral are constants, it is possible to interchange the integral and the partial derivative.

$$\begin{aligned}\int_{-h(x)}^{h(x)} \kappa_m \frac{\partial^2 \phi_m}{\partial x^2}\, dz &= \int_{-1}^{1} \frac{\partial}{\partial x}\left(\kappa_m \frac{\partial \phi_m}{\partial x} h\,(x)\right) d\hat{z} - \int_{-1}^{1} \kappa_m \frac{\partial \phi_m}{\partial x}\frac{\partial h}{\partial x}\, d\hat{z} \\ &= \frac{\partial}{\partial x}\int_{-1}^{1} \kappa_m \frac{\partial \phi_m}{\partial x} h\,(x)\; d\hat{z} - \frac{\partial h}{\partial x}\int_{-1}^{1} \kappa_m \frac{\partial \phi_m}{\partial x}\, d\hat{z}\end{aligned} \tag{4.11}$$

Integration by parts is applied again, allowing the second partial derivative to be interchanged with the integral.

$$\begin{aligned}\int_{-h(x)}^{h(x)} \kappa_m \frac{\partial^2 \phi_m}{\partial x^2}\, dz =& \frac{\partial}{\partial x}\int_{-1}^{1} \kappa_m \frac{\partial \phi_m}{\partial x} h\,(x)\; d\hat{z} - \frac{\partial h}{\partial x}\int_{-1}^{1} \kappa_m \frac{\partial \phi_m}{\partial x}\, d\hat{z} \\ =& \kappa_m \frac{\partial^2}{\partial x^2}\int_{-1}^{1} \phi_m h\,(x)\; d\hat{z} - \kappa_m \frac{\partial}{\partial x}\left(\frac{\partial h}{\partial x}\int_{-1}^{1} \phi^m\, d\hat{z}\right) \\ & - \kappa_m \frac{\partial h}{\partial x}\frac{\partial}{\partial x}\left(\int_{-1}^{1} \phi_m\, d\hat{z}\right)\end{aligned} \tag{4.12}$$

The variables are changed back to the original space from the domain Ω_m.

$$\begin{aligned}\int_{-h(x)}^{h(x)} \kappa_m \frac{\partial^2 \phi_m}{\partial x^2}\, dz =& \kappa_m \frac{\partial^2}{\partial x^2}\int_{-1}^{1} \phi_m h\,(x)\; d\hat{z} - \kappa_m \frac{\partial}{\partial x}\left(\frac{\partial h}{\partial x}\int_{-1}^{1} \phi^m\, d\hat{z}\right) \\ & - \kappa_m \frac{\partial h}{\partial x}\frac{\partial}{\partial x}\left(\int_{-1}^{1} \phi_m\, d\hat{z}\right) \\ =& \kappa_m \frac{\partial^2}{\partial x^2}\left(\frac{2h\,(x)}{2h\,(x)}\int_{-h(x)}^{h(x)} \phi_m\, dz\right) - \kappa_m \frac{\partial}{\partial x}\left(\frac{\partial h}{\partial x}\frac{2}{2h\,(x)}\int_{-h(x)}^{h(x)} \phi^m\, dz\right) \\ & - \kappa_m \frac{\partial h}{\partial x}\frac{\partial}{\partial x}\left(\frac{2}{2h\,(x)}\int_{-h(x)}^{h(x)} \phi_m\, dz\right)\end{aligned} \tag{4.13}$$

The average electric potential along z can be determined by integrating the electric potential over the electrodeposited crack domain Ω_m:

$$\tilde{\phi}_m = \frac{1}{2h\left(x\right)} \int_{-h(x)}^{h(x)} \phi_m \, dz \tag{4.14}$$

Equation 4.13 can be written in terms of the average electric potential using Equation 4.14:

$$\begin{aligned} \int_{-h(x)}^{h(x)} \kappa_m \frac{\partial^2 \phi_m}{\partial x^2} \, dz =& \kappa_m \frac{\partial^2}{\partial x^2} \left(\frac{2h\left(x\right)}{2h\left(x\right)} \int_{-h(x)}^{h(x)} \phi_m \, dz \right) - \kappa_m \frac{\partial}{\partial x} \left(\frac{\partial h}{\partial x} \frac{2}{2h\left(x\right)} \int_{-h(x)}^{h(x)} \phi^m \, dz \right) \\ & - \kappa_m \frac{\partial h}{\partial x} \frac{\partial}{\partial x} \left(\frac{2}{2h\left(x\right)} \int_{-h(x)}^{h(x)} \phi_m \, dz \right) \\ =& 2\kappa_m \frac{\partial^2 h\tilde{\phi}_m}{\partial x^2} - 2\kappa_m \frac{\partial}{\partial x} \left(\frac{\partial h}{\partial x} \tilde{\phi}_m \right) - 2\kappa_m \frac{\partial h}{\partial x} \frac{\partial \tilde{\phi}_m}{\partial x} \end{aligned} \tag{4.15}$$

Equation 4.15 is rewritten by expanding the partial derivative of its first term.

$$\begin{aligned} \int_{-h(x)}^{h(x)} \kappa_m \frac{\partial^2 \phi_m}{\partial x^2} \, dz =& 2\kappa_m \frac{\partial^2 h\tilde{\phi}_m}{\partial x^2} - 2\kappa_m \frac{\partial}{\partial x} \left(\frac{\partial h}{\partial x} \tilde{\phi}_m \right) - 2\kappa_m \frac{\partial h}{\partial x} \frac{\partial \tilde{\phi}_m}{\partial x} \\ =& 2\kappa_m \frac{\partial}{\partial x} \left(\frac{\partial h\tilde{\phi}_m}{\partial x} \right) - 2\kappa_m \frac{\partial}{\partial x} \left(\frac{\partial h}{\partial x} \tilde{\phi}_m \right) - 2\kappa_m \frac{\partial h}{\partial x} \frac{\partial \tilde{\phi}_m}{\partial x} \\ =& 2\kappa_m \frac{\partial}{\partial x} \left(\frac{\partial h}{\partial x} \tilde{\phi}_m + h \frac{\partial \tilde{\phi}_m}{\partial x} \right) - 2\kappa_m \frac{\partial}{\partial x} \left(\frac{\partial h}{\partial x} \tilde{\phi}_m \right) - 2\kappa_m \frac{\partial h}{\partial x} \frac{\partial \tilde{\phi}_m}{\partial x} \\ =& 2\kappa_m \frac{\partial}{\partial x} \left(h \frac{\partial \tilde{\phi}_m}{\partial x} \right) - 2\kappa_m \frac{\partial h}{\partial x} \frac{\partial \tilde{\phi}_m}{\partial x} \end{aligned} \tag{4.16}$$

Equation 4.16 can be further rewritten by expanding the first term of this expression for a second time. Simplifying this expression gives the final result of the first term of Equation 4.8

$$\begin{aligned} \int_{-h(x)}^{h(x)} \kappa_m \frac{\partial^2 \phi_m}{\partial x^2} \, dz =& 2\kappa_m \frac{\partial}{\partial x} \left(h \frac{\partial \tilde{\phi}_m}{\partial x} \right) - 2\kappa_m \frac{\partial h}{\partial x} \frac{\partial \tilde{\phi}_m}{\partial x} \\ =& 2\kappa_m \frac{\partial h}{\partial x} \frac{\partial \tilde{\phi}_m}{\partial x} + 2\kappa_m h \frac{\partial^2 \tilde{\phi}_m}{\partial x^2} - 2\kappa_m \frac{\partial h}{\partial x} \frac{\partial \tilde{\phi}_m}{\partial x} \\ =& 2h\kappa_m \frac{\partial^2 \tilde{\phi}_m}{\partial x^2} \end{aligned} \tag{4.17}$$

Next to consider is the second term of Equation 4.8, which can be evaluated directly:

$$\begin{aligned} \int_{-h(x)}^{h(x)} \kappa_m \frac{\partial^2 \phi_m}{\partial z^2} \, dz =& \left[\kappa_m \frac{\partial \phi_m}{\partial z} \right]_{-h(x)}^{h(x)} \\ =& \kappa_m \frac{\partial \phi_m}{\partial z} \left(x, h\left(x\right)\right) - \kappa_m \frac{\partial \phi_m}{\partial z} \left(x, -h\left(x\right)\right) \end{aligned} \tag{4.18}$$

The boundary condition on the crack surface Γ^+, as defined in Equation 4.5, is rewritten for use in Equation 4.18.

$$\begin{aligned} \kappa_m \nabla \phi_m \cdot \mathbf{n}^+ &= -\kappa_{SE} \nabla \phi_{SE} \cdot \mathbf{n}_\gamma \\ \kappa_m \frac{\partial \phi_m}{\partial z} \left(x, h\left(x\right)\right) &= \kappa_{SE} \frac{\partial \phi_{SE}}{\partial z} \left(x, h\left(x\right)\right) \end{aligned} \tag{4.19}$$

A + is added to the expression to indicate that this boundary condition applies on the upper crack surface Γ^+.

$$\begin{aligned} \kappa_m \frac{\partial \phi_m}{\partial z} \left(x, h\left(x\right)\right) &= \kappa_{SE} \frac{\partial \phi_{SE}}{\partial z} \left(x, h\left(x\right)\right) \\ &= \kappa_{SE}^+ \frac{\partial \phi_{SE}^+}{\partial z} \end{aligned} \tag{4.20}$$

The boundary condition for the lower crack surface Γ^- is similarly rewritten. To indicate that this boundary condition applies on Γ^-, a $-$ is added to the expression, resulting in the following formulation:

$$\kappa_m \frac{\partial \phi_m}{\partial z}(x, -h(x)) = \kappa_{SE}^- \frac{\partial \phi_{SE}^-}{\partial z} \tag{4.21}$$

The boundary conditions given by Equation 4.20 and Equation 4.21 are applied to Equation 4.18.

$$\begin{aligned} \int_{-h(x)}^{h(x)} \kappa_m \frac{\partial^2 \phi_m}{\partial z^2}\, dz &= \kappa_m \frac{\partial \phi_m}{\partial z}(x, h(x)) - \kappa_m \frac{\partial \phi_m}{\partial z}(x, -h(x)) \\ &= \kappa_{SE}^+ \frac{\partial \phi_{SE}^+}{\partial z} - \kappa_{SE}^- \frac{\partial \phi_{SE}^-}{\partial z} \end{aligned} \tag{4.22}$$

A new operator, called the jump operator, is now defined as the difference between the upper and lower boundaries:

$$[\![a]\!] = a^+ - a^- \tag{4.23}$$

Applying the jump operator on Equation 4.22 gives the final expression for the second term of Equation 4.8:

$$\begin{aligned} \int_{-h(x)}^{h(x)} \kappa_m \frac{\partial^2 \phi_m}{\partial z^2}\, dz &= \kappa_{SE}^+ \frac{\partial \phi_{SE}^+}{\partial z} - \kappa_{SE}^- \frac{\partial \phi_{SE}^-}{\partial z} \\ &= \left[\!\!\left[\kappa_{SE} \frac{\partial \phi_{SE}}{\partial z} \right]\!\!\right] \\ &= [\![\kappa_{SE} \nabla \phi_{SE}]\!] \cdot \boldsymbol{n} \end{aligned} \tag{4.24}$$

The last term to consider is the right-hand side of Equation 4.8. This integral is solved by using the assumption that $L \gg w$, resulting in a very small domain Ω_m, as discussed earlier. Therefore, it is assumed that the change in the integrand within this domain is minimal and can be considered constant, resulting in the following expression:

$$\begin{aligned} \int_{-h(x)}^{h(x)} F\dot{\xi}\, dz &= \left[F\dot{\xi} z \right]_{-h(x)}^{h(x)} \\ &= 2hF\dot{\xi} \end{aligned} \tag{4.25}$$

All the terms in Equation 4.8 are evaluated and presented in Equation 4.17, Equation 4.24, and Equation 4.25. Substituting these three expressions back yields the adjusted version of the governing equation on the domain Γ.

$$\begin{aligned} \int_{-h(x)}^{h(x)} \kappa_m \frac{\partial^2 \phi_m}{\partial x^2}\, dz + \int_{-h(x)}^{h(x)} \kappa_m \frac{\partial^2 \phi_m}{\partial z^2}\, dz &= \int_{-h(x)}^{h(x)} F\dot{\xi}\, dz \\ 2h\kappa_m \frac{\partial^2 \tilde{\phi}_m}{\partial x^2} + [\![\kappa_{SE} \nabla \phi_{SE}]\!] \cdot \boldsymbol{n} &= 2hF\dot{\xi} \end{aligned} \tag{4.26}$$

From Figure 4.1, it can be observed that the crack opening w equals $2h$, thus Equation 4.26 can also be expressed in terms of the crack opening.

$$\begin{aligned} 2h\kappa_m \frac{\partial^2 \tilde{\phi}_m}{\partial x^2} + [\![\kappa_{SE} \nabla \phi_{SE}]\!] \cdot \boldsymbol{n} &= 2hF\dot{\xi} \\ w\kappa_m \frac{\partial^2 \tilde{\phi}_m}{\partial x^2} + [\![\kappa_{SE} \nabla \phi_{SE}]\!] \cdot \boldsymbol{n} &= wF\dot{\xi} \end{aligned} \tag{4.27}$$

The expression shown in Equation 4.27 represents the governing equation of the electric field that is valid inside the electrodeposited crack subdomain Ω_m but projected onto the centerline of the crack domain. The system defining the electric field can be redefined using this expression.

$$\begin{cases} -\text{div}\left(\kappa_{SE} \nabla \phi_{SE}\right) = 0 & \text{in} \quad \Omega_{SE} \\ w\kappa_m \frac{\partial^2 \tilde{\phi}_m}{\partial x^2} + [\![\kappa_{SE} \nabla \phi_{SE}]\!] \cdot \boldsymbol{n} = wF\dot{\xi} & \text{on} \quad \Gamma \\ \kappa_{SE} \nabla \phi_{SE} \cdot \mathbf{n}^+ = -\kappa_m \nabla \phi_m \cdot \mathbf{n}_\gamma & \text{on} \quad \Gamma^+ \\ \kappa_{SE} \nabla \phi_{SE} \cdot \mathbf{n}^- = -\kappa_m \nabla \phi_m \cdot \mathbf{n}_\gamma & \text{on} \quad \Gamma^- \end{cases} \tag{4.28}$$

4.2. Continuous Galerkin formulation

A weak form for the system of the electric field is defined. Initially, the domain of the solid electrolyte, denoted as Ω_{SE}, is considered. Consequently, a continuous test function, η, is defined as a continuous Galerkin approach is currently employed. This function is defined in such a way that it equals zero on the boundary $\partial\Omega_{SE} \setminus (\Gamma^+ \cup \Gamma^-)$ when a referential electric field is defined on this domain. Using this test function yields the following weak form for Ω_{SE}:

$$\int_{\Omega_{SE}} -\text{div}\left(\kappa_{SE}\nabla\phi_{SE}\right)\eta\, d\Omega_{SE} = 0 \tag{4.29}$$

The expression of the weak form shown in Equation 4.29 is rewritten using integration by parts:

$$\begin{aligned} \int_{\Omega_{SE}} -\text{div}\left(\kappa_{SE}\nabla\phi_{SE}\right)\eta\, d\Omega_{SE} &= 0 \\ \int_{\Omega_{SE}} \kappa_{SE}\nabla\phi_{SE}\cdot\nabla\eta\, d\Omega_{SE} - \int_{\Omega_{SE}} \text{div}\left(\kappa_{SE}\nabla\phi_{SE}\eta\right)\, d\Omega_{SE} &= 0 \end{aligned} \tag{4.30}$$

The divergence rule can be applied on the second term of Equation 4.30:

$$\begin{aligned} \int_{\Omega_{SE}} \kappa_{SE}\nabla\phi_{SE}\cdot\nabla\eta\, d\Omega_{SE} - \int_{\Omega_{SE}} \text{div}\left(\kappa_{SE}\nabla\phi_{SE}\eta\right)\, d\Omega_{SE} &= 0 \\ \int_{\Omega_{SE}} \kappa_{SE}\nabla\phi_{SE}\cdot\nabla\eta\, d\Omega_{SE} - \int_{\partial\Omega_{SE}} \kappa_{SE}\nabla\phi_{SE}\cdot\boldsymbol{n}\eta\, d\partial\Omega_{SE} &= 0 \end{aligned} \tag{4.31}$$

The way the test function is defined earlier results in a second term in Equation 4.31, which is only nonzero at the crack surfaces Γ^+ and Γ^-. Thus, this term can be expressed in terms of the crack surfaces:

$$\begin{aligned} \int_{\Omega_{SE}} \kappa_{SE}\nabla\phi_{SE}\cdot\nabla\eta\, d\Omega_{SE} - \int_{\partial\Omega_{SE}} \kappa_{SE}\nabla\phi_{SE}\cdot\boldsymbol{n}\eta\, d\partial\Omega_{SE} &= 0 \\ \int_{\Omega_{SE}} \kappa_{SE}\nabla\phi_{SE}\cdot\nabla\eta\, d\Omega_{SE} - \int_{\Gamma^+} \kappa^+_{SE}\nabla\phi^+_{SE}\cdot\boldsymbol{n}^+\eta^+\, d\Gamma^+ - \int_{\Gamma^-} \kappa^-_{SE}\nabla\phi^-_{SE}\cdot\boldsymbol{n}^-\eta^-\, d\Gamma^- &= 0 \end{aligned} \tag{4.32}$$

The normal vector $\boldsymbol{n}$ can be defined as $\boldsymbol{n} = \boldsymbol{n}^+$. Utilizing the small crack assumption, $\boldsymbol{n}^-$ can be defined as $\boldsymbol{n}^- = -\boldsymbol{n}$ for the lower crack surface. Furthermore, η will remain continuous across the domain boundary Γ, implying that $\eta^+ = \eta^- = \eta$. When these points are taken into account in Equation 4.32, the jump from the lower crack surface to the upper crack surface becomes part of the expression of the weak form:

$$\begin{aligned} \int_{\Omega_{SE}} \kappa_{SE}\nabla\phi_{SE}\cdot\nabla\eta\, d\Omega_{SE} - \int_{\Gamma^+} \kappa^+_{SE}\nabla\phi^+_{SE}\cdot\boldsymbol{n}^+\eta^+\, d\Gamma^+ - \int_{\Gamma^-} \kappa^-_{SE}\nabla\phi^-_{SE}\cdot\boldsymbol{n}^-\eta^-\, d\Gamma^- &= 0 \\ \int_{\Omega_{SE}} \kappa_{SE}\nabla\phi_{SE}\cdot\nabla\eta\, d\Omega_{SE} - \left(\int_{\Gamma^+} \kappa^+_{SE}\nabla\phi^+_{SE}\cdot\boldsymbol{n}\eta\, d\Gamma^+ - \int_{\Gamma^-} \kappa^-_{SE}\nabla\phi^-_{SE}\cdot\boldsymbol{n}\eta\, d\Gamma^-\right) &= 0 \\ \int_{\Omega\setminus\Gamma} \kappa_{SE}\nabla\phi_{SE}\cdot\nabla\eta\, d\Omega_{SE} - \int_{\Gamma} [\![\kappa_{SE}\nabla\phi_{SE}]\!]\cdot\boldsymbol{n}\eta\, d\Gamma &= 0 \end{aligned} \tag{4.33}$$

The next step is to define the weak form of the electrodeposited subdomain Ω_m projected onto Γ, using the same test function η as was used for the weak form of the other subdomain.

$$\begin{aligned} \int_{\Gamma}\left(wF\dot{\xi} - [\![\kappa_{SE}\nabla\phi_{SE}]\!]\cdot\boldsymbol{n} - w\kappa_m\frac{\partial^2\tilde{\phi}_m}{\partial x^2}\right)\eta\, d\Gamma &= 0 \\ \int_{\Gamma} wF\dot{\xi}\eta\, d\Gamma - \int_{\Gamma} [\![\kappa_{SE}\nabla\phi_{SE}]\!]\cdot\boldsymbol{n}\eta\, d\Gamma - \int_{\Gamma} w\kappa_m\frac{\partial^2\tilde{\phi}_m}{\partial x^2}\eta\, d\Gamma &= 0 \end{aligned} \tag{4.34}$$

The last term of Equation 4.34 can be rewritten using integration by parts:

$$\int_{\Gamma} w\kappa_m\frac{\partial^2\tilde{\phi}_m}{\partial x^2}\eta\, d\Gamma = \int_{\Gamma}\frac{\partial}{\partial x}\left(w\kappa_m\frac{\partial\tilde{\phi}_m}{\partial x}\eta\right)\, d\Gamma - \int_{\Gamma}\kappa_m\frac{\partial\tilde{\phi}_m}{\partial x}\frac{\partial w\eta}{\partial x}\, d\Gamma \tag{4.35}$$

The first term of Equation 4.35 can be evaluated at the boundaries of Γ:

$$\begin{aligned}\int_\Gamma w\kappa_m \frac{\partial^2\tilde{\phi}_m}{\partial x^2}\eta\, d\Gamma &= \int_\Gamma \frac{\partial}{\partial x}\left(w\kappa_m \frac{\partial\tilde{\phi}_m}{\partial x}\eta\right) d\Gamma - \int_\Gamma \kappa_m \frac{\partial\tilde{\phi}_m}{\partial x}\frac{\partial w\eta}{\partial x}\, d\Gamma \\ &= \left[w\kappa_m \frac{\partial\tilde{\phi}_m}{\partial x}\eta\right]_0^L - \int_\Gamma \kappa_m \frac{\partial\tilde{\phi}_m}{\partial x}\frac{\partial w\eta}{\partial x}\, d\Gamma\end{aligned} \tag{4.36}$$

At the upper limit of Γ, the crack opening is zero, causing this term to disappear and resulting in the following expression.

$$\begin{aligned}\int_\Gamma w\kappa_m \frac{\partial^2\tilde{\phi}_m}{\partial x^2}\eta\, d\Gamma &= \left[w\kappa_m \frac{\partial\tilde{\phi}_m}{\partial x}\eta\right]_0^L - \int_\Gamma \kappa_m \frac{\partial\tilde{\phi}_m}{\partial x}\frac{\partial w\eta}{\partial x}\, d\Gamma \\ &= -w\kappa_m \frac{\partial\tilde{\phi}_m}{\partial x}\eta\,(0,0) - \int_\Gamma \kappa_m \frac{\partial\tilde{\phi}_m}{\partial x}\frac{\partial w\eta}{\partial x}\, d\Gamma\end{aligned} \tag{4.37}$$

Equation 4.37 can now be substituted back in Equation 4.34

$$\begin{aligned}\int_\Gamma wF\dot{\xi}\eta\, d\Gamma - \int_\Gamma [\![\kappa_{SE}\nabla\phi_{SE}]\!]\cdot\boldsymbol{n}\eta\, d\Gamma - \int_\Gamma w\kappa_m \frac{\partial^2\tilde{\phi}_m}{\partial x^2}\eta\, d\Gamma = 0 \\ \int_\Gamma wF\dot{\xi}\eta\, d\Gamma + \int_\Gamma \kappa_m \frac{\partial\tilde{\phi}_m}{\partial x}\frac{\partial w\eta}{\partial x}\, d\Gamma - \int_\Gamma [\![\kappa_{SE}\nabla\phi_{SE}]\!]\cdot\boldsymbol{n}\eta\, d\Gamma + w\kappa_m \frac{\partial\tilde{\phi}_m}{\partial x}\eta\,(0,0) = 0\end{aligned} \tag{4.38}$$

The weak form of the solid electrolyte and the electrodeposited crack are combined into a unified weak form by taking the difference between Equation 4.38 and Equation 4.33, resulting in the cancellation of the term involving the jump of the electric potential.

$$\begin{aligned}\int_\Gamma wF\dot{\xi}\eta\, d\Gamma + \int_\Gamma \kappa_m \frac{\partial\tilde{\phi}_m}{\partial x}\frac{\partial w\eta}{\partial x}\, d\Gamma - \int_\Gamma [\![\kappa_{SE}\nabla\phi_{SE}]\!]\cdot\boldsymbol{n}\eta\, d\Gamma + w\kappa_m \frac{\partial\tilde{\phi}_m}{\partial x}\eta\,(0,0) - \\ \int_{\Omega\setminus\Gamma} \kappa_{SE}\nabla\phi_{SE}\cdot\nabla\eta\, d\Omega_{SE} + \int_\Gamma [\![\kappa_{SE}\nabla\phi_{SE}]\!]\cdot\boldsymbol{n}\eta\, d\Gamma = 0 \\ \int_{\Omega\setminus\Gamma} \kappa_{SE}\nabla\phi_{SE}\cdot\nabla\eta\, d\Omega_{SE} - \int_\Gamma \kappa_m \frac{\partial\tilde{\phi}_m}{\partial x}\frac{\partial w\eta}{\partial x}\, d\Gamma - w\kappa_m \frac{\partial\tilde{\phi}_m}{\partial x}\eta\,(0,0) = \int_\Gamma wF\dot{\xi}\eta\, d\Gamma\end{aligned} \tag{4.39}$$

The continuity of the electric potential allows for the definition of a generic electric potential for the entire domain.

$$\phi = \begin{cases}\phi_{SE} \text{ in} & \Omega \\ \tilde{\phi}_m \text{ on} & \Gamma\end{cases} \tag{4.40}$$

The expression for the generic electric potential, as shown in Equation 4.40, is employed in Equation 4.39 to derive the global weak form for the electric field.

$$\begin{aligned}\int_{\Omega\setminus\Gamma} \kappa_{SE}\nabla\phi_{SE}\cdot\nabla\eta\, d\Omega_{SE} - \int_\Gamma \kappa_m \frac{\partial\tilde{\phi}_m}{\partial x}\frac{\partial w\eta}{\partial x}\, d\Gamma - w\kappa_m \frac{\partial\tilde{\phi}_m}{\partial x}\eta\,(0,0) = \int_\Gamma wF\dot{\xi}\eta\, d\Gamma \\ \int_\Omega \kappa_{SE}\nabla\phi\cdot\nabla\eta\, d\Omega - \int_\Gamma \kappa_m \frac{\partial\phi}{\partial x}\frac{\partial w\eta}{\partial x}\, d\Gamma - w\kappa_m \frac{\partial\phi}{\partial x}\eta\,(0,0) = \int_\Gamma wF\dot{\xi}\eta\, d\Gamma\end{aligned} \tag{4.41}$$

4.3. Continuous Galerkin discretization

This section transforms the weak form shown in Equation 4.41 into the local element stiffness matrix. This process is shown using a simple mesh consisting of 4 elements (see Figure 4.2) is considered. The weak form is solved for the electric potential, which is approximated by a summation of continuous shape functions η_i multiplied by unknown amplitudes ϕ_i:

$$\phi = \sum_{i=1} \phi_i \eta_i \tag{4.42}$$

The gradient of the electric potential becomes the following expression, considering that the amplitudes are constant values:

$$\nabla\phi = \sum_{i=1} \phi_i \nabla\eta_i \tag{4.43}$$

"The hybrid formulation of the continuous Galerkin method, presented in Equation 4.41, comprises both bulk and interface components, each separately implemented in the code. First, the bulk expression is considered.

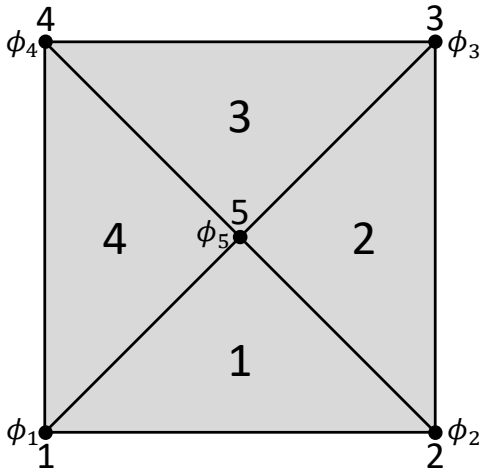

Figure 4.2: Example of a small mesh with four elements.

4.3.1. Bulk part

The bulk part of the continuous Galerkin weak form is isolated from the general weak form and shown below:

$$\int_{\Omega} \kappa_{SE} \nabla\phi \cdot \nabla\eta \, d\Omega \tag{4.44}$$

This expression is defined for the random triangle mesh elements. However, the code is implemented more generally, so a regular triangle element is employed. The domain of the random element is then transformed to the standard domain using the Jacobian.

$$\int_{\Omega^*} J\kappa_{SE} \nabla\phi \cdot \nabla\eta \, d\Omega \tag{4.45}$$

The integrals are solved numerically by multiplying the integrand with a quadrature weight w_q and summing it over a set of quadrature points, where the function is evaluated. These quadrature weights, along with the Jacobian, can be combined into a general variable W_q.

$$\begin{aligned} \int_{\Omega^*} J\kappa_{SE} \nabla\phi \cdot \nabla\eta \, d\Omega &\approx \sum_{e,q=1} w_{e,q} J_{e,q} \left(\kappa_{SE} \nabla\phi \cdot \nabla\eta\right) \\ &= \sum_{e,q=1} W_{e,q} \left(\kappa_{SE} \nabla\phi \cdot \nabla\eta\right)_{e,q} \end{aligned} \tag{4.46}$$

The gradient of the approximate solution of the electric potential (Equation 4.43) can be substituted into Equation 4.46.

$$\sum_{e,q=1} W_{e,q} \left(\kappa_{SE} \nabla\phi \cdot \nabla\eta\right)_{e,q} = \sum_{e,q=1} W_{e,q} \left(\kappa_{SE} \sum_{i=1} \left(\phi_i \nabla\eta_i\right) \cdot \nabla\eta\right)_q \tag{4.47}$$

The weak form shown in Equation 4.47 is used to compute an element matrix for each element, which are then combined into the global stiffness matrix. For instance, the element matrix of element 1 in Figure 4.2 is derived, and the remaining element matrices are obtained in a similar manner. Although Equation 4.47 approximates the weak form using multiple quadrature points, only the first quadrature point is presented in the subsequent derivation for clarity.

$$\sum_{q=1} W_q \left(\kappa_{SE} \sum_{i=1} \left(\phi_i \nabla\eta_i\right) \cdot \nabla\eta\right)_q = W\kappa_{SE} \sum_{i=1} \left(\phi_i \nabla\eta_i\right) \cdot \nabla\eta + \ldots \tag{4.48}$$

The combined Jacobian and quadrature point variable W, along with the conductivity κ_{SE}, are further combined into a generalized variable K:

$$W\kappa_{SE}\sum_{i=1}\left(\phi_i\nabla\eta_i\right)\cdot\nabla\eta = K\sum_{i=1}\left(\phi_i\nabla\eta_i\right)\cdot\nabla\eta \tag{4.49}$$

The shape functions contributing to the element matrix are those corresponding to the nodes of the specific element. All other shape functions are zero for that element. As illustrated in Figure 4.2, element 1 comprises nodes 1, 2, and 5. Consequently, the shape functions η_1, η_2, and η_5 contribute to the element matrix of element 1. Therefore, when the summation is fully expanded, Equation 4.49 becomes the following expression:

$$K\sum_{i=1}\left(\phi_i\nabla\eta_i\right)\cdot\nabla\eta = K\left(\phi_1\nabla\eta_1+\phi_2\nabla\eta_2+\phi_5\nabla\eta_5\right)\cdot\nabla\eta \tag{4.50}$$

The shape functions are also used as test functions to obtain a system of equations:

$$\begin{aligned} &K\left(\phi_1\nabla\eta_1+\phi_2\nabla\eta_2+\phi_5\nabla\eta_5\right)\cdot\nabla\eta_1\\ &K\left(\phi_1\nabla\eta_1+\phi_2\nabla\eta_2+\phi_5\nabla\eta_5\right)\cdot\nabla\eta_2\\ &K\left(\phi_1\nabla\eta_1+\phi_2\nabla\eta_2+\phi_5\nabla\eta_5\right)\cdot\nabla\eta_5 \end{aligned} \tag{4.51}$$

The equation represented by Equation 4.51 can also be expressed in matrix-vector notation, yielding the element matrix for the first quadrature point of element 1.

$$\begin{bmatrix} \nabla\eta_1\cdot K\nabla\eta_1 & \nabla\eta_1\cdot K\nabla\eta_2 & \nabla\eta_1\cdot K\nabla\eta_5\\ \nabla\eta_2\cdot K\nabla\eta_1 & \nabla\eta_2\cdot K\nabla\eta_2 & \nabla\eta_2\cdot K\nabla\eta_5\\ \nabla\eta_5\cdot K\nabla\eta_1 & \nabla\eta_5\cdot K\nabla\eta_2 & \nabla\eta_5\cdot K\nabla\eta_5 \end{bmatrix}\begin{pmatrix}\phi_1\\ \phi_2\\ \phi_5\end{pmatrix} \tag{4.52}$$

The complete element stiffness matrix is obtained by summing Equation 4.52 over all the quadrature points.

$$\sum_{q=1}\begin{bmatrix} \nabla\eta_{q,1}\cdot K_q\nabla\eta_{q,1} & \nabla\eta_{q,1}\cdot K_q\nabla\eta_{q,2} & \nabla\eta_{q,1}\cdot K_q\nabla\eta_{q,5}\\ \nabla\eta_{q,2}\cdot K_q\nabla\eta_{q,1} & \nabla\eta_{q,2}\cdot K_q\nabla\eta_{q,2} & \nabla\eta_{q,2}\cdot K_q\nabla\eta_{q,5}\\ \nabla\eta_{q,5}\cdot K_q\nabla\eta_{q,1} & \nabla\eta_{q,5}\cdot K_q\nabla\eta_{q,2} & \nabla\eta_{q,5}\cdot K_q\nabla\eta_{q,5} \end{bmatrix}\begin{pmatrix}\phi_1\\ \phi_2\\ \phi_5\end{pmatrix} \tag{4.53}$$

4.3.2. Interface part

The interface part of the weak form is isolated and shown below. A slight modification has been made for clarity, as the derivation presented in Section 4.1 specifically illustrates the derivation of a horizontal crack. However, it's important to note that the crack can propagate in any direction. Hence, instead of using dx, dl is employed to signify that the crack can extend in any direction. Furthermore, for simplicity, the crack opening is assumed to remain constant:

$$w\int_\Gamma \kappa_m\frac{\partial\phi}{\partial l}\frac{\partial\eta}{\partial l}\,d\Gamma \tag{4.54}$$

The jacobian for line integrals is defined in the following way:

$$J=\frac{ds}{dl}=\sqrt{\left(\frac{dx}{ds}\right)^2+\left(\frac{dy}{ds}\right)^2} \tag{4.55}$$

A parametrization is applied to generalize the line elements:

$$\begin{aligned} w\int_{\Gamma^*}\kappa_m\frac{\partial\phi}{\partial l}\frac{\partial\eta}{\partial l}\,d\Gamma =& w\int_{\Gamma}\kappa_m\frac{\partial\phi}{\partial s}\frac{ds}{dl}\frac{\partial\eta}{\partial s}\frac{ds}{dl}J\,ds \\ =& w\int_{\Gamma}\kappa_m\frac{\partial\phi}{\partial s}\frac{\partial\eta}{\partial s}\left(\frac{1}{\sqrt{\left(\frac{dx}{ds}\right)^2+\left(\frac{dy}{ds}\right)^2}}\right)^2\sqrt{\left(\frac{dx}{ds}\right)^2+\left(\frac{dy}{ds}\right)^2}\,ds \\ =& w\int_{\Gamma}\kappa_m\frac{\partial\phi}{\partial s}\frac{\partial\eta}{\partial s}\frac{1}{\sqrt{\left(\frac{dx}{ds}\right)^2+\left(\frac{dy}{ds}\right)^2}}\,ds \end{aligned} \tag{4.56}$$

The integral is solved numerically by multiplying the integrand with the quadrature weight and summing over the quadrature points:

$$w\int_{\Gamma}\kappa_m\frac{\partial\phi}{\partial s}\frac{\partial\eta}{\partial s}\frac{1}{\sqrt{\left(\frac{dx}{ds}\right)^2+\left(\frac{dy}{ds}\right)^2}}\,ds \approx w\sum_{q=1}\frac{w_q\kappa_m}{\sqrt{\left(\frac{dx}{ds}\right)^2+\left(\frac{dy}{ds}\right)^2}}\left(\frac{\partial\phi}{\partial s}\frac{\partial\eta}{\partial s}\right)_q \tag{4.57}$$

The crack opening w, the quadrature point w_q and the conductivity κ_m are combined into a single variable K_q. Additionally, the approximate solution of the electric potential shown in Equation 4.42 is substituted in Equation 4.57:

$$w\sum_{q=1}\frac{w_q\kappa_m}{\sqrt{\left(\frac{dx}{ds}\right)^2+\left(\frac{dy}{ds}\right)^2}}\left(\frac{\partial\phi}{\partial s}\frac{\partial\eta}{\partial s}\right)_q = \sum_{q=1}\frac{K_q}{\sqrt{\left(\frac{dx}{ds}\right)^2+\left(\frac{dy}{ds}\right)^2}}\left(\sum_{i=1}\left(\phi_i\frac{\partial\eta_i}{\partial s}\right)\frac{\partial\eta}{\partial s}\right)_q \tag{4.58}$$

The weak form shown in Equation 4.58 is the version implemented in the code. Similarly to the bulk expression, an element interface matrix is established for every element, which will be combined into the global stiffness matrix. For clarity, only the interface element between triangle elements 1 and 4 in Figure 4.2 is displayed. Additionally, only the first quadrature point is shown for the remaining part of the derivation.

$$\sum_{q=1}\frac{K_q}{\sqrt{\left(\frac{dx}{ds}\right)^2+\left(\frac{dy}{ds}\right)^2}}\left(\sum_{i=1}\left(\phi_i\frac{\partial\eta_i}{\partial s}\right)\frac{\partial\eta}{\partial s}\right)_q = \frac{K}{\sqrt{\left(\frac{dx}{ds}\right)^2+\left(\frac{dy}{ds}\right)^2}}\sum_{i=1}\left(\phi_i\frac{\partial\eta_i}{\partial s}\right)\frac{\partial\eta}{\partial s}+\ldots \tag{4.59}$$

The only shape functions that contribute to this element are those corresponding to the nodes of the element. The other shape functions are zero for this element. In this case, these are the functions η_1 and η_5.

$$\frac{K}{\sqrt{\left(\frac{dx}{ds}\right)^2+\left(\frac{dy}{ds}\right)^2}}\sum_{i=1}\left(\phi_i\frac{\partial\eta_i}{\partial s}\right)\frac{\partial\eta}{\partial s} = \frac{K}{\sqrt{\left(\frac{dx}{ds}\right)^2+\left(\frac{dy}{ds}\right)^2}}\left(\phi_1\frac{\partial\eta_1}{\partial s}+\phi_5\frac{\partial\eta_5}{\partial s}\right)\frac{\partial\eta}{\partial s} \tag{4.60}$$

The same shape functions are also employed as test functions to obtain the system of equations.

$$\begin{gathered} \frac{K}{\sqrt{\left(\frac{dx}{ds}\right)^2+\left(\frac{dy}{ds}\right)^2}}\left(\phi_1\frac{\partial\eta_1}{\partial s}+\phi_5\frac{\partial\eta_5}{\partial s}\right)\frac{\partial\eta_1}{\partial s} \\ \frac{K}{\sqrt{\left(\frac{dx}{ds}\right)^2+\left(\frac{dy}{ds}\right)^2}}\left(\phi_1\frac{\partial\eta_1}{\partial s}+\phi_5\frac{\partial\eta_5}{\partial s}\right)\frac{\partial\eta_5}{\partial s} \end{gathered} \tag{4.61}$$

The element interface matrix is obtained by expressing this system of equations in matrix-vector notation.

$$\begin{bmatrix} \frac{K}{\sqrt{\left(\frac{dx}{ds}\right)^2+\left(\frac{dy}{ds}\right)^2}}\frac{\partial\eta_1}{\partial s}\frac{\partial\eta_1}{\partial s} & \frac{K}{\sqrt{\left(\frac{dx}{ds}\right)^2+\left(\frac{dy}{ds}\right)^2}}\frac{\partial\eta_5}{\partial s}\frac{\partial\eta_1}{\partial s} \\ \frac{K}{\sqrt{\left(\frac{dx}{ds}\right)^2+\left(\frac{dy}{ds}\right)^2}}\frac{\partial\eta_1}{\partial s}\frac{\partial\eta_5}{\partial s} & \frac{K}{\sqrt{\left(\frac{dx}{ds}\right)^2+\left(\frac{dy}{ds}\right)^2}}\frac{\partial\eta_5}{\partial s}\frac{\partial\eta_5}{\partial s} \end{bmatrix} \begin{pmatrix} \phi_1 \\ \phi_5 \end{pmatrix} \tag{4.62}$$

The contributions from all quadrature points are summed to obtain the total element interface matrix.

$$\sum_{q=1} \begin{bmatrix} \frac{K_q}{\sqrt{\left(\frac{dx}{ds}\right)^2+\left(\frac{dy}{ds}\right)^2}}\frac{\partial\eta_{q,1}}{\partial s}\frac{\partial\eta_{q,1}}{\partial s} & \frac{K_q}{\sqrt{\left(\frac{dx}{ds}\right)^2+\left(\frac{dy}{ds}\right)^2}}\frac{\partial\eta_{q,5}}{\partial s}\frac{\partial\eta_{q,1}}{\partial s} \\ \frac{K_q}{\sqrt{\left(\frac{dx}{ds}\right)^2+\left(\frac{dy}{ds}\right)^2}}\frac{\partial\eta_{q,1}}{\partial s}\frac{\partial\eta_{q,5}}{\partial s} & \frac{K_q}{\sqrt{\left(\frac{dx}{ds}\right)^2+\left(\frac{dy}{ds}\right)^2}}\frac{\partial\eta_{q,5}}{\partial s}\frac{\partial\eta_{q,5}}{\partial s} \end{bmatrix} \begin{pmatrix} \phi_1 \\ \phi_5 \end{pmatrix} \tag{4.63}$$

The weak for can now also be expressed in terms of the stiffness matrices by summing the bulk (Equation 4.53) and interface element (Equation 4.63) stiffness matrix over all the elements. Take note that not all parts are considered in this weak form. The chemical parts of the weak form are not yet considered.

$$\begin{aligned} &\int_\Omega \kappa_{SE}\nabla\phi\cdot\nabla\eta\, d\Omega - \int_\Gamma \kappa_m \frac{\partial\phi}{\partial x}\frac{\partial w\eta}{\partial x}\, d\Gamma - w\kappa_m\frac{\partial\phi}{\partial x}\eta\,(0,0) = \\ &\sum_{e,q=1} \begin{bmatrix} \nabla\eta_{e,q,1}\cdot K_{e,q}\nabla\eta_{e,q,1} & \nabla\eta_{e,q,1}\cdot K_{e,q}\nabla\eta_{e,q,2} & \nabla\eta_{e,q,1}\cdot K_{e,q}\nabla\eta_{e,q,5} \\ \nabla\eta_{e,q,2}\cdot K_{e,q}\nabla\eta_{e,q,1} & \nabla\eta_{e,q,2}\cdot K_{e,q}\nabla\eta_{e,q,2} & \nabla\eta_{e,q,2}\cdot K_{e,q}\nabla\eta_{e,q,5} \\ \nabla\eta_{e,q,5}\cdot K_{e,q}\nabla\eta_{e,q,1} & \nabla\eta_{e,q,5}\cdot K_{e,q}\nabla\eta_{e,q,2} & \nabla\eta_{e,q,5}\cdot K_{e,q}\nabla\eta_{e,q,5} \end{bmatrix} \begin{pmatrix} \phi_{e,1} \\ \phi_{e,2} \\ \phi_{e,3} \end{pmatrix} \\ &- \sum_{e,q=1} \begin{bmatrix} \frac{K_{e,q}}{\sqrt{\left(\frac{dx}{ds}\right)^2+\left(\frac{dy}{ds}\right)^2}}\frac{\partial\eta_{e,q,1}}{\partial s}\frac{\partial\eta_{e,q,1}}{\partial s} & \frac{K_{e,q}}{\sqrt{\left(\frac{dx}{ds}\right)^2+\left(\frac{dy}{ds}\right)^2}}\frac{\partial\eta_{e,q,5}}{\partial s}\frac{\partial\eta_{e,q,1}}{\partial s} \\ \frac{K_{e,q}}{\sqrt{\left(\frac{dx}{ds}\right)^2+\left(\frac{dy}{ds}\right)^2}}\frac{\partial\eta_{e,q,1}}{\partial s}\frac{\partial\eta_{e,q,5}}{\partial s} & \frac{K_{e,q}}{\sqrt{\left(\frac{dx}{ds}\right)^2+\left(\frac{dy}{ds}\right)^2}}\frac{\partial\eta_{e,q,5}}{\partial s}\frac{\partial\eta_{e,q,5}}{\partial s} \end{bmatrix} \begin{pmatrix} \phi_{e,1} \\ \phi_{e,2} \end{pmatrix} \end{aligned} \tag{4.64}$$

4.4. Discontinuous Galerkin formulation

The weak forms derived previously employ a continuous Galerkin formulation. This chapter revisits the weak form, utilizing a Discontinuous Galerkin formulation. This approach introduces two main differences in the weak form. Firstly, in the discontinuous Galerkin formulation, the weak form is defined elementwise, requiring the summation of all contributions from the elements. Secondly, the test function used to obtain the weak form is discontinuous.

The formulation now becomes elementwise, with the domain Ω discretized into Ω_h, defined as the union of all element sets.

$$\Omega_h = \bigcup_{e=1}^{E} \bar{\Omega}^e \tag{4.65}$$

Where the element set $\bar{\Omega}^e$ is defined as the union of the open domain of the element with the boundary of the element:

$$\bar{\Omega}^e = \Omega^e \cup \partial\Omega^e \tag{4.66}$$

The boundary between elements is denoted by adding subscript I to the variable. Thus, the boundary between elements for the entire domain can be expressed as shown below:

$$\partial_I\Omega_h = \left(\bigcup_{e=1}^{E} \partial\Omega^e\right) \setminus \partial\Omega_h \tag{4.67}$$

The Dirichlet and Neumann boundaries per element are defined as the intersections between the element boundary and, respectively, the Dirichlet and Neumann boundaries of the domain.

$$\begin{aligned} \partial_D\Omega^e &= \partial\Omega^e \cap \partial_D\Omega_h \\ \partial_N\Omega^e &= \partial\Omega^e \cap \partial_N\Omega_h \end{aligned} \tag{4.68}$$

The boundary of the element can be defined as the combination of the boundaries between the elements and the Neumann and Dirichlet boundaries applied to that element.

$$\partial\Omega^e = \partial_D\Omega^e \cup \partial_N\Omega^e \cup \partial_I\Omega^e \tag{4.69}$$

First, we consider the bulk expression of the domain, as shown in Equation 4.28. The updated version of the weak form is presented below:

$$\sum_e \int_{\Omega^e_{SE}} -\text{div}\left(\kappa_{SE}\nabla\phi_{SE}\right)\delta\eta\, d\Omega^e_{SE} = 0 \tag{4.70}$$

Equation 4.70 is adjusted similarly to its continuous Galerkin counterpart. Initially, integration by parts is applied to the weak form, allowing the application of divergence theory to the resulting divergence term:

$$\begin{aligned}\sum_e \int_{\Omega^e_{SE}} -\text{div}\left(\kappa_{SE}\nabla\phi_{SE}\right)\delta\eta\, d\Omega^e_{SE} &= \sum_e \int_{\Omega^e_{SE}} \kappa_{SE}\nabla\phi_{SE}\cdot\nabla\delta\eta\, d\Omega^e_{SE} - \sum_e \int_{\Omega^e_{SE}} \text{div}\left(\kappa_{SE}\nabla\phi_{SE}\delta\eta\right)\, d\Omega^e_{SE} \\ &= \sum_e \int_{\Omega^e_{SE}} \kappa_{SE}\nabla\phi_{SE}\cdot\nabla\delta\eta\, d\Omega^e_{SE} - \sum_e \int_{\partial\Omega^e_{SE}} \kappa_{SE}\nabla\phi_{SE}\cdot\boldsymbol{n}\delta\eta\, d\Gamma\end{aligned} \tag{4.71}$$

The second term of Equation 4.71 can be rewritten by expanding the summation. To demonstrate this, a small example is considered using a mesh of three elements, as illustrated in Figure 4.3. Additionally, only the terms for the first interface will be shown for clarity, as the expression for the other interfaces gives the same result.

$$\begin{aligned}&\sum_e \int_{\partial\Omega^e_{SE}} \kappa_{SE}\nabla\phi_{SE}\cdot\boldsymbol{n}\delta\eta\, d\Gamma = \\ &\int_{\partial\Omega^{1,2}_{SE}} \kappa^1_{SE}\nabla\phi^1_{SE}\delta\eta^1\cdot\boldsymbol{n}^{1,2}\, d\Gamma + \\ &\int_{\partial\Omega^{2,3}_{SE}} \kappa^2_{SE}\nabla\phi^2_{SE}\delta\eta^2\cdot\boldsymbol{n}^{2,3}\, d\Gamma + ...\end{aligned} \tag{4.72}$$

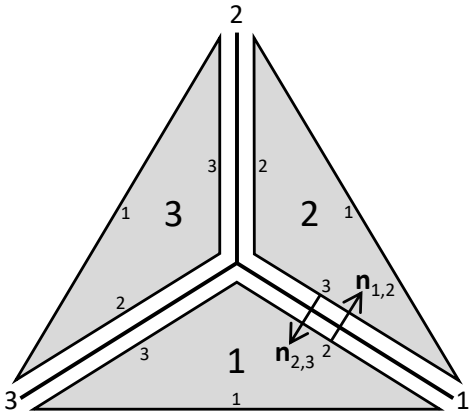

Figure 4.3: Example of a small mesh with three bulk and interface elements. The normal vectors of the adjacent elements are shown for the first interface.

The interface of element 2 (the top part) and the interface of element 1 (the bottom part) are again distinguished using the + and − signs, respectively.

$$\begin{aligned}\sum_e \int_{\partial\Omega^e_{SE}} \kappa_{SE}\nabla\phi_{SE}\cdot\boldsymbol{n}\delta\eta\, d\Gamma = &\int_{\partial\Omega^{1,2}_{SE}} \kappa^-_{SE}\nabla\phi^-_{SE}\delta\eta^-\cdot\boldsymbol{n}^-\, d\Gamma \\ &+ \int_{\partial\Omega^{2,3}_{SE}} \kappa^+_{SE}\nabla\phi^+_{SE}\delta\eta^+\cdot\boldsymbol{n}^+\, d\Gamma + ...\end{aligned} \tag{4.73}$$

The boundary conditions shown in the third and fourth lines of Equation 4.28 are once again utilized to express the expression in terms of the electric potential of the electrodeposited crack.

$$\begin{aligned}\sum_e \int_{\partial\Omega^e_{SE}} \kappa_{SE}\nabla\phi_{SE}\cdot\boldsymbol{n}\delta\eta\, d\Gamma &= \int_{\partial\Omega^{1,2}_{SE}} \kappa^-_{SE}\nabla\phi^-_{SE}\delta\eta^-\cdot\boldsymbol{n}^-\, d\Gamma + \int_{\partial\Omega^{2,3}_{SE}} \kappa^+_{SE}\nabla\phi^+_{SE}\delta\eta^+\cdot\boldsymbol{n}^+\, d\Gamma + ... \\ &= -\int_{\partial\Omega^{1,2}_{SE}} \kappa^-_m\nabla\phi^-_m\delta\eta^-\cdot\boldsymbol{n}^-\, d\Gamma - \int_{\partial\Omega^{2,3}_{SE}} \kappa^+_m\nabla\phi^+_m\delta\eta^+\cdot\boldsymbol{n}^+\, d\Gamma + ...\end{aligned} \tag{4.74}$$

The normals for both interfaces are parallel but in opposite directions. Therefore, a general normal $\boldsymbol{n}$ is

defined, which is in the same direction as $\boldsymbol{n}^-$ and thus opposite to $\boldsymbol{n}^+$, and substituted into Equation 4.74.

$$\begin{aligned}\sum_e \int_{\partial\Omega^e_{SE}} \kappa_{SE}\nabla\phi_{SE}\cdot\boldsymbol{n}\delta\eta\, d\Gamma &= -\int_{\partial\Omega^{1,2}_{SE}} \kappa_m^-\nabla\phi_m^-\delta\eta^-\cdot\boldsymbol{n}^-\, d\Gamma - \int_{\partial\Omega^{2,3}_{SE}} \kappa_m^+\nabla\phi_m^+\delta\eta^+\cdot\boldsymbol{n}^+\, d\Gamma + ... \\ &= \int_{\partial\Omega^{2,3}_{SE}} \kappa_m^+\nabla\phi_m^+\delta\eta^+\cdot\boldsymbol{n}\, d\Gamma - \int_{\partial\Omega^{1,2}_{SE}} \kappa_m^-\nabla\phi_m^-\delta\eta^-\cdot\boldsymbol{n}\, d\Gamma + ... \\ &= \int_{\partial\Omega^{1}_{SE}} \left(\kappa_m^+\nabla\phi_m^+\delta\eta^+ - \kappa_m^-\nabla\phi_m^-\delta\eta^-\right)\cdot\boldsymbol{n}\, d\Gamma + ...\end{aligned} \tag{4.75}$$

The jump, as specified in Equation 4.23, becomes apparent in Equation 4.75, allowing this expression to be rewritten using the jump operator. In contrast to the continuous Galerkin formulation, the test function becomes part of the jump operator, as it is no longer continuous and can jump between elements.

$$\begin{aligned}\sum_e \int_{\partial\Omega^e_{SE}} \kappa_{SE}\nabla\phi_{SE}\cdot\boldsymbol{n}\delta\eta\, d\Gamma &= \int_{\partial\Omega^{1}_{SE}} \left(\kappa_m^+\nabla\phi_m^+\delta\eta^+ - \kappa_m^-\nabla\phi_m^-\delta\eta^-\right)\cdot\boldsymbol{n}\, d\Gamma + ... \\ &= \int_{\partial\Omega^{1}_{SE}} [\![\kappa_m\nabla\phi_m\delta\eta]\!]\cdot\boldsymbol{n}\, d\Gamma + ...\end{aligned} \tag{4.76}$$

The jump operator of two functions can be split into two separate expressions, as shown in Appendix E. For convenience, the final result of the derivation is presented below:

$$\begin{aligned}[\![a\boldsymbol{b}]\!] &= \frac{a^+ + a^-}{2}\left(\boldsymbol{b}^+ - \boldsymbol{b}^-\right) + \left(a^+ - a^-\right)\frac{\boldsymbol{b}^+ + \boldsymbol{b}^-}{2} \\ &= \{a\}[\![\boldsymbol{b}]\!] + [\![a]\!]\{\boldsymbol{b}\}\end{aligned} \tag{4.77}$$

The average operator is appeared in Equation 4.77, which is provided below:

$$\{a\} = \frac{a^+ + a^-}{2} \tag{4.78}$$

Equation 4.76 is rewritten by applying Equation 4.77 to this expression:

$$\begin{aligned}\sum_e \int_{\partial\Omega^e_{SE}} \kappa_{SE}\nabla\phi_{SE}\cdot\boldsymbol{n}\delta\eta\, d\Gamma &= \int_{\partial\Omega^{1}_{SE}} [\![\kappa_m\nabla\phi_m\delta\eta]\!]\cdot\boldsymbol{n}\, d\Gamma + ... \\ &= \int_{\partial\Omega^{1}_{SE}} \left\{\kappa_m\nabla\phi_m\right\}[\![\delta\eta]\!]\cdot\boldsymbol{n}\, d\Gamma + \int_{\partial\Omega^{1}_{SE}} [\![\kappa_m\nabla\phi_m]\!]\{\delta\eta\}\cdot\boldsymbol{n}\, d\Gamma + ...\end{aligned} \tag{4.79}$$

A closer look is taken at the first integral of Equation 4.79, considering that $\boldsymbol{n}$ is constant and can be placed inside the average. Additionally, it is noted that a horizontal crack is considered in this derivation.

$$\begin{aligned}\int_{\partial\Omega^{1}_{SE}} \left\{\kappa_m\nabla\phi_m\right\}[\![\delta\eta]\!]\cdot\boldsymbol{n}\, d\Gamma &= \int_{\partial\Omega^{1}_{SE}} \kappa_m\left\{\nabla\phi_m\cdot\boldsymbol{n}\right\}[\![\delta\eta]\!]\, d\Gamma \\ &= \int_{\partial\Omega^{1}_{SE}} \kappa_m\left\{\frac{\partial\phi}{\partial z}\right\}[\![\delta\eta]\!]\, d\Gamma\end{aligned} \tag{4.80}$$

The average operator $\left\{\frac{\partial\phi}{\partial z}\right\}$ in Equation 4.80 can also be expressed in integral form, which can be evaluated:

$$\begin{aligned}\int_{\partial\Omega^{1}_{SE}} \left\{\kappa_m\nabla\phi_m\right\}[\![\delta\eta]\!]\, d\Gamma &= \int_{\partial\Omega^{1}_{SE}} \kappa_m\left(\frac{1}{w}\int_{-h}^{h}\frac{\partial\phi}{\partial z}\, dz\right)[\![\delta\eta]\!]\, d\Gamma \\ &= \int_{\partial\Omega^{1}_{SE}} \frac{\kappa_m}{w}\left(\phi_m(h) - \phi_m(-h)\right)[\![\delta\eta]\!]\, d\Gamma\end{aligned} \tag{4.81}$$

The evaluation of the electric potential at the upper and lower boundaries of the crack, $\phi_m(h)$ and $\phi_m(-h)$ respectively, can also be denoted as ϕ^+ and ϕ^-.

$$\begin{aligned}\int_{\partial\Omega^1_{SE}} \left\{\kappa_m \nabla\phi_m\right\} [\![\delta\eta]\!]\, d\Gamma &= \int_{\partial\Omega^1_{SE}} \frac{\kappa_m}{w}\left(\phi_m(h) - \phi_m(-h)\right) [\![\delta\eta]\!]\, d\Gamma \\ &= \int_{\partial\Omega^1_{SE}} \frac{\kappa_m}{w}\left(\phi_m^+ - \phi_m^-\right) [\![\delta\eta]\!]\, d\Gamma\end{aligned} \tag{4.82}$$

In Equation 4.82, the jump operator (Equation 4.23) becomes evident and is subsequently substituted into this expression:

$$\begin{aligned}\int_{\partial\Omega^1_{SE}} \left\{\kappa_m \nabla\phi_m\right\} [\![\delta\eta]\!]\, d\Gamma &= \int_{\partial\Omega^1_{SE}} \frac{\kappa_m}{w}\left(\phi_m^+ - \phi_m^-\right) [\![\delta\eta]\!]\, d\Gamma \\ &= \int_{\partial\Omega^1_{SE}} \frac{\kappa_m}{w} [\![\phi_m]\!] [\![\delta\eta]\!]\, d\Gamma\end{aligned} \tag{4.83}$$

Equation 4.83 is used to replace the first integral of Equation 4.79:

$$\begin{aligned}\sum_e \int_{\partial\Omega^e_{SE}} \kappa_{SE}\nabla\phi_{SE}\cdot\boldsymbol{n}\delta\eta\, d\Gamma &= \int_{\partial\Omega^1_{SE}} \left\{\kappa_m\nabla\phi_m\right\} [\![\delta\eta]\!]\cdot\boldsymbol{n}\, d\Gamma + \int_{\partial\Omega^1_{SE}} [\![\kappa_m\nabla\phi_m]\!]\{\delta\eta\}\cdot\boldsymbol{n}\, d\Gamma + ... \\ &= \int_{\partial\Omega^1_{SE}} \frac{\kappa_m}{w}[\![\phi_m]\!][\![\delta\eta]\!]\, d\Gamma + \int_{\partial\Omega^1_{SE}} [\![\kappa_m\nabla\phi_m]\!]\{\delta\eta\}\cdot\boldsymbol{n}\, d\Gamma + ...\end{aligned} \tag{4.84}$$

The second integral of Equation 4.85 is rewritten in terms of the electric potential for the solid electrolyte, utilizing the boundary conditions as shown in Equation 4.28. Equation 4.83 is used to replace the first integral of Equation 4.79:

$$\begin{aligned}\sum_e \int_{\partial\Omega^e_{SE}} \kappa_{SE}\nabla\phi_{SE}\cdot\boldsymbol{n}\delta\eta\, d\Gamma &= \int_{\partial\Omega^1_{SE}} \frac{\kappa_m}{w}[\![\phi_m]\!][\![\delta\eta]\!]\, d\Gamma + \int_{\partial\Omega^1_{SE}} [\![\kappa_m\nabla\phi_m]\!]\{\delta\eta\}\cdot\boldsymbol{n}\, d\Gamma + ... \\ &= \int_{\partial\Omega^1_{SE}} \frac{\kappa_m}{w}[\![\phi_m]\!][\![\delta\eta]\!]\, d\Gamma + \int_{\partial\Omega^1_{SE}} [\![\kappa_{SE}\nabla\phi_{SE}]\!]\{\delta\eta\}\cdot\boldsymbol{n}\, d\Gamma + ...\end{aligned} \tag{4.85}$$

If the derivation shown above is applied to every interface, the same expression is obtained for all interfaces. This implies that the expression can also be written with the boundary between the elements $\partial_I\Omega_h$ as the domain, considering all terms of the summation.

$$\begin{aligned}\sum_e \int_{\partial\Omega^e_{SE}} \kappa_{SE}\nabla\phi_{SE}\cdot\boldsymbol{n}\delta\eta\, d\Gamma &= \int_{\partial\Omega^1_{SE}} \frac{\kappa_m}{w}[\![\phi_m]\!][\![\delta\eta]\!]\, d\Gamma + \int_{\partial\Omega^1_{SE}} [\![\kappa_{SE}\nabla\phi_{SE}]\!]\{\delta\eta\}\cdot\boldsymbol{n}\, d\Gamma + ... \\ &= \int_{\partial_I\Omega_h} \frac{\kappa_m}{w}[\![\phi_m]\!][\![\delta\eta]\!]\, d\Gamma + \int_{\partial_I\Omega_h} [\![\kappa_{SE}\nabla\phi_{SE}]\!]\{\delta\eta\}\cdot\boldsymbol{n}\, d\Gamma\end{aligned} \tag{4.86}$$

Equation 4.79 can now be substituted back into Equation 4.71. Additionally, if the summation in the first term of Equation 4.71 is expanded, the domain of this term changes to Ω_h:

$$\begin{aligned}\sum_e \int_{\Omega^e_{SE}} -\mathrm{div}\left(\kappa_{SE}\nabla\phi_{SE}\right)\delta\eta\, d\Omega^e_{SE} &= \sum_e \int_{\Omega^e_{SE}} \kappa_{SE}\nabla\phi_{SE}\cdot\nabla\delta\eta\, d\Omega^e_{SE} - \sum_e \int_{\partial\Omega^e_{SE}} \kappa_{SE}\nabla\phi_{SE}\cdot\boldsymbol{n}\delta\eta\, d\Gamma \\ &= \int_{\Omega_h} \kappa_{SE}\nabla\phi_{SE}\cdot\nabla\delta\eta\, d\Omega - \int_{\partial_I\Omega_h} \frac{\kappa_m}{w}[\![\phi_m]\!][\![\delta\eta]\!]\, d\Gamma \\ &\quad - \int_{\partial_I\Omega_h} [\![\kappa_{SE}\nabla\phi_{SE}]\!]\{\delta\eta\}\cdot\boldsymbol{n}\, d\Gamma\end{aligned} \tag{4.87}$$

At uncracked interfaces, continuity between elements needs to be enforced. However, the discontinuous Galerkin formulation does not strongly enforce continuity. Therefore, a quadratic stabilization term must be added to the formulation to weakly enforce continuity. Additionally, this ensures that the

numerical solution remains stable. In the case of scalar problems, a term proportional to $[\![\phi_{SE}]\!]\,[\![\delta\eta]\!]$ should be added [40]. Adding this term to the weak form yields the following result:

$$\begin{aligned}\sum_e \int_{\Omega^e_{SE}} -\mathrm{div}\left(\kappa_{SE}\nabla\phi_{SE}\right)\delta\eta\, d\Omega^e_{SE} = &\int_{\Omega_h} \kappa_{SE}\nabla\phi_{SE}\cdot\nabla\delta\eta\, d\Omega - \int_{\partial_I\Omega_h} \frac{\kappa_m}{w}\,[\![\phi_m]\!]\,[\![\delta\eta]\!]\; d\Gamma \\ &- \int_{\partial_I\Omega_h} [\![\kappa_{SE}\nabla\phi_{SE}]\!]\,\{\delta\eta\}\cdot\boldsymbol{n}\, d\Gamma + \int_{\partial_I\Omega_h} \frac{\beta}{h}\,[\![\phi_{SE}]\!]\,[\![\delta\eta]\!]\; d\Gamma\end{aligned} \tag{4.88}$$

The stability term added above to the weak form to enforce interelement continuity should only be applied to the uncracked part of the mesh. Additionally, at the cracked interfaces, the interface part will replace the third term of Equation 4.88, similar to the continuous Galerkin method. Thus, it is necessary to distinguish between the cracked and uncracked interfaces in the weak form. Therefore, a binary operator α is introduced to the expression. α equals 0 before crack nucleation and 1 after crack nucleation. Applying this results in the final form of the bulk part of the weak form:

$$\begin{aligned}\sum_e \int_{\Omega^e_{SE}} -\mathrm{div}\left(\kappa_{SE}\nabla\phi_{SE}\right)\delta\eta\, d\Omega^e_{SE} = &\int_{\Omega_h} \kappa_{SE}\nabla\phi_{SE}\cdot\nabla\delta\eta\, d\Omega - \int_{\partial_I\Omega_h} \alpha\frac{\kappa_m}{w}\,[\![\phi_m]\!]\,[\![\delta\eta]\!]\; d\Gamma \\ &- \int_{\partial_I\Omega_h} \alpha\,[\![\kappa_{SE}\nabla\phi_{SE}]\!]\,\{\delta\eta\}\cdot\boldsymbol{n}\, d\Gamma \\ &- \int_{\partial_I\Omega_h} (1-\alpha)\,[\![\kappa_{SE}\nabla\phi_{SE}]\!]\,\{\delta\eta\}\cdot\boldsymbol{n}\, d\Gamma \\ &+ \int_{\partial_I\Omega_h} (1-\alpha)\,\frac{\beta}{h}\,[\![\phi_{SE}]\!]\,[\![\delta\eta]\!]\; d\Gamma\end{aligned} \tag{4.89}$$

The weak form of the interface is also redefined in a similar manner to the bulk weak form. Using a discontinuous test function, the weak form is derived from the governing equation valid in the electrodeposited crack and projected onto Γ, as shown in Equation 4.28. Since the weak form is elementwise, the expression is summed over the cracked interfaces. The chosen test function is the average of the test functions of the adjacent bulk elements. This results in the following expression:

$$\sum_i \int_{\Gamma^i} \left(wF\dot{\xi} - [\![\kappa_{SE}\nabla\phi_{SE}]\!]\cdot\boldsymbol{n} - w\kappa_m\frac{\partial^2\tilde{\phi}_m}{\partial x^2}\right)\{\delta\eta\}\; d\Gamma^i = 0 \tag{4.90}$$

When expanding the summation, the cracked interfaces are taken into account. The weak form is then multiplied by the α operator introduced earlier, allowing for consideration of all interfaces of the domain. Utilizing the operator in this manner ensures that terms are omitted where no crack nucleation has occurred ($\alpha = 0$) and are introduced at the crack sites ($\alpha = 1$).

$$\begin{aligned}\int_{\partial_I\Omega_h} \alpha\left(wF\dot{\xi} - [\![\kappa_{SE}\nabla\phi_{SE}]\!]\cdot\boldsymbol{n} - w\kappa_m\frac{\partial^2\tilde{\phi}_m}{\partial x^2}\right)\{\delta\eta\}\; d\Gamma = 0 \\ \int_{\partial_I\Omega_h} \alpha w F\dot{\xi}\,\{\delta\eta\}\; d\Gamma - \int_{\partial_I\Omega_h} \alpha\,[\![\kappa_{SE}\nabla\phi_{SE}]\!]\cdot\boldsymbol{n}\,\{\delta\eta\}\; d\Gamma - \int_{\partial_I\Omega_h} \alpha w\kappa_m\frac{\partial^2\tilde{\phi}_m}{\partial x^2}\,\{\delta\eta\}\; d\Gamma = 0\end{aligned} \tag{4.91}$$

The last integral of Equation 4.91 can be rewritten using integration by parts:

$$\int_{\partial_I\Omega_h} \alpha w\kappa_m\frac{\partial^2\tilde{\phi}_m}{\partial x^2}\,\{\delta\eta\}\; d\Gamma = \int_{\partial_I\Omega_h} \frac{\partial}{\partial x}\left(\alpha w\kappa_m\frac{\partial\tilde{\phi}_m}{\partial x}\,\{\delta\eta\}\right) d\Gamma - \int_{\partial_I\Omega_h} \alpha\kappa_m\frac{\partial\tilde{\phi}_m}{\partial x}\frac{\partial\left(w\,\{\delta\eta\}\right)}{\partial x}\, d\Gamma \tag{4.92}$$

The first term of Equation 4.92 can be directly evaluated at the boundaries of the crack. At the upper boundary, where the crack opening is zero, the term drops, resulting in the following expression:

$$\begin{aligned}\int_{\partial_I\Omega_h} \alpha w\kappa_m\frac{\partial^2\tilde{\phi}_m}{\partial x^2}\,\{\delta\eta\}\; d\Gamma &= \left[\alpha w\kappa_m\frac{\partial\tilde{\phi}_m}{\partial x}\,\{\delta\eta\}\right]_0^L - \int_{\partial_I\Omega_h} \alpha\kappa_m\frac{\partial\tilde{\phi}_m}{\partial x}\frac{\partial\left(w\,\{\delta\eta\}\right)}{\partial x}\, d\Gamma \\ &= -\alpha w\kappa_m\frac{\partial\tilde{\phi}_m}{\partial x}\,\{\delta\eta\}\,(0,0) - \int_{\partial_I\Omega_h} \alpha\kappa_m\frac{\partial\tilde{\phi}_m}{\partial x}\frac{\partial\left(w\,\{\delta\eta\}\right)}{\partial x}\, d\Gamma\end{aligned} \tag{4.93}$$

Equation 4.93 can be substituted back in Equation 4.91:

$$\begin{aligned}
&\int_{\partial_I\Omega_h} \alpha w F \dot{\xi} \{\delta\eta\}\, d\Gamma - \int_{\partial_I\Omega_h} \alpha \left[\!\left[\kappa_{SE}\nabla\phi_{SE}\right]\!\right]\cdot \boldsymbol{n} \{\delta\eta\}\, d\Gamma - \int_{\partial_I\Omega_h} \alpha w \kappa_m \frac{\partial^2\tilde{\phi}_m}{\partial x^2}\{\delta\eta\}\, d\Gamma = 0 \\
&\int_{\partial_I\Omega_h} \alpha w F \dot{\xi} \{\delta\eta\}\, d\Gamma - \int_{\partial_I\Omega_h} \alpha \left[\!\left[\kappa_{SE}\nabla\phi_{SE}\right]\!\right]\cdot \boldsymbol{n} \{\delta\eta\}\, d\Gamma + \int_{\partial_I\Omega_h} \alpha\kappa_m \frac{\partial\tilde{\phi}_m}{\partial x}\frac{\partial\left(w\{\delta\eta\}\right)}{\partial x}\, d\Gamma + \\
&\qquad\qquad \alpha w \kappa_m \frac{\partial\tilde{\phi}_m}{\partial x}\{\delta\eta\}(0,0) = 0
\end{aligned} \tag{4.94}$$

The hybrid unified version of the weak form is created by combining the bulk (Equation 4.89) and the interface (Equation 4.94) weak form by subtracting both expressions from each other:

$$\begin{aligned}
&\int_{\Omega_h} \kappa_{SE}\nabla\phi_{SE}\cdot\nabla\delta\eta\, d\Omega - \int_{\partial_I\Omega_h} \alpha\frac{\kappa_m}{w}\left[\!\left[\phi_m\right]\!\right]\left[\!\left[\delta\eta\right]\!\right] d\Gamma - \int_{\partial_I\Omega_h} \alpha \left[\!\left[\kappa_{SE}\nabla\phi_{SE}\right]\!\right]\{\delta\eta\}\cdot\boldsymbol{n}\, d\Gamma \\
&- \int_{\partial_I\Omega_h} (1-\alpha)\left[\!\left[\kappa_{SE}\nabla\phi_{SE}\right]\!\right]\{\delta\eta\}\cdot\boldsymbol{n}\, d\Gamma + \int_{\partial_I\Omega_h}(1-\alpha)\frac{\beta}{h}\left[\!\left[\phi_{SE}\right]\!\right]\left[\!\left[\delta\eta\right]\!\right] d\Gamma - \int_{\partial_I\Omega_h} \alpha w F\dot{\xi}\{\delta\eta\}\, d\Gamma \\
&+ \int_{\partial_I\Omega_h} \alpha \left[\!\left[\kappa_{SE}\nabla\phi_{SE}\right]\!\right]\cdot\boldsymbol{n}\{\delta\eta\}\, d\Gamma - \int_{\partial_I\Omega_h}\alpha\kappa_m\frac{\partial\tilde{\phi}_m}{\partial x}\frac{\partial\left(w\{\delta\eta\}\right)}{\partial x}\, d\Gamma - \alpha w\kappa_m\frac{\partial\tilde{\phi}_m}{\partial x}\{\delta\eta\}(0,0) = 0
\end{aligned} \tag{4.95}$$

Simplifying Equation 4.95 gives the final expression of the weak form:

$$\begin{aligned}
&\int_{\Omega_h} \kappa_{SE}\nabla\phi_{SE}\cdot\nabla\delta\eta\, d\Omega - \int_{\partial_I\Omega_h} \alpha\frac{\kappa_m}{w}\left[\!\left[\phi_m\right]\!\right]\left[\!\left[\delta\eta\right]\!\right] d\Gamma - \int_{\partial_I\Omega_h}(1-\alpha)\left[\!\left[\kappa_{SE}\nabla\phi_{SE}\right]\!\right]\{\delta\eta\}\cdot\boldsymbol{n}\, d\Gamma \\
&+ \int_{\partial_I\Omega_h}(1-\alpha)\frac{\beta}{h}\left[\!\left[\phi_{SE}\right]\!\right]\left[\!\left[\delta\eta\right]\!\right] d\Gamma - \int_{\partial_I\Omega_h}\alpha w F\dot{\xi}\{\delta\eta\}\, d\Gamma - \int_{\partial_I\Omega_h}\alpha\kappa_m\frac{\partial\tilde{\phi}_m}{\partial x}\frac{\partial\left(w\{\delta\eta\}\right)}{\partial x}\, d\Gamma \\
&- \alpha w\kappa_m\frac{\partial\tilde{\phi}_m}{\partial x}\{\delta\eta\}(0,0) = 0
\end{aligned} \tag{4.96}$$

4.5. Discontinuous Galerkin discretization

The weak form shown in Equation 4.96 is transferred into an element stiffness matrix in this section, which is a similar process to the transformation of the continuous Galerkin counterpart shown before. In this case, the solution for the electric potential in discontinuous Galerkin methods involves approximating it with a combination of Discontinuous Shape Functions (η) and unknown amplitudes (ϕ). This approximation yields a similar expression to that of continuous Galerkin methods, as shown in Equation 4.42.

Figure 4.4 illustrates the butterfly element used in Discontinuous Galerkin, employing first-order test functions. The butterfly element comprises two triangle elements with three nodes each. Notably, these elements have separate nodes at their shared interface, meaning triangle elements do not share nodes when used in butterfly elements. Consequently, the interface between these elements, crucial for the weak form's interface parts, is not directly modeled. Instead, it is considered by using the average and jump of values associated with the interface nodes, denoted as a and b. These interface nodes do not contribute to the stiffness matrix.

Furthermore, Figure 4.4 illustrates that test functions of nodes not part of a particular interface are zero at that interface, implying they do not contribute to the stiffness matrix. In this instance, nodes 1 and 6 have no contribution. Although the resulting element matrix is theoretically a 6×6 matrix, for clarity, only nonzero contributions are depicted in the derivation.

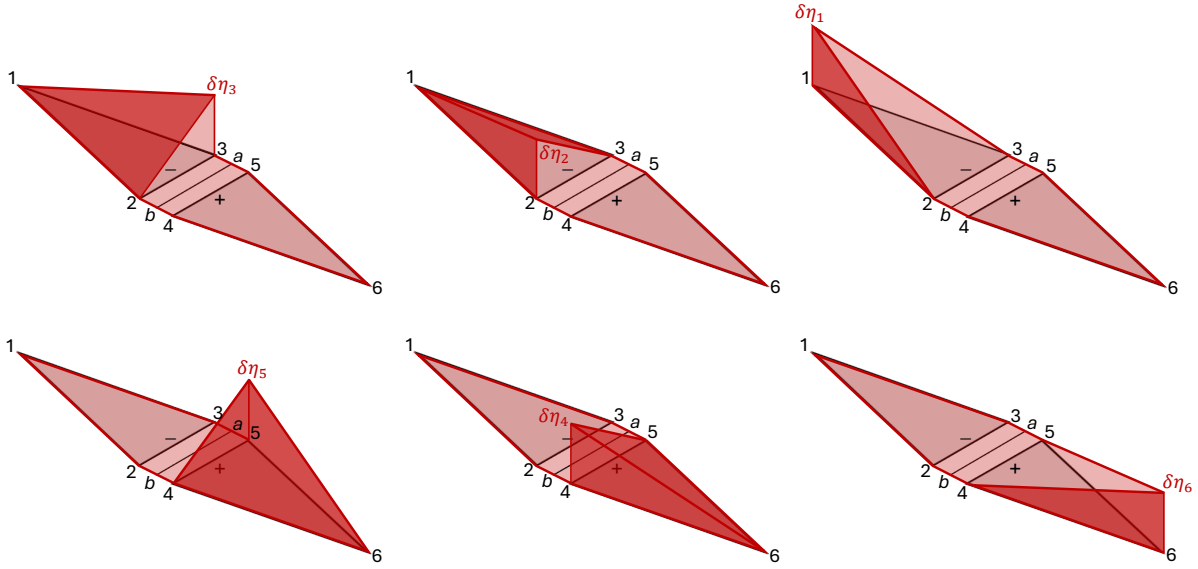

Figure 4.4: A schematic view depicts the discontinuous first-order test functions for each node of the butterfly elements, which consist of a combination of two triangle elements, each comprising three nodes. The interface element between these elements is not directly modeled but is conceptually depicted and replaced during derivation by average and jump operators applied between the nodes at the interface.

The discontinuous weak form of the hybrid formulation, as depicted in Equation 4.96, comprises several integrals. The first integral, representing the bulk term, closely resembles its continuous Galerkin counterpart, yielding the same stiffness matrix as illustrated in Equation 4.53. The primary distinction lies in the discontinuous nature of the shape functions. Therefore, this integral is not separately derived, and the continuous Galerkin element stiffness matrix is used, taking into account the different shape functions.

The remaining weak form integrals are similarly transformed into stiffness matrices. Firstly, the integrals correspond to the uncracked part of the domain, represented by the $(1-\alpha)$ terms in Equation 4.96. The expressions no longer show the $(1-\alpha)$ and α terms because the distinction is made differently by creating separate stiffness matrices for the uncracked and cracked parts. Beginning with the first integral of the uncracked part, this integral is mapped to the standard domain using the Jacobian.

$$\int_{\partial_I\Omega_h} [\![\kappa_{SE}\nabla\phi_{SE}]\!]\,\{\delta\eta\}\cdot\boldsymbol{n}\,d\Gamma = \int_{\partial_I\Omega_h^*} J\,[\![\kappa_{SE}\nabla\phi_{SE}]\!]\,\{\delta\eta\}\cdot\boldsymbol{n}\,d\Gamma \tag{4.97}$$

These integrals are solved numerically, approximating the integral by multiplying the integrand by quadrature weights at the quadrature points. Additionally, the expression is simplified by combining the quadrature weights and Jacobian into a single variable $W_{e,q}$.

$$\begin{aligned}\int_{\partial_I\Omega_h^*} J\,[\![\kappa_{SE}\nabla\phi_{SE}]\!]\,\{\delta\eta\}\cdot\boldsymbol{n}\,d\Gamma &= \sum_{e,q=1} w_{e,q}J_{e,q}\,[\![\kappa_{SE}\nabla\phi_{SE}]\!]_{e,q}\,\{\delta\eta\}_{e,q}\cdot\boldsymbol{n}\\ &= \sum_{e,q=1} W_{e,q}\,[\![\kappa_{SE}\nabla\phi_{SE}]\!]_{e,q}\,\{\delta\eta\}_{e,q}\cdot\boldsymbol{n}\end{aligned} \tag{4.98}$$

The approximate solution of the electric potential Equation 4.42 is substituted into Equation 4.98

$$\sum_{e,q=1} W_{e,q}\,[\![\kappa_{SE}\nabla\phi_{SE}]\!]_{e,q}\,\{\delta\eta\}_{e,q}\cdot\boldsymbol{n} = \sum_{e,q=1} W_{e,q}\left[\!\!\left[\kappa_{SE}\sum_{i=a}^{b}\phi_i\nabla\eta_i\right]\!\!\right]_{e,q}\{\delta\eta\}_{e,q}\cdot\boldsymbol{n} \tag{4.99}$$

For every element and quadrature point, the stiffness matrix has the same form. Therefore, the derivation continues for only a single element and quadrature point. Additionally, the summation of

the approximate solution is expanded.

$$\sum_{e,q=1} W_{e,q} \left[\!\!\left[\kappa_{SE} \sum_{i=a}^{b} \phi_i \nabla \eta_i \right]\!\!\right]_{e,q} \{\delta\eta\}_{e,q} \cdot \boldsymbol{n} = W \left[\!\!\left[\kappa_{SE} \phi_a \nabla \eta_a + \phi_b \nabla \eta_b \right]\!\!\right] \{\delta\eta\} \cdot \boldsymbol{n} + \ldots \tag{4.100}$$

The jump operator of the approximate solution is rewritten using the definition shown in Equation 4.23:

$$\begin{aligned} W \left[\!\!\left[\kappa_{SE} \phi_a \nabla \eta_a \cdot \boldsymbol{n} + \kappa_{SE} \phi_b \nabla \eta_b \cdot \boldsymbol{n} \right]\!\!\right] \{\delta\eta\} = & W \Big(\left(\kappa_{SE} \phi_a \nabla \eta_a \cdot \boldsymbol{n} \right)^+ - \left(\kappa_{SE} \phi_a \nabla \eta_a \cdot \boldsymbol{n} \right)^- \\ & + \left(\kappa_{SE} \phi_b \nabla \eta_b \cdot \boldsymbol{n} \right)^+ - \left(\kappa_{SE} \phi_b \nabla \eta_b \cdot \boldsymbol{n} \right)^- \Big) \{\delta\eta\} \end{aligned} \tag{4.101}$$

The plus and minus sides of the interface nodes a and b correspond to the function associated with the particular nodes of the butterfly elements. As seen in Figure 4.4, the plus and minus sides of node a correspond to nodes 5 and 3, respectively. Similarly, The plus and minus sides of node b correspond to nodes 4 and 2, respectively. These functions are substituted into Equation 4.101:

$$\begin{aligned} & W \Big(\left(\kappa_{SE} \phi_a \nabla \eta_a \cdot \boldsymbol{n} \right)^+ - \left(\kappa_{SE} \phi_a \nabla \eta_a \cdot \boldsymbol{n} \right)^- + \left(\kappa_{SE} \phi_b \nabla \eta_b \cdot \boldsymbol{n} \right)^+ - \left(\kappa_{SE} \phi_b \nabla \eta_b \cdot \boldsymbol{n} \right)^- \Big) \{\delta\eta\} = \\ & W \left(\kappa_{SE} \phi_5 \nabla \eta_5 \cdot \boldsymbol{n} - \kappa_{SE} \phi_3 \nabla \eta_3 \cdot \boldsymbol{n} + \kappa_{SE} \phi_4 \nabla \eta_4 \cdot \boldsymbol{n} - \kappa_{SE} \phi_2 \nabla \eta_2 \cdot \boldsymbol{n} \right) \{\delta\eta\} \end{aligned} \tag{4.102}$$

A system of equations is obtained from Equation 4.102 by using the shape functions adjacent to the particular interface as test functions.

$$\begin{aligned} & W \left(-\kappa_{SE} \phi_2 \nabla \eta_2 \cdot \boldsymbol{n} - \kappa_{SE} \phi_3 \nabla \eta_3 \cdot \boldsymbol{n} + \kappa_{SE} \phi_4 \nabla \eta_4 \cdot \boldsymbol{n} + \kappa_{SE} \phi_5 \nabla \eta_5 \cdot \boldsymbol{n} \right) \{\delta\eta_2\} \\ & W \left(-\kappa_{SE} \phi_2 \nabla \eta_2 \cdot \boldsymbol{n} - \kappa_{SE} \phi_3 \nabla \eta_3 \cdot \boldsymbol{n} + \kappa_{SE} \phi_4 \nabla \eta_4 \cdot \boldsymbol{n} + \kappa_{SE} \phi_5 \nabla \eta_5 \cdot \boldsymbol{n} \right) \{\delta\eta_3\} \\ & W \left(-\kappa_{SE} \phi_2 \nabla \eta_2 \cdot \boldsymbol{n} - \kappa_{SE} \phi_3 \nabla \eta_3 \cdot \boldsymbol{n} + \kappa_{SE} \phi_4 \nabla \eta_4 \cdot \boldsymbol{n} + \kappa_{SE} \phi_5 \nabla \eta_5 \cdot \boldsymbol{n} \right) \{\delta\eta_4\} \\ & W \left(-\kappa_{SE} \phi_2 \nabla \eta_2 \cdot \boldsymbol{n} - \kappa_{SE} \phi_3 \nabla \eta_3 \cdot \boldsymbol{n} + \kappa_{SE} \phi_4 \nabla \eta_4 \cdot \boldsymbol{n} + \kappa_{SE} \phi_5 \nabla \eta_5 \cdot \boldsymbol{n} \right) \{\delta\eta_5\} \end{aligned} \tag{4.103}$$

The average of the test function is defined in the following way.

$$\begin{aligned} \{\delta\eta\} &= \{\delta\varphi_i \eta_i\} \\ &= \left(\frac{1}{2} \delta\varphi_i^+ \eta_i^+ + \frac{1}{2} \delta\varphi_i^- \eta_i^- \right) \end{aligned} \tag{4.104}$$

Here, $\delta\varphi_i$ represents the amplitude of the particular node, and η_i denotes the shape function, which is also used to approximate the electric potential. The shape function is equal on both the plus and minus sides and can be factored out of the brackets:

$$\begin{aligned} \{\delta\eta\} &= \left(\frac{1}{2} \delta\varphi_i^+ \eta_i^+ + \frac{1}{2} \delta\varphi_i^- \eta_i^- \right) \\ &= \frac{1}{2} \left(\delta\varphi_i^+ + \delta\varphi_i^- \right) \eta_i \end{aligned} \tag{4.105}$$

Equation 4.105 can be applied to the test functions of the nodes used in the system of equations shown in Equation 4.103.

$$\begin{aligned} & W \left(-\kappa_{SE} \phi_2 \nabla \eta_2 \cdot \boldsymbol{n} - \kappa_{SE} \phi_3 \nabla \eta_3 \cdot \boldsymbol{n} + \kappa_{SE} \phi_4 \nabla \eta_4 \cdot \boldsymbol{n} + \kappa_{SE} \phi_5 \nabla \eta_5 \cdot \boldsymbol{n} \right) \frac{1}{2} \left(\delta\varphi_2^+ + \delta\varphi_2^- \right) \eta_2 \\ & W \left(-\kappa_{SE} \phi_2 \nabla \eta_2 \cdot \boldsymbol{n} - \kappa_{SE} \phi_3 \nabla \eta_3 \cdot \boldsymbol{n} + \kappa_{SE} \phi_4 \nabla \eta_4 \cdot \boldsymbol{n} + \kappa_{SE} \phi_5 \nabla \eta_5 \cdot \boldsymbol{n} \right) \frac{1}{2} \left(\delta\varphi_3^+ + \delta\varphi_3^- \right) \eta_3 \\ & W \left(-\kappa_{SE} \phi_2 \nabla \eta_2 \cdot \boldsymbol{n} - \kappa_{SE} \phi_3 \nabla \eta_3 \cdot \boldsymbol{n} + \kappa_{SE} \phi_4 \nabla \eta_4 \cdot \boldsymbol{n} + \kappa_{SE} \phi_5 \nabla \eta_5 \cdot \boldsymbol{n} \right) \frac{1}{2} \left(\delta\varphi_4^+ + \delta\varphi_4^- \right) \eta_4 \\ & W \left(-\kappa_{SE} \phi_2 \nabla \eta_2 \cdot \boldsymbol{n} - \kappa_{SE} \phi_3 \nabla \eta_3 \cdot \boldsymbol{n} + \kappa_{SE} \phi_4 \nabla \eta_4 \cdot \boldsymbol{n} + \kappa_{SE} \phi_5 \nabla \eta_5 \cdot \boldsymbol{n} \right) \frac{1}{2} \left(\delta\varphi_5^+ + \delta\varphi_5^- \right) \eta_5 \end{aligned} \tag{4.106}$$

As seen in Figure 4.4, $\delta\varphi^+$ and $\delta\varphi^-$ can be 0 or 1, depending on the test function. For instance, for the second test function $\delta\eta_2$, the positive amplitude $\delta\varphi_2^+$ equals 0, while the negative amplitude $\delta\varphi_2^-$ equals

1. Similarly, the amplitudes for the other test functions are defined. Applying this to the system of equations of Equation 4.106 for all the test functions gives the following result:

$$\begin{aligned}
&W\left(-\kappa_{SE}\phi_2\nabla\eta_2\cdot\boldsymbol{n}-\kappa_{SE}\phi_3\nabla\eta_3\cdot\boldsymbol{n}+\kappa_{SE}\phi_4\nabla\eta_4\cdot\boldsymbol{n}+\kappa_{SE}\phi_5\nabla\eta_5\cdot\boldsymbol{n}\right)\frac{1}{2}\left(0+1\right)\eta_2\\
&W\left(-\kappa_{SE}\phi_2\nabla\eta_2\cdot\boldsymbol{n}-\kappa_{SE}\phi_3\nabla\eta_3\cdot\boldsymbol{n}+\kappa_{SE}\phi_4\nabla\eta_4\cdot\boldsymbol{n}+\kappa_{SE}\phi_5\nabla\eta_5\cdot\boldsymbol{n}\right)\frac{1}{2}\left(0+1\right)\eta_3\\
&W\left(-\kappa_{SE}\phi_2\nabla\eta_2\cdot\boldsymbol{n}-\kappa_{SE}\phi_3\nabla\eta_3\cdot\boldsymbol{n}+\kappa_{SE}\phi_4\nabla\eta_4\cdot\boldsymbol{n}+\kappa_{SE}\phi_5\nabla\eta_5\cdot\boldsymbol{n}\right)\frac{1}{2}\left(1+0\right)\eta_4\\
&W\left(-\kappa_{SE}\phi_2\nabla\eta_2\cdot\boldsymbol{n}-\kappa_{SE}\phi_3\nabla\eta_3\cdot\boldsymbol{n}+\kappa_{SE}\phi_4\nabla\eta_4\cdot\boldsymbol{n}+\kappa_{SE}\phi_5\nabla\eta_5\cdot\boldsymbol{n}\right)\frac{1}{2}\left(1+0\right)\eta_5
\end{aligned} \tag{4.107}$$

This results in the final form of the system of equations:

$$\begin{aligned}
&\frac{1}{2}W\left(-\kappa_{SE}\phi_2\nabla\eta_2\cdot\boldsymbol{n}-\kappa_{SE}\phi_3\nabla\eta_3\cdot\boldsymbol{n}+\kappa_{SE}\phi_4\nabla\eta_4\cdot\boldsymbol{n}+\kappa_{SE}\phi_5\nabla\eta_5\cdot\boldsymbol{n}\right)\eta_2\\
&\frac{1}{2}W\left(-\kappa_{SE}\phi_2\nabla\eta_2\cdot\boldsymbol{n}-\kappa_{SE}\phi_3\nabla\eta_3\cdot\boldsymbol{n}+\kappa_{SE}\phi_4\nabla\eta_4\cdot\boldsymbol{n}+\kappa_{SE}\phi_5\nabla\eta_5\cdot\boldsymbol{n}\right)\eta_3\\
&\frac{1}{2}W\left(-\kappa_{SE}\phi_2\nabla\eta_2\cdot\boldsymbol{n}-\kappa_{SE}\phi_3\nabla\eta_3\cdot\boldsymbol{n}+\kappa_{SE}\phi_4\nabla\eta_4\cdot\boldsymbol{n}+\kappa_{SE}\phi_5\nabla\eta_5\cdot\boldsymbol{n}\right)\eta_4\\
&\frac{1}{2}W\left(-\kappa_{SE}\phi_2\nabla\eta_2\cdot\boldsymbol{n}-\kappa_{SE}\phi_3\nabla\eta_3\cdot\boldsymbol{n}+\kappa_{SE}\phi_4\nabla\eta_4\cdot\boldsymbol{n}+\kappa_{SE}\phi_5\nabla\eta_5\cdot\boldsymbol{n}\right)\eta_5
\end{aligned} \tag{4.108}$$

The contribution of the first quadrature point to the element stiffness matrix is now obtained by expressing the system of equations in matrix-vector notation.

$$\begin{bmatrix}
-\frac{1}{2}\kappa_{SE}W\nabla\eta_2\cdot\boldsymbol{n}\eta_2 & -\frac{1}{2}\kappa_{SE}W\nabla\eta_3\cdot\boldsymbol{n}\eta_2 & \frac{1}{2}\kappa_{SE}W\nabla\eta_4\cdot\boldsymbol{n}\eta_2 & \frac{1}{2}\kappa_{SE}W\nabla\eta_5\cdot\boldsymbol{n}\eta_2\\
-\frac{1}{2}\kappa_{SE}W\nabla\eta_2\cdot\boldsymbol{n}\eta_3 & -\frac{1}{2}\kappa_{SE}W\nabla\eta_3\cdot\boldsymbol{n}\eta_3 & \frac{1}{2}\kappa_{SE}W\nabla\eta_4\cdot\boldsymbol{n}\eta_3 & \frac{1}{2}\kappa_{SE}W\nabla\eta_5\cdot\boldsymbol{n}\eta_3\\
-\frac{1}{2}\kappa_{SE}W\nabla\eta_2\cdot\boldsymbol{n}\eta_4 & -\frac{1}{2}\kappa_{SE}W\nabla\eta_3\cdot\boldsymbol{n}\eta_4 & \frac{1}{2}\kappa_{SE}W\nabla\eta_4\cdot\boldsymbol{n}\eta_4 & \frac{1}{2}\kappa_{SE}W\nabla\eta_5\cdot\boldsymbol{n}\eta_4\\
-\frac{1}{2}\kappa_{SE}W\nabla\eta_2\cdot\boldsymbol{n}\eta_5 & -\frac{1}{2}\kappa_{SE}W\nabla\eta_3\cdot\boldsymbol{n}\eta_5 & \frac{1}{2}\kappa_{SE}W\nabla\eta_4\cdot\boldsymbol{n}\eta_5 & \frac{1}{2}\kappa_{SE}W\nabla\eta_5\cdot\boldsymbol{n}\eta_5
\end{bmatrix}\begin{pmatrix}\phi_2\\\phi_3\\\phi_4\\\phi_5\end{pmatrix} \tag{4.109}$$

The whole element stiffness matrix is obtained by summing over all quadrature points.

$$\sum_{q=1}\begin{bmatrix}
-\frac{1}{2}\kappa_{SE_q}W_q\nabla\eta_{q,2}\cdot\boldsymbol{n}\eta_{q,2} & -\frac{1}{2}\kappa_{SE_q}W_q\nabla\eta_{q,3}\cdot\boldsymbol{n}\eta_{q,2} & \frac{1}{2}\kappa_{SE_q}W_q\nabla\eta_{q,4}\cdot\boldsymbol{n}\eta_{q,2} & \frac{1}{2}\kappa_{SE_q}W_q\nabla\eta_{q,5}\cdot\boldsymbol{n}\eta_{q,2}\\
-\frac{1}{2}\kappa_{SE_q}W_q\nabla\eta_{q,2}\cdot\boldsymbol{n}\eta_{q,3} & -\frac{1}{2}\kappa_{SE_q}W_q\nabla\eta_{q,3}\cdot\boldsymbol{n}\eta_{q,3} & \frac{1}{2}\kappa_{SE_q}W_q\nabla\eta_{q,4}\cdot\boldsymbol{n}\eta_{q,3} & \frac{1}{2}\kappa_{SE_q}W_q\nabla\eta_{q,5}\cdot\boldsymbol{n}\eta_{q,3}\\
-\frac{1}{2}\kappa_{SE_q}W_q\nabla\eta_{q,2}\cdot\boldsymbol{n}\eta_{q,4} & -\frac{1}{2}\kappa_{SE_q}W_q\nabla\eta_{q,3}\cdot\boldsymbol{n}\eta_{q,4} & \frac{1}{2}\kappa_{SE_q}W_q\nabla\eta_{q,4}\cdot\boldsymbol{n}\eta_{q,4} & \frac{1}{2}\kappa_{SE_q}W_q\nabla\eta_{q,5}\cdot\boldsymbol{n}\eta_{q,4}\\
-\frac{1}{2}\kappa_{SE_q}W_q\nabla\eta_{q,2}\cdot\boldsymbol{n}\eta_{q,5} & -\frac{1}{2}\kappa_{SE_q}W_q\nabla\eta_{q,3}\cdot\boldsymbol{n}\eta_{q,5} & \frac{1}{2}\kappa_{SE_q}W_q\nabla\eta_{q,4}\cdot\boldsymbol{n}\eta_{q,5} & \frac{1}{2}\kappa_{SE_q}W_q\nabla\eta_{q,5}\cdot\boldsymbol{n}\eta_{q,5}
\end{bmatrix}\begin{pmatrix}\phi_2\\\phi_3\\\phi_4\\\phi_5\end{pmatrix} \tag{4.110}$$

The second integral, which constitutes the uncracked part of the weak form, represents the stability term. Similar to the previous integral, the domain is transformed using the Jacobian, and the integral is solved numerically.

$$\begin{aligned}
\int_{\partial_I\Omega_h}\frac{\beta}{h}\left[\!\left[\phi_{SE}\right]\!\right]\left[\!\left[\delta\eta\right]\!\right]\,d\Gamma &= \int_{\partial_I\Omega_h^*}\frac{\beta}{h}J\left[\!\left[\phi_{SE}\right]\!\right]\left[\!\left[\delta\eta\right]\!\right]\,d\Gamma\\
&= \sum_{e,q=1}w_{e,q}J_{e,q}\frac{\beta}{h}\left[\!\left[\phi_{SE}\right]\!\right]_{e,q}\left[\!\left[\delta\eta\right]\!\right]_{e,q}
\end{aligned} \tag{4.111}$$

The approximate solution of the electric potential (Equation 4.42) can be substituted into Equation 4.111. Additionally, the quadrature weight w and the Jacobian J are combined into a single variable W.

$$\sum_{e,q=1}w_{e,q}J_{e,q}\frac{\beta}{h}\left[\!\left[\phi_{SE}\right]\!\right]_{e,q}\left[\!\left[\delta\eta\right]\!\right]_{e,q} = \sum_{e,q=1}W_{e,q}\frac{\beta}{h}\left[\!\left[\sum_{i=a}^{b}\phi_i\eta_i\right]\!\right]_{e,q}\left[\!\left[\delta\eta\right]\!\right]_{e,q} \tag{4.112}$$

The stiffness matrix that will be obtained is general for all elements and quadrature points. Therefore, only one element and quadrature point are shown for the remaining part of the derivation.

$$\sum_{e,q=1} W_{e,q} \frac{\beta}{h} \left[\!\!\left[\sum_{i=a}^{b} \phi_i \eta_i \right]\!\!\right]_{e,q} [\![\delta\eta]\!]_{e,q} = W \frac{\beta}{h} [\![\phi_a \eta_a + \phi_b \eta_b]\!] [\![\delta\eta]\!] + ... \tag{4.113}$$

The definition of the jump operator (Equation 4.23) is utilized to rewrite the approximate solution of the electric potential in Equation 4.113.

$$W \frac{\beta}{h} [\![\phi_a \eta_a + \phi_b \eta_b]\!] [\![\delta\eta]\!] = W \frac{\beta}{h} \left(\left(\phi_a \eta_a\right)^+ - \left(\phi_a \eta_a\right)^- + \left(\phi_b \eta_b\right)^+ - \left(\phi_b \eta_b\right)^- \right) [\![\delta\eta]\!] \tag{4.114}$$

The plus and minus sides of the interface nodes a and b can be replaced in the same manner as demonstrated previously in Equation 4.102. Thus, the a^+ side is replaced by the fifth node function, the a^- side by the third node function, the b^+ side by the fourth node function, and the b^- side by the second node function.

$$W \frac{\beta}{h} \left(\left(\phi_a \eta_a\right)^+ - \left(\phi_a \eta_a\right)^- + \left(\phi_b \eta_b\right)^+ - \left(\phi_b \eta_b\right)^- \right) [\![\delta\eta]\!] = W \frac{\beta}{h} \left(\phi_5 \eta_5 - \phi_3 \eta_3 + \phi_4 \eta_4 - \phi_2 \eta_2 \right) [\![\delta\eta]\!] \tag{4.115}$$

The system of equations is obtained by using the nodal test functions of the specific element in Equation 4.115.

$$\begin{aligned}
&W \frac{\beta}{h} \left(-\phi_2 \eta_2 - \phi_3 \eta_3 + \phi_4 \eta_4 + \phi_5 \eta_5 \right) [\![\delta\eta_2]\!] \\
&W \frac{\beta}{h} \left(-\phi_2 \eta_2 - \phi_3 \eta_3 + \phi_4 \eta_4 + \phi_5 \eta_5 \right) [\![\delta\eta_3]\!] \\
&W \frac{\beta}{h} \left(-\phi_2 \eta_2 - \phi_3 \eta_3 + \phi_4 \eta_4 + \phi_5 \eta_5 \right) [\![\delta\eta_4]\!] \\
&W \frac{\beta}{h} \left(-\phi_2 \eta_2 - \phi_3 \eta_3 + \phi_4 \eta_4 + \phi_5 \eta_5 \right) [\![\delta\eta_5]\!]
\end{aligned} \tag{4.116}$$

The jump of the test function is defined below, considering that the shape function is the same on both the plus and minus sides.

$$\begin{aligned}
\{\delta\eta\} &= [\![\delta\varphi_i \eta_i]\!] \\
&= \left(\delta\varphi_i^+ \eta_i^+ - \delta\varphi_i^- \eta_i^- \right) \\
&= \left(\delta\varphi_i^+ + \delta\varphi_i^- \right) \eta_i
\end{aligned} \tag{4.117}$$

The definition of the jump (Equation 4.117) of the test functions can be applied to the system of equations (Equation 4.116).

$$\begin{aligned}
&W \frac{\beta}{h} \left(-\phi_2 \eta_2 - \phi_3 \eta_3 + \phi_4 \eta_4 + \phi_5 \eta_5 \right) \left(\delta\varphi_2^+ - \delta\varphi_2^- \right) \eta_2 \\
&W \frac{\beta}{h} \left(-\phi_2 \eta_2 - \phi_3 \eta_3 + \phi_4 \eta_4 + \phi_5 \eta_5 \right) \left(\delta\varphi_3^+ - \delta\varphi_3^- \right) \eta_3 \\
&W \frac{\beta}{h} \left(-\phi_2 \eta_2 - \phi_3 \eta_3 + \phi_4 \eta_4 + \phi_5 \eta_5 \right) \left(\delta\varphi_4^+ - \delta\varphi_4^- \right) \eta_4 \\
&W \frac{\beta}{h} \left(-\phi_2 \eta_2 - \phi_3 \eta_3 + \phi_4 \eta_4 + \phi_5 \eta_5 \right) \left(\delta\varphi_5^+ - \delta\varphi_5^- \right) \eta_5
\end{aligned} \tag{4.118}$$

Similar to before, φ^+ and φ^- can be either 0 or 1 depending on the shape functions shown in Figure 4.4, which adjusts the system of equations as follows:

$$\begin{aligned}
&W \frac{\beta}{h} \left(-\phi_2 \eta_2 - \phi_3 \eta_3 + \phi_4 \eta_4 + \phi_5 \eta_5 \right) (0 - 1) \eta_2 \\
&W \frac{\beta}{h} \left(-\phi_2 \eta_2 - \phi_3 \eta_3 + \phi_4 \eta_4 + \phi_5 \eta_5 \right) (0 - 1) \eta_3 \\
&W \frac{\beta}{h} \left(-\phi_2 \eta_2 - \phi_3 \eta_3 + \phi_4 \eta_4 + \phi_5 \eta_5 \right) (1 - 0) \eta_4 \\
&W \frac{\beta}{h} \left(-\phi_2 \eta_2 - \phi_3 \eta_3 + \phi_4 \eta_4 + \phi_5 \eta_5 \right) (1 - 0) \eta_5
\end{aligned} \tag{4.119}$$

Simplifying this expression gives:

$$\begin{aligned}
&-W\frac{\beta}{h}\left(-\phi_2\eta_2-\phi_3\eta_3+\phi_4\eta_4+\phi_5\eta_5\right)\eta_2\\
&-W\frac{\beta}{h}\left(-\phi_2\eta_2-\phi_3\eta_3+\phi_4\eta_4+\phi_5\eta_5\right)\eta_3\\
&W\frac{\beta}{h}\left(-\phi_2\eta_2-\phi_3\eta_3+\phi_4\eta_4+\phi_5\eta_5\right)\eta_4\\
&W\frac{\beta}{h}\left(-\phi_2\eta_2-\phi_3\eta_3+\phi_4\eta_4+\phi_5\eta_5\right)\eta_5
\end{aligned} \tag{4.120}$$

The element stiffness matrix is obtained by writing Equation 4.120 in matrix-vector notation and summing over all the quadrature points.

$$\sum_{q=1}\begin{bmatrix}
W_q\frac{\beta}{h}\eta_{q,2}\eta_2 & W_q\frac{\beta}{h}\eta_{q,3}\eta_{q,2} & -W_q\frac{\beta}{h}\eta_{q,4}\eta_{q,2} & -W_q\frac{\beta}{h}\eta_{q,5}\eta_{q,2}\\
W_q\frac{\beta}{h}\eta_{q,2}\eta_3 & W_q\frac{\beta}{h}\eta_{q,3}\eta_{q,3} & -W_q\frac{\beta}{h}\eta_{q,4}\eta_{q,3} & -W_q\frac{\beta}{h}\eta_{q,5}\eta_{q,3}\\
-W_q\frac{\beta}{h}\eta_{q,2}\eta_4 & -W_q\frac{\beta}{h}\eta_{q,3}\eta_{q,4} & W_q\frac{\beta}{h}\eta_{q,4}\eta_{q,4} & W_q\frac{\beta}{h}\eta_{q,5}\eta_{q,4}\\
-W_q\frac{\beta}{h}\eta_{q,2}\eta_5 & -W_q\frac{\beta}{h}\eta_{q,3}\eta_{q,5} & W_q\frac{\beta}{h}\eta_{q,4}\eta_{q,5} & W_q\frac{\beta}{h}\eta_{q,5}\eta_{q,5}
\end{bmatrix}\begin{pmatrix}\phi_2\\\phi_3\\\phi_4\\\phi_5\end{pmatrix} \tag{4.121}$$

The electrodeposited crack terms, denoted by α in Equation 4.96, are the next terms to be discussed. The first term under consideration is the second term of this expression, which bears great similarities to the stability term of the uncracked part derived earlier. Both terms feature a double jump term with a coefficient in front. Consequently, the derivation of the element stiffness matrix for this term follows the same process, with only the final result shown below.

$$\begin{aligned}
&\int_{\partial_I\Omega_h}\alpha\frac{\kappa_m}{w}\left[\!\left[\phi_m\right]\!\right]\left[\!\left[\delta\eta\right]\!\right]\,d\Gamma\rightarrow\\
&\sum_{q=1}\begin{bmatrix}
W_q\frac{\kappa_m}{w}_q\eta_{q,2}\eta_2 & W_q\frac{\kappa_m}{w}_q\eta_{q,3}\eta_{q,2} & -W_q\frac{\kappa_m}{w}_q\eta_{q,4}\eta_{q,2} & -W_q\frac{\kappa_m}{w}_q\eta_{q,5}\eta_{q,2}\\
W_q\frac{\kappa_m}{w}_q\eta_{q,2}\eta_3 & W_q\frac{\kappa_m}{w}_q\eta_{q,3}\eta_{q,3} & -W_q\frac{\kappa_m}{w}_q\eta_{q,4}\eta_{q,3} & -W_q\frac{\kappa_m}{w}_q\eta_{q,5}\eta_{q,3}\\
-W_q\frac{\kappa_m}{w}_q\eta_{q,2}\eta_4 & -W_q\frac{\kappa_m}{w}_q\eta_{q,3}\eta_{q,4} & W_q\frac{\kappa_m}{w}_q\eta_{q,4}\eta_{q,4} & W_q\frac{\kappa_m}{w}_q\eta_{q,5}\eta_{q,4}\\
-W_q\frac{\kappa_m}{w}_q\eta_{q,2}\eta_5 & -W_q\frac{\kappa_m}{w}_q\eta_{q,3}\eta_{q,5} & W_q\frac{\kappa_m}{w}_q\eta_{q,4}\eta_{q,5} & W_q\frac{\kappa_m}{w}_q\eta_{q,5}\eta_{q,5}
\end{bmatrix}\begin{pmatrix}\phi_2\\\phi_3\\\phi_4\\\phi_5\end{pmatrix}
\end{aligned} \tag{4.122}$$

The second and final integral of the cracked part of the weak form is also rewritten. Similar to the other integrals, the domain is transformed, and the integral is solved numerically.

$$\begin{aligned}
\int_{\partial_I\Omega_h}\kappa_m\frac{\partial\tilde{\phi}_m}{\partial x}\frac{\partial\left(w\left\{\delta\eta\right\}\right)}{\partial x}\,d\Gamma&=\int_{\partial_I\Omega_h^*}J\kappa_m\frac{\partial\tilde{\phi}_m}{\partial x}\frac{\partial\left(w\left\{\delta\eta\right\}\right)}{\partial x}\,d\Gamma\\
&=\sum_{e,q=1}w_{e,q}J_{e,q}\kappa_m\frac{\partial\tilde{\phi}_m}{\partial x}_{e,q}\frac{\partial\left(w\left\{\delta\eta\right\}\right)}{\partial x}_{e,q}
\end{aligned} \tag{4.123}$$

The quadrature weight and the Jacobian can be combined, and the rest of the derivation is written for just one element and quadrature point.

$$\sum_{e,q=1}w_{e,q}J_{e,q}\kappa_m\frac{\partial\tilde{\phi}_m}{\partial x}_{e,q}\frac{\partial\left(w\left\{\delta\eta\right\}\right)}{\partial x}_{e,q}=W\kappa_m\frac{\partial\tilde{\phi}_m}{\partial x}\frac{\partial\left(w\left\{\delta\eta\right\}\right)}{\partial x}+... \tag{4.124}$$

In Section 4.1, $\tilde{\phi}_m$ is defined as the average of the electric potential over the electrodeposited crack domain. Consequently, this term can also be expressed using the average operator. Furthermore, the

electric potential can be represented in terms of the assumed solution shown in Equation 4.42.

$$\begin{aligned} W\kappa_m \frac{\partial \tilde{\phi}_m}{\partial x} \frac{\partial \left(w \left\{\delta\eta\right\}\right)}{\partial x} &= W\kappa_m \frac{\partial \left\{\sum_{i=a}^{b} \phi_i \eta_i\right\}}{\partial x} \frac{\partial \left(w \left\{\delta\eta\right\}\right)}{\partial x} \\ &= W\kappa_m \left\{\sum_{i=a}^{b} \phi_i \frac{\partial \eta_i}{\partial x}\right\} \frac{\partial \left(w \left\{\delta\eta\right\}\right)}{\partial x} \\ &= W\kappa_m \left\{\phi_a \frac{\partial \eta_a}{\partial x} + \phi_b \frac{\partial \eta_b}{\partial x}\right\} \frac{\partial \left(w \left\{\delta\eta\right\}\right)}{\partial x} \end{aligned} \tag{4.125}$$

The crack length w in Equation 4.125 is initially assumed to be constant. Furthermore, the average operator is fully expressed.

$$\begin{aligned} &W\kappa_m \left\{\phi_a \frac{\partial \eta_a}{\partial x} + \phi_b \frac{\partial \eta_b}{\partial x}\right\} \frac{\partial \left(w \left\{\delta\eta\right\}\right)}{\partial x} = \\ &Ww\kappa_m \left(\left(\frac{1}{2}\phi_a \frac{\partial \eta_a}{\partial x}\right)^+ + \left(\frac{1}{2}\phi_a \frac{\partial \eta_a}{\partial x}\right)^- + \left(\frac{1}{2}\phi_b \frac{\partial \eta_b}{\partial x}\right)^+ + \left(\frac{1}{2}\phi_b \frac{\partial \eta_b}{\partial x}\right)^-\right) \frac{\partial \left\{\delta\eta\right\}}{\partial x} \end{aligned} \tag{4.126}$$

Similar to the other integrals, the plus and minus sides of the interface nodes are replaced by the nodal functions of the interface:

$$\begin{aligned} &Ww\kappa_m \left(\left(\frac{1}{2}\phi_a \frac{\partial \eta_a}{\partial x}\right)^+ + \left(\frac{1}{2}\phi_a \frac{\partial \eta_a}{\partial x}\right)^- + \left(\frac{1}{2}\phi_b \frac{\partial \eta_b}{\partial x}\right)^+ + \left(\frac{1}{2}\phi_b \frac{\partial \eta_b}{\partial x}\right)^-\right) \frac{\partial \left\{\delta\eta\right\}}{\partial x} = \\ &Ww\kappa_m \left(\frac{1}{2}\phi_5 \frac{\partial \eta_5}{\partial x} + \frac{1}{2}\phi_3 \frac{\partial \eta_3}{\partial x} + \frac{1}{2}\phi_4 \frac{\partial \eta_4}{\partial x} + \frac{1}{2}\phi_2 \frac{\partial \eta_2}{\partial x}\right) \frac{\partial \left\{\delta\eta\right\}}{\partial x} \end{aligned} \tag{4.127}$$

The system of equations is obtained using the test functions of the corresponding nodes:

$$\begin{aligned} &Ww\kappa_m \left(\frac{1}{2}\phi_2 \frac{\partial \eta_2}{\partial x} + \frac{1}{2}\phi_3 \frac{\partial \eta_3}{\partial x} + \frac{1}{2}\phi_4 \frac{\partial \eta_4}{\partial x} + \frac{1}{2}\phi_5 \frac{\partial \eta_5}{\partial x}\right) \frac{\partial \left\{\delta\eta_2\right\}}{\partial x} \\ &Ww\kappa_m \left(\frac{1}{2}\phi_2 \frac{\partial \eta_2}{\partial x} + \frac{1}{2}\phi_3 \frac{\partial \eta_3}{\partial x} + \frac{1}{2}\phi_4 \frac{\partial \eta_4}{\partial x} + \frac{1}{2}\phi_5 \frac{\partial \eta_5}{\partial x}\right) \frac{\partial \left\{\delta\eta_3\right\}}{\partial x} \\ &Ww\kappa_m \left(\frac{1}{2}\phi_2 \frac{\partial \eta_2}{\partial x} + \frac{1}{2}\phi_3 \frac{\partial \eta_3}{\partial x} + \frac{1}{2}\phi_4 \frac{\partial \eta_4}{\partial x} + \frac{1}{2}\phi_5 \frac{\partial \eta_5}{\partial x}\right) \frac{\partial \left\{\delta\eta_4\right\}}{\partial x} \\ &Ww\kappa_m \left(\frac{1}{2}\phi_2 \frac{\partial \eta_2}{\partial x} + \frac{1}{2}\phi_3 \frac{\partial \eta_3}{\partial x} + \frac{1}{2}\phi_4 \frac{\partial \eta_4}{\partial x} + \frac{1}{2}\phi_5 \frac{\partial \eta_5}{\partial x}\right) \frac{\partial \left\{\delta\eta_5\right\}}{\partial x} \end{aligned} \tag{4.128}$$

The definition of the average of the test function, as shown in Equation 4.104, can be substituted into Equation 4.128. Since the amplitudes $\delta\varphi_i^+$ and $\delta\varphi_i^-$ are constants, the derivative remains only for the shape function η_i.

$$\begin{aligned} &Ww\kappa_m \left(\frac{1}{2}\phi_2 \frac{\partial \eta_2}{\partial x} + \frac{1}{2}\phi_3 \frac{\partial \eta_3}{\partial x} + \frac{1}{2}\phi_4 \frac{\partial \eta_4}{\partial x} + \frac{1}{2}\phi_5 \frac{\partial \eta_5}{\partial x}\right) \frac{1}{2}\left(\delta\varphi_2^+ + \delta\varphi_2^-\right) \frac{\partial \eta_2}{\partial x} \\ &Ww\kappa_m \left(\frac{1}{2}\phi_2 \frac{\partial \eta_2}{\partial x} + \frac{1}{2}\phi_3 \frac{\partial \eta_3}{\partial x} + \frac{1}{2}\phi_4 \frac{\partial \eta_4}{\partial x} + \frac{1}{2}\phi_5 \frac{\partial \eta_5}{\partial x}\right) \frac{1}{2}\left(\delta\varphi_3^+ + \delta\varphi_3^-\right) \frac{\partial \eta_3}{\partial x} \\ &Ww\kappa_m \left(\frac{1}{2}\phi_2 \frac{\partial \eta_2}{\partial x} + \frac{1}{2}\phi_3 \frac{\partial \eta_3}{\partial x} + \frac{1}{2}\phi_4 \frac{\partial \eta_4}{\partial x} + \frac{1}{2}\phi_5 \frac{\partial \eta_5}{\partial x}\right) \frac{1}{2}\left(\delta\varphi_4^+ + \delta\varphi_4^-\right) \frac{\partial \eta_4}{\partial x} \\ &Ww\kappa_m \left(\frac{1}{2}\phi_2 \frac{\partial \eta_2}{\partial x} + \frac{1}{2}\phi_3 \frac{\partial \eta_3}{\partial x} + \frac{1}{2}\phi_4 \frac{\partial \eta_4}{\partial x} + \frac{1}{2}\phi_5 \frac{\partial \eta_5}{\partial x}\right) \frac{1}{2}\left(\delta\varphi_5^+ + \delta\varphi_5^-\right) \frac{\partial \eta_5}{\partial x} \end{aligned} \tag{4.129}$$

The amplitudes $\delta\varphi_i^+$ and $\delta\varphi_i^-$ vary in the same manner as in the other integrals, giving the following

result:

$$\begin{aligned}
&W w \kappa_m \left(\frac{1}{2}\phi_2\frac{\partial \eta_2}{\partial x} + \frac{1}{2}\phi_3\frac{\partial \eta_3}{\partial x} + \frac{1}{2}\phi_4\frac{\partial \eta_4}{\partial x} + \frac{1}{2}\phi_5\frac{\partial \eta_5}{\partial x}\right)\frac{1}{2}(0+1)\frac{\partial \eta_2}{\partial x}\\
&W w \kappa_m \left(\frac{1}{2}\phi_2\frac{\partial \eta_2}{\partial x} + \frac{1}{2}\phi_3\frac{\partial \eta_3}{\partial x} + \frac{1}{2}\phi_4\frac{\partial \eta_4}{\partial x} + \frac{1}{2}\phi_5\frac{\partial \eta_5}{\partial x}\right)\frac{1}{2}(0+1)\frac{\partial \eta_3}{\partial x}\\
&W w \kappa_m \left(\frac{1}{2}\phi_2\frac{\partial \eta_2}{\partial x} + \frac{1}{2}\phi_3\frac{\partial \eta_3}{\partial x} + \frac{1}{2}\phi_4\frac{\partial \eta_4}{\partial x} + \frac{1}{2}\phi_5\frac{\partial \eta_5}{\partial x}\right)\frac{1}{2}(1+0)\frac{\partial \eta_4}{\partial x}\\
&W w \kappa_m \left(\frac{1}{2}\phi_2\frac{\partial \eta_2}{\partial x} + \frac{1}{2}\phi_3\frac{\partial \eta_3}{\partial x} + \frac{1}{2}\phi_4\frac{\partial \eta_4}{\partial x} + \frac{1}{2}\phi_5\frac{\partial \eta_5}{\partial x}\right)\frac{1}{2}(1+0)\frac{\partial \eta_5}{\partial x}
\end{aligned} \tag{4.130}$$

Simplifying Equation 4.130 gives the final system of equations:

$$\begin{aligned}
&W w \kappa_m \left(\frac{1}{4}\phi_2\frac{\partial \eta_2}{\partial x} + \frac{1}{4}\phi_3\frac{\partial \eta_3}{\partial x} + \frac{1}{4}\phi_4\frac{\partial \eta_4}{\partial x} + \frac{1}{4}\phi_5\frac{\partial \eta_5}{\partial x}\right)\frac{\partial \eta_2}{\partial x}\\
&W w \kappa_m \left(\frac{1}{4}\phi_2\frac{\partial \eta_2}{\partial x} + \frac{1}{4}\phi_3\frac{\partial \eta_3}{\partial x} + \frac{1}{4}\phi_4\frac{\partial \eta_4}{\partial x} + \frac{1}{4}\phi_5\frac{\partial \eta_5}{\partial x}\right)\frac{\partial \eta_3}{\partial x}\\
&W w \kappa_m \left(\frac{1}{4}\phi_2\frac{\partial \eta_2}{\partial x} + \frac{1}{4}\phi_3\frac{\partial \eta_3}{\partial x} + \frac{1}{4}\phi_4\frac{\partial \eta_4}{\partial x} + \frac{1}{4}\phi_5\frac{\partial \eta_5}{\partial x}\right)\frac{\partial \eta_4}{\partial x}\\
&W w \kappa_m \left(\frac{1}{4}\phi_2\frac{\partial \eta_2}{\partial x} + \frac{1}{4}\phi_3\frac{\partial \eta_3}{\partial x} + \frac{1}{4}\phi_4\frac{\partial \eta_4}{\partial x} + \frac{1}{4}\phi_5\frac{\partial \eta_5}{\partial x}\right)\frac{\partial \eta_5}{\partial x}
\end{aligned} \tag{4.131}$$

The element stiffness matrix is obtained by expressing Equation 4.131 in matrix-vector notation and summing over all the quadrature points.

$$\sum_{q=1}\begin{bmatrix}
\frac{1}{4}W_q w_q \kappa_m \frac{\partial \eta_{q,2}}{\partial x}\frac{\partial \eta_{q,2}}{\partial x} & \frac{1}{4}W_q w_q \kappa_m \frac{\partial \eta_{q,3}}{\partial x}\frac{\partial \eta_{q,2}}{\partial x} & \frac{1}{4}W_q w_q \kappa_m \frac{\partial \eta_{q,4}}{\partial x}\frac{\partial \eta_{q,2}}{\partial x} & \frac{1}{4}W_q w_q \kappa_m \frac{\partial \eta_{q,5}}{\partial x}\frac{\partial \eta_{q,2}}{\partial x}\\
\frac{1}{4}W_q w_q \kappa_m \frac{\partial \eta_{q,2}}{\partial x}\frac{\partial \eta_{q,3}}{\partial x} & \frac{1}{4}W_q w_q \kappa_m \frac{\partial \eta_{q,3}}{\partial x}\frac{\partial \eta_{q,3}}{\partial x} & \frac{1}{4}W_q w_q \kappa_m \frac{\partial \eta_{q,4}}{\partial x}\frac{\partial \eta_{q,3}}{\partial x} & \frac{1}{4}W_q w_q \kappa_m \frac{\partial \eta_{q,5}}{\partial x}\frac{\partial \eta_{q,3}}{\partial x}\\
\frac{1}{4}W_q w_q \kappa_m \frac{\partial \eta_{q,2}}{\partial x}\frac{\partial \eta_{q,4}}{\partial x} & \frac{1}{4}W_q w_q \kappa_m \frac{\partial \eta_{q,3}}{\partial x}\frac{\partial \eta_{q,4}}{\partial x} & \frac{1}{4}W_q w_q \kappa_m \frac{\partial \eta_{q,4}}{\partial x}\frac{\partial \eta_{q,4}}{\partial x} & \frac{1}{4}W_q w_q \kappa_m \frac{\partial \eta_{q,5}}{\partial x}\frac{\partial \eta_{q,4}}{\partial x}\\
\frac{1}{4}W_q w_q \kappa_m \frac{\partial \eta_{q,2}}{\partial x}\frac{\partial \eta_{q,5}}{\partial x} & \frac{1}{4}W_q w_q \kappa_m \frac{\partial \eta_{q,3}}{\partial x}\frac{\partial \eta_{q,5}}{\partial x} & \frac{1}{4}W_q w_q \kappa_m \frac{\partial \eta_{q,4}}{\partial x}\frac{\partial \eta_{q,5}}{\partial x} & \frac{1}{4}W_q w_q \kappa_m \frac{\partial \eta_{q,5}}{\partial x}\frac{\partial \eta_{q,5}}{\partial x}
\end{bmatrix}\begin{pmatrix}\phi_2\\ \phi_3\\ \phi_4\\ \phi_5\end{pmatrix} \tag{4.132}$$

All the different element stiffness matrices are determined. Thus, the weak form can be expressed in terms of the stiffness matrices when the element stiffness matrices are summed over all the elements. The uncracked and cracked weak forms are presented separately, starting with the uncracked weak form below. Note that, due to space limitation, the element stiffness matrix of Equation 4.110 is split

into two separate matrices.

$$
\begin{aligned}
&\int_{\Omega_h} \kappa_{SE} \nabla\phi_{SE} \cdot \nabla\delta\eta \, d\Omega - \int_{\partial_I\Omega_h} (1-\alpha) \left[\!\left[\kappa_{SE}\nabla\phi_{SE}\right]\!\right] \{\delta\eta\} \cdot \boldsymbol{n} \, d\Gamma + \int_{\partial_I\Omega_h} \frac{\beta}{h} \left[\!\left[\phi_{SE}\right]\!\right] \left[\!\left[\delta\eta\right]\!\right] \, d\Gamma = \\
&\sum_{e,q=1} \begin{bmatrix} \nabla\eta_{e,q,1}\cdot K_{e,q}\nabla\eta_{e,q,1} & \nabla\eta_{e,q,1}\cdot K_{e,q}\nabla\eta_{e,q,2} & \nabla\eta_{e,q,1}\cdot K_{e,q}\nabla\eta_{e,q,5} \\ \nabla\eta_{e,q,2}\cdot K_{e,q}\nabla\eta_{e,q,1} & \nabla\eta_{e,q,2}\cdot K_{e,q}\nabla\eta_{e,q,2} & \nabla\eta_{e,q,2}\cdot K_{e,q}\nabla\eta_{e,q,5} \\ \nabla\eta_{e,q,5}\cdot K_{e,q}\nabla\eta_{e,q,1} & \nabla\eta_{e,q,5}\cdot K_{e,q}\nabla\eta_{e,q,2} & \nabla\eta_{e,q,5}\cdot K_{e,q}\nabla\eta_{e,q,5} \end{bmatrix} \begin{pmatrix} \phi_{e,1} \\ \phi_{e,2} \\ \phi_{e,3} \end{pmatrix} \\
&- \sum_{e,q=1} \left(\begin{bmatrix} -\frac{1}{2}\kappa_{SE_{e,q}} W_{e,q} \nabla\eta_{e,q,2}\cdot\boldsymbol{n}\eta_{e,q,2} & -\frac{1}{2}\kappa_{SE_{e,q}} W_{e,q} \nabla\eta_{e,q,3}\cdot\boldsymbol{n}\eta_{e,q,2} & 0 & 0 \\ -\frac{1}{2}\kappa_{SE_{e,q}} W_{e,q} \nabla\eta_{e,q,2}\cdot\boldsymbol{n}\eta_{e,q,3} & -\frac{1}{2}\kappa_{SE_{e,q}} W_{e,q} \nabla\eta_{e,q,3}\cdot\boldsymbol{n}\eta_{e,q,3} & 0 & 0 \\ -\frac{1}{2}\kappa_{SE_{e,q}} W_{e,q} \nabla\eta_{e,q,2}\cdot\boldsymbol{n}\eta_{e,q,4} & -\frac{1}{2}\kappa_{SE_{e,q}} W_{e,q} \nabla\eta_{e,q,3}\cdot\boldsymbol{n}\eta_{e,q,4} & 0 & 0 \\ -\frac{1}{2}\kappa_{SE_{e,q}} W_{e,q} \nabla\eta_{e,q,2}\cdot\boldsymbol{n}\eta_{e,q,5} & -\frac{1}{2}\kappa_{SE_{e,q}} W_{e,q} \nabla\eta_{e,q,3}\cdot\boldsymbol{n}\eta_{e,q,5} & 0 & 0 \end{bmatrix} \right. \\
&\quad + \begin{bmatrix} 0 & 0 & \frac{1}{2}\kappa_{SE_{e,q}} W_{e,q} \nabla\eta_{e,q,4}\cdot\boldsymbol{n}\eta_{e,q,2} & \frac{1}{2}\kappa_{SE_{e,q}} W_{e,q} \nabla\eta_{e,q,5}\cdot\boldsymbol{n}\eta_{e,q,2} \\ 0 & 0 & \frac{1}{2}\kappa_{SE_{e,q}} W_{e,q} \nabla\eta_{e,q,4}\cdot\boldsymbol{n}\eta_{e,q,3} & \frac{1}{2}\kappa_{SE_{e,q}} W_{e,q} \nabla\eta_{e,q,5}\cdot\boldsymbol{n}\eta_{e,q,3} \\ 0 & 0 & \frac{1}{2}\kappa_{SE_{e,q}} W_{e,q} \nabla\eta_{e,q,4}\cdot\boldsymbol{n}\eta_{e,q,4} & \frac{1}{2}\kappa_{SE_{e,q}} W_{e,q} \nabla\eta_{e,q,5}\cdot\boldsymbol{n}\eta_{e,q,4} \\ 0 & 0 & \frac{1}{2}\kappa_{SE_{e,q}} W_{e,q} \nabla\eta_{e,q,4}\cdot\boldsymbol{n}\eta_{e,q,5} & \frac{1}{2}\kappa_{SE_{e,q}} W_{e,q} \nabla\eta_{e,q,5}\cdot\boldsymbol{n}\eta_{e,q,5} \end{bmatrix} \\
&\quad \left. - \begin{bmatrix} W_{e,q}\frac{\beta}{h}\eta_{e,q,2}\eta_2 & W_{e,q}\frac{\beta}{h}\eta_{e,q,3}\eta_{e,q,2} & -W_{e,q}\frac{\beta}{h}\eta_{e,q,4}\eta_{e,q,2} & -W_{e,q}\frac{\beta}{h}\eta_{e,q,5}\eta_{e,q,2} \\ W_{e,q}\frac{\beta}{h}\eta_{e,q,2}\eta_3 & W_{e,q}\frac{\beta}{h}\eta_{e,q,3}\eta_{e,q,3} & -W_{e,q}\frac{\beta}{h}\eta_{e,q,4}\eta_{e,q,3} & -W_{e,q}\frac{\beta}{h}\eta_{e,q,5}\eta_{e,q,3} \\ -W_{e,q}\frac{\beta}{h}\eta_{e,q,2}\eta_4 & -W_{e,q}\frac{\beta}{h}\eta_{e,q,3}\eta_{e,q,4} & W_{e,q}\frac{\beta}{h}\eta_{e,q,4}\eta_{e,q,4} & W_{e,q}\frac{\beta}{h}\eta_{e,q,5}\eta_{e,q,4} \\ -W_{e,q}\frac{\beta}{h}\eta_{e,q,2}\eta_5 & -W_{e,q}\frac{\beta}{h}\eta_{e,q,3}\eta_{e,q,5} & W_{e,q}\frac{\beta}{h}\eta_{e,q,4}\eta_{e,q,5} & W_{e,q}\frac{\beta}{h}\eta_{e,q,5}\eta_{e,q,5} \end{bmatrix} \right) \begin{pmatrix} \phi_{e,2} \\ \phi_{e,3} \\ \phi_{e,4} \\ \phi_{e,5} \end{pmatrix}
\end{aligned}
\tag{4.133}
$$

Similarly, the cracked weak form is presented:

$$
\begin{aligned}
&\int_{\Omega_h} \kappa_{SE} \nabla\phi_{SE} \cdot \nabla\delta\eta \, d\Omega - \alpha w \kappa_m \frac{\partial\tilde{\phi}_m}{\partial x} \{\delta\eta\}(0,0) - \int_{\partial_I\Omega_h} \alpha \frac{\kappa_m}{w} \left[\!\left[\phi_m\right]\!\right] \left[\!\left[\delta\eta\right]\!\right] \, d\Gamma = \\
&\sum_{e,q=1} \begin{bmatrix} \nabla\eta_{e,q,1}\cdot K_{e,q}\nabla\eta_{e,q,1} & \nabla\eta_{e,q,1}\cdot K_{e,q}\nabla\eta_{e,q,2} & \nabla\eta_{e,q,1}\cdot K_{e,q}\nabla\eta_{e,q,5} \\ \nabla\eta_{e,q,2}\cdot K_{e,q}\nabla\eta_{e,q,1} & \nabla\eta_{e,q,2}\cdot K_{e,q}\nabla\eta_{e,q,2} & \nabla\eta_{e,q,2}\cdot K_{e,q}\nabla\eta_{e,q,5} \\ \nabla\eta_{e,q,5}\cdot K_{e,q}\nabla\eta_{e,q,1} & \nabla\eta_{e,q,5}\cdot K_{e,q}\nabla\eta_{e,q,2} & \nabla\eta_{e,q,5}\cdot K_{e,q}\nabla\eta_{e,q,5} \end{bmatrix} \begin{pmatrix} \phi_{e,1} \\ \phi_{e,2} \\ \phi_{e,3} \end{pmatrix} - \sum_{e,q=1} \\
&\left(\begin{bmatrix} \frac{1}{4}W_{e,q}w_{e,q}\kappa_m \frac{\partial\eta_{e,q,2}}{\partial x}\frac{\partial\eta_{e,q,2}}{\partial x} & \frac{1}{4}W_{e,q}w_{e,q}\kappa_m \frac{\partial\eta_{e,q,3}}{\partial x}\frac{\partial\eta_{e,q,2}}{\partial x} & \frac{1}{4}W_{e,q}w_{e,q}\kappa_m \frac{\partial\eta_{e,q,4}}{\partial x}\frac{\partial\eta_{e,q,2}}{\partial x} & \frac{1}{4}W_{e,q}w_{e,q}\kappa_m \frac{\partial\eta_{e,q,5}}{\partial x}\frac{\partial\eta_{e,q,2}}{\partial x} \\ \frac{1}{4}W_{e,q}w_{e,q}\kappa_m \frac{\partial\eta_{e,q,2}}{\partial x}\frac{\partial\eta_{e,q,3}}{\partial x} & \frac{1}{4}W_{e,q}w_{e,q}\kappa_m \frac{\partial\eta_{e,q,3}}{\partial x}\frac{\partial\eta_{e,q,3}}{\partial x} & \frac{1}{4}W_{e,q}w_{e,q}\kappa_m \frac{\partial\eta_{e,q,4}}{\partial x}\frac{\partial\eta_{e,q,3}}{\partial x} & \frac{1}{4}W_{e,q}w_{e,q}\kappa_m \frac{\partial\eta_{e,q,5}}{\partial x}\frac{\partial\eta_{e,q,3}}{\partial x} \\ \frac{1}{4}W_{e,q}w_{e,q}\kappa_m \frac{\partial\eta_{e,q,2}}{\partial x}\frac{\partial\eta_{e,q,4}}{\partial x} & \frac{1}{4}W_{e,q}w_{e,q}\kappa_m \frac{\partial\eta_{e,q,3}}{\partial x}\frac{\partial\eta_{e,q,4}}{\partial x} & \frac{1}{4}W_{e,q}w_{e,q}\kappa_m \frac{\partial\eta_{e,q,4}}{\partial x}\frac{\partial\eta_{e,q,4}}{\partial x} & \frac{1}{4}W_{e,q}w_{e,q}\kappa_m \frac{\partial\eta_{e,q,5}}{\partial x}\frac{\partial\eta_{e,q,4}}{\partial x} \\ \frac{1}{4}W_{e,q}w_{e,q}\kappa_m \frac{\partial\eta_{e,q,2}}{\partial x}\frac{\partial\eta_{e,q,5}}{\partial x} & \frac{1}{4}W_{e,q}w_{e,q}\kappa_m \frac{\partial\eta_{e,q,3}}{\partial x}\frac{\partial\eta_{e,q,5}}{\partial x} & \frac{1}{4}W_{e,q}w_{e,q}\kappa_m \frac{\partial\eta_{e,q,4}}{\partial x}\frac{\partial\eta_{e,q,5}}{\partial x} & \frac{1}{4}W_{e,q}w_{e,q}\kappa_m \frac{\partial\eta_{e,q,5}}{\partial x}\frac{\partial\eta_{e,q,5}}{\partial x} \end{bmatrix} \right. \\
&\left. + \begin{bmatrix} W_{e,q}\frac{\kappa_m}{w}{}_{e,q}\eta_{e,q,2}\eta_2 & W_{e,q}\frac{\kappa_m}{w}{}_{e,q}\eta_{e,q,3}\eta_{e,q,2} & -W_{e,q}\frac{\kappa_m}{w}{}_{e,q}\eta_{e,q,4}\eta_{e,q,2} & -W_{e,q}\frac{\kappa_m}{w}{}_{e,q}\eta_{e,q,5}\eta_{e,q,2} \\ W_{e,q}\frac{\kappa_m}{w}{}_{e,q}\eta_{e,q,2}\eta_3 & W_{e,q}\frac{\kappa_m}{w}{}_{e,q}\eta_{e,q,3}\eta_{e,q,3} & -W_{e,q}\frac{\kappa_m}{w}{}_{e,q}\eta_{e,q,4}\eta_{e,q,3} & -W_{e,q}\frac{\kappa_m}{w}{}_{e,q}\eta_{e,q,5}\eta_{e,q,3} \\ -W_{e,q}\frac{\kappa_m}{w}{}_{e,q}\eta_{e,q,2}\eta_4 & -W_{e,q}\frac{\kappa_m}{w}{}_{e,q}\eta_{e,q,3}\eta_{e,q,4} & W_{e,q}\frac{\kappa_m}{w}{}_{e,q}\eta_{e,q,4}\eta_{e,q,4} & W_{e,q}\frac{\kappa_m}{w}{}_{e,q}\eta_{e,q,5}\eta_{e,q,4} \\ -W_{e,q}\frac{\kappa_m}{w}{}_{e,q}\eta_{e,q,2}\eta_5 & -W_{e,q}\frac{\kappa_m}{w}{}_{e,q}\eta_{e,q,3}\eta_{e,q,5} & W_{e,q}\frac{\kappa_m}{w}{}_{e,q}\eta_{e,q,4}\eta_{e,q,5} & W_{e,q}\frac{\kappa_m}{w}{}_{e,q}\eta_{e,q,5}\eta_{e,q,5} \end{bmatrix} \right) \begin{pmatrix} \phi_{e,2} \\ \phi_{e,3} \\ \phi_{e,4} \\ \phi_{e,5} \end{pmatrix}
\end{aligned}
\tag{4.134}
$$

5

Verification and Validation

This chapter discusses the verification and validation of the numerical model derived in the previous chapters. The verification is based on two parts. First, the physical interpretation of the results is considered. The limit cases of the crack conductivity yield results that are known. The numerical solution should converge to these results. Secondly, the analytical solution from subsection 5.1.1 is used to verify the results by comparing the numerical solution with the analytical one. Secondly, the results are validated by comparing quantitatively the results of the numerical model with a phase-field model.

5.1. Verification against 1D analytical solution

This section first discusses the derivation of the analytical solution, which is then used in the subsequent part of this section to verify the results.

5.1.1. Derivation of the analytical solution in 1D

As depicted in Figure 5.1, a special case is utilized to verify the results obtained with the numerical model. In this scenario, the crack spans the entire width of the solid electrolyte, dividing it into three parts: the first solid electrolyte part, the lithium part, and the second solid electrolyte part denoted in Figure 5.1 as 1, M, and 2, respectively. The crack has grown perpendicular to the current flow, resulting in a constant electric potential along the x-axis. Additionally, the electric deposition rate $\dot{\xi}$ is set to zero. These simplified factors allow for the possibility of solving this case analytically.

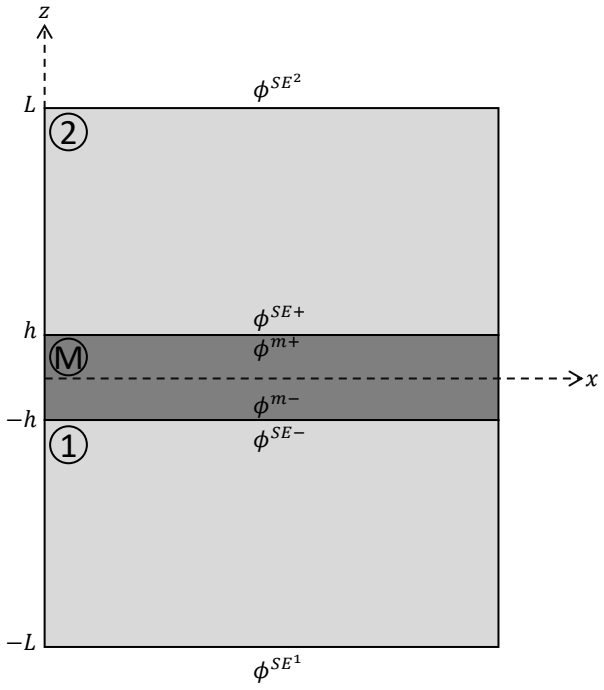

Figure 5.1: Schematic picture of the simplified case used for verifying the numerical model. In this scenario, the solid electrolyte consists of three parts: the first solid electrolyte part, the lithium crack part, and the second solid electrolyte part, denoted by 1, m, and 2, respectively. The electric potential at the boundaries between the lithium crack and solid electrolyte is denoted by ϕ^{SE^-}, ϕ^{m^-}, ϕ^{SE^+}, and ϕ^{m^+}. ϕ^{SE^1} and ϕ^{SE^2} denote the Dirichlet boundaries at $z = -L$ and $z = L$.

Using the simplifications described above, the expression for the electric field in the solid electrolyte ($h < z < L$ and $-h > z > -L$), as shown in Equation 4.5, simplifies to the following expression:

$$\kappa_{SE} \frac{d^2 \phi_{SE}}{dz^2} = 0 \tag{5.1}$$

Similarly, the expression for the electric field in the electrodeposited lithium crack ($-h < z < h$) is simplified to the following expression:

$$\kappa_m \frac{d^2\phi_m}{dz^2} = 0 \tag{5.2}$$

At the bottom ($z = -L$) and top ($z = L$) of the solid electrolyte, the electric potential is specified by the Dirichlet boundary conditions ϕ^{SE^1} and ϕ^{SE^2}. Neumann boundary conditions are applied at the boundaries between the solid electrolyte and the electrodeposited crack, consistent with the boundary condition shown in Equation 4.5. Furthermore, the electric potential is assumed to remain continuous at the boundary between the solid electrolyte and the electrodeposited crack. An overview of these boundary conditions is provided in Equation 5.3.

$$\begin{cases} \phi^1 = \phi^{SE^1} & \text{at} \quad z = -L \\ \phi^2 = \phi^{SE^2} & \text{at} \quad z = L \\ \kappa_m \frac{d\phi_m}{dz} = \kappa_{SE} \frac{d\phi^1}{dz} & \text{at} \quad z = -h \\ \kappa_m \frac{d\phi_m}{dz} = \kappa_{SE} \frac{d\phi^2}{dz} & \text{at} \quad z = h \\ \phi^- = \phi^{SE^-} = \phi^{m^-} & \text{at} \quad z = -h \\ \phi^+ = \phi^{SE^+} = \phi^{m^+} & \text{at} \quad z = h \end{cases} \tag{5.3}$$

The continuity of the electric potential is ensured by the fifth and sixth conditions in Equation 5.3, which restrict the possible values of ϕ^+ and ϕ^- without fully constraining these variables. The specific values of these variables are determined by solving the differential equation.

The electric potential for the solid electrolyte will be determined by integrating Equation 5.1 and Equation 5.2 twice. However, initially, the expression is integrated once to derive the expression for the first derivative of the electric potential.

$$\frac{\partial \phi}{\partial x} = \begin{cases} \frac{\partial \phi^1}{\partial x} = C_1 & \text{at} \quad -L \leq z \leq -h \\ \frac{\partial \phi^m}{\partial x} = C_2 & \text{at} \quad -h \leq z \leq h \\ \frac{\partial \phi^2}{\partial x} = C_3 & \text{at} \quad h \leq z \leq L \end{cases} \tag{5.4}$$

The third and fourth boundary conditions shown in Equation 5.3 are used to derive the relations between C_1, C_2, and C_3 by first substituting Equation 5.4 into the third boundary condition and subsequently into the fourth boundary condition. Applying the third boundary condition yields:

$$\begin{aligned} \kappa_m \frac{d\phi_m}{dz} &= \kappa_{SE} \frac{d\phi^1}{dz} \quad \text{at} \quad z = -h \\ \frac{d\phi_m}{dz} &= \frac{\kappa_{SE}}{\kappa_m} \frac{d\phi^1}{dz} \\ C_2 &= \frac{\kappa_{SE}}{\kappa_m} C_1 \end{aligned} \tag{5.5}$$

Similarly, the expression is derived from the fourth boundary condition:

$$\begin{aligned} \kappa_m \frac{d\phi_m}{dz} &= \kappa_{SE} \frac{d\phi^2}{dz} \quad \text{at} \quad z = h \\ \frac{d\phi_m}{dz} &= \frac{\kappa_{SE}}{\kappa_m} \frac{d\phi^2}{dz} \\ C_2 &= \frac{\kappa_{SE}}{\kappa_m} C_3 \end{aligned} \tag{5.6}$$

Substituting Equation 5.6 into Equation 5.5 also yields a relation between C_1 and C_3:

$$\begin{aligned} C_2 &= \frac{\kappa_{SE}}{\kappa_m} C_1 \\ \frac{\kappa_{SE}}{\kappa_m} C_3 &= \frac{\kappa_{SE}}{\kappa_m} C_1 \\ C_3 &= C_1 \end{aligned} \tag{5.7}$$

Now that the relations between C_1, C_2, and C_3 have been defined, Equation 5.1 can be integrated for a second time, giving the following result:

$$\phi = \begin{cases} \phi^1 = C_1 z + C_4 & \text{at} \quad -L \leq z \leq -h \\ \phi^m = C_2 z + C_5 & \text{at} \quad -h \leq z \leq h \\ \phi^2 = C_3 z + C_6 & \text{at} \quad h \leq z \leq L \end{cases} \tag{5.8}$$

The first two boundary conditions are now employed to specify the behavior of the electric potential further. Clarity is enhanced by indicating the value at $z = -h$ as ϕ^-. This unknown value will be subsequently replaced by its corresponding expression. Similarly, the value of the electric potential at $z = h$ is denoted as ϕ^+ and will also be replaced later with the actual expression for this variable.

First, the expression for part one of the solid electrolyte is refined using the first boundary condition and the electric potential value at $z = -h$. Substituting these values into the expression for the electric potential gives the following result:

$$\begin{aligned} \phi^1(-L) = \phi^{SE^1} &= -C_1 L + C_4 \\ \phi^{SE^1} + C_1 L &= C_4 \end{aligned} \tag{5.9}$$

$$\phi^1(-h) = \phi^- = -C_1 h + C_4 \tag{5.10}$$

Equation 5.9 is susbstituted into Equation 5.10:

$$\begin{aligned} \phi^- &= -C_1 h + C_4 \\ \phi^- &= -C_1 h + \phi^{SE^1} + C_1 L \\ C_1 &= \frac{\phi^- - \phi^{SE^1}}{L - h} \end{aligned} \tag{5.11}$$

C_4 is now determined by substituting Equation 5.11 back into Equation 5.9:

$$\begin{aligned} C_4 &= \phi^{SE^1} + C_1 L \\ &= \phi^{SE^1} + \frac{\phi^- - \phi^{SE^1}}{L - h} L \\ &= \frac{\phi^- L - \phi^{SE^1} h}{L - h} \end{aligned} \tag{5.12}$$

The electric potential in the first part of the solid electrolyte can be reformulated using the expressions for C_1 and C_4 shown above:

$$\begin{aligned} \phi^1 &= C_1 z + C_4 \\ &= \frac{\phi^- - \phi^{SE^1}}{L - h} z + \frac{\phi^- L - \phi^{SE^1} h}{L - h} \\ &= -\phi^{SE^1} \frac{h + z}{L - h} + \phi^- \frac{L + z}{L - h} \end{aligned} \tag{5.13}$$

The expression for the electric potential in the second part of the solid electrolyte ($h \leq z \leq L$) is derived using the same procedure as described for part 1 of the solid electrolyte. In this case, we employ the

second boundary condition of Equation 5.3 and the value of the electric potential at $z = h$. This gives the following expression for this region:

$$\begin{aligned}\phi^2 &= C_3 z + C_6 \\ &= \frac{\phi^{SE^2} - \phi^+}{L-h} z + \frac{\phi^+ L - \phi^{SE^2} h}{L-h} \\ &= -\phi^{SE^2} \frac{h-z}{L-h} + \phi^+ \frac{L-z}{L-h}\end{aligned} \tag{5.14}$$

The expression for the electric potential in the crack ($-h \leq z \leq h$) is determined using the unknown values of the electric potential at $z = -h$ and $z = h$:

$$\begin{aligned}\phi^m &= C_2 z + C_5 \\ &= \frac{\phi^+ - \phi^-}{2h} z + \frac{\phi^+ + \phi^-}{2} \\ &= \phi^+ \frac{h+z}{2h} + \phi^- \frac{h-z}{2h}\end{aligned} \tag{5.15}$$

Combining Equation 5.13, Equation 5.14, and Equation 5.15 gives the result for the entire domain:

$$\phi = \begin{cases} \phi^1 = -\phi^{SE^1} \frac{h+z}{L-h} + \phi^- \frac{L+z}{L-h} & \text{at} \quad -L \leq z \leq -h \\ \phi^m = \phi^+ \frac{h+z}{2h} + \phi^- \frac{h-z}{2h} & \text{at} \quad -h \leq z \leq h \\ \phi^2 = -\phi^{SE^2} \frac{h-z}{L-h} + \phi^+ \frac{L-z}{L-h} & \text{at} \quad h \leq z \leq L \end{cases} \tag{5.16}$$

The constants C_1, C_2, and C_3 are as shown before in Equation 5.4, equal to the gradient of the electric potential. So, these constants can also be written in terms of ϕ^{SE^1}, ϕ^{SE^2}, ϕ^-, and ϕ^+:

$$C_1 = \frac{\phi^- - \phi^{SE^1}}{L-h} \tag{5.17}$$

$$C_2 = \frac{\phi^+ - \phi^-}{2h} \tag{5.18}$$

$$C_3 = \frac{\phi^{SE^2} - \phi^+}{L-h} \tag{5.19}$$

The relation between C_1 and C_2 (Equation 5.5) is used to obtain an expression for ϕ^+:

$$\begin{aligned} C_2 &= \frac{\kappa_{SE}}{\kappa_m} C_1 \\ \frac{\phi^+ - \phi^-}{2h} &= \frac{\kappa_{SE}}{\kappa_m} \frac{\phi^- - \phi^{SE^1}}{L-h} \\ \phi^+ &= \phi^- + 2h \frac{\kappa_{SE}}{\kappa_m} \frac{\phi^- - \phi^{SE^1}}{L-h} \\ \phi^+ &= \phi^- + 2h \frac{\kappa_{SE}}{\kappa_m} \frac{\phi^-}{L-h} - 2h \frac{\kappa_{SE}}{\kappa_m} \frac{\phi^{SE^1}}{L-h} \end{aligned} \tag{5.20}$$

Similarly, the relation between C_2 and C_3 (Equation 5.6) is used to obtain an expression for ϕ^-.

$$\begin{aligned} C_2 &= \frac{\kappa_{SE}}{\kappa_m} C_3 \\ \frac{\phi^+ - \phi^-}{2h} &= \frac{\kappa_{SE}}{\kappa_m} \frac{\phi^{SE^2} - \phi^+}{L-h} \\ \phi^- &= \phi^+ - 2h \frac{\kappa_{SE}}{\kappa_m} \frac{\phi^{SE^2} - \phi^+}{L-h} \\ \phi^- &= \phi^+ - 2h \frac{\kappa_{SE}}{\kappa_m} \frac{\phi^{SE^2}}{L-h} + 2h \frac{\kappa_{SE}}{\kappa_m} \frac{\phi^+}{L-h} \end{aligned} \tag{5.21}$$

Equation 5.21 is substituted into Equation 5.20 to solve for ϕ^+:

$$\begin{aligned}
\phi^+ =& \phi^- + 2h\frac{\kappa_{SE}}{\kappa_m}\frac{\phi^-}{L-h} - 2h\frac{\kappa_{SE}}{\kappa_m}\frac{\phi^{SE^1}}{L-h} \\
\phi^+ =& \phi^+ - 2h\frac{\kappa_{SE}}{\kappa_m}\frac{\phi^{SE^2}}{L-h} + 2h\frac{\kappa_{SE}}{\kappa_m}\frac{\phi^+}{L-h} + 2h\frac{\kappa_{SE}}{\kappa_m}\frac{1}{L-h}\left(\phi^+ - 2h\frac{\kappa_{SE}}{\kappa_m}\frac{\phi^{SE^2}}{L-h} + 2h\frac{\kappa_{SE}}{\kappa_m}\frac{\phi^+}{L-h}\right) \\
& - 2h\frac{\kappa_{SE}}{\kappa_m}\frac{\phi^{SE^1}}{L-h} \\
0 =& -2h\frac{\kappa_{SE}}{\kappa_m}\frac{\phi^{SE^2}}{L-h} + 2h\frac{\kappa_{SE}}{\kappa_m}\frac{\phi^+}{L-h} + 2h\frac{\kappa_{SE}}{\kappa_m}\frac{1}{L-h}\left(\phi^+ - 2h\frac{\kappa_{SE}}{\kappa_m}\frac{\phi^{SE^2}}{L-h} + 2h\frac{\kappa_{SE}}{\kappa_m}\frac{\phi^+}{L-h}\right) \\
& - 2h\frac{\kappa_{SE}}{\kappa_m}\frac{\phi^{SE^1}}{L-h}
\end{aligned} \tag{5.22}$$

Both sides of Equation 5.22 are multiplied by $\frac{\kappa_m}{\kappa_{SE}}\frac{h-L}{2h}$.

$$\begin{aligned}
0 =& -2h\frac{\kappa_{SE}}{\kappa_m}\frac{\phi^{SE^2}}{L-h} + 2h\frac{\kappa_{SE}}{\kappa_m}\frac{\phi^+}{L-h} + 2h\frac{\kappa_{SE}}{\kappa_m}\frac{1}{L-h}\left(\phi^+ - 2h\frac{\kappa_{SE}}{\kappa_m}\frac{\phi^{SE^2}}{L-h} + 2h\frac{\kappa_{SE}}{\kappa_m}\frac{\phi^+}{L-h}\right) \\
& - 2h\frac{\kappa_{SE}}{\kappa_m}\frac{\phi^{SE^1}}{L-h} \\
0 =& -\phi^{SE^2} + \phi^+ + \phi^+ - 2h\frac{\kappa_{SE}}{\kappa_m}\frac{\phi^{SE^2}}{L-h} + 2h\frac{\kappa_{SE}}{\kappa_m}\frac{\phi^+}{L-h} - \phi^{SE^1}
\end{aligned} \tag{5.23}$$

Equation 5.23 is rewritten resulting in the expression for ϕ^+:

$$\begin{aligned}
0 =& -\phi^{SE^2} + \phi^+ + \phi^+ - 2h\frac{\kappa_{SE}}{\kappa_m}\frac{\phi^{SE^2}}{L-h} + 2h\frac{\kappa_{SE}}{\kappa_m}\frac{\phi^+}{L-h} - \phi^{SE^1} \\
\left(2\kappa_m(L-h) + 2h\kappa_{SE}\right)\phi^+ =& \left(\phi^{SE^1} + \phi^{SE^2}\right)\kappa_m(L-h) + 2h\phi^{SE^2}\kappa_{SE} \\
\phi^+ =& \frac{\left(\phi^{SE^1} + \phi^{SE^2}\right)\kappa_m(L-h) + 2h\phi^{SE^2}\kappa_{SE}}{2\kappa_m(L-h) + 2h\kappa_{SE}}
\end{aligned} \tag{5.24}$$

Now, ϕ^- is determined by substituting the expression of ϕ^+ (Equation 5.24) back into Equation 5.21.

$$\begin{aligned}
\phi^- =& \phi^+ - 2h\frac{\kappa_{SE}}{\kappa_m}\frac{\phi^{SE^2}}{L-h} + 2h\frac{\kappa_{SE}}{\kappa_m}\frac{\phi^+}{L-h} \\
=& \frac{\left(\phi^{SE^1} + \phi^{SE^2}\right)\kappa_m(L-h) + 2h\phi^{SE^2}\kappa_{SE}}{2\kappa_m(L-h) + 2h\kappa_{SE}} - \frac{\kappa_{SE}}{\kappa_m}\frac{2h\phi^{SE^2}}{(L-h)} + \\
& \frac{\kappa_{SE}}{\kappa_m}\frac{2h}{(L-h)}\frac{\left(\phi^{SE^1} + \phi^{SE^2}\right)\kappa_m(L-h) + 2h\phi^{SE^2}\kappa_{SE}}{2\kappa_m(L-h) + 2h\kappa_{SE}}
\end{aligned} \tag{5.25}$$

All terms in Equation 5.25 can be brought under the same denominator. Simplifying this results gives

the final expression for ϕ^-:

$$\begin{aligned}
\phi^- =& \frac{\left(\phi^{SE^1} + \phi^{SE^2}\right)\kappa_m\left(L-h\right) + 2h\phi^{SE^2}\kappa_{SE}}{2\kappa_m\left(L-h\right) + 2h\kappa_{SE}} - \frac{\frac{\kappa_{SE}}{\kappa_m}\frac{2h\phi^{SE^2}}{(L-h)}\left(2\kappa_m\left(L-h\right) + 2h\kappa_{SE}\right)}{2\kappa_m\left(L-h\right) + 2h\kappa_{SE}} \\
&+ \frac{\frac{\kappa_{SE}}{\kappa_m}\frac{2h}{(L-h)}\left(\left(\phi^{SE^1} + \phi^{SE^2}\right)\kappa_m\left(L-h\right) + 2h\phi^{SE^2}\kappa_{SE}\right)}{2\kappa_m\left(L-h\right) + 2h\kappa_{SE}} \\
=& \frac{\left(\phi^{SE^1} + \phi^{SE^2}\right)\kappa_m\left(L-h\right) + 2h\phi^{SE^2}\kappa_{SE}}{2\kappa_m\left(L-h\right) + 2h\kappa_{SE}} - \frac{4h\phi^{SE^2}\kappa_{SE} + \frac{4h^2\kappa_{SE}^2\phi^{SE^2}}{\kappa_m(L-h)}}{2\kappa_m\left(L-h\right) + 2h\kappa_{SE}} \\
&+ \frac{2h\kappa_{SE}\left(\phi^{SE^1} + \phi^{SE^2}\right) + \frac{4h^2\kappa_{SE}^2\phi^{SE^2}}{\kappa_m(L-h)}}{2\kappa_m\left(L-h\right) + 2h\kappa_{SE}} \\
=& \frac{\left(\phi^{SE^1} + \phi^{SE^2}\right)\kappa_m\left(L-h\right) + 2h\phi^{SE^1}\kappa_{SE}}{2\kappa_m\left(L-h\right) + 2h\kappa_{SE}}
\end{aligned} \tag{5.26}$$

The expression for the electric potential, as shown in Equation 5.16, is now rewritten using the expressions for ϕ^+ and ϕ^-, which were derived in Equation 5.24 and Equation 5.26, respectively. This starts with the part of the expression that is valid between $-L \leq z \leq -h$:

$$\begin{aligned}
\phi^1 =& -\phi^{SE^1}\frac{h+z}{L-h} + \phi^-\frac{L+z}{L-h} \\
=& -\phi^{SE^1}\frac{h+z}{L-h} + \frac{\left(\phi^{SE^1+h} + \phi^{SE^2}\right)K_m(L-h) + 2h\phi^{SE^1}K_{SE}}{2k_m(L-h) + 2hK_{SE}}\frac{L+z}{L-h} \\
=& \frac{-2\phi^{SE^1}K_m(h+z) - 2h\phi^{SE^1}k_{SE}\frac{h+z}{L-h} + \left(\phi^{SE^1} + \phi^{SE^2}\right)k_m(L+z) + 2h\phi^{SE^1}k_{SE}\frac{L+z}{L-h}}{2k_m(L-h) + 2hK_{SE}} \\
=& \frac{\left(\phi^{SE^1} + \phi^{SE^2}\right)k_mL - \left(\phi^{SE^1} - \phi^{SE^2}\right)k_mz - 2h\phi^{SE^1}K_m}{2k_m(L-h) + 2hK_{SE}} + \\
& \frac{2h\phi^{SE^1}K_{SE}\frac{L-h}{L-h} + \phi^{SE^1}K_mL - \phi^{SE^1}K_mL}{2k_m(L-h) + 2hK_{SE}} \\
=& \frac{-\left(\phi^{SE^1} - \phi^{SE^2}\right)k_mL - \left(\phi^{SE^1} - \phi^{SE^2}\right)k_mZ + (2k_m(L-h) + 2hk_{SE})\,\phi^{SE^1}}{2k_m(L-h) + 2hk_{SE}} \\
=& \frac{\left(\phi^{SE^2} - \phi^{SE^1}\right)k_m}{2k_m(L-h) + 2hk_{SE}}(z+L) + \phi^{SE^1}
\end{aligned} \tag{5.27}$$

Secondly, the final expression of the electric potential valid between $-h \leq z \leq h$ is determined:

$$\begin{aligned}
\phi^m =& \phi^+\frac{h+z}{2h} + \phi^-\frac{h-z}{2h} \\
=& \frac{\left(\phi^{SE^1} + \phi^{SE^2}\right)k_m(L-h) + 2h\phi^{SE^2}k_{SE}}{2k_m(L-h) + 2hk_{SE}}\frac{h+z}{2h} + \\
& \frac{\left(\phi^{SE^1} + \phi^{SE^2}\right)k_m(L-h) + 2h\phi^{SE^1}k_{SE}}{2k_m(L-h) + 2hk_{SE}}\frac{h-z}{2h} \\
=& \frac{\left(\phi^{SE^2} - \phi^{SE^1}\right)k_{SE}}{2k_m(L-h) + 2hk_{SE}}z + \frac{1}{2}\frac{\left(\phi^{SE^1} + \phi^{SE^2}\right)(2k_m(L-h) + 2hK_{SE})}{2k_m(L-h) + 2hk_{SE}} \\
=& \frac{\left(\phi^{SE^2} - \phi^{SE^1}\right)k_{SE}}{2k_m(L-h) + 2hk_{SE}}z + \frac{\phi^{SE^1} + \phi^{SE^2}}{2}
\end{aligned} \tag{5.28}$$

Finally, the electric potential between $h \leq z \leq l$ is also determined:

$$
\begin{aligned}
\phi^2 =& -\phi^{SE^2}\frac{h-z}{L-h} + \phi^{+}\frac{L-z}{L-h} \\
=& -\phi^{SE^2}\frac{h-z}{L-h} + \frac{\left(\phi^{SE^1}+\phi^{SE^2}\right)K_m(L-h)+2h\phi^{SE^2}k_{SE}}{2k_m(L-h)+2hK_{SE}}\frac{L-z}{L-h} \\
=& \frac{-2\phi^{SE^2}K_m(h-z)-2h\phi^{SE^2}K_{SE}\frac{h-z}{L-h}+\left(\phi^{SE^1}+\phi^{SE^2}\right)k_m(L-z)+2h\phi^{SE^2}k_{SE}\frac{L+z}{L-h}}{2k_m(L-h)+2hK_{SE}} \\
=& \frac{\left(\phi^{SE^1}+\phi^{SE^2}\right)k_mL-\left(\phi^{SE^1}-\phi^{SE^2}\right)k_mz-2h\phi^{SE^2}k_m}{2k_m(L-h)+2hk_{SE}} + \\
& \frac{2h\phi^{SE^2}k_{SE}\frac{L-h}{L-h}+\phi^{SE^2}K_mL-\phi^{SE^2}k_mL}{2k_m(L-h)+2hK_{SE}} \\
=& \frac{\left(\phi^{SE^1}-\phi^{SE^2}\right)k_mL-\left(\phi^{SE^1}-\phi^{SE^2}\right)k_mZ+\left(2k_m(L-h)+2hk_{SE}\right)\phi^{SE^2}}{2k_m(L-h)+2hk_{SE}} \\
=& \frac{\left(\phi^{SE^2}-\phi^{SE^1}\right)k_m}{2k_m(L-h)+2hk_{SE}}(z-L)+\phi^{SE^2}
\end{aligned}
\tag{5.29}
$$

The electric potential of the whole domain is determined by the combination of the expressions of the three subdomains shown above:

$$
\phi = \begin{cases}
\frac{\left(\phi^{SE^2}-\phi^{SE^1}\right)\kappa_m}{2\kappa_m(L-h)+2h\kappa_{SE}}(z+L)+\phi^{SE^1} & \text{at} \quad -L \leq z \leq -h \\
\frac{\left(\phi^{SE^2}-\phi^{SE^1}\right)\kappa_{SE}}{2\kappa_m(L-h)+2h\kappa_{SE}}z+\frac{\phi^{SE^1}+\phi^{SE^2}}{2} & \text{at} \quad -h \leq z \leq h \\
\frac{\left(\phi^{SE^2}-\phi^{SE^1}\right)\kappa_m}{2\kappa_m(L-h)+2h\kappa_{SE}}(z-L)+\phi^{SE^2} & \text{at} \quad h \leq z \leq L
\end{cases}
\tag{5.30}
$$

5.1.2. Numerical results

Figure 5.2 depicts the configuration employed for verifying the numerical model. This solid-state battery is divided into two sections by an electrodeposited lithium crack. Dirichlet boundary conditions are imposed at the top and bottom of the solid-state battery, with different values defined for the conductivity of the crack and the solid electrolyte. The specific values utilized for verification are detailed in Table 5.1. The crack conductivity is not included in this table as it varies during the verification process.

An important assumption made in Section 4.1 for deriving the weak form is that the crack opening is significantly smaller than the crack width. However, Figure 5.2 illustrates that this assumption does not hold for the configuration used in the verification process. The reason for this discrepancy is that the simplified configuration used for obtaining an analytical solution yields a linear result. In this case, accurate results can be attained for this specific configuration even with large crack openings relative to the crack width. Nonetheless, this assumption remains crucial in the general nonlinear case. The larger crack opening in this example leads to greater disparities between both sides of the solid electrolyte, thus rendering the results clearer.

Table 5.1: Actucal values of the variables used for the verification.

symbol	Value	unit
L	0.0002	m
w	0.0001	m
κ^{SE}	1	S/m
ϕ^{SE1}	-5	V
ϕ^{SE2}	1	V

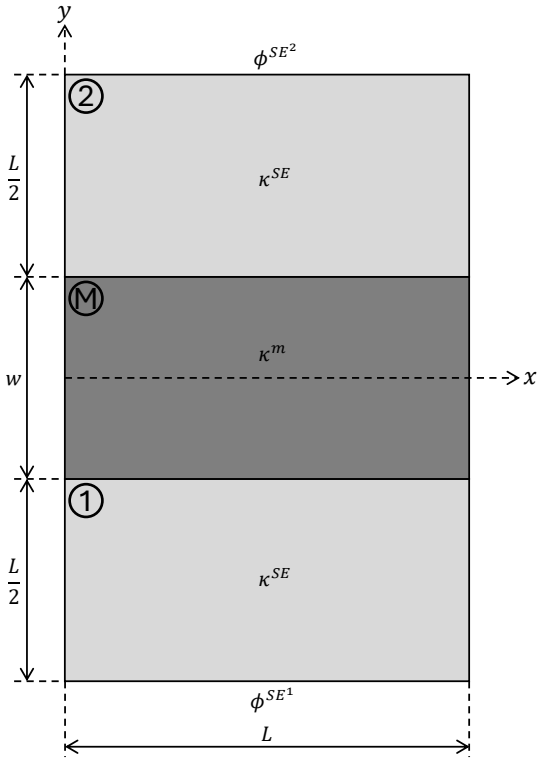

Figure 5.2: Schematic picture of the configuration used for the verification of the numerical model. The figure shows the dimensions of the solid-state battery, the Dirichlet boundary conditions, and the conductivity of both the solid electrolyte and the electrodeposited lithium crack.

Continuous Galerkin formulation

Figure 5.3 displays the numerical results obtained from the continuous Galerkin formulation for two distinct scenarios. In Figure 5.3a, the result is depicted for the ratio $\frac{\kappa_m}{\kappa_{SE}} = 1$, while Figure 5.3b shows the outcome for a significantly larger ratio of $\frac{\kappa_m}{\kappa_{SE}} = 100$. However, when compared, both results are identical. This similarity arises from the shape function in Equation 4.33 (Section 4.2), which enforces continuity between the upper and lower crack boundaries at $\frac{w}{2}$ and $-\frac{w}{2}$, respectively, as illustrated in Figure 5.2. This means that the electric potential must be equal at both boundaries. Such continuity enforcement is stronger than that used in the analytical case, which ensures continuity only between the solid electrolyte and the crack at the upper and lower crack boundaries, without enforcing it between the upper and lower boundaries. This implies that the electric potential at $\frac{w}{2}$ must be equal in the crack domain and the solid electrolyte domain, and the same applies at $-\frac{w}{2}$, but the values for the electric potential at these points can differ. The stronger continuity enforcement of the continuous Galerkin discretization is generally inaccurate. This continuity assumption can only be used when the conductivity inside the crack is much higher than that for the solid electrolyte, causing the lithium to act as a perfect conductor. In the case of solid-state batteries, lithium conductivity is notably high [46], so despite the stronger continuity assumption, accurate results can be obtained using Continuous Galerkin in this specific application. Nevertheless, it is essential to acknowledge that generalized outcomes for different conductivities lack accuracy. In contrast, discontinuous Galerkin does not impose the stronger continuity assumption, making it a more versatile method. Therefore, the primary validation against the analytical solution is conducted using this formulation.

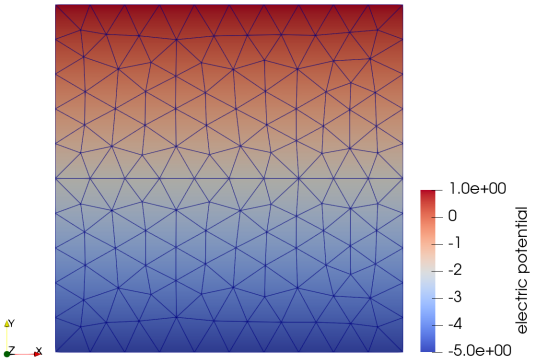

(a) Results for conductivity ratio $\frac{\kappa_m}{\kappa_{SE}} = 1$

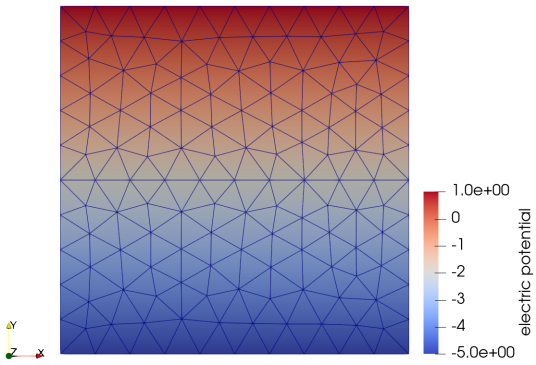

(b) Results for conductivity ratio $\frac{\kappa_m}{\kappa_{SE}} = 100$

Figure 5.3: The results of the continuous Galerkin formulation for two different conductivity ratios show no differences in outcome, despite the varying ratios, due to the stronger enforced continuity of the continuous Galerkin discretization, which is only valid when the conductivity of the crack is much higher than the conductivity of the solid electrolyte. Therefore, only the results of Figure 5.3b are accurate. The discontinuous Galerkin discretization is applied to overcome the inaccuracies and obtain a more versatile formulation that is valid for all conductivity ratios.

Discontinuous Galerkin formulation

For the verification, various ratios between the conductivity of the solid electrolyte and the lithium crack are considered. Figure 5.4 displays the results when the conductivity between the solid electrolyte and the crack is equal. It can be clearly observed that in the x-direction, the conductivity remains constant. This is a consequence of the configuration used to derive the analytical model, and it is valid for every conductivity ratio. Therefore, numerical and analytical results are compared solely in the y-direction, as shown in Figure 5.5 and Figure 5.6. The graphs are divided into the solid electrolyte section and the cracked section, which are distinguished by a grey interface in the plots. The numerical results, represented by dots connected by a blue dotted line, do not include data within the crack. This limitation arises because only the average electric potential is obtained for the cracked part, resulting in only a dotted line inside the crack, which represents a linear interpolation between the two boundary points of the solid electrolyte and the lithium crack. In contrast, the analytical solution provides results for both the solid electrolyte and the crack without distinguishing between the two domains, as indicated by a red line in the graphs.

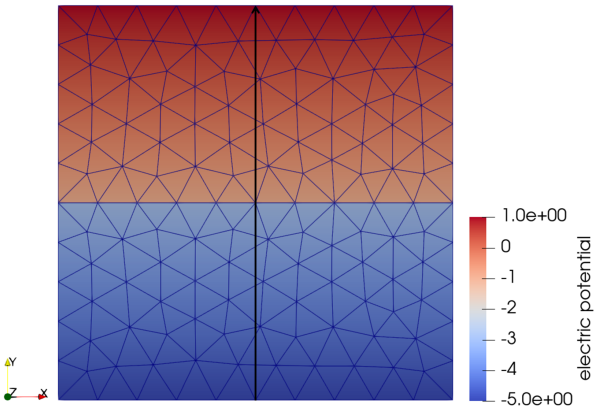

Figure 5.4: A 2D plot of the numerical results for a conductivity ratio $\frac{\kappa_m}{\kappa_{SE}} = 1$, showing no variation in electric potential along the x-direction. The arrow indicates the direction of the plot for the subsequent graphs.

Beginning with a ratio of $\frac{\kappa_m}{\kappa_{SE}} = 1$, as illustrated in Figure 5.5a, when the conductivity of both materials is equal, the behavior of the uncracked and cracked parts should be identical. Although the cracked part is not directly modeled in the numerical solution, it is evident that both domains yield the same results because the interpolation line between the two boundaries maintains the same slope as the solid electrolyte sections. Moreover, this finding aligns with the analytical results.

Figure 5.5b and Figure 5.5c show the results for $\frac{\kappa_m}{\kappa_{SE}} = 2$ and $\frac{\kappa_m}{\kappa_{SE}} = 1000$, respectively. As $\frac{\kappa_m}{\kappa_{SE}}$ approaches infinity, the lithium crack offers no electric resistance, resulting in no change in electric potential within the crack. This phenomenon is observed in Figure 5.5c when $\frac{\kappa_m}{\kappa_{SE}} = 1000$. Hence, a significantly high ratio between the conductivity of the solid electrolyte and the lithium crack demonstrates the expected behavior. Additionally, in Figure 5.5b, where $\frac{\kappa_m}{\kappa_{SE}} = 2$, the difference in electric potential between both boundaries at the crack diminishes, aligning with expectations for higher ratios. The numerical results are also consistent with the analytical results.

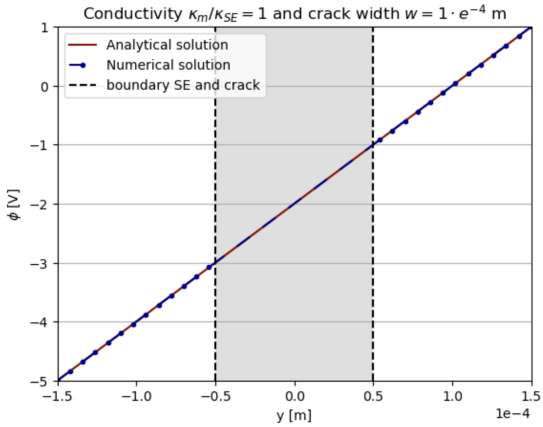

(a) The electric potential against the z-axis is plotted for a conductivity ratio of $\frac{\kappa_m}{\kappa_{SE}} = 1$, indicating that both materials have the same response. This uniform behavior is evident in the plots, where both the solid electrolyte and the lithium crack exhibit the same linear trend.

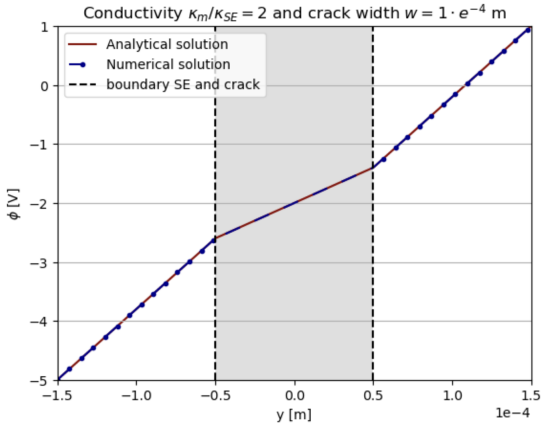

(b) The electric potential along the z-axis is plotted for a conductivity ratio of $\frac{\kappa_m}{\kappa_{SE}} = 2$, leading to a decrease in the difference in electric potential between both sides of the solid electrolyte due to the higher conductivity of the lithium crack.

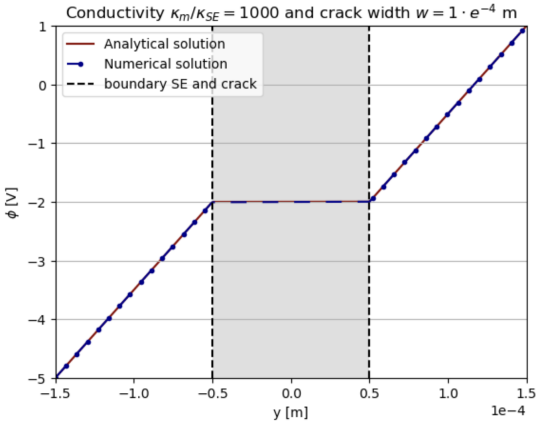

(c) The electric potential along the z-axis is plotted for a conductivity ratio of $\frac{\kappa_m}{\kappa_{SE}} = 1000$, resulting in a converged solution representing the limit case when the conductivity of the lithium crack approaches infinity. In this scenario, perfect conduction occurs, resulting in equal electric potential at both sides of the lithium crack.

Figure 5.5: A numerical and analytical comparison of the electric potential for a conductivity ratio of $\frac{\kappa_m}{\kappa_{SE}}$ equal to or greater than one. The gray area in the graphs depicts the cracked domain, which is not directly modeled in the numerical solution, and only an average value is obtained for the electric potential. This results in a discontinuity equal to the difference between the upper and lower sides of the crack. The plots show a linear interpolation between both sides of the crack.

In Figure 5.6a and Figure 5.6b, the results for $\frac{\kappa_m}{\kappa_{SE}} = 0.5$ and $\frac{\kappa_m}{\kappa_{SE}} = 0.001$ are presented. In these cases, the ratios between the electric potential of the lithium crack and the solid electrolyte are becoming very small. This indicates that the crack begins to behave as an insulator. In the limit case, when the crack becomes a perfect insulator, the solid electrolytes should be completely decoupled, resulting in a discontinuity in the electric potential from one side of the solid electrolyte to the other. This behavior is precisely observed in Figure 5.6b when $\frac{\kappa_m}{\kappa_{SE}} = 0.001$. When $\frac{\kappa_m}{\kappa_{SE}} = 0.5$, the insulation properties of the crack are not yet sufficiently high to behave as a perfect insulator. However, the difference between both sides of the crack increases compared to a ratio of $\frac{\kappa_m}{\kappa_{SE}} = 1$, indicating a trend towards the limit case. Furthermore, both insulating results align perfectly with the analytical predictions.

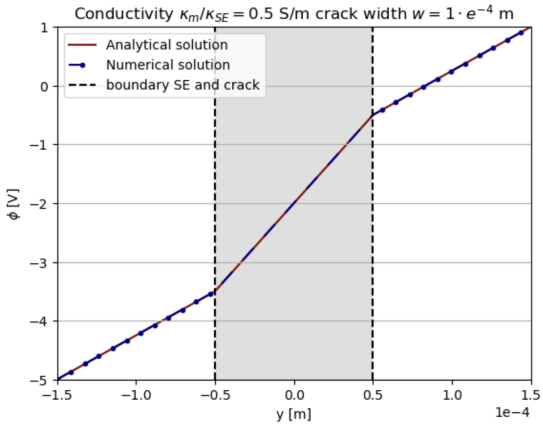

(a) The electric potential against the z-axis is plotted for a conductivity ratio of $\frac{\kappa_m}{\kappa_{SE}} = 0.5$, leading to a increase of electric potential between both sides of the solid electrolyte due to the higher insulating properties of the lithium crack.

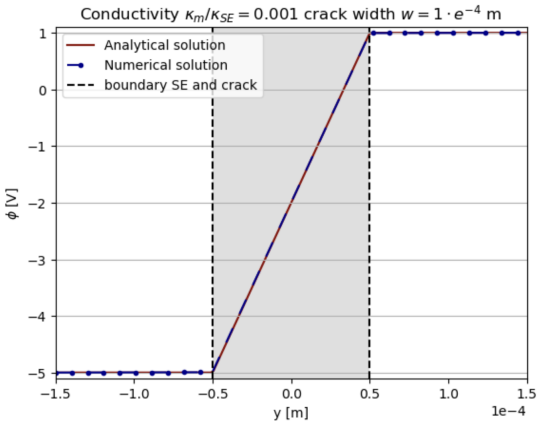

(b) The electric potential along the z-axis is plotted for a conductivity ratio of $\frac{\kappa_m}{\kappa_{SE}} = 0.001$, resulting in a converged solution representing the limit case when the conductivity of the lithium crack approaches zero. In this scenario, perfect insulation occurs, leading to the complete decoupling of the solid electrolyte parts.

Figure 5.6: A numerical and analytical comparison of the electric potential for a conductivity ratio of $\frac{\kappa_m}{\kappa_{SE}}$ lower than one. The gray area in the graphs depicts the cracked domain, which is not directly modeled in the numerical solution, and only an average value is obtained for the electric potential. This results in a discontinuity equal to the difference between the upper and lower sides of the crack. The plots show a linear interpolation between both sides of the crack.

Figure 5.7 shows the results for the limit cases, where the crack opening is significantly smaller than the crack width, ensuring that all assumptions are met. Similar behavior is observed compared to the results obtained with a larger crack opening. In the case of the conductivity ratio $\frac{\kappa_m}{\kappa_{SE}} = 1$ (Figure 5.7a), the same linear relation as seen in Figure 5.5a is observed. However, due to the smaller crack opening, the change in electric potential along the crack is smaller, resulting in a smaller jump in electric potential between both sides of the solid electrolyte. For the conductivity ratio $\frac{\kappa_m}{\kappa_{SE}} = 1000$ (Figure 5.7b), the electric potential remains constant along the crack, which is the same behavior depicted in Figure 5.5c. Figure 5.7c displays the result of an isolating crack. Here, the electric potential varies along the solid electrolyte, contrasting with Figure 5.6b, where the electric potential changes only within the crack. This results from a conductivity ratio $\frac{\kappa_m}{\kappa_{SE}} = 0.001$, which is too low to obtain perfect insulation behavior with such a small crack opening. However, the results go to the limit case, indicating that a lower conductivity ratio would indeed result in perfect insulating behavior.

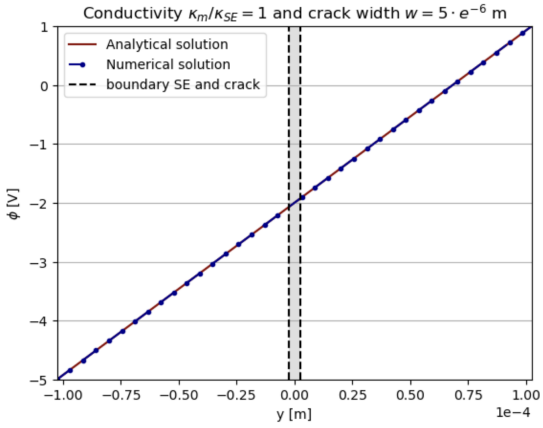

(a) When $\frac{\kappa_m}{\kappa_{SE}} = 1$, linear behavior is observed across the entire domain. However, the smaller crack opening leads to a smaller jump between both sides of the solid electrolyte.

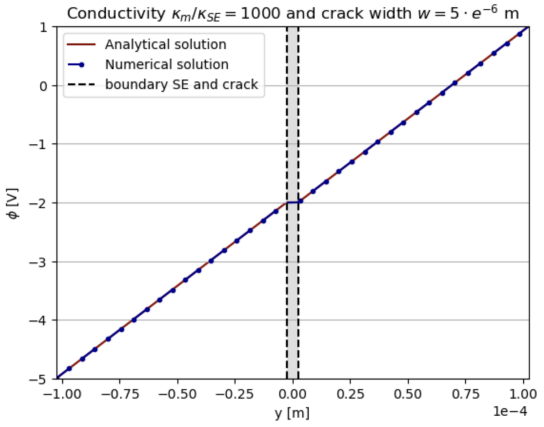

(b) When $\frac{\kappa_m}{\kappa_{SE}} = 1000$, it results in a perfectly conductive crack, ensuring that the electric potential remains constant along the crack.

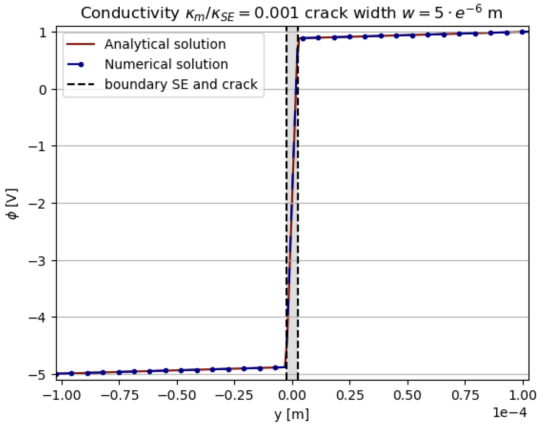

(c) When $\frac{\kappa_m}{\kappa_{SE}} = 0.001$, it indicates an insulating crack. However, due to the smaller crack opening, the conductivity ratio is not sufficiently low to exhibit perfect insulating behavior of the crack, resulting in a slight change in electric potential along the solid electrolyte.

Figure 5.7: Overview of the results for a small crack opening. The gray area in the graphs depicts the cracked domain, which is not directly modeled in the numerical solution, and only an average value is obtained for the electric potential. This results in a discontinuity equal to the difference between the upper and lower sides of the crack. The plots show a linear interpolation between both sides of the crack.

5.2. Validation against available computational results (phase-field model solution)

The configuration used in the previous sections was established primarily for deriving an analytical model. However, this setup does not accurately represent the conditions observed during dendrite propagation in a solid-state battery. In reality, Dirichlet boundary conditions should be applied to the faces perpendicular to the crack rather than the parallel faces as previously assumed. Moreover, the analytical model only accounts for the final stage, where the crack has fully propagated through the solid electrolyte. Therefore, this section introduces an alternative configuration, depicted in Figure 5.8, showing new locations for the Dirichlet boundary conditions and a crack that extends only to the middle of the solid electrolyte.

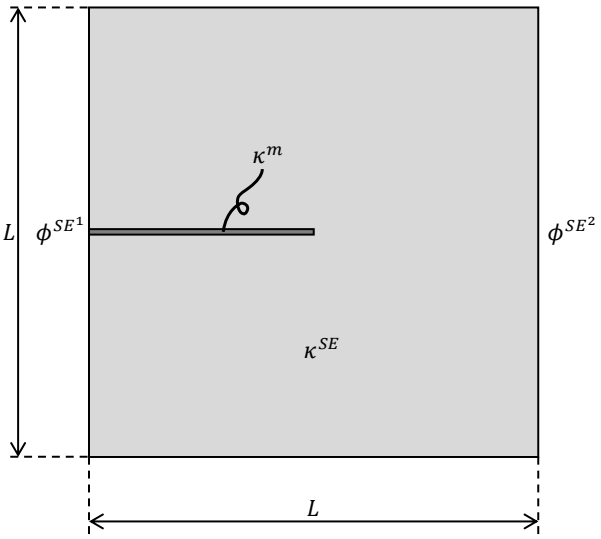

Figure 5.8: An alternative configuration of the solid electrolyte involves applying Dirichlet boundary conditions at the faces perpendicular to the crack, with the crack only propagated to the middle of the solid electrolyte.

The configuration of Figure 5.8 is equal to the setup employed in the work of Bistri and Leo [2], which is shown in Chapter 3. The electric potential results obtained in the new model can be compared with those of Bistri and Leo to validate the model. The properties specified in this paper are adopted for the new model to achieve this comparison. This means that the conductivity ratio becomes $\frac{\kappa_m}{\kappa_{SE}} = 1 \cdot e^9$, the left Dirichlet boundary condition $\phi^{SE^1} = 0$ and the right Dirichlet boundary condition $\phi^{SE^2} = 0.2$. Under this configuration, the results exhibit nonlinearity, meaning that neglecting the small crack opening is no longer possible. Therefore, a crack opening of $w = 5 \cdot e^{-6}$ m is considered.

Another consequence of the nonlinear results is the influence of the mesh on the outcomes. Previously,

the mesh did not affect the results due to linearity. Figure 5.9 demonstrates that this is no longer the case. This figure presents numerical results for a mesh size of $h = 0.1L$. Inside the crack, the electric potential remains close to zero due to the high conductivity value at this location. Beyond the crack, the conductivity of the solid electrolyte is much lower, necessitating an increase in electro potential. However, due to the coarse mesh, the electric potential overshoots, resulting in an inaccurate electric potential pattern. A mesh convergence study, as shown in Figure 5.10, is conducted to determine the appropriate mesh size. The location of the plots in the mesh refinement study is indicated with an arrow in Figure 5.9. It can be observed that refining the mesh leads to a rapid increase in accuracy. After the first refinement, a significant improvement is already evident, but accurate results are only achieved after a second refinement. The final refinement shows minimal deviation from the previous one. This indicates that a mesh size of $h = 0.04L$ is sufficient to obtain accurate results.

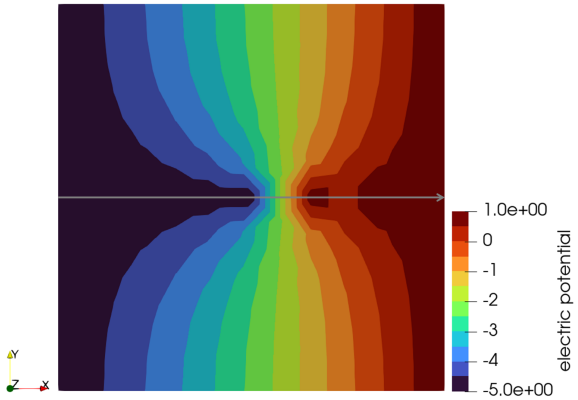

Figure 5.9: The numerical results of the crack propagation until the middle of the solid electrolyte with a mesh size of $h = 0.1L$. These results indicate that the mesh size is too coarse, as the electric potential overshoots after the crack. The arrow in the figure indicates the location of the mesh refinement study.

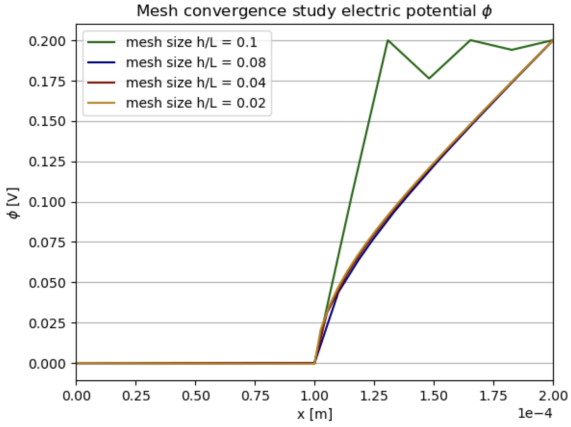

Figure 5.10: The mesh convergence study shows that the first refinement already leads to a significant improvement in the results. The second refinement gives a further improvement of the results but an additional improvement gives similar results.

The refined mesh is used to perform a quantitative comparison between the numerical results shown in Figure 5.11 and those of Bistri and Leo shown in Figure 5.12. The results of the numerical model exhibit significant similarities with the work of Bistri and Leo. In both simulations, the electric potential remains zero along the crack and increases afterward toward the second Dirichlet boundary condition. The main difference between the two models lies in the width of the cracked zone. The crack opening in the new model has become smaller compared to the work of Bistri and Leo. The contrast lies within the phase field model, where cracks are modeled as smoothed volumetric phenomena, as opposed to the new model, which considers sharp edges, leading to a narrower crack width. Validation against experiments would be necessary to assess which solution is more predictive.

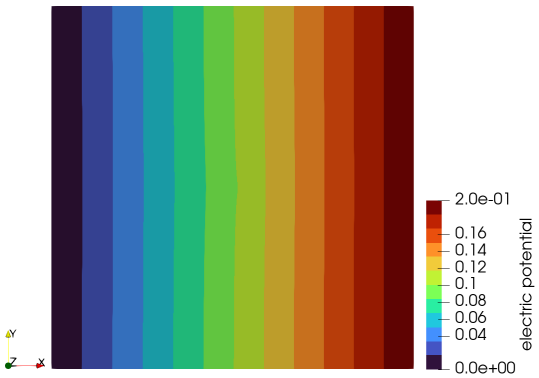

(a) Numerical results of the new model for a solid electrolyte without a crack

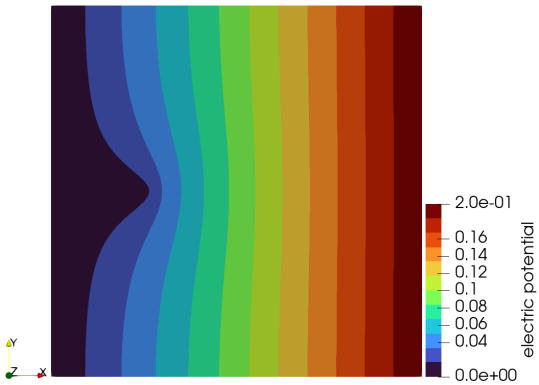

(b) Numerical results of the new model for a solid electrolyte with a crack that goes until a quarter of the solid electrolyte

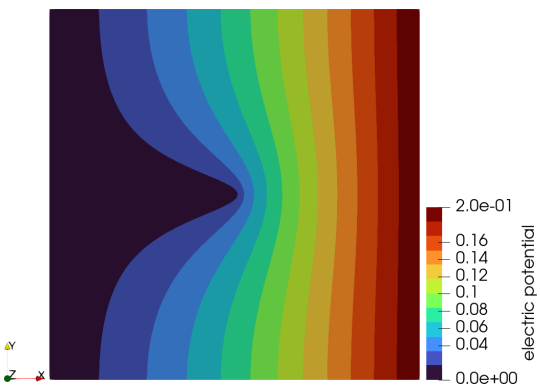

(c) Numerical results of the new model for a solid electrolyte with a crack that goes until half of the solid electrolyte

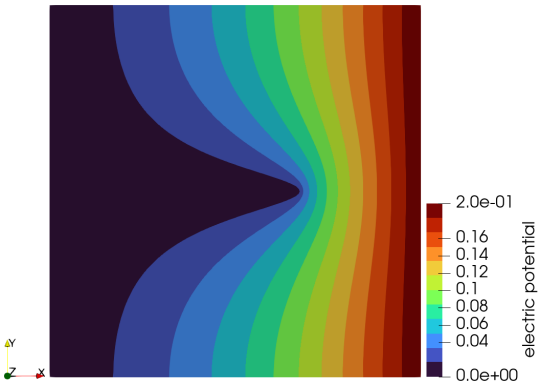

(d) Numerical results of the new model for a solid electrolyte with a crack that goes until two third of the solid electrolyte

Figure 5.11: Numerical results of the new model

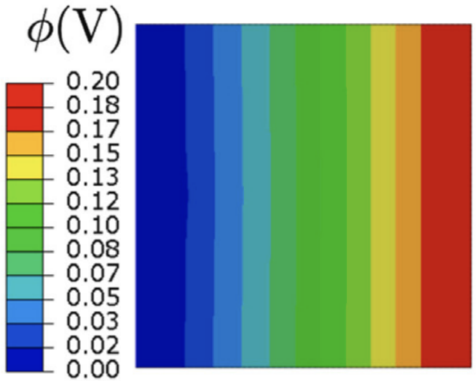

(a) Numerical results of the work of Bistri and Leo for a solid electrolyte without a crack

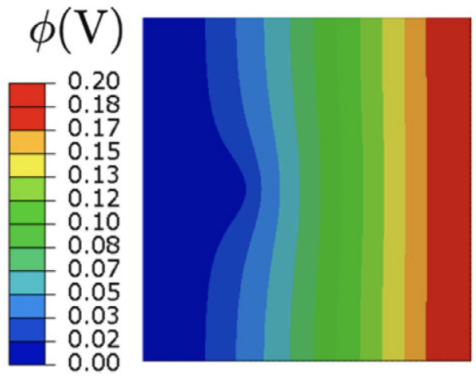

(b) Numerical results of the work of Bistri and Leo for a solid electrolyte with a crack that goes until a quarter of the solid electrolyte

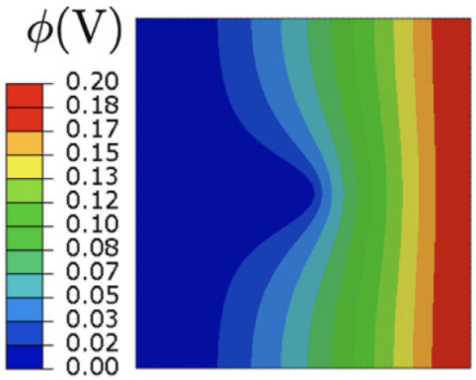

(c) Numerical results of the work of Bistri and Leo for a solid electrolyte with a crack that goes until half of the solid electrolyte

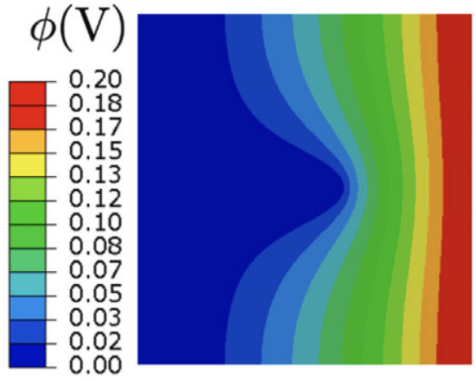

(d) Numerical results of the work of Bistri and Leo for a solid electrolyte with a crack that goes until two third of the solid electrolyte

Figure 5.12: Numerical results of the work of Bistri and Leo (adjusted from [2])

6

Conclusion

This research aimed to develop a new computational model to accurately solve partial differential equations in a cracked domain, specifically considering the physics inside a sharp crack. This goal comes from the literature study on solid-state batteries, where the new failure mode, dendrite propagation, had only been modeled using phase-field models, which rely on a smooth fracture description. Alternatively, the crack can also be modeled using a discrete method, introducing the crack as a discontinuity in the model and enabling the possibility of splitting the cracked and uncracked parts into two separate domains. A computational model can now be defined that couples the internal physics of the crack with the adjacent environment. Implementing such a method requires the development of a new methodology to solve the partial differential equations within the crack. This has led to the formulation of the following main question:

Research question (RQ)

Is it possible to formulate a computational model that accurately and efficiently captures the coupling of in-crack physics with the adjacent environment, while explicitly describing the crack as a sharp discontinuity?

This study has successfully developed a new methodology for solving partial differential equations in a crack domain, which couples the in-crack physics with the adjacent environment. It is achieved by projecting the governing equation of the two-dimensional crack domain in the tangential direction of the crack, thus yielding a one-dimensional representation of the governing equation within the cracked domain. This one-dimensional representation of the crack and the two-dimensional bulk domain are then combined into a single expression, resulting in a hybrid-dimensional formulation of the governing equation. The methodology is specifically applied to the electric governing equation of the solid-state battery, which is solved for the electric potential.

In the first step, the new formulation of the governing equation is discretized using continuous Galerkin to obtain the weak form. This weak form is then transformed into an element stiffness matrix, which is incorporated into the global stiffness matrix by the code to solve the resulting system of equations for the electric potential. The results obtained by the numerical model are verified against an analytical solution for a specific configuration that can be solved analytically.

However, the results of this discretization only match the correct solution in a limiting case: when the conductivity of the crack tends towards infinity. This discrepancy arises because, in this specific scenario, the electric potential between both sides of the solid electrolyte remains continuous, whereas in all other cases, a jump occurs between both sides. Unfortunately, the shape functions used in this discretization are continuous and cannot capture this jump.

In the context of solid-state batteries, where the conductivity of lithium is significantly high, the continuous Galerkin approach remains viable for this application. However, it should be noted that the generality of the method is compromised when employing this discretization.

The limited results of the continuous Galerkin discretization, combined with the optimal compatibility of the discontinuous Galerkin method with parallel computing required when the whole model is implemented, have shown the necessity of defining a discontinuous Galerkin discretization for the governing equation. This effort has yielded a new weak form, which is subsequently transformed into an element stiffness matrix and integrated into the global stiffness matrix, which is solved by the code.

The results obtained with this discretization exhibit a perfect alignment with the analytical model across all configurations, resulting in a significantly more flexible method than its continuous Galerkin counterpart.

Secondly, the model has been validated by comparing the numerical model results with the model of Bistri and Leo. While both models yield quantitatively similar results, the crack opening in the new numerical model is smaller than that in the phase field model. This distinction arises from the fundamental differences in the modeling approach. In phase field modeling, cracks are modeled as smoothed volumetric phenomena, whereas the new method employs sharp edges. Validation against experiments would be necessary to assess which solution is more predictive.

The new methodology for solving partial differential equations has proven successful in computing the electric potential. To extend this approach to modeling dendrite propagation, it is necessary to also rewrite the chemical governing equations in this hybrid-dimensional formulation and add the coupling with fracture mechanics. This will enable the development of a coupled model combining all three areas of physics.

6.1. Recommendations

Based on the research and the findings presented in this study, the recommendations center on advancing the model to enable the comprehensive solution of the coupled application of solid-state batteries, resulting in the following set of recommendations:

1. Rewriting the governing equation without phase-field variables: In the work of Bistri and Leo, the chemical governing equation for the electrodeposition of lithium inside the crack is expressed using phase-field variables. It is necessary to rewrite the chemical boundary condition without employing a phase-field variable.
2. Implementation of Mechanical and Chemical Governing Equations: This study primarily addresses the implementation and verification of the electric governing equation. However, to solve the complete dendrite propagation problem, it is essential to solve both the mechanical and chemical governing equations along with the coupling between these different domains. Therefore, future work should focus on integrating all three areas of physics into a coupled model for dendrite propagation.
3. Verification and validation of the completely coupled model: A new verification method should be established to ensure that the method is functioning as expected. The work of Bistri and Leo can be further used to validate this work. This study can facilitate a more comprehensive comparison once all three couplings are integrated into a single model.
4. Applying a modeling method to a novel approach aimed at preventing short circuits caused by dendrite propagation: A promising solution to improve the life span of solid-state batteries is dendrite deflection by applying a load to the solid electrolyte, which delays or even prevents the dendrites from growing to the other side of the solid electrolyte. For the development of this solution, it is of crucial importance that this behavior can be modeled so that the required forces for deflection and the dendrite trajectory can be accurately determined. This enables the possibility of significantly improving the biggest disadvantage of solid-state batteries, making it possible to reach the full potential of solid-state batteries.

Bibliography

[1] T. Verhelle. *Mercedes invests in solid-state battery technology of ProLogium*. 2022.

[2] D. Bistri and C. V. D. Leo. "A continuum electro-chemo-mechanical gradient theory coupled with damage: Application to Li-metal filament growth in all-solid-state batteries". *J. Mech. Phys. Solids* 174 (2023), p. 105252. DOI: 10.1016/j.jmps.2023.105252.

[3] Y. Tian, G. Zeng, A. Rutt, T. Shi, H. Kim, J. Wang, J. Koettgen, Y. Sun, B. Ouyang, T. Chen, Z. Lun, Z. Rong, K. Persson, and G. Ceder. "Promises and Challenges of Next-Generation "Beyond Li-ion" Batteries for Electric Vehicles and Grid Decarbonization". *Chem. Rev* 121 (2021), pp. 1623–1669. DOI: 10.1021/acs.chemrev.0c00767.

[4] D. S. Lee, D. W. Fahey, A. Skowron, M. R. Allen, U. Burkhardt, Q. Chen, S. J. Doherty, S. Freeman, P. M. Forster, J. Fuglestvedt, A. Gettelman, R. R. D. León, L. L. Lim, M. T. Lund, R. J. Millar, B. Owen, J. E. Penner, G. Pitari, M. J. Prather, R. Sausen, and L. J. Wilcox. "The contribution of global aviation to anthropogenic climate forcing for 2000 to 2018". *Atmospheric Environment* 244 (Jan. 2021). DOI: 10.1016/j.atmosenv.2020.117834.

[5] V. Viswanathan, A. H. Epstein, Y. M. Chiang, E. Takeuchi, M. Bradley, J. Langford, and M. Winter. "The challenges and opportunities of battery-powered flight". *Nature 2022 601:7894* 601 (7894 Jan. 2022), pp. 519–525. DOI: 10.1038/s41586-021-04139-1.

[6] M. Nagao, A. Hayashi, M. Tatsumisago, T. Kanetsuku, T. Tsuda, and S. Kuwabata. "In situ SEM study of a lithium deposition and dissolution mechanism in a bulk-type solid-state cell with a Li2S–P2S5 solid electrolyte". *Physical Chemistry Chemical Physics* 15 (42 Oct. 2013), pp. 18600–18606. DOI: 10.1039/C3CP51059J.

[7] Z. Ning, D. S. Jolly, G. Li, R. D. Meyere, S. D. Pu, Y. Chen, J. Kasemchainan, J. Ihli, C. Gong, B. Liu, D. L. Melvin, A. Bonnin, O. Magdysyuk, P. Adamson, G. O. Hartley, C. W. Monroe, T. J. Marrow, and P. G. Bruce. "Visualizing plating-induced cracking in lithium-anode solid-electrolyte cells". *Nature Materials 2021 20:8* 20 (8 Apr. 2021), pp. 1121–1129. DOI: 10.1038/S41563-021-00967-8.

[8] J. A. Lewis, C. Lee, Y. Liu, S. Y. Han, D. Prakash, E. J. Klein, H. W. Lee, and M. T. McDowell. "Role of Areal Capacity in Determining Short Circuiting of Sulfide-Based Solid-State Batteries". *ACS Applied Materials and Interfaces* 14 (3 Jan. 2022), pp. 4051–4060. DOI: 10.1021/ACSAMI.1C20139/ASSET/IMAGES/LARGE/AM1C20139_0006.JPEG.

[9] C. Monroe and J. Newman. "The Impact of Elastic Deformation on Deposition Kinetics at Lithium/Polymer Interfaces" (2005). DOI: 10.1149/1.1850854.

[10] C. D. Fincher, C. E. Athanasiou, C. Gilgenbach, M. Wang, B. W. Sheldon, W. C. Carter, and Y. M. Chiang. "Controlling dendrite propagation in solid-state batteries with engineered stress". *Joule* 6 (12 Dec. 2022), pp. 2794–2809. DOI: 10.1016/J.JOULE.2022.10.011.

[11] J. Gai, F. Ma, Z. Zhang, D. Sun, Y. Jin, Y. Guo, and W. Kim. "Flexible Organic-Inorganic Composite Solid Electrolyte with Asymmetric Structure for Room Temperature Solid-State Li-Ion Batteries". *ACS Sustainable Chemistry and Engineering* 7 (19 Oct. 2019), pp. 15896–15903. DOI: 10.1021/ACSSUSCHEMENG.9B01869/SUPPL_FILE/SC9B01869_SI_001.PDF.

[12] H. Al-Salih, M. S. E. Houache, E. A. Baranova, and Y. Abu-Lebdeh. "Composite Cathodes for Solid-State Lithium Batteries: "Catholytes" the Underrated Giants". *Advanced Energy and Sustainability Research* 3 (8 Aug. 2022), p. 2200032. DOI: 10.1002/AESR.202200032.

[13] R. C. Massé, C. Liu, Y. Li, L. Mai, and G. Cao. "Energy storage through intercalation reactions: electrodes for rechargeable batteries". *National Science Review* 4 (1 Jan. 2017), pp. 26–53. DOI: 10.1093/NSR/NWW093.

[14] T. F. Fuller and J. N. Harb. *Electrochemical engineering*. 2018.

[15] D. Grazioli, ·. M. Magri, ·. A. Salvadori, and B. A. Salvadori. "Computational modeling of Li-ion batteries". *Computational Mechanics* 58 (2016), pp. 889–909. DOI: 10.1007/s00466-016-1325-8.

[16] Y. Zhao, P. Stein, Y. Bai, M. Al-Siraj, Y. Yang, and B.-X. Xu. "A review on modeling of electro-chemo-mechanics in lithium-ion batteries" (2018). DOI: 10.1016/j.jpowsour.2018.12.011.

[17] J. Tian, Z. Chen, and Y. Zhao. "Review on Modeling for Chemo-mechanical Behavior at Interfaces of All-Solid-State Lithium-Ion Batteries and Beyond" (2022). DOI: 10.1021/acsomega.1c06793.

[18] D. Bistri, A. Afshar, and C. V. D. Leo. "Modeling the chemo-mechanical behavior of all-solid-state batteries: a review." *Meccanica* 56 (6 June 2021), pp. 1523–1554. DOI: 10.1007/S11012-020-01209-Y/FIGURES/8.

[19] J. A. Lewis, J. Tippens, F. J. Q. Cortes, and M. T. Mcdowell. "Chemo-Mechanical Challenges in Solid-State Batteries" (2019). DOI: 10.1016/j.trechm.2019.06.013.

[20] Y. Zhao, R. Wang, and E. Martínez-Pañeda. "A phase field electro-chemo-mechanical formulation for predicting void evolution at the Li–electrolyte interface in all-solid-state batteries". *Journal of the Mechanics and Physics of Solids* 167 (Oct. 2022), p. 104999. DOI: 10.1016/J.JMPS.2022.104999.

[21] W. Manalastas, J. Rikarte, R. J. Chater, R. Brugge, A. Aguadero, L. Buannic, A. Llordés, F. Aguesse, and J. Kilner. "Mechanical failure of garnet electrolytes during Li electrodeposition observed by in-operando microscopy" (2018). DOI: 10.1016/j.jpowsour.2018.11.041.

[22] P. Wang, W. Qu, W. L. Song, H. Chen, R. Chen, and D. Fang. "Electro–Chemo–Mechanical Issues at the Interfaces in Solid-State Lithium Metal Batteries". *Advanced Functional Materials* 29 (27 July 2019). DOI: 10.1002/ADFM.201900950.

[23] J. A. Lewis, F. J. Q. Cortes, M. G. Boebinger, J. Tippens, T. S. Marchese, N. Kondekar, X. Liu, M. Chi, and M. T. McDowell. "Interphase Morphology between a Solid-State Electrolyte and Lithium Controls Cell Failure". *ACS Energy Letters* 4 (2 Feb. 2019), pp. 591–599. DOI: 10.1021/ACSENERGYLETT.9B00093/SUPPL_FILE/NZ9B00093_SI_001.PDF.

[24] L. Porz, T. Swamy, B. W. Sheldon, D. Rettenwander, T. Frömling, H. L. Thaman, S. Berendts, R. Uecker, W. C. Carter, and Y. M. Chiang. "Mechanism of Lithium Metal Penetration through Inorganic Solid Electrolytes". *Advanced Energy Materials* 7 (20 Oct. 2017). DOI: 10.1002/AENM.201701003.

[25] E. Kazyak, R. Garcia-Mendez, W. S. LePage, A. Sharafi, A. L. Davis, A. J. Sanchez, K. H. Chen, C. Haslam, J. Sakamoto, and N. P. Dasgupta. "Li Penetration in Ceramic Solid Electrolytes: Operando Microscopy Analysis of Morphology, Propagation, and Reversibility". *Matter* 2 (4 Apr. 2020), pp. 1025–1048. DOI: 10.1016/j.matt.2020.02.008.

[26] F. Han, A. S. Westover, J. Yue, X. Fan, F. Wang, M. Chi, D. N. Leonard, N. J. Dudney, H. Wang, and C. Wang. "High electronic conductivity as the origin of lithium dendrite formation within solid electrolytes". *Nature Energy 2019 4:3* 4 (3 Jan. 2019), pp. 187–196. DOI: 10.1038/S41560-018-0312-Z.

[27] T. Krauskopf, H. Hartmann, W. G. Zeier, and rgen Janek. "Toward a Fundamental Understanding of the Lithium Metal Anode in Solid-State Batteries - An Electrochemo-Mechanical Study on the Garnet-Type Solid Electrolyte" (2019). DOI: 10.1021/acsami.9b02537.

[28] J. Kasemchainan, S. Zekoll, D. S. Jolly, Z. Ning, G. O. Hartley, J. Marrow, and P. G. Bruce. "Critical stripping current leads to dendrite formation on plating in lithium anode solid electrolyte cells". *Nature Materials 2019 18:10* 18 (10 July 2019), pp. 1105–1111. DOI: 10.1038/S41563-019-0438-9.

[29] U. Pillai. "Damage modelling in fibre-reinforced composite laminates using phase field approach". University of Nottingham, 2021.

[30] B. Talamini, Y. Mao, and L. Anand. "Progressive damage and rupture in polymers". *Journal of the Mechanics and Physics of Solids* 111 (Feb. 2018), pp. 434–457. DOI: 10.1016/j.jmps.2017.11.013.

[31] Y. Mao and L. Anand. "Fracture of elastomeric materials by crosslink failure". *Journal of Applied Mechanics, Transactions ASME* 85 (8 Aug. 2018). DOI: 10.1115/1.4040100.

[32] G. Bucci and J. Christensen. "Modeling of lithium electrodeposition at the lithium/ceramic electrolyte interface: The role of interfacial resistance and surface defects". *Journal of Power Sources* 441 (2019), p. 227186. DOI: 10.1016/j.jpowsour.2019.227186.

[33] S. Narayan and L. Anand. "On Modeling the Detrimental Effects of Inhomogeneous Plating-and-Stripping at a Lithium-Metal/Solid-Electrolyte Interface in a Solid-State-Battery". *Journal of The Electrochemical Society* 167 (4 Mar. 2020), p. 040525. DOI: 10.1149/1945-7111/ab75c1.

[34] S. Narayan and L. Anand. "A large deformation elastic-viscoplastic model for lithium". *Extreme Mechanics Letters* 24 (2018), pp. 21–29. DOI: 10.1016/j.eml.2018.08.006.

[35] C. Yuan, X. Gao, Y. Jia, W. Zhang, Q. Wu, and J. Xu. "Coupled crack propagation and dendrite growth in solid electrolyte of all-solid-state battery". *Nano Energy* 86 (2021), p. 106057. DOI: 10.1016/j.nanoen.2021.106057.

[36] C. Yuan, W. Lu, and J. Xu. "Unlocking the Electrochemical–Mechanical Coupling Behaviors of Dendrite Growth and Crack Propagation in All-Solid-State Batteries". *Advanced Energy Materials* 11 (36 Sept. 2021), p. 2101807. DOI: 10.1002/AENM.202101807.

[37] S. Rezaei, J. N. Okoe-Amon, C. A. Varkey, A. Asheri, H. Ruan, and B. X. Xu. "A cohesive phase-field fracture model for chemo-mechanical environments: Studies on degradation in battery materials". *Theoretical and Applied Fracture Mechanics* 124 (Apr. 2023). DOI: 10.1016/j.tafmec.2023.103758.

[38] S. Rezaei, A. Harandi, T. Brepols, and S. Reese. "An anisotropic cohesive fracture model: Advantages and limitations of length-scale insensitive phase-field damage models A R T I C L E I N F O Keywords: Anisotropic cohesive fracture Phase-field damage model Length-scale insensitive". *Engineering Fracture Mechanics* 261 (2022), p. 108177. DOI: 10.1016/j.engfracmech.2021.108177.

[39] B. Giovanardi. "Numerical Modeling of Hydro-Mechanical Coupling in Deformable Porous Media: Compaction and Fractures". Politecnico di Milano, 2016.

[40] R. Radovitzky, A. Seagraves, M. Tupek, and L. Noels. "A scalable 3D fracture and fragmentation algorithm based on a hybrid, discontinuous Galerkin, Cohesive Element Method". 200 (2011), pp. 326–344. DOI: 10.1016/j.cma.2010.08.014.

[41] G. Bucci, T. Swamy, Y. M. Chiang, and W. C. Carter. "Modeling of internal mechanical failure of all-solid-state batteries during electrochemical cycling, and implications for battery design". *Journal of Materials Chemistry A* 5 (36 2017), pp. 19422–19430. DOI: 10.1039/c7ta03199h.

[42] S. Rezaei, A. Asheri, and B.-X. Xu. "A consistent framework for chemo-mechanical cohesive fracture and its application in solid-state batteries". *Journal of the Mechanics and Physics of Solids journal homepage* 157 (2021). DOI: 10.1016/j.jmps.2021.104612.

[43] B. Giovanardi, S. Serebrinsky, and R. Radovitzky. "A fully-coupled computational framework for large-scale simulation of fluid-driven fracture propagation on parallel computers" (2020).

[44] M. Klinsmann, F. E. Hildebrand, M. Ganser, and R. M. Mcmeeking. "Dendritic cracking in solid electrolytes driven by lithium insertion". *Journal of Power Sources* 442 (2019), p. 227226. DOI: 10.1016/j.jpowsour.2019.227226.

[45] B. Giovanardi, L. Formaggia, A. Scotti, and P. Zunino. "Unfitted FEM for modelling the interaction of multiple fractures in a poroelastic medium". *Lecture Notes in Computational Science and Engineering* 121 (2018). DOI: 10.13140/RG.2.2.33012.35207.

[46] L. Chen, H. W. Zhang, L. Y. Liang, Z. Liu, Y. Qi, P. Lu, J. Chen, and L.-Q. Chen. "Modulation of dendritic patterns during electrodeposition: A nonlinear phase-field model" (2015). DOI: 10.1016/j.jpowsour.2015.09.055.

[47] M. Ganser, F. E. Hildebrand, M. Klinsmann, M. Hanauer, M. Kamlah, and R. M. McMeeking. "An Extended Formulation of Butler-Volmer Electrochemical Reaction Kinetics Including the Influence of Mechanics". *Journal of The Electrochemical Society* 166 (4 Mar. 2019), H167–H176. DOI: 10.1149/2.1111904JES/XML.

[48] K. B. P. M. S. Pedersen, B. Baxter, B. Templeton, C. Rishøj, C. Schröppel, D. Boley, D. L. Theobald, E. Hoegh-Rasmussen, E. Karseras, G. Martius, G. Casteel, J. Larsen, J. B. Gao, J. Struckmeier, K. Dedecius, K. T. Abou-Moustafa, K. Strimmer, L. Christiansen, L. K. Hansen, L. Wilkinson, L. He, L. Thibaut, M. Froeb, M. Hubatka, M. Barão, O. Winther, P. Sakov, S. Hattinger, T. Pedersen, V. Sima, and V. Rabaud. *The Matrix Cookbook*. 2012.

[49] M. E. Gurtin, E. Fried, and L. Anand. *The Mechanics and Thermodynamics of Continua*. Cambridge University Press, 2010.

A

About the Template

A.1. License

B

Full derivation governing equations

This chapter describes the derivation of the governing equations and is based on the work of Bistri and Leo [2].

In this work, vector and second-order tensor variables are distinguished from scalar variables by making these quantities bold. Additionally, to differentiate between vector and second-order tensor variables, all vector variables are denoted with lowercase symbols, while uppercase symbols denote second-order tensor variables. The derivation primarily takes place in the reference configuration. Therefore, the variables are, in principle, reference properties unless a bar is added above the symbol, indicating a property in the current configuration.

B.1. Balance equations

The derivation considers a solid conductor adjacent to a metallic electrode of compound M. Defects are present at the interface between the solid conductor and the electrode. Examples of such defects include pores, voids, and cracks. These defects can be viewed as empty spaces within the solid conductor that can be filled by depositing the metallic compound into these areas. This process can be modeled using a general electrodeposition reaction. Cations, denoted by M^{n+}, are conducted through the solid electrolyte to the interface with the electrode. These cations can then react with the electrons of the electrode (e^-) to deposit M-atoms into the defects. The half-cell reaction that describes this process is shown below:

$$M^{n+} + e^- \rightarrow M \tag{B.1}$$

The electrodeposition of the electric compound per unit reference volume inside the defects is denoted by ξ. The maximum amount of metallic compound that can be deposited inside a crack before it is fully filled is denoted by ξ_{max}. The electrodeposition process can be normalized using Equation B.2.

$$\bar{\xi} = \frac{\xi}{\xi_{max}} \quad \in \quad [0, 1] \tag{B.2}$$

No metallic compound is deposited inside the crack when $\bar{\xi} = 0$. Conversely, the crack is fully filled by electrodeposited metallic compound when $\bar{\xi} = 1$. The electrodeposition $\bar{\xi}$ can only occur in damaged zones.

B.1.1. Mass balance

The global mass balance is defined in the expression below:

$$\frac{\partial}{\partial t} \int_{\mathcal{R}} c \, dV = - \int_{\partial \mathcal{R}} \boldsymbol{h} \cdot \boldsymbol{n} \, dA - \frac{\partial}{\partial t} \int_{\mathcal{R}} \xi \, dV \tag{B.3}$$

Here, $c\,(\boldsymbol{x}, t)$ denotes the number of moles of the mobile ionic species per unit reference volume, $\xi\,(\boldsymbol{x}, t)$ represents the number of moles of the electrodeposited species per unit reference volume, and $\boldsymbol{h}\,(\boldsymbol{x}, t)$ is

the referential flux of the mobile ionic species across the solid conductor.

Equation B.3 can be rewritten by applying the divergence theorem to the second term, converting the surface integral into a volume integral:

$$\frac{\partial}{\partial t}\int_{\mathcal{R}} c\, dV = -\int_{\mathcal{R}} \operatorname{div}(\boldsymbol{h})\, dV - \frac{\partial}{\partial t}\int_{\mathcal{R}} \xi\, dV \tag{B.4}$$

The integrals used in Equation B.4 are with respect to the reference domain. This implies that the integrals do not depend on time, allowing for the swapping of integrals and derivative operators:

$$\begin{aligned}\int_{\mathcal{R}} \frac{\partial c}{\partial t}\, dV &= -\int_{\mathcal{R}} \operatorname{div}(\boldsymbol{h})\, dV - \int_{\mathcal{R}} \frac{\partial \xi}{\partial t}\, dV \\ \int_{\mathcal{R}} \dot{c}\, dV &= -\int_{\mathcal{R}} \operatorname{div}(\boldsymbol{h})\, dV - \int_{\mathcal{R}} \dot{\xi}\, dV\end{aligned} \tag{B.5}$$

All terms can be brought to one side, and the integrals can be combined into a single integral.

$$\begin{aligned}\int_{\mathcal{R}} \dot{c}\, dV + \int_{\mathcal{R}} \operatorname{div}(\boldsymbol{h})\, dV + \int_{\mathcal{R}} \dot{\xi}\, dV &= 0 \\ \int_{\mathcal{R}} \dot{c} + \operatorname{div}(\boldsymbol{h}) + \dot{\xi}\, dV &= 0\end{aligned} \tag{B.6}$$

The current form of the mass balance can be localized:

$$\begin{aligned}\dot{c} + \operatorname{div}(\boldsymbol{h}) + \dot{\xi} &= 0 \\ \dot{c} &= -\operatorname{div}(\boldsymbol{h}) - \dot{\xi}\end{aligned} \tag{B.7}$$

The divergence term in Equation B.7 represents the transport of ionic species across the solid host. The $\dot{\xi}$ term in this expression defines the ionic consumption, leading to the formation of the ionic compound inside the defect.

B.1.2. Charge balance

The charge of the cations in the initial state is given by the following expression:

$$Fc^{+}(\boldsymbol{x}, 0) \tag{B.8}$$

The expression for the anions can be defined in the same way:

$$Fc^{-}(\boldsymbol{x}, 0) \tag{B.9}$$

Here, F represents Faraday's constant. In the case of electroneutrality, the number of cations and anions are equal, leading to the following valid expression:

$$\begin{aligned}Fc^{+}(\boldsymbol{x}, 0) - Fc^{-}(\boldsymbol{x}, 0) &= 0 \\ c^{+}(\boldsymbol{x}, 0) - c^{-}(\boldsymbol{x}, 0) &= 0\end{aligned} \tag{B.10}$$

This means that initially, a fixed amount of charged species are considered:

$$c^{+}(\boldsymbol{x}, 0) = c^{-}(\boldsymbol{x}, 0) \equiv c_0 \tag{B.11}$$

The number of cations changes over time, so for $t > 0$, the expression for the cations becomes:

$$Fc(\boldsymbol{x}, t) \tag{B.12}$$

It is assumed that the anions are immobile and do not change over time. This means the concentration remains equal to c_0. Therefore, the expression for the anions can also be written as follows:

$$Fc_0 \tag{B.13}$$

The net charge per unit reference volume over time is obtained by subtracting Equation B.13 from Equation B.12:

$$\begin{aligned} q &= Fc - Fc_0 \\ q &= F\left(c - c_0\right) \end{aligned} \tag{B.14}$$

The time derivative of the net charge is taken to obtain the charge balance.

$$\dot{q} = F\dot{c} \tag{B.15}$$

The balance of mass (Equation B.7) is substituted into the charge balance (Equation B.15):

$$\begin{aligned} \dot{q} &= F\dot{c} \\ &= F\left(-\operatorname{div}\left(\boldsymbol{h}\right) - \dot{\xi}\right) \\ &= -F\operatorname{div}\left(\boldsymbol{h}\right) - F\dot{\xi} \end{aligned} \tag{B.16}$$

Faraday's constant is, as the name already suggests, a constant so that it can be written inside the divergence term in Equation B.16:

$$\begin{aligned} \dot{q} &= -F\operatorname{div}\left(\boldsymbol{h}\right) - F\dot{\xi} \\ &= -\operatorname{div}\left(F\boldsymbol{h}\right) - F\dot{\xi} \end{aligned} \tag{B.17}$$

$$\boldsymbol{i} = F\boldsymbol{h} \tag{B.18}$$

The definition of current density can be observed in the divergence term of the charge balance, allowing for the substitution of Equation B.18 into Equation B.17.

$$\begin{aligned} \dot{q} &= -\operatorname{div}\left(F\boldsymbol{h}\right) - F\dot{\xi} \\ \dot{q} &= -\operatorname{div}\left(\boldsymbol{i}\right) - F\dot{\xi} \end{aligned} \tag{B.19}$$

B.1.3. Electrostatics

The referential electric field is denoted by $\boldsymbol{e}(\boldsymbol{x}, t)$. In the case of a polarizable material, there is also a vector field $\boldsymbol{d}(\boldsymbol{x}, t)$, which is called the electric displacement. A polarizable material is a substance that can develop dipoles when subjected to an electric field. Dipoles consist of a pair of equal and opposite electric charges separated by a small distance. For electrostatic conditions, two of Maxwell's governing equations must be satisfied. The first is Faraday's law, which, in the case of electrostatics, is equal to the following expression:

$$\operatorname{curl}\left(\boldsymbol{e}\right) = \boldsymbol{0} \tag{B.20}$$

Equation B.20 is automatically satisfied when the electric field is represented as the gradient of the electrostatic potential $\phi(\boldsymbol{x}, t)$. This is because the curl of the gradient of a scalar field is, by definition, zero. Therefore, the electric field can be defined as follows:

$$\boldsymbol{e} = -\nabla\phi \tag{B.21}$$

The negative sign added to $\nabla\phi$ in Equation B.21 arises from the convention that the electric field points from regions of high potential to low potential, whereas the gradient indicates the direction of the greatest change in ϕ.

The second equation is given by Gauss's law, which states that the divergence of the displacement field must be equal to the charge density q.

$$\operatorname{div}\left(\boldsymbol{d}\right) = q \tag{B.22}$$

B.2. Kinematics

The deformation mapping from the reference to the current configuration is given by Equation B.23:

$$\boldsymbol{y} = \hat{\boldsymbol{y}}\left(\boldsymbol{x}, t\right) \tag{B.23}$$

The deformation gradient $\boldsymbol{F}$ is the gradient of the deformation $\hat{\boldsymbol{y}}$.

$$\boldsymbol{F} = \nabla \hat{\boldsymbol{y}} \tag{B.24}$$

The velocity v is the material time derivative of the deformation.

$$\boldsymbol{v} = \frac{\partial \hat{\boldsymbol{y}}}{\partial t} \tag{B.25}$$

The velocity gradient is the gradient of the velocity in the current configuration:

$$.\boldsymbol{L} = \nabla_y \bar{v} \tag{B.26}$$

The velocity gradient and the deformation gradient can be related by Equation B.27.

$$\boldsymbol{L} = \dot{\boldsymbol{F}} \boldsymbol{F}^{-1} \tag{B.27}$$

The deformation gradient is divided into a mechanical and chemical part using a multiplicative decomposition.

$$\boldsymbol{F} = \boldsymbol{F}^{mechanical} \boldsymbol{F}^{chemical} = \boldsymbol{F}^m \boldsymbol{F}^c \tag{B.28}$$

The tensor $\boldsymbol{F}^c$ represents the local distortion of the material near $\boldsymbol{x}$ due to chemical phenomena and consists of the following parts:

1. Species transport across the solid conductor.
2. Distortion caused by the electrodeposition of new material inside the solid conductor.

The chemical deformation tensor $\boldsymbol{F}^c$ replaces the continuous creation of new material and the resulting distortions. In this way, electrodeposition is considered without explicit accounting for the temporal evolution of the domain. $\boldsymbol{F}^m$ represents the distortion resulting from macroscopic stresses caused by elastic stretching and rotation of the material.

The Jacobian gives the volume ratio:

$$J = \det(\boldsymbol{F}) > 0 \tag{B.29}$$

A separate mechanical and chemical Jacobian can be defined:

$$\begin{aligned} J^m &= \det(\boldsymbol{F}^m) > 0 \\ J^c &= \det(\boldsymbol{F}^c) > 0 \end{aligned} \tag{B.30}$$

The Jacobian can be split into the mechanical and the chemical Jacobian by substituting Equation B.28 into Equation C.48:

$$\begin{aligned} J &= \det(\boldsymbol{F}) \\ &= \det(\boldsymbol{F}^m \boldsymbol{F}^c) \\ &= \det(\boldsymbol{F}^m) \det(\boldsymbol{F}^c) \\ &= J^m J^c \end{aligned} \tag{B.31}$$

Next is the introduction of the polar decomposition, where the deformation gradient is split into a pure deformation and a rigid body rotation. This decomposition is used for the mechanical deformation gradient.

$$\boldsymbol{F}^m = \boldsymbol{Q}^m \boldsymbol{U}^m = \boldsymbol{V}^m \boldsymbol{Q}^m \tag{B.32}$$

Where $\boldsymbol{Q}^m$ is a rotation matrix and $\boldsymbol{U}^m$ and $\boldsymbol{V}^m$ are the right and left stretch tensors, which are symmetric and positive definite. The general $\boldsymbol{U}$ and $\boldsymbol{V}$ are defined below:

$$\begin{aligned} \boldsymbol{U} &= \sqrt{\boldsymbol{F}^T \boldsymbol{F}} \\ \boldsymbol{V} &= \sqrt{\boldsymbol{F} \boldsymbol{F}^T} \end{aligned} \tag{B.33}$$

The square of these tensors is the right and left Cauchy-Green strain tensors, denoted as $\boldsymbol{C}$ and $\boldsymbol{G}$, respectively.

$$\begin{aligned} \boldsymbol{C} &= \boldsymbol{F}^T \boldsymbol{F} \\ \boldsymbol{G} &= \boldsymbol{F}\boldsymbol{F}^T \end{aligned} \tag{B.34}$$

The right Cauchy Green stain tensor can be written for the mechanical deformation gradient:

$$\boldsymbol{C}^m = \boldsymbol{F}^{mT} \boldsymbol{F}^m \tag{B.35}$$

The relation between the deformation gradient and the velocity gradient defined in Equation B.27 is reconsidered by substituting the multiplicative decomposition of the deformation gradient (Equation B.28) into this expression and rewriting the result.

$$\begin{aligned} \boldsymbol{L} &= \dot{\boldsymbol{F}} \boldsymbol{F}^{-1} \\ &= \frac{\partial}{\partial t} \left(\boldsymbol{F}^m \boldsymbol{F}^c\right) \left(\boldsymbol{F}^m \boldsymbol{F}^c\right)^{-1} \\ &= \left(\dot{\boldsymbol{F}}^m \boldsymbol{F}^c + \boldsymbol{F}^m \dot{\boldsymbol{F}}^c\right) \boldsymbol{F}^{c-1} \boldsymbol{F}^{m-1} \\ &= \dot{\boldsymbol{F}}^m \boldsymbol{F}^c \boldsymbol{F}^{c-1} \boldsymbol{F}^{m-1} + \boldsymbol{F}^m \dot{\boldsymbol{F}}^c \boldsymbol{F}^{c-1} \boldsymbol{F}^{m-1} \\ &= \dot{\boldsymbol{F}}^m \boldsymbol{F}^{m-1} + \boldsymbol{F}^m \dot{\boldsymbol{F}}^c \boldsymbol{F}^{c-1} \boldsymbol{F}^{m-1} \end{aligned} \tag{B.36}$$

The chemical and mechanical velocity gradients did arise in Equation B.36 and are shown below:

$$\begin{aligned} \boldsymbol{L}^m &= \dot{\boldsymbol{F}}^m \boldsymbol{F}^{m-1} \\ \boldsymbol{L}^c &= \dot{\boldsymbol{F}}^c \boldsymbol{F}^{c-1} \end{aligned} \tag{B.37}$$

Equation B.37 is substituted into Equation B.36:

$$\begin{aligned} \boldsymbol{L} &= \dot{\boldsymbol{F}}^m \boldsymbol{F}^{m-1} + \boldsymbol{F}^m \dot{\boldsymbol{F}}^c \boldsymbol{F}^{c-1} \boldsymbol{F}^{m-1} \\ &= \boldsymbol{L}^m + \boldsymbol{F}^m \boldsymbol{L}^c \boldsymbol{F}^{m-1} \end{aligned} \tag{B.38}$$

The velocity gradient can be divided into the symmetric stretching tensor and the skew-symmetric spin tensor. This is shown for both the mechanical and the chemical velocity gradients.

$$\begin{aligned} \boldsymbol{L}^m &= \boldsymbol{D}^m + \boldsymbol{W}^m \\ \boldsymbol{L}^c &= \boldsymbol{D}^c + \boldsymbol{W}^c \end{aligned} \tag{B.39}$$

Additionally, the chemical velocity gradient is decomposed into $\boldsymbol{L}^d$ and $\boldsymbol{L}^r$, as shown in Equation B.40. Here, $\boldsymbol{L}^d$ accounts for the deformation of a material point resulting from the transport of ionic species across the solid conductor. On the other hand, $\boldsymbol{L}^r$ accounts for deformations resulting from the electrodeposition of new material.

$$\boldsymbol{L}^c = \boldsymbol{L}^d + \boldsymbol{L}^r \tag{B.40}$$

Up to this point, the kinematics have been treated in the most general form. However, moving forward, the conductor is assumed to consist of a single ion. In these materials, only a single cation moves across the conductor while the anions remain immobile. This assumption results in a negligible concentration gradient within the bulk of the solid conductor, and deviations from electroneutrality are insignificant. Additionally, Li-ions cause no deformations upon removing or adding a lithium atom. Therefore, the transport of ionic species across the solid conductor does not result in deformations. This implies that deformations associated with ionic transport can be neglected, or in other words, $\boldsymbol{L}^d$, simplifying Equation B.40 to the following expression:

$$\boldsymbol{L}^c = \boldsymbol{L}^r \tag{B.41}$$

Secondly, the assumption is made that the chemical deformation is irrotational, meaning that the spin tensor is zero. This results in the simplification of Equation B.39.

$$\boldsymbol{L}^c = \boldsymbol{D}^c \tag{B.42}$$

Equation B.42 can now be substituted into Equation B.41:

$$\begin{aligned} \boldsymbol{L}^c &= \boldsymbol{L}^r \\ \boldsymbol{D}^c &= \boldsymbol{D}^r \end{aligned} \tag{B.43}$$

Here, $\boldsymbol{D}^r$ represents the electrodeposition-induced stretching, which depends on the deposition rate as follows:

$$\boldsymbol{D}^r = \dot{\xi}\boldsymbol{N}^r \tag{B.44}$$

Here, $\boldsymbol{N}^r$ represents the direction of electrodeposition-induced deformations. The final simplification involves considering solely elastic deformations, resulting in the mechanical deformation gradient being expressed as follows:

$$\boldsymbol{F}^m = \boldsymbol{F}^e \tag{B.45}$$

The velocity gradient in Equation B.38 is rewritten once more by substituting Equation B.27, Equation B.39, and Equation B.43 into this expression.

$$\begin{aligned} \boldsymbol{L} &= \boldsymbol{L}^m + \boldsymbol{F}^m \boldsymbol{L}^c \boldsymbol{F}^{m-1} \\ \dot{\boldsymbol{F}}\boldsymbol{F}^{-1} &= \dot{\boldsymbol{F}}^m \boldsymbol{F}^{m-1} + \boldsymbol{F}^m \boldsymbol{D}^r \boldsymbol{F}^{m-1} \end{aligned} \tag{B.46}$$

Equation B.46 is further rewritten by substituting Equation B.24, Equation B.44, and Equation B.45 into this expression.

$$\begin{aligned} \dot{\boldsymbol{F}}\boldsymbol{F}^{-1} &= \dot{\boldsymbol{F}}^m \boldsymbol{F}^{m-1} + \boldsymbol{F}^m \boldsymbol{D}^r \boldsymbol{F}^{m-1} \\ \frac{\partial}{\partial t}\left(\nabla_{\boldsymbol{x}} \hat{\boldsymbol{y}}\right) \boldsymbol{F}^{-1} &= \dot{\boldsymbol{F}}^e \boldsymbol{F}^{e-1} + \boldsymbol{F}^e \left(\dot{\xi}\boldsymbol{N}^r\right) \boldsymbol{F}^{e-1} \end{aligned} \tag{B.47}$$

The time derivative and the gradient of the first term in Equation B.47 can be interchanged, leading to the definition of velocity appearing in the expression. Consequently, Equation B.25 can be substituted.

$$\begin{aligned} \frac{\partial}{\partial t}\left(\nabla_{\boldsymbol{x}} \hat{\boldsymbol{y}}\right) \boldsymbol{F}^{-1} &= \dot{\boldsymbol{F}}^e \boldsymbol{F}^{e-1} + \boldsymbol{F}^e \left(\dot{\xi}\boldsymbol{N}^r\right) \boldsymbol{F}^{e-1} \\ \nabla_{\boldsymbol{x}} \left(\frac{\partial}{\partial t} \hat{\boldsymbol{y}}\right) \boldsymbol{F}^{-1} &= \dot{\boldsymbol{F}}^e \boldsymbol{F}^{e-1} + \boldsymbol{F}^e \left(\dot{\xi}\boldsymbol{N}^r\right) \boldsymbol{F}^{e-1} \\ \nabla_{\boldsymbol{x}} \left(\boldsymbol{v}\right) \boldsymbol{F}^{-1} &= \dot{\boldsymbol{F}}^e \boldsymbol{F}^{e-1} + \boldsymbol{F}^e \left(\dot{\xi}\boldsymbol{N}^r\right) \boldsymbol{F}^{e-1} \end{aligned} \tag{B.48}$$

B.3. Governing balance laws

This section shows the derivation of the governing balance laws

B.3.1. Balance of forces via the principle of virtual power

The principle of virtual power is explained in Appendix C and will be used to derive the remaining balance laws. The derivation starts by adding all the virtual velocities to a generalized virtual velocity list shown below:

$$\mathcal{V} = \left(\tilde{\boldsymbol{y}}, \tilde{\boldsymbol{F}}^e, \tilde{\xi}, \tilde{\nabla\xi}\right) \tag{B.49}$$

The virtual velocities are kinematically constrained by the relation obtained in Equation B.48 and must be satisfied in this approach.

$$\nabla_{\boldsymbol{x}} \tilde{\boldsymbol{y}} \boldsymbol{F}^{-1} = \tilde{\boldsymbol{F}}^e \boldsymbol{F}^{e-1} + \boldsymbol{F}^e \left(\tilde{\xi}\boldsymbol{N}^r\right) \boldsymbol{F}^{e-1} \tag{B.50}$$

The internal and external power for any part $\mathcal{R}$ of the reference body $\mathcal{B}$ are formulated to define how forces contribute to power expenditure on $\mathcal{R}$.

$$\begin{aligned} \mathcal{W}\left(\mathcal{R}, \mathcal{V}\right) &= \int_{\partial\mathcal{R}} \boldsymbol{s}\left(\boldsymbol{n}\right) \cdot \tilde{\boldsymbol{y}}\, dA_x + \int_{\mathcal{R}} \boldsymbol{f} \cdot \tilde{\boldsymbol{y}}\, dV_x + \int_{\partial\mathcal{R}} \eta\tilde{\xi}\, dA_x \\ \mathcal{I}\left(\mathcal{R}, \mathcal{V}\right) &= \int_{\mathcal{R}} \boldsymbol{H}^e \cdot \tilde{\boldsymbol{F}}^e + E\tilde{\xi} + \boldsymbol{g} \cdot \tilde{\nabla\xi}\, dV_x \end{aligned} \tag{B.51}$$

Here, $\boldsymbol{H}^e$ and $\boldsymbol{s}(\boldsymbol{n})$ represent the macroscopic force system conjugates, while E, $\boldsymbol{g}$, and η are the microscopic force system conjugates defined for the kinematic variables.

The principle of virtual power consists of 2 basic requirements:

1. Virtual power balance, so $\mathcal{W}(\mathcal{R}, \mathcal{V}) = \mathcal{I}(\mathcal{R}, \mathcal{V})$ for all generalized virtual velocities
2. Frame-indifference, so $\mathcal{W}(\mathcal{R}, \mathcal{V})$ is invariant under all frame changes

The virtual power balance becomes the following expression, considering the requirements shown above:

$$\begin{gathered}\mathcal{W}(\mathcal{R}, \mathcal{V}) = \mathcal{I}(\mathcal{R}, \mathcal{V}) \\ \int_{\partial\mathcal{R}} \boldsymbol{s}(\boldsymbol{n}) \cdot \tilde{\boldsymbol{y}}\, dA_x + \int_{\mathcal{R}} \boldsymbol{f} \cdot \tilde{\boldsymbol{y}}\, dV_x + \int_{\partial\mathcal{R}} \eta\tilde{\xi}\, dA_x = \int_{\mathcal{R}} \boldsymbol{H}^e \cdot \tilde{\boldsymbol{F}}^e + E\tilde{\xi} + \boldsymbol{g} \cdot \nabla\tilde{\xi}\, dV_x\end{gathered} \tag{B.52}$$

First, the macroscopic force balance is determined. The virtual velocities can be chosen arbitrarily as long as the kinematic constraint is met. The macroscopic force balance is obtained by setting all microscopic virtual velocities to zero ($\tilde{\eta} = 0$, $\nabla\tilde{\eta} = 0$). The kinematic constraint becomes the following expression:

$$\begin{aligned}\nabla_{\boldsymbol{x}}\tilde{\boldsymbol{y}}\boldsymbol{F}^{-1} &= \tilde{\boldsymbol{F}}^e\boldsymbol{F}^{e-1} + \boldsymbol{F}^e\left(\tilde{\xi}\boldsymbol{N}^r\right)\boldsymbol{F}^{e-1} \\ \nabla_{\boldsymbol{x}}\tilde{\boldsymbol{y}}\boldsymbol{F}^{-1} &= \tilde{\boldsymbol{F}}^e\boldsymbol{F}^{e-1} \\ \tilde{\boldsymbol{F}}^e &= \nabla_{\boldsymbol{x}}\tilde{\boldsymbol{y}}\boldsymbol{F}^{-1}\boldsymbol{F}^e\end{aligned} \tag{B.53}$$

The virtual power balance can be simplified by applying the defined virtual velocities and substituting the kinematic constraints (Equation B.53):

$$\begin{aligned}\int_{\partial\mathcal{R}} \boldsymbol{s}(\boldsymbol{n}) \cdot \tilde{\boldsymbol{y}}\, dA_x + \int_{\mathcal{R}} \boldsymbol{f} \cdot \tilde{\boldsymbol{y}}\, dV_x + \int_{\partial\mathcal{R}} \eta\tilde{\xi}\, dA_x &= \int_{\mathcal{R}} \boldsymbol{H}^e \cdot \tilde{\boldsymbol{F}}^e + E\tilde{\xi} + \boldsymbol{g} \cdot \nabla\tilde{\xi}\, dV_x \\ \int_{\partial\mathcal{R}} \boldsymbol{s}(\boldsymbol{n}) \cdot \tilde{\boldsymbol{y}}\, dA_x + \int_{\mathcal{R}} \boldsymbol{f} \cdot \tilde{\boldsymbol{y}}\, dV_x &= \int_{\mathcal{R}} \boldsymbol{H}^e \cdot \nabla_{\boldsymbol{x}}\tilde{\boldsymbol{y}}\boldsymbol{F}^{-1}\boldsymbol{F}^e\, dV_x\end{aligned} \tag{B.54}$$

The decomposition of the deformation gradient into the mechanical and chemical parts (Equation B.28) is utilized to rewrite the power balance further. The mechanical part of the deformation gradient is assumed to be equal to the elastic deformation gradient and is substituted into Equation B.54.

$$\begin{aligned}\int_{\partial\mathcal{R}} \boldsymbol{s}(\boldsymbol{n}) \cdot \tilde{\boldsymbol{y}}\, dA_x + \int_{\mathcal{R}} \boldsymbol{f} \cdot \tilde{\boldsymbol{y}}\, dV_x &= \int_{\mathcal{R}} \boldsymbol{H}^e \cdot \nabla_{\boldsymbol{x}}\tilde{\boldsymbol{y}}\boldsymbol{F}^{-1}\boldsymbol{F}^e\, dV_x \\ &= \int_{\mathcal{R}} \boldsymbol{H}^e \cdot \nabla_{\boldsymbol{x}}\tilde{\boldsymbol{y}}\left(\boldsymbol{F}^e\boldsymbol{F}^c\right)^{-1}\boldsymbol{F}^e\, dV_x \\ &= \int_{\mathcal{R}} \boldsymbol{H}^e \cdot \nabla_{\boldsymbol{x}}\tilde{\boldsymbol{y}}\boldsymbol{F}^{c-1}\boldsymbol{F}^{e-1}\boldsymbol{F}^e\, dV_x \\ &= \int_{\mathcal{R}} \boldsymbol{H}^e\boldsymbol{F}^{c-T} \cdot \nabla_{\boldsymbol{x}}\tilde{\boldsymbol{y}}\, dV_x\end{aligned} \tag{B.55}$$

The Piola stress tensor is defined in the following way:

$$\boldsymbol{P} = \boldsymbol{H}^e\boldsymbol{F}^{c-T} \tag{B.56}$$

The Piola stress tensor can be substituted into the power balance:

$$\begin{aligned}\int_{\partial\mathcal{R}} \boldsymbol{s}(\boldsymbol{n}) \cdot \tilde{\boldsymbol{y}}\, dA_x + \int_{\mathcal{R}} \boldsymbol{f} \cdot \tilde{\boldsymbol{y}}\, dV_x &= \int_{\mathcal{R}} \boldsymbol{H}^e\boldsymbol{F}^{c-T} \cdot \nabla_{\boldsymbol{x}}\tilde{\boldsymbol{y}}\, dV_x \\ &= \int_{\mathcal{R}} \boldsymbol{P} \cdot \nabla_{\boldsymbol{x}}\tilde{\boldsymbol{y}}\, dV_x\end{aligned} \tag{B.57}$$

The right-hand side is rewritten using the following relation:

$$\begin{aligned}\operatorname{div}\left(\boldsymbol{A}^T\boldsymbol{u}\right) &= \boldsymbol{A} \cdot \nabla\boldsymbol{u} + \operatorname{div}(\boldsymbol{A}) \cdot \boldsymbol{u} \\ \boldsymbol{A} \cdot \nabla\boldsymbol{u} &= \operatorname{div}\left(\boldsymbol{A}^T\boldsymbol{u}\right) - \operatorname{div}(\boldsymbol{A}) \cdot \boldsymbol{u}\end{aligned} \tag{B.58}$$

The relation shown in Equation B.58 can be applied on the right-hand side of the power balance:

$$\int_{\mathcal{R}} \boldsymbol{P} \cdot \nabla_{\boldsymbol{x}}\tilde{\boldsymbol{y}}\, dV_x = \int_{\mathcal{R}} \operatorname{div}\left(\boldsymbol{P}^T\tilde{\boldsymbol{y}}\right) dV_x - \int_{\mathcal{R}} \operatorname{div}(\boldsymbol{P}) \cdot \tilde{\boldsymbol{y}}\, dV_x \tag{B.59}$$

The divergence therm for a vector is used to rewrite the expression further:

$$\begin{aligned}\int_{\mathcal{R}} \operatorname{div}\left(\boldsymbol{P}^T\tilde{\boldsymbol{y}}\right)\, dV_x - \int_{\mathcal{R}} \operatorname{div}(\boldsymbol{P})\cdot\tilde{\boldsymbol{y}}\, dV_x &= \int_{\partial\mathcal{R}} \boldsymbol{P}^T\tilde{\boldsymbol{y}}\cdot\boldsymbol{n}\, dA_x - \int_{\mathcal{R}} \operatorname{div}(\boldsymbol{P})\cdot\tilde{\boldsymbol{y}}\, dV_x \\ &= \int_{\partial\mathcal{R}} \boldsymbol{P}\boldsymbol{n}\cdot\tilde{\boldsymbol{y}}\, dA_x - \int_{\mathcal{R}} \operatorname{div}(\boldsymbol{P})\cdot\tilde{\boldsymbol{y}}\, dV_x\end{aligned} \tag{B.60}$$

The right-hand side (Equation B.60) can be substituted back into the virtual power balance (Equation B.57), and the expression can be rewritten.

$$\begin{aligned}\int_{\partial\mathcal{R}} \boldsymbol{s}(\boldsymbol{n})\cdot\tilde{\boldsymbol{y}}\, dA_x + \int_{\mathcal{R}} \boldsymbol{f}\cdot\tilde{\boldsymbol{y}}\, dV_x &= \int_{\mathcal{R}} \boldsymbol{P}\cdot\nabla_{\boldsymbol{x}}\tilde{\boldsymbol{y}}\, dV_x \\ \int_{\partial\mathcal{R}} \boldsymbol{s}(\boldsymbol{n})\cdot\tilde{\boldsymbol{y}}\, dA_x + \int_{\mathcal{R}} \boldsymbol{f}\cdot\tilde{\boldsymbol{y}}\, dV_x &= \int_{\partial\mathcal{R}} \boldsymbol{P}\boldsymbol{n}\cdot\tilde{\boldsymbol{y}}\, dA_x - \int_{\mathcal{R}} \operatorname{div}(\boldsymbol{P})\cdot\tilde{\boldsymbol{y}}\, dV_x \\ \int_{\partial\mathcal{R}} (\boldsymbol{s}(\boldsymbol{n}) - \boldsymbol{P}\boldsymbol{n})\cdot\tilde{\boldsymbol{y}}\, dA_x + \int_{\mathcal{R}} (\operatorname{div}(\boldsymbol{P}) + \boldsymbol{f})\cdot\tilde{\boldsymbol{y}}\, dV_x &= 0\end{aligned} \tag{B.61}$$

The fundamental lemma of the calculus of variations (discussed in more detail in the derivation shown in Appendix C) is utilized to derive the macroscopic force balance and the traction boundary condition presented below:

$$\begin{aligned}\operatorname{div}(\boldsymbol{P}) + \boldsymbol{f} &= \boldsymbol{0} \\ \boldsymbol{s}(\boldsymbol{n}) - \boldsymbol{P}\boldsymbol{n} &= \boldsymbol{0}\end{aligned} \tag{B.62}$$

The Piola stress tensor $\boldsymbol{P}$ is related to the Cauchy stress tensor $\boldsymbol{T}$ by the following relation:

$$\boldsymbol{P} = J\boldsymbol{T}\boldsymbol{F}^{-T} \tag{B.63}$$

A relation between the Piola stress tensor and the stress $\boldsymbol{H}^e$ was previously defined in Equation B.56, which is then substituted into Equation B.97 to obtain the expression for $\boldsymbol{H}^e$.

$$\begin{aligned}\boldsymbol{P} &= J\boldsymbol{T}\boldsymbol{F}^{-T} \\ \boldsymbol{H}^e\boldsymbol{F}^{c-T} &= J\boldsymbol{T}\boldsymbol{F}^{-T} \\ \boldsymbol{H}^e &= J\boldsymbol{T}\boldsymbol{F}^{-T}\boldsymbol{F}^{cT} \\ \boldsymbol{H}^e &= J\boldsymbol{T}\left(\boldsymbol{F}^c\boldsymbol{F}^{-1}\right)^T\end{aligned} \tag{B.64}$$

The decomposition of the deformation gradient is used again to simplify Equation B.64.

$$\begin{aligned}\boldsymbol{H}^e &= J\boldsymbol{T}\left(\boldsymbol{F}^c\boldsymbol{F}^{-1}\right)^T \\ &= J\boldsymbol{T}\left(\boldsymbol{F}^c\left(\boldsymbol{F}^e\boldsymbol{F}^c\right)^{-1}\right)^T \\ &= J\boldsymbol{T}\left(\boldsymbol{F}^c\boldsymbol{F}^{c-1}\boldsymbol{F}^{e-1}\right)^T \\ &= J\boldsymbol{T}\boldsymbol{F}^{e-T}\end{aligned} \tag{B.65}$$

The second force balance obtained is the microforce balance. This is achieved by setting the macro velocity $\tilde{\boldsymbol{y}}$ to zero, which has the following effect on the kinematic constraint:

$$\begin{aligned}\nabla_{\boldsymbol{x}}\tilde{\boldsymbol{y}}\boldsymbol{F}^{-1} &= \tilde{\boldsymbol{F}}^e\boldsymbol{F}^{e-1} + \boldsymbol{F}^e\left(\tilde{\xi}\boldsymbol{N}^r\right)\boldsymbol{F}^{e-1} \\ \tilde{\boldsymbol{F}}^e\boldsymbol{F}^{e-1} &= -\boldsymbol{F}^e\left(\tilde{\xi}\boldsymbol{N}^r\right)\boldsymbol{F}^{e-1} \\ \tilde{\boldsymbol{F}}^e &= -\boldsymbol{F}^e\left(\tilde{\xi}\boldsymbol{N}^r\right)\end{aligned} \tag{B.66}$$

The scalar tensor product of $\boldsymbol{H}^e$ (as shown in Equation B.65) and $\tilde{\boldsymbol{F}}^e$ is computed.

$$\begin{aligned}\boldsymbol{H}^e\cdot\tilde{\boldsymbol{F}}^e &= J\boldsymbol{T}\boldsymbol{F}^{e-T}\cdot -\boldsymbol{F}^e\left(\tilde{\xi}\boldsymbol{N}^r\right) \\ &= \left(-J\boldsymbol{F}^{eT}\boldsymbol{T}\boldsymbol{F}^{e-T}\cdot\boldsymbol{N}^r\right)\tilde{\xi}\end{aligned} \tag{B.67}$$

The Jacobian is decomposed into the chemical and mechanical parts, as shown in Equation B.31, considering that only elastic deformation is present, so the validity of $J^m = J^e$ holds.

$$\begin{aligned} \boldsymbol{H}^e \cdot \tilde{\boldsymbol{F}}^e &= \left(-J\boldsymbol{F}^{eT}\boldsymbol{T}\boldsymbol{F}^{e-T} \cdot \boldsymbol{N}^r\right)\tilde{\xi} \\ &= \left(-J^c J^e \boldsymbol{F}^{eT}\boldsymbol{T}\boldsymbol{F}^{e-T} \cdot \boldsymbol{N}^r\right)\tilde{\xi} \end{aligned} \tag{B.68}$$

A new stress called the Mandel stress is introduced, and its definition is provided below:

$$\boldsymbol{M}^e = J^e \boldsymbol{F}^{eT}\boldsymbol{T}\boldsymbol{F}^{e-T} \tag{B.69}$$

The Mandel stress is substituted in Equation B.70:

$$\begin{aligned} \boldsymbol{H}^e \cdot \tilde{\boldsymbol{F}}^e &= \left(-J^c J^e \boldsymbol{F}^{eT}\boldsymbol{T}\boldsymbol{F}^{e-T} \cdot \boldsymbol{N}^r\right)\tilde{\xi} \\ &= \left(-J^c \boldsymbol{M}^e \cdot \boldsymbol{N}^r\right)\tilde{\xi} \end{aligned} \tag{B.70}$$

The new virtual velocity field is substituted into the original virtual power balance:

$$\begin{aligned} \int_{\partial\mathcal{R}} \boldsymbol{s}\,(\boldsymbol{n}) \cdot \tilde{\boldsymbol{y}}\, dA_x + \int_{\mathcal{R}} \boldsymbol{f} \cdot \tilde{\boldsymbol{y}}\, dV_x + \int_{\partial\mathcal{R}} \eta\tilde{\xi}\, dA_x &= \int_{\mathcal{R}} \boldsymbol{H}^e \cdot \tilde{\boldsymbol{F}}^e + E\tilde{\xi} + \boldsymbol{g} \cdot \nabla\tilde{\xi}\, dV_x \\ \int_{\partial\mathcal{R}} \eta\tilde{\xi}\, dA_x &= \int_{\mathcal{R}} \left(-J^c \boldsymbol{M}^e \cdot \boldsymbol{N}^r\right)\tilde{\xi} + E\tilde{\xi} + \boldsymbol{g} \cdot \nabla\tilde{\xi}\, dV_x \end{aligned} \tag{B.71}$$

A new relation is introduced, allowing for the rewriting of Equation B.71.

$$\begin{aligned} \operatorname{div}(\alpha\boldsymbol{u}) &= \boldsymbol{u} \cdot \nabla\alpha + \alpha \operatorname{div}(\boldsymbol{u}) \\ \boldsymbol{u} \cdot \nabla\alpha &= \operatorname{div}(\alpha\boldsymbol{u}) - \alpha \operatorname{div}(\boldsymbol{u}) \end{aligned} \tag{B.72}$$

The term $\boldsymbol{g} \cdot \nabla\tilde{\xi}$ is rewritten using Equation B.72.

$$\boldsymbol{g} \cdot \nabla\tilde{\xi} = \operatorname{div}\left(\tilde{\xi}\boldsymbol{g}\right) - \tilde{\xi} \operatorname{div}(\boldsymbol{g}) \tag{B.73}$$

Equation B.73 is substituted in the virtual power balance of Equation B.71:

$$\begin{aligned} \int_{\partial\mathcal{R}} \eta\tilde{\xi}\, dA_x &= \int_{\mathcal{R}} \left(-J^c \boldsymbol{M}^e \cdot \boldsymbol{N}^r\right)\tilde{\xi} + E\tilde{\xi} + \boldsymbol{g} \cdot \nabla\tilde{\xi}\, dV_x \\ &= \int_{\mathcal{R}} \left(-J^c \boldsymbol{M}^e \cdot \boldsymbol{N}^r\right)\tilde{\xi} + E\tilde{\xi} - \tilde{\xi} \operatorname{div}(\boldsymbol{g})\, dV_x + \int_{\mathcal{R}} \operatorname{div}\left(\tilde{\xi}\boldsymbol{g}\right)\, dV_x \end{aligned} \tag{B.74}$$

The second term of the right-hand side of Equation B.74 is rewritten using the divergence theorem of a vector field.

$$\begin{aligned} \int_{\partial\mathcal{R}} \eta\tilde{\xi}\, dA_x &= \int_{\mathcal{R}} \left(-J^c \boldsymbol{M}^e \cdot \boldsymbol{N}^r\right)\tilde{\xi} + E\tilde{\xi} - \tilde{\xi} \operatorname{div}(\boldsymbol{g})\, dV_x + \int_{\mathcal{R}} \operatorname{div}\left(\tilde{\xi}\boldsymbol{g}\right)\, dV_x \\ &= \int_{\mathcal{R}} \left(-J^c \boldsymbol{M}^e \cdot \boldsymbol{N}^r\right)\tilde{\xi} + E\tilde{\xi} - \tilde{\xi} \operatorname{div}(\boldsymbol{g})\, dV_x + \int_{\partial\mathcal{R}} \tilde{\xi}\boldsymbol{g} \cdot \boldsymbol{n}\, dA_x \end{aligned} \tag{B.75}$$

The surface and volume integrals are grouped together.

$$\begin{aligned} &\int_{\partial\mathcal{R}} \eta\tilde{\xi}\, dA_x = \int_{\mathcal{R}} \left(-J^c \boldsymbol{M}^e \cdot \boldsymbol{N}^r\right)\tilde{\xi} + E\tilde{\xi} - \tilde{\xi} \operatorname{div}(\boldsymbol{g})\, dV_x + \int_{\partial\mathcal{R}} \tilde{\xi}\boldsymbol{g} \cdot \boldsymbol{n}\, dA_x \\ &\int_{\partial\mathcal{R}} (\eta - \boldsymbol{g} \cdot \boldsymbol{n})\,\tilde{\xi}\, dA_x + \int_{\mathcal{R}} \left(J^c \boldsymbol{M}^e \cdot \boldsymbol{N}^r - E + \operatorname{div}(\boldsymbol{g})\right)\tilde{\xi}\, dV_x = 0 \end{aligned} \tag{B.76}$$

The fundamental lemma of the calculus of variations is utilized again to derive the microforce balance and its corresponding boundary condition.

$$\begin{aligned} E - J^c \boldsymbol{M}^e \cdot \boldsymbol{N}^r - \operatorname{div}(\boldsymbol{g}) &= 0 \\ \eta - \boldsymbol{g} \cdot \boldsymbol{n} &= 0 \end{aligned} \tag{B.77}$$

B.3.2. Balance of energy, entropy imbalance, and free energy imbalance

The free energy imbalance is defined below:

$$\mathcal{D} = \mathcal{W} - \frac{d}{dt}(\mathcal{G} + \mathcal{K}) + \Theta \tag{B.78}$$

Where $\mathcal{D}$ is the dissipation, $\mathcal{W}$ is the external power, $\mathcal{G}$ is the free energy, $\mathcal{K}$ is the kinetic energy, and Θ is the thermal production of energy. For an isothermal process, the thermal production of energy is negligible, so Θ can be removed from the free energy imbalance.

$$\mathcal{D} = \mathcal{W} - \frac{d}{dt}(\mathcal{G} + \mathcal{K}) \tag{B.79}$$

The kinetic energy becomes negligible when it is assumed that the inertial effects are neglected. The free energy imbalance simplifies to the following expression:

$$\begin{aligned} \mathcal{D} &= \mathcal{W} - \frac{d}{dt}(\mathcal{G} + \mathcal{K}) \geq 0 \\ &= \mathcal{W} - \dot{\mathcal{G}} - \dot{\mathcal{K}} \geq 0 \\ &= \mathcal{W} - \dot{\mathcal{G}} \geq 0 \end{aligned} \tag{B.80}$$

The free energy in the referential configuration is defined below:

$$\mathcal{G} = \int_{\mathcal{R}} \psi_x \, dV_x \tag{B.81}$$

Equation B.81 can be substituted into Equation B.80:

$$\begin{aligned} \mathcal{D} &= \mathcal{W} - \dot{\mathcal{G}} \geq 0 \\ \mathcal{D} &= \mathcal{W} - \int_{\mathcal{R}} \dot{\psi}_x \, dV_x \geq 0 \\ \int_{\mathcal{R}} \dot{\psi}_x \, dV_x &\leq \mathcal{W} \end{aligned} \tag{B.82}$$

The energy carried by species transport is not yet considered in Equation B.82. Therefore, $\mathcal{T}$ is added to the expressions, representing the energy flow due to species transport, and is defined as follows:

$$\mathcal{T} = -\int_{\partial\mathcal{R}} \mu \boldsymbol{h} \cdot \boldsymbol{n} \, dA_x \tag{B.83}$$

The final part to consider is the power expended due to the electromagnetic energy flux $\mathcal{H}$, which is given below:

$$\mathcal{H} = -\int_{\mathcal{R}} \phi \boldsymbol{i} \cdot \boldsymbol{n} \, dA_x - \int_{\partial\mathcal{R}} \phi \dot{\boldsymbol{d}} \cdot \boldsymbol{n} \, dA_x \tag{B.84}$$

The definition of the current density (Equation B.18) can be substituted into Equation B.84

$$\begin{aligned} \mathcal{H} &= -\int_{\mathcal{R}} \phi \boldsymbol{i} \cdot \boldsymbol{n} \, dA_x - \int_{\partial\mathcal{R}} \phi \dot{\boldsymbol{d}} \cdot \boldsymbol{n} \, dA_x \\ &= -\int_{\mathcal{R}} F\phi \boldsymbol{h} \cdot \boldsymbol{n} \, dA_x - \int_{\partial\mathcal{R}} \phi \dot{\boldsymbol{d}} \cdot \boldsymbol{n} \, dA_x \end{aligned} \tag{B.85}$$

The final version of the free energy imbalance is obtained by adding the energy flow due to species transport $\mathcal{T}$ (see Equation B.83) and the electromagnetic energy flux $\mathcal{H}$ (see Equation B.85):

$$\begin{aligned} &\int_{\mathcal{R}} \dot{\psi}_x \, dV_x \leq \mathcal{W} + \mathcal{T} + \mathcal{H} \\ &\int_{\mathcal{R}} \dot{\psi}_x \, dV_x \leq \mathcal{W} - \int_{\partial\mathcal{R}} \mu \boldsymbol{h} \cdot \boldsymbol{n} \, dA_x - \int_{\mathcal{R}} F\phi \boldsymbol{h} \cdot \boldsymbol{n} \, dA_x - \int_{\partial\mathcal{R}} \phi \dot{\boldsymbol{d}} \cdot \boldsymbol{n} \, dA_x \\ &\int_{\mathcal{R}} \dot{\psi}_x \, dV_x \leq \mathcal{W} - \int_{\partial\mathcal{R}} \left(\mu + F\phi\right) \boldsymbol{h} \cdot \boldsymbol{n} \, dA_x - \int_{\partial\mathcal{R}} \phi \dot{\boldsymbol{d}} \cdot \boldsymbol{n} \, dA_x \end{aligned} \tag{B.86}$$

The electropotential and the chemical potential are combined into the electrochemical potential, which is defined below:

$$\mu^e = \mu + F\phi \tag{B.87}$$

Equation B.87 is substituted into Equation B.86:

$$\begin{aligned} \int_{\mathcal{R}} \dot{\psi}_x \, dV_x &\leq \mathcal{W} - \int_{\partial\mathcal{R}} \left(\mu + F\phi\right) \boldsymbol{h} \cdot \boldsymbol{n} \, dA_x - \int_{\partial\mathcal{R}} \phi \dot{\boldsymbol{d}} \cdot \boldsymbol{n} \, dA_x \\ \int_{\mathcal{R}} \dot{\psi}_x \, dV_x &\leq \mathcal{W} - \int_{\partial\mathcal{R}} \mu^e \boldsymbol{h} \cdot \boldsymbol{n} \, dA_x - \int_{\partial\mathcal{R}} \phi \dot{\boldsymbol{d}} \cdot \boldsymbol{n} \, dA_x \end{aligned} \tag{B.88}$$

The second Piola stress tensor $\boldsymbol{S}^e$ is now also defined:

$$\boldsymbol{S}^e = \boldsymbol{F}^{e-1}\boldsymbol{P} \tag{B.89}$$

The relation between the Piola stress tensor and the Cauchy stress tensor (Equation B.97) is substituted in Equation B.89:

$$\begin{aligned} \boldsymbol{S}^e &= \boldsymbol{F}^{e-1}\boldsymbol{P} \\ &= J^e \boldsymbol{F}^{e-1}\boldsymbol{T}\boldsymbol{F}^{e-T} \end{aligned} \tag{B.90}$$

Equation B.90 is further rewritten by introducing the identity tensor as $\boldsymbol{F}^{e-T}\boldsymbol{F}^{eT}$ into this expression:

$$\begin{aligned} \boldsymbol{S}^e &= J^e \boldsymbol{F}^{e-1}\boldsymbol{T}\boldsymbol{F}^{e-T} \\ &= J^e \boldsymbol{F}^{e-1}\boldsymbol{F}^{e-T}\boldsymbol{F}^{eT}\boldsymbol{T}\boldsymbol{F}^{e-T} \\ &= \left(\boldsymbol{F}^{eT}\boldsymbol{F}^e\right)^{-1} J^e \boldsymbol{F}^{eT}\boldsymbol{T}\boldsymbol{F}^{e-T} \end{aligned} \tag{B.91}$$

The expressions for the right Cauchy-Green strain tensor (Equation B.34) and the Mandel stress (Equation B.69) are substituted into the expression for the second Piola stress tensor (Equation B.92):

$$\begin{aligned} \boldsymbol{S}^e &= \left(\boldsymbol{F}^{eT}\boldsymbol{F}^e\right)^{-1} J^e \boldsymbol{F}^{eT}\boldsymbol{T}\boldsymbol{F}^{e-T} \\ &= \boldsymbol{C}^{e-1}\boldsymbol{M}^e \end{aligned} \tag{B.92}$$

A closer look is taken to the stress power $\boldsymbol{H}^e \cdot \dot{\boldsymbol{F}}^e$, which is part of the internal power. Previously, the stress $\boldsymbol{H}^e$ is related to the Cauchy stress tensor $\boldsymbol{T}$ by Equation B.65. This expression is used to define the stress power:

$$\begin{aligned} \boldsymbol{H}^e \cdot \dot{\boldsymbol{F}}^e &= J\boldsymbol{T}\boldsymbol{F}^{e-T} \cdot \dot{\boldsymbol{F}}^e \\ &= J\boldsymbol{T} \cdot \dot{\boldsymbol{F}}^e \boldsymbol{F}^{e-1} \end{aligned} \tag{B.93}$$

The relation between the deformation and velocity gradient (Equation B.27) is substituted into Equation B.93:

$$\begin{aligned} \boldsymbol{H}^e \cdot \dot{\boldsymbol{F}}^e &= J\boldsymbol{T} \cdot \dot{\boldsymbol{F}}^e \boldsymbol{F}^{e-1} \\ &= J\boldsymbol{T} \cdot \boldsymbol{L}^e \end{aligned} \tag{B.94}$$

Since the Cauchy stress tensor is symmetric, only the symmetric part of the velocity gradient is used in the scalar-tensor product of Equation B.94.

$$\begin{aligned} \boldsymbol{H}^e \cdot \dot{\boldsymbol{F}}^e &= J\boldsymbol{T} \cdot \boldsymbol{L}^e \\ &= \frac{1}{2} J\boldsymbol{T} \cdot \left(\boldsymbol{L}^e + \boldsymbol{L}^{eT}\right) \end{aligned} \tag{B.95}$$

The relation between the deformation and velocity gradient is once again employed for further rewriting.

$$\begin{aligned}
\boldsymbol{H}^e \cdot \dot{\boldsymbol{F}}^e &= \frac{1}{2} J \boldsymbol{T} \cdot \left(\boldsymbol{L}^e + \boldsymbol{L}^{eT} \right) \\
&= \frac{1}{2} J \boldsymbol{T} \cdot \left(\dot{\boldsymbol{F}}^e \boldsymbol{F}^{e-1} + \left(\dot{\boldsymbol{F}}^e \boldsymbol{F}^{e-1} \right)^T \right) \\
&= \frac{1}{2} J \boldsymbol{T} \cdot \left(\dot{\boldsymbol{F}}^e \boldsymbol{F}^{e-1} + \boldsymbol{F}^{e-T} \dot{\boldsymbol{F}}^{eT} \right) \\
&= \frac{1}{2} J \boldsymbol{T} \cdot \left(\boldsymbol{F}^{e-T} \boldsymbol{F}^{eT} \dot{\boldsymbol{F}}^e \boldsymbol{F}^{e-1} + \boldsymbol{F}^{e-T} \dot{\boldsymbol{F}}^{eT} \boldsymbol{F}^e \boldsymbol{F}^{e-1} \right) \\
&= \frac{1}{2} J \boldsymbol{T} \cdot \boldsymbol{F}^{e-T} \left(\boldsymbol{F}^{eT} \dot{\boldsymbol{F}}^e + \dot{\boldsymbol{F}}^{eT} \boldsymbol{F}^e \right) \boldsymbol{F}^{e-1} \\
&= \frac{1}{2} J \boldsymbol{F}^{e-1} \boldsymbol{T} \boldsymbol{F}^{e-T} \cdot \left(\boldsymbol{F}^{eT} \dot{\boldsymbol{F}}^e + \dot{\boldsymbol{F}}^{eT} \boldsymbol{F}^e \right)
\end{aligned} \tag{B.96}$$

Equation B.96 is further rewritten by reconsidering the implications of Equation B.97 in a different way.

$$\boldsymbol{T} = \frac{1}{J} \boldsymbol{P} \boldsymbol{F}^T \tag{B.97}$$

Additionally, the time derivative of the right Cauchy Green strain tensor is defined:

$$\begin{aligned}
\boldsymbol{C} &= \boldsymbol{F}^T \boldsymbol{F} \\
\dot{\boldsymbol{C}} &= \dot{\boldsymbol{F}}^T \boldsymbol{F} + \boldsymbol{F}^T \dot{\boldsymbol{F}}
\end{aligned} \tag{B.98}$$

Equation B.97 and Equation B.98 are substituted into Equation B.96 considering that Equation B.98 is substituted as the elastic deformation gradient, ensuring that only the elastic part of the Jacobian is added.

$$\begin{aligned}
\boldsymbol{H}^e \cdot \dot{\boldsymbol{F}}^e &= \frac{1}{2} J \boldsymbol{F}^{e-1} \boldsymbol{T} \boldsymbol{F}^{e-T} \cdot \left(\boldsymbol{F}^{eT} \dot{\boldsymbol{F}}^e + \dot{\boldsymbol{F}}^{eT} \boldsymbol{F}^e \right) \\
&= \frac{1}{2} J \boldsymbol{F}^{e-1} \frac{1}{J^e} \boldsymbol{P} \boldsymbol{F}^{eT} \boldsymbol{F}^{e-T} \cdot \dot{\boldsymbol{C}}^e \\
&= \frac{1}{2} J \frac{1}{J^e} \boldsymbol{F}^{e-1} \boldsymbol{P} \cdot \dot{\boldsymbol{C}}^e
\end{aligned} \tag{B.99}$$

The final expression for $\boldsymbol{H}^e \cdot \dot{\boldsymbol{F}}^e$ is obtained by substituting the second Piola stress tensor (Equation B.89) and the mechanical/chemical decomposition of the Jacobian (Equation B.31) into Equation B.99.

$$\begin{aligned}
\boldsymbol{H}^e \cdot \dot{\boldsymbol{F}}^e &= \frac{1}{2} J \frac{1}{J^e} \boldsymbol{F}^{e-1} \boldsymbol{P} \cdot \dot{\boldsymbol{C}}^e \\
&= \frac{1}{2} J^e J^c \frac{1}{J^e} \boldsymbol{S}^e \cdot \dot{\boldsymbol{C}}^e \\
&= \frac{1}{2} J^c \boldsymbol{S}^e \cdot \dot{\boldsymbol{C}}^e
\end{aligned} \tag{B.100}$$

The next step involves revisiting the internal and external energy, previously defined with virtual velocities in Equation B.51. Now, the internal and external energy are redefined using the actual velocity fields:

$$\begin{aligned}
\mathcal{W}(\mathcal{R}, \mathcal{V}) &= \int_{\partial \mathcal{R}} \boldsymbol{s}(\boldsymbol{n}) \cdot \dot{\boldsymbol{y}} \, dA_x + \int_{\mathcal{R}} \boldsymbol{f} \cdot \dot{\boldsymbol{y}} \, dV_x + \int_{\partial \mathcal{R}} \eta \dot{\xi} \, dA_x \\
\mathcal{I}(\mathcal{R}, \mathcal{V}) &= \int_{\mathcal{R}} \boldsymbol{H}^e \cdot \dot{\boldsymbol{F}}^e + E \dot{\xi} + \boldsymbol{g} \cdot \nabla \dot{\xi} \, dV_x
\end{aligned} \tag{B.101}$$

The free energy imbalance (Equation B.88) involves the external power. However, the internal energy can be utilized instead due to the energy balance $\mathcal{W} = \mathcal{I}$. Since the internal energy comprises only volume integrals, it is chosen to substitute the internal energy into the free energy imbalance.

$$\begin{aligned}
\int_{\mathcal{R}} \dot{\psi}_x \, dV_x &\leq \mathcal{W} - \int_{\partial \mathcal{R}} \mu^e \boldsymbol{h} \cdot \boldsymbol{n} \, dA_x - \int_{\partial \mathcal{R}} \phi \dot{\boldsymbol{d}} \cdot \boldsymbol{n} \, dA_x \\
\int_{\mathcal{R}} \dot{\psi}_x \, dV_x &\leq \int_{\mathcal{R}} \boldsymbol{H}^e \cdot \dot{\boldsymbol{F}}^e + E \dot{\xi} + \boldsymbol{g} \cdot \nabla \dot{\xi} \, dV_x - \int_{\partial \mathcal{R}} \mu^e \boldsymbol{h} \cdot \boldsymbol{n} \, dA_x - \int_{\partial \mathcal{R}} \phi \dot{\boldsymbol{d}} \cdot \boldsymbol{n} \, dA_x
\end{aligned} \tag{B.102}$$

The alternative expression for $\boldsymbol{H}^e \cdot \dot{\boldsymbol{F}}^e$ (Equation B.100) is substituted into the free energy imbalance:

$$\begin{aligned}\int_{\mathcal{R}} \dot{\psi}_x \, dV_x &\leq \int_{\mathcal{R}} \boldsymbol{H}^e \cdot \dot{\boldsymbol{F}}^e + E\dot{\xi} + \boldsymbol{g} \cdot \nabla\dot{\xi} \, dV_x - \int_{\partial\mathcal{R}} \mu^e \boldsymbol{h} \cdot \boldsymbol{n} \, dA_x - \int_{\partial\mathcal{R}} \phi\dot{\boldsymbol{d}} \cdot \boldsymbol{n} \, dA_x \\ \int_{\mathcal{R}} \dot{\psi}_x \, dV_x &\leq \int_{\mathcal{R}} \frac{1}{2} J^c \boldsymbol{S}^e \cdot \dot{\boldsymbol{C}}^e + E\dot{\xi} + \boldsymbol{g} \cdot \nabla\dot{\xi} \, dV_x - \int_{\partial\mathcal{R}} \mu^e \boldsymbol{h} \cdot \boldsymbol{n} \, dA_x - \int_{\partial\mathcal{R}} \phi\dot{\boldsymbol{d}} \cdot \boldsymbol{n} \, dA_x\end{aligned} \tag{B.103}$$

The divergence theorem is utilized to rewrite the boundary terms into volume integrals, beginning with the first boundary term $\mu^e \boldsymbol{h} \cdot \boldsymbol{n}$ and considering the relation used in Equation B.72.

$$\begin{aligned}\int_{\partial\mathcal{R}} \mu^e \boldsymbol{h} \cdot \boldsymbol{n} \, dA_x &= \int_{\mathcal{R}} \operatorname{div}(\mu^e \boldsymbol{h}) \, dV_x \\ &= \int_{\mathcal{R}} \boldsymbol{h}\nabla\mu^e + \mu^e \operatorname{div}(\boldsymbol{h}) \, dV_x\end{aligned} \tag{B.104}$$

The second boundary term is rewritten in the same manner as the first boundary term, utilizing the relation from Equation B.72.

$$\begin{aligned}\int_{\partial\mathcal{R}} \phi\dot{\boldsymbol{d}} \cdot \boldsymbol{n} \, dA_x &= \int_{\mathcal{R}} \operatorname{div}(\phi\dot{\boldsymbol{d}}) \, dV_x \\ &= \int_{\mathcal{R}} \dot{\boldsymbol{d}} \cdot \nabla\phi + \phi \operatorname{div}(\dot{\boldsymbol{d}}) \, dV_x\end{aligned} \tag{B.105}$$

The free energy imbalance incorporates substitutions of Equation B.104 and Equation B.105, allowing all terms to be combined into a single integral.

$$\begin{aligned}&\int_{\mathcal{R}} \dot{\psi}_x \, dV_x \leq \int_{\mathcal{R}} \frac{1}{2} J^c \boldsymbol{S}^e \cdot \dot{\boldsymbol{C}}^e + E\dot{\xi} + \boldsymbol{g} \cdot \nabla\dot{\xi} + \, dV_x - \int_{\partial R} \mu^e \boldsymbol{h} \cdot \boldsymbol{n} \, dA_x - \int_{\partial R} \phi\dot{\boldsymbol{d}} \cdot \boldsymbol{n} \, dA_x \\ &\int_{\mathcal{R}} \dot{\psi}_x \, dV_x \leq \int_{\mathcal{R}} \frac{1}{2} J^c \boldsymbol{S}^e \cdot \dot{\boldsymbol{C}}^e + E\dot{\xi} + \boldsymbol{g} \cdot \nabla\dot{\xi} \, dV_x - \int_{\mathcal{R}} \boldsymbol{h} \cdot \nabla\mu^e + \mu^e \operatorname{div}(\boldsymbol{h}) \, dV_x \\ &- \int_{\mathcal{R}} \dot{\boldsymbol{d}} \cdot \nabla\phi + \phi \operatorname{div}(\boldsymbol{d}) \, dV_x \\ &\int_{\mathcal{R}} \dot{\psi}_x \, dV_x - \int_{\mathcal{R}}^{R} \frac{1}{2} J^c \boldsymbol{S}^e \cdot \dot{\boldsymbol{C}}^e + E\dot{\xi} + \boldsymbol{g} \cdot \nabla\dot{\xi} \, dV_x + \int_{\mathcal{R}} \boldsymbol{h} \cdot \nabla\mu^e + \mu^e \operatorname{div}(\boldsymbol{h}) \, dV_x \\ &+ \int_{\mathcal{R}} \dot{\boldsymbol{d}} \cdot \nabla\phi + \phi \operatorname{div}(\dot{\boldsymbol{d}}) \, dV_x \leq 0 \\ &\int_{\mathcal{R}} \dot{\psi}_x - \frac{1}{2} J^c \boldsymbol{S}^e \cdot \dot{\boldsymbol{C}}^e - E\dot{\xi} - \boldsymbol{g} \cdot \nabla\dot{\xi} + \mu^e \operatorname{div}(\boldsymbol{h}) + \phi \operatorname{div}(\boldsymbol{d}) + \nabla\phi \cdot \boldsymbol{d} + \boldsymbol{h} \cdot \nabla\mu^e \, dV_x \leq 0\end{aligned} \tag{B.106}$$

The first divergence term in Equation B.106 disappears when rewriting the mass balance defined in Equation B.7, which can be expressed as:

$$\begin{aligned}\dot{c} &= -\operatorname{div}(\boldsymbol{h}) - \dot{\xi} \\ \operatorname{div}(\boldsymbol{h}) &= -\dot{c} - \dot{\xi}\end{aligned} \tag{B.107}$$

Equation B.107 is substituted into Equation B.106:

$$\begin{aligned}&\int_{\mathcal{R}} \dot{\psi}_x - \frac{1}{2} J^c \boldsymbol{S}^e \cdot \dot{\boldsymbol{C}}^e - E\dot{\xi} - \boldsymbol{g} \cdot \nabla\dot{\xi} + \mu^e \operatorname{div}(\boldsymbol{h}) + \phi \operatorname{div}(\boldsymbol{d}) + \nabla\phi \cdot \boldsymbol{d} + \boldsymbol{h} \cdot \nabla\mu^e \, dV_x \leq 0 \\ &\int_{\mathcal{R}} \dot{\psi}_x - \frac{1}{2} J^c \boldsymbol{S}^e \cdot \dot{\boldsymbol{C}}^e - E\dot{\xi} - \boldsymbol{g} \cdot \nabla\dot{\xi} + \mu^e \left(-\dot{c} - \dot{\xi}\right) + \phi \operatorname{div}(\boldsymbol{d}) + \nabla\phi \cdot \boldsymbol{d} + \boldsymbol{h} \cdot \nabla\mu^e \, dV_x \leq 0\end{aligned} \tag{B.108}$$

The second divergence term is rewritten by examining the time derivative of the Gauss law (Equa-

tion B.22) component-wise.

$$\begin{aligned}\dot{q} = \frac{\partial}{\partial t}\operatorname{div}(\boldsymbol{d}) &= \frac{\partial}{\partial t}\sum_i \frac{\partial d_i}{\partial x_i} \\ &= \sum_i \frac{\partial}{\partial t}\frac{\partial}{\partial x_i} d_i \\ &= \sum_i \frac{\partial}{\partial x_i}\frac{\partial}{\partial t} d_i \\ &= \sum_i \frac{\partial}{\partial x_i}\dot{d}_i \\ &= \operatorname{div}\left(\dot{\boldsymbol{d}}\right)\end{aligned} \tag{B.109}$$

The time derivative of the net charge q is defined earlier in Equation B.15 and is then substituted into Equation B.109.

$$\begin{aligned}\operatorname{div}\left(\dot{\boldsymbol{d}}\right) =& \dot{q} \\ =& F\dot{c}\end{aligned} \tag{B.110}$$

Equation B.110 is substituted into Equation B.108:

$$\begin{aligned}\int_{\mathcal{R}} \dot{\psi}_x - \frac{1}{2}J^c \boldsymbol{S}^e \cdot \dot{\boldsymbol{C}}^e - E\dot{\xi} - \boldsymbol{g}\cdot\nabla\dot{\xi} + \mu^e\left(-\dot{c} - \dot{\xi}\right) + \phi\operatorname{div}(\boldsymbol{d}) + \nabla\phi\cdot\boldsymbol{d} + \boldsymbol{h}\cdot\nabla\mu^e\, dV_x \leq 0 \\ \int_{\mathcal{R}} \dot{\psi}_x - \frac{1}{2}J^c \boldsymbol{S}^e \cdot \dot{\boldsymbol{C}}^e - E\dot{\xi} - \boldsymbol{g}\cdot\nabla\dot{\xi} - \mu^e\dot{c} - \mu^e\dot{\xi} + F\phi\dot{c} + \nabla\phi\cdot\boldsymbol{d} + \boldsymbol{h}\cdot\nabla\mu^e\, dV_x \leq 0\end{aligned} \tag{B.111}$$

The definition of the electrochemical potential is provided earlier in Equation B.87 and is employed to rewrite the term $\mu^e\dot{c}$ in such a way that the term $F\phi\dot{c}$ cancels out.

$$\begin{aligned}\int_{\mathcal{R}} \dot{\psi}_x - \frac{1}{2}J^c \boldsymbol{S}^e \cdot \dot{\boldsymbol{C}}^e - E\dot{\xi} - \boldsymbol{g}\cdot\nabla\dot{\xi} - \mu^e\dot{c} - \mu^e\dot{\xi} + F\phi\dot{c} + \nabla\phi\cdot\boldsymbol{d} + \boldsymbol{h}\cdot\nabla\mu^e\, dV_x \leq 0 \\ \int_{\mathcal{R}} \dot{\psi}_x - \frac{1}{2}J^c \boldsymbol{S}^e \cdot \dot{\boldsymbol{C}}^e - E\dot{\xi} - \boldsymbol{g}\cdot\nabla\dot{\xi} - \left(\mu + F\phi\right)\dot{c} - \mu^e\dot{\xi} + F\phi\dot{c} + \nabla\phi\cdot\boldsymbol{d} + \boldsymbol{h}\cdot\nabla\mu^e\, dV_x \leq 0 \\ \int_{\mathcal{R}} \dot{\psi}_x - \frac{1}{2}J^c \boldsymbol{S}^e \cdot \dot{\boldsymbol{C}}^e - E\dot{\xi} - \boldsymbol{g}\cdot\nabla\dot{\xi} - \mu\dot{c} - \mu^e\dot{\xi} + \nabla\phi\cdot\boldsymbol{d} + \boldsymbol{h}\cdot\nabla\mu^e\, dV_x \leq 0\end{aligned} \tag{B.112}$$

A final adjustment to the free energy imbalance is made by substituting the solution of the electric field (Equation B.21) into this expression:

$$\begin{aligned}\int_{\mathcal{R}} \dot{\psi}_x - \frac{1}{2}J^c \boldsymbol{S}^e \cdot \dot{\boldsymbol{C}}^e - E\dot{\xi} - \boldsymbol{g}\cdot\nabla\dot{\xi} - \mu\dot{c} - \mu^e\dot{\xi} + \nabla\phi\cdot\boldsymbol{d} + \boldsymbol{h}\cdot\nabla\mu^e\, dV_x \leq 0 \\ \int_{\mathcal{R}} \dot{\psi}_x - \frac{1}{2}J^c \boldsymbol{S}^e \cdot \dot{\boldsymbol{C}}^e - E\dot{\xi} - \boldsymbol{g}\cdot\nabla\dot{\xi} - \mu\dot{c} - \mu^e\dot{\xi} - \boldsymbol{e}\cdot\boldsymbol{d} + \boldsymbol{h}\cdot\nabla\mu^e\, dV_x \leq 0\end{aligned} \tag{B.113}$$

The free energy energy can now be localized:

$$\begin{aligned}\dot{\psi}_x - \frac{1}{2}J^c \boldsymbol{S}^e \cdot \dot{\boldsymbol{C}}^e - E\dot{\xi} - \boldsymbol{g}\cdot\nabla\dot{\xi} - \mu\dot{c} - \mu^e\dot{\xi} - \boldsymbol{e}\cdot\boldsymbol{d} + \boldsymbol{h}\cdot\nabla\mu^e \leq 0 \\ \frac{1}{2}J^c \boldsymbol{S}^e \cdot \dot{\boldsymbol{C}}^e + E\dot{\xi} + \boldsymbol{g}\cdot\nabla\dot{\xi} + \mu\dot{c} + \mu^e\dot{\xi} + \boldsymbol{e}\cdot\boldsymbol{d} - \boldsymbol{h}\cdot\nabla\mu^e - \dot{\psi}_x \geq 0\end{aligned} \tag{B.114}$$

The expression shown in Equation B.114 is also referred to as the dissipation $\mathcal{D}$.

$$\mathcal{D} = \frac{1}{2}J^c \boldsymbol{S}^e \cdot \dot{\boldsymbol{C}}^e + E\dot{\xi} + \boldsymbol{g}\cdot\nabla\dot{\xi} + \mu\dot{c} + \mu^e\dot{\xi} + \boldsymbol{e}\cdot\boldsymbol{d} - \boldsymbol{h}\cdot\nabla\mu^e - \dot{\psi}_x \geq 0 \tag{B.115}$$

B.4. Constitutive theory

In this section, the energetic and dissipative constitutive equations are defined.

B.4.1. Energetic constitutive equations

The constitutive equations for the free energy ψ, the second Piola stress $\boldsymbol{S}^e$, the chemical potential μ, and the electric field $\boldsymbol{e}$ are introduced driven by the free energy imbalance.

$$\begin{aligned} \Psi_x &= \hat{\psi}_x(\Lambda) \\ \boldsymbol{S}^e &= \hat{S}^e(\Lambda) \\ \mu &= \hat{\mu}(\Lambda) \\ \boldsymbol{e} &= \hat{\boldsymbol{e}}(\Lambda) \end{aligned} \tag{B.116}$$

Here, Λ represents the list of variables:

$$\Lambda = (\boldsymbol{c}, c, \xi, \nabla\xi, \boldsymbol{d}) \tag{B.117}$$

The time derivative of the free energy imbalance is obtained using the chain rule applied to the free energy.

$$\dot{\psi}_x = \frac{\partial \hat{\psi}_x}{\partial \boldsymbol{C}^e} \cdot \dot{\boldsymbol{C}}^e + \frac{\partial \hat{\psi}_x}{\partial c}\dot{c} + \frac{\partial \hat{\psi}_x}{\partial \xi}\dot{\xi} + \frac{\partial \hat{\psi}_x}{\partial \nabla\xi} \cdot \nabla\dot{\xi} + \frac{\partial \hat{\psi}_x}{\partial \boldsymbol{d}} \cdot \dot{\boldsymbol{d}} \tag{B.118}$$

Equation B.118 is substituted into Equation B.114:

$$\begin{aligned} &\dot{\psi}_x - \frac{1}{2}J^c \boldsymbol{S}^e \cdot \dot{\boldsymbol{C}}^e - E\dot{\xi} - \boldsymbol{g} \cdot \nabla\dot{\xi} - \mu\dot{c} - \mu^e\dot{\xi} - \boldsymbol{e} \cdot \boldsymbol{d} + \boldsymbol{h} \cdot \nabla\mu^e \leq 0 \\ &\frac{\partial \hat{\psi}_x}{\partial \boldsymbol{C}^e} \cdot \dot{\boldsymbol{C}}^e + \frac{\partial \hat{\psi}_x}{\partial c}\dot{c} + \frac{\partial \hat{\psi}_x}{\partial \xi}\dot{\xi} + \frac{\partial \hat{\psi}_x}{\partial \nabla\xi} \cdot \nabla\dot{\xi} + \frac{\partial \hat{\psi}_x}{\partial \boldsymbol{d}} \cdot \dot{\boldsymbol{d}} - \frac{1}{2}J^c \boldsymbol{S}^e \cdot \dot{\boldsymbol{C}}^e - E\dot{\xi} - \boldsymbol{g} \cdot \nabla\dot{\xi} - \mu\dot{c} - \mu^e\dot{\xi} - \boldsymbol{e} \cdot \boldsymbol{d} \\ &+ \boldsymbol{h} \cdot \nabla\mu^e \leq 0 \\ &\left(\frac{\partial \hat{\psi}_x}{\partial \boldsymbol{C}^e} - \frac{1}{2}J^c \boldsymbol{S}^e\right) \cdot \dot{\boldsymbol{C}}^e + \left(\frac{\partial \hat{\psi}_x}{\partial c} - \mu\right)\dot{c} + \left(\frac{\partial \hat{\psi}_x}{\partial \xi} - E - \mu^e\right)\dot{\xi} + \left(\frac{\partial \hat{\psi}_x}{\partial \nabla\boldsymbol{\xi}} - \boldsymbol{g}\right) \cdot \nabla\dot{\xi} + \left(\frac{\partial \hat{\psi}_x}{\partial \boldsymbol{d}} - \boldsymbol{e}\right) \cdot \dot{d} \\ &+ \boldsymbol{h} \cdot \nabla\mu^e \leq 0 \end{aligned} \tag{B.119}$$

Processes associated with diffusion (governed by $\dot{c}$) and migration (governed by $\boldsymbol{d}$) are considered energetic. On the other hand, processes associated with electrodeposition (governed by $\dot{\xi}$) are dissipative. One exception exists for the power conjugate of $\nabla\dot{\xi}$. This term is considered entirely energetic because all reaction-dissipative processes are already accounted for by the term $\dot{\xi}$.

The inequality of Equation B.119 must hold for all values of the energetic terms $\left\{\dot{\boldsymbol{C}}^e, \dot{c}, \nabla\dot{\xi}, \boldsymbol{d}\right\}$. This condition is satisfied only when these terms vanish from the expression. Otherwise, selecting certain terms may lead to a violation of the inequality. Thus, the free energy determines the following quantities via the state relations:

- The second Piola stress $\boldsymbol{S}^e$:

$$\begin{aligned} &\frac{\partial \hat{\psi}_x}{\partial \boldsymbol{C}^e} - \frac{1}{2}J^c \boldsymbol{S}^e = \boldsymbol{0} \\ &\boldsymbol{S}^e = \frac{2}{J^c}\frac{\partial \hat{\psi}_x}{\partial \boldsymbol{C}^e} \end{aligned} \tag{B.120}$$

- The chemical potential μ :

$$\begin{aligned} &\frac{\partial \hat{\psi}_x}{\partial c} - \mu = 0 \\ &\mu = \frac{\partial \hat{\psi}_x}{\partial c} \end{aligned} \tag{B.121}$$

- The vector micro stress g :

$$\begin{aligned} \frac{\partial \hat{\psi}_x}{\partial \nabla \xi} - \boldsymbol{g} &= \boldsymbol{0} \\ \boldsymbol{g} &= \frac{\partial \hat{\psi}_x}{\partial \nabla \hat{\xi}} \end{aligned} \tag{B.122}$$

- The electric field $\boldsymbol{e}$:

$$\begin{aligned} \frac{\partial \hat{\psi}_x}{\partial \boldsymbol{d}} - \boldsymbol{e} &= 0 \\ \boldsymbol{e} &= \frac{\partial \hat{\psi}_x}{\partial \boldsymbol{d}} \end{aligned} \tag{B.123}$$

Substituting Equation B.121 into the expression for the electrochemical potential (Equation B.87) yields:

$$\begin{aligned} \mu^e =& \mu + F\phi \\ =& \frac{\partial \hat{\psi}_x}{\partial c} + F\phi \end{aligned} \tag{B.124}$$

B.4.2. Dissipative constitutive equations

The state relations from Equation B.120 to Equation B.123 are applied to Equation B.119:

$$\begin{aligned} &\left(\frac{\partial \hat{\psi}_x}{\partial \boldsymbol{C}^e} - \frac{1}{2} J^c \boldsymbol{S}^e\right) \cdot \dot{\boldsymbol{C}}^e + \left(\frac{\partial \hat{\psi}_x}{\partial c} - \mu\right) \dot{c} + \left(\frac{\partial \hat{\psi}_x}{\partial \xi} - E - \mu^e\right) \dot{\xi} + \left(\frac{\partial \hat{\psi}_x}{\partial \nabla \boldsymbol{\xi}} - \boldsymbol{g}\right) \cdot \nabla \dot{\xi} + \left(\frac{\partial \hat{\psi}_x}{\partial \boldsymbol{d}} - \boldsymbol{e}\right) \cdot \dot{d} \\ &+ \boldsymbol{h} \cdot \nabla \mu^e \leq 0 \\ &\left(\frac{\partial \hat{\psi}_x}{\partial \xi} - E - \mu^e\right) \dot{\xi} + \boldsymbol{h} \cdot \nabla \mu^e \leq 0 \end{aligned} \tag{B.125}$$

Multiplying Equation B.125 by minus one results in the formation of the dissipation by the remaining terms. The resulting expression is called the reduced dissipation inequality.

$$\begin{aligned} \left(\frac{\partial \hat{\psi}_x}{\partial \xi} - E - \mu^e\right) \dot{\xi} + \boldsymbol{h} \cdot \nabla \mu^e &\leq 0 \\ \mathcal{D} = -\left(\frac{\partial \hat{\psi}_x}{\partial \xi} - E - \mu^e\right) \dot{\xi} - \boldsymbol{h} \cdot \nabla \mu^e &\geq 0 \end{aligned} \tag{B.126}$$

The electrochemical potential of the electrodeposited species is defined below:

$$\mu^\xi = \frac{\partial \hat{\psi}_x}{\partial \xi} - E \tag{B.127}$$

Equation B.127 is substituted in the reduced dissipation inequality (Equation B.126):

$$\begin{aligned} \mathcal{D} &= -\left(\frac{\partial \hat{\psi}_x}{\partial \xi} - E - \mu^e\right) \dot{\xi} - \boldsymbol{h} \cdot \nabla \mu^e \geq 0 \\ \mathcal{D} &= -\left(\mu^\xi - \mu^e\right) \dot{\xi} - \boldsymbol{h} \cdot \nabla \mu^e \geq 0 \end{aligned} \tag{B.128}$$

The thermodynamic driving force for electrodeposition is defined as a difference in the electrochemical potential of the species participating in the reaction:

$$\mathcal{F} = \mu^\xi - \mu^e \tag{B.129}$$

The thermodynamic driving force Equation B.129 is substituted in the reduced dissipation inequality (Equation B.128):

$$\begin{aligned} \mathcal{D} &= -\left(\mu^\xi - \mu^e\right) \dot{\xi} - \boldsymbol{h} \cdot \nabla \mu^e \geq 0 \\ \mathcal{D} &= -\mathcal{F} \dot{\xi} - \boldsymbol{h} \cdot \nabla \mu^e \geq 0 \end{aligned} \tag{B.130}$$

Next, Fick's law is introduced, asserting that the species flux depends linearly on the electrochemical potential gradient $\nabla\mu^e$ via the mobility tensor $\boldsymbol{M}_{\text{mob}}$.

$$\boldsymbol{h} = -\boldsymbol{M}_{mob}\nabla\mu^e \tag{B.131}$$

Equation B.131 is substituted in the reduced dissipation inequality (Equation B.130):

$$\begin{aligned}\mathcal{D} &= -\mathcal{F}\dot{\xi} - \boldsymbol{h}\cdot\nabla\mu^e \geq 0\\ \mathcal{D} &= -\mathcal{F}\dot{\xi} - \nabla\mu^e\cdot\boldsymbol{M}_{mob}\nabla\mu^e \geq 0\end{aligned} \tag{B.132}$$

The final results are obtained under the assumption that each term in the reduced dissipation inequality satisfies the inequality individually.

$$-\mathcal{F}\dot{\xi} \geq 0 \tag{B.133}$$

$$\nabla\mu^e\cdot\boldsymbol{M}_{mob}\nabla\mu^e \geq 0 \tag{B.134}$$

In terms of the dissipation caused by electrodeposition (as shown in Equation B.133), it is assumed that $\dot{\xi} > 0$ if and only if $\mathcal{F} < 0$, and vice versa for $\dot{\xi} < 0$ if and only if $\mathcal{F} > 0$. The implication of Equation B.134 is that it imposes the constraint that M_{mob} must be positive semi-definite. Together, these restrictions ensure that the reduced dissipation inequality (Equation B.132) is not violated.

B.5. Specialization of the constitutive equations

The theory derived above is of a general nature. This chapter specializes it for the electrodeposition of lithium in solid-state batteries, introducing constitutive equations that focus on the following processes:

1. The occurrence of plating and subsequent fracture resulting from the electrodeposition of Li-metal in single-ion conductors.
2. The coupling between electric, chemical, and mechanical influences on the electrodeposition kinetics and the morphological evolution of lithium metal filaments within the solid-state electrolyte.

The general electrodeposition reaction described in Equation B.1 is now explicitly tailored for lithium metal plating.

$$\begin{aligned}M^{n+} + e^- &\rightarrow M\\ Li^+ + e^- &\rightarrow Li\end{aligned} \tag{B.135}$$

B.5.1. Electrodeposition-induced deformation

It begins with specifying how the electrodeposition of lithium on the reaction side induces mechanical deformation. The deformations induced by electrodeposition were previously defined as irrotational, implying the following relationship between stretching, velocity gradient, and deformation gradient due to electrodeposition:

$$\begin{aligned}\boldsymbol{D}^r &= \boldsymbol{L}^r\\ &= \dot{\boldsymbol{F}}^r\boldsymbol{F}^{r-1}\end{aligned} \tag{B.136}$$

The stretching tensor induced by electrodeposition, denoted as $\boldsymbol{D}^r$, is assumed to be anisotropic and can thus be defined as follows:

$$\boldsymbol{D}^r = \dot{\epsilon}^r\boldsymbol{m}_r\otimes\boldsymbol{m}_r \tag{B.137}$$

Where $\boldsymbol{m}_r$ is the unit vector that represents the direction of deformations due to electrodeposition. Experimental observations have shown that deformations caused by the electrodeposition of lithium metal preferentially occur normal to the reaction front (i.e., normal to the conductor/metal interface) [47]. Therefore, $\boldsymbol{m}_r$ is defined as follows:

$$\boldsymbol{m}_r = \frac{\nabla\bar{\xi}}{\left|\nabla\bar{\xi}\right|} \tag{B.138}$$

Equation B.137 is used to obtain a relation between $\boldsymbol{D}^r$ and $\dot{\epsilon}^r$ by using the trace of $\boldsymbol{D}^r$:

$$\begin{aligned}\text{tr}\,(\boldsymbol{D}^r) &= \text{tr}\,(\dot{\epsilon}^r\boldsymbol{m}_r\otimes\boldsymbol{m}_r)\\ &= \dot{\epsilon}^r\,\text{tr}\,(\boldsymbol{m}_r\otimes\boldsymbol{m}_r)\\ &= \dot{\epsilon}^r\boldsymbol{m}_r\cdot\boldsymbol{m}_r\end{aligned} \tag{B.139}$$

The dot product of two identical unit vectors is, by definition, equal to 1. Therefore, the relation shown in Equation B.139 simplifies to the following expression:

$$\begin{aligned} \dot{\epsilon}^r \boldsymbol{m}_r \cdot \boldsymbol{m}_r &= \operatorname{tr}(\boldsymbol{D}^r) \\ \dot{\epsilon}^r &= \operatorname{tr}(\boldsymbol{D}^r) \end{aligned} \tag{B.140}$$

Where $\dot{\epsilon}^r$ represents the volumetric strain rate for reaction induced deformations

The Jacobian represents the ratio between deformed and undeformed volumes. Therefore, the volume change can be defined as the Jacobian minus one, under the assumption that the volumetric changes due to electrodeposition varies linearly with the extent of the reaction.

$$\begin{aligned} J^r - 1 &= \Omega\xi \\ J^r &= 1 + \Omega\xi \end{aligned} \tag{B.141}$$

The time derivative of the Jacobian is obtained by taking the derivative of the determinant of the deformation gradient with respect to time. In Appendix D, the derivation of this time derivative of the determinant is shown. Using this final result, as depicted in Equation D.21, the time derivative of the Jacobian is obtained.

$$\begin{aligned} \dot{j}^r &= \frac{\partial}{\partial t} \det(\boldsymbol{F}^r) \\ \dot{j}^r &= \det(\boldsymbol{F}^r) \operatorname{tr}\left(\dot{\boldsymbol{F}}^r \boldsymbol{F}^{r-1}\right) \\ \dot{j}^r &= J^r \operatorname{tr}\left(\dot{\boldsymbol{F}}^r \boldsymbol{F}^{r-1}\right) \\ \dot{j}^r J^{r-1} &= \operatorname{tr}\left(\dot{\boldsymbol{F}}^r \boldsymbol{F}^{r-1}\right) \end{aligned} \tag{B.142}$$

The electrodeposition-induced stretching tensor (Equation B.136) becomes apparent in Equation B.142 and is subsequently substituted into this expression.

$$\begin{aligned} \dot{j}^r J^{r-1} &= \operatorname{tr}\left(\dot{\boldsymbol{F}}^r \boldsymbol{F}^{r-1}\right) \\ &= \operatorname{tr}(\boldsymbol{D}^r) \end{aligned} \tag{B.143}$$

As shown previously, the trace of $\boldsymbol{D}^r$ is equal to the volumetric strain rate $\dot{\epsilon}^r$ (Equation B.141), and it is substituted into this expression.

$$\begin{aligned} \dot{j}^r J^{r-1} &= \operatorname{tr}\left(\dot{\boldsymbol{F}}^r \boldsymbol{F}^{r-1}\right) \\ &= \dot{\epsilon}^r \end{aligned} \tag{B.144}$$

The Jacobian is defined before in Equation B.141 and substituted in Equation B.145:

$$\begin{aligned} \dot{\epsilon}^r &= \dot{j}^r J^{r-1} \\ &= \frac{\frac{\partial}{\partial t}(1 + \Omega\xi)}{1 + \Omega\xi} \\ &= \frac{\Omega\dot{\xi}}{1 + \Omega\xi} \end{aligned} \tag{B.145}$$

Returning to the electrodeposition-induced stretching tensor $\boldsymbol{D}^r$ defined in Equation B.137, $\dot{\epsilon}^r$ is replaced by the expression derived above.

$$\begin{aligned} \boldsymbol{D}^r &= \dot{\epsilon}^r \boldsymbol{m}_r \otimes \boldsymbol{m}_r \\ &= \frac{\Omega\dot{\xi}}{1 + \Omega\xi} \boldsymbol{m}_r \otimes \boldsymbol{m}_r \end{aligned} \tag{B.146}$$

In Section B.2, the electrodeposition-induced stretching tensor $\boldsymbol{D}^r$ is defined in Equation B.44 using the tensor $\boldsymbol{N}^r$, which represents the direction of electrodeposition-induced deformations. This tensor $\boldsymbol{N}^r$

can be expressed by substituting Equation B.146 into Equation B.44.

$$\begin{aligned}\dot{\xi}\boldsymbol{N}^r &= D^r \\ \dot{\xi}\boldsymbol{N}^r &= \frac{\Omega\dot{\xi}}{1+\Omega\xi}\boldsymbol{m}_r \otimes \boldsymbol{m}_r \\ \boldsymbol{N}^r &= \frac{\Omega}{1+\Omega\xi}\boldsymbol{m}_r \otimes \boldsymbol{m}_r\end{aligned} \tag{B.147}$$

B.5.2. Free energy

"Next, a separable free energy per unit reference volume is considered, as shown below:

$$\hat{\psi}_x\left(c^e, c, \xi, \nabla\xi, \boldsymbol{d}\right) = \psi_x^m(\boldsymbol{C}^e, \xi) + \psi_x^c(c) + \psi_x^{\xi}(\xi) + \psi_x^{\nabla\xi}(|\nabla\xi|) + \psi_x^e\left(\boldsymbol{c^e}, \xi, \boldsymbol{d}\right) \tag{B.148}$$

All individual functions in Equation B.148 are defined as isotropic functions of their arguments. This implies that the resulting free energy remains unchanged under rotations. Each individual function will now be discussed in detail.

$\psi_x^m(\boldsymbol{C}^e, \xi, d)$ represents the contribution to changes in the free energy density resulting from elastic deformations of the host material. Due to the isotropic of the free energy function, the right Cauchy Green strain function can be written in terms of the principal invariants.

$$\psi_x^m(\boldsymbol{C}, \xi, d) = \psi_x^m\left(\mathcal{I}_{\boldsymbol{C}^e}, \xi\right) \tag{B.149}$$

The list $\mathcal{I}_{\boldsymbol{C}^e}$ is defined as follows:

$$\mathcal{I}_{\boldsymbol{C}^e} = \left(\boldsymbol{I}_1\left(\boldsymbol{C}^e\right), \boldsymbol{I}_2\left(\boldsymbol{C}^e\right), \boldsymbol{I}_3\left(\boldsymbol{C}^e\right)\right) \tag{B.150}$$

The constitutive relation for the second Piola stress tensor was previously defined in Equation B.120, and it is now applied along with the mechanical contribution of the free energy. Therefore, possible stress contributions, such as the Maxwell stress due to electrostatics, are neglected due to their small contribution.

$$\begin{aligned}\boldsymbol{S}^e &= \frac{2}{J^c}\frac{\partial\hat{\psi}_x^m\left(\boldsymbol{C}^e, \xi\right)}{\partial\boldsymbol{C}^e} \\ &= \frac{2}{J^c}\frac{\partial\hat{\psi}_x^m\left(\mathcal{I}_{\boldsymbol{C}^e}, \xi\right)}{\partial\boldsymbol{C}^e}\end{aligned} \tag{B.151}$$

It follows from Equation B.151 that the second Piola stress tensor $\boldsymbol{S}^e$ is an isotropic function of the right Cauchy Green strain tensor $\boldsymbol{C}^e$. A property from isotropic tensor functions are that they commute:

$$\boldsymbol{C}^e\boldsymbol{S}^e = \boldsymbol{S}^e\boldsymbol{C}^e \tag{B.152}$$

By definition, both tensors are symmetric, a property utilized to rewrite Equation B.152.

$$\begin{aligned}\boldsymbol{C}^e\boldsymbol{S}^e &= \boldsymbol{S}^e\boldsymbol{C}^e \\ &= \boldsymbol{S}^{eT}\boldsymbol{C}^{eT} = \left(\boldsymbol{C}^e\boldsymbol{S}^e\right)^T\end{aligned} \tag{B.153}$$

The relationship between the Mantel stress $\boldsymbol{M}^e$, the second Piola stress $\boldsymbol{S}^e$, and the Cauchy-Green strain tensor $\boldsymbol{C}^e$ was previously provided in Equation B.92 and is now rewritten.

$$\begin{aligned}\boldsymbol{S}^e &= \boldsymbol{C}^{e-1}\boldsymbol{M}^e \\ \boldsymbol{M}^e &= \boldsymbol{C}^e\boldsymbol{S}^e\end{aligned} \tag{B.154}$$

"The expression in Equation B.154 is substituted into Equation B.153 to illustrate the symmetry of the Mandel stress.

$$\begin{aligned}\boldsymbol{C}^e\boldsymbol{S}^e &= \left(\boldsymbol{C}^e\boldsymbol{S}^e\right)^T \\ \boldsymbol{M}^e &= \boldsymbol{M}^{eT}\end{aligned} \tag{B.155}$$

The next step is to rewrite the Cauchy-Green strain tensor C^e using spectral decomposition.

$$\boldsymbol{C}^e = \sum_{i=1}^{3} \omega_i^e \boldsymbol{r}_i^e \otimes \boldsymbol{r}_i^e \tag{B.156}$$

With:

$$\omega_i^e = \left(\lambda_i^e\right)^2 \tag{B.157}$$

So, Equation B.156 can also be written in terms of λ_i^e.

$$\boldsymbol{C}^e = \sum_{i=1}^{3} \omega_i^e \boldsymbol{r}_i^e \otimes \boldsymbol{r}_i^e = \sum_{i=1}^{3} \left(\lambda_i^e\right)^2 \boldsymbol{r}_i^e \otimes \boldsymbol{r}_i^e \tag{B.158}$$

Here, $\left(\boldsymbol{r}_1^e, \boldsymbol{r}_2^e, \boldsymbol{r}_3^e\right)$ are the orthonormal eigenvectors of $\boldsymbol{C}^e$ and $\boldsymbol{U}^e$. $\left(\lambda_1^e, \lambda_2^e, \lambda_3^e\right)$ are the positive eigenvalues of $\boldsymbol{U}^e$. With these definitions, the mechanical free energy density can now be expressed in terms of the principal stretches.

$$\psi_x^m(\boldsymbol{C}^e, \xi) = \psi_x^m\left(\lambda_1, \lambda_2, \lambda_3, \xi\right) \tag{B.159}$$

$\frac{\partial \psi_x^m}{\partial \boldsymbol{C}^e}$ is rewritten in terms of the principal stretches using the chain rule:

$$\frac{\partial \psi_x^m\left(\boldsymbol{C}^e, \xi\right)}{\partial \boldsymbol{C}^e} = \sum_{i=1}^{3} \frac{\partial \psi_x^m}{\partial \lambda_i} \frac{\partial \lambda_i}{\partial \omega_i} \frac{\partial \omega_i}{\partial \boldsymbol{C}^e} \tag{B.160}$$

First, the partial derivative $\frac{\partial \lambda_i}{\partial \omega_i}$ is determined by taking the derivative of Equation B.157:

$$\begin{aligned} \lambda_i^e &= \sqrt{\omega_i^e} \\ \frac{\partial \lambda_i^e}{\partial \omega_i} &= \frac{1}{2\sqrt{\omega_i^e}} \\ &= \frac{1}{2\lambda_i^e} \end{aligned} \tag{B.161}$$

The partial derivative $\frac{\partial \omega_i}{\partial \boldsymbol{C}^e}$ is obtained from the matrixcookbook [48] and shown below:

$$\frac{\partial \omega_i}{\partial \boldsymbol{C}^e} = 1 \tag{B.162}$$

Equation B.161 and Equation B.162 are substituted in Equation B.160

$$\begin{aligned} \frac{\partial \psi_x^m\left(\boldsymbol{C}^e, \xi\right)}{\partial \boldsymbol{C}^e} &= \sum_{i=1}^{3} \frac{\partial \psi_x^m}{\partial \lambda_i} \frac{\partial \lambda_i}{\partial \omega_i} \frac{\partial \omega_i}{\partial \boldsymbol{C}^e} \\ &= \sum_{i=1}^{3} \frac{1}{2\lambda_i^e} \frac{\partial \psi_x^m}{\partial \lambda_i} \end{aligned} \tag{B.163}$$

The next step is to return to the Mandel stress expression shown in Equation B.154 and substitute the constitutive relation of the second Piola stress tensor $\boldsymbol{S}^e$ (as given in Equation B.151) into this expression.

$$\begin{aligned} \boldsymbol{M}^e &= \boldsymbol{C}^e \boldsymbol{S}^e \\ &= \frac{2}{J^c} \boldsymbol{C}^e \frac{\partial \hat{\psi}_x^m\left(\boldsymbol{C}^e, \xi\right)}{\partial \boldsymbol{C}^e} \end{aligned} \tag{B.164}$$

The spectral decomposition of the Cauchy green strain tensor $\boldsymbol{C}^e$ (Equation B.158) and Equation B.163 can be substituted in Equation B.164:

$$\begin{aligned}\boldsymbol{M}^e =& \frac{2}{J^c}\boldsymbol{C}^e \frac{\partial \hat{\psi}_x^m\left(\boldsymbol{C}^e, \xi\right)}{\partial \boldsymbol{C}^e} \\ =& \frac{2}{J^c}\sum_{i=1}^{3}\left(\lambda_i^e\right)^2 \frac{1}{2\lambda_i^e}\frac{\partial \psi_x^m}{\partial \lambda_i}\boldsymbol{r}_i^e \otimes \boldsymbol{r}_i^e \\ =& \frac{1}{J^c}\sum_{i=1}^{3}\lambda_i^e \frac{\partial \psi_x^m}{\partial \lambda_i}\boldsymbol{r}_i^e \otimes \boldsymbol{r}_i^e\end{aligned} \tag{B.165}$$

The next definition to introduce is that of the logarithmic elastic strain.

$$\boldsymbol{E}^e = \ln|U^e| = \sum_{i=1}^{3} E_i^e\, \boldsymbol{r}_i \otimes \boldsymbol{r}_i \tag{B.166}$$

The principle values of the logarithmic elastic strain are defined below:

$$E_i^e = \ln\left|\lambda_i^e\right| \tag{B.167}$$

Substituting Equation B.167 into Equation B.166 gives:

$$\begin{aligned}\boldsymbol{E}^e =& \ln|U^e| = \sum_{i=1}^{3} E_i^e\, \boldsymbol{r}_i \otimes \boldsymbol{r}_i \\ =& \ln\left|\lambda_i^e\right| \boldsymbol{r}_i \otimes \boldsymbol{r}_i\end{aligned} \tag{B.168}$$

The chain rule is used again to rewrite the partial derivative of the mechanical free energy in terms of the principal values of the logarithmic elastic strain.

$$\frac{\partial \hat{\psi}_x^m\left(\lambda_1^e, \lambda_2^e, \lambda_3^e, \xi\right)}{\partial \lambda_i^e} = \frac{\partial \psi_x^m}{\partial E_i^e}\frac{\partial E_i^e}{\partial \lambda_i^e} \tag{B.169}$$

$\frac{\partial E_i^e}{\partial \lambda_i^e}$ is obtained by taking the derivative of Equation B.170:

$$\begin{aligned}E_i^e =& \ln\left|\lambda_i^e\right| \\ \frac{\partial E_i^e}{\partial \lambda_i^e} =& \frac{1}{\lambda_i^e}\end{aligned} \tag{B.170}$$

Equation B.170 is substituted in Equation B.169:

$$\begin{aligned}\frac{\partial \hat{\psi}_x^m\left(\lambda_1^e, \lambda_2^e, \lambda_3^e, \xi\right)}{\partial \lambda_i^e} =& \frac{\partial \psi_x^m}{\partial E_i^e}\frac{\partial E_i^e}{\partial \lambda_i^e} \\ =& \frac{1}{\lambda_i^e}\frac{\partial \psi_x^m}{\partial E_i^e}\end{aligned} \tag{B.171}$$

Equation B.171 is substituted in Equation B.165 to obtain the expression of the Mantel stress with the principle values of the logarithmic elastic strain:

$$\begin{aligned}\boldsymbol{M}^e =& \frac{1}{J^c}\sum_{i=1}^{3}\lambda_i^e \frac{\partial \psi_x^m}{\partial \lambda_i}\boldsymbol{r}_i^e \otimes \boldsymbol{r}_i^e \\ =& \frac{1}{J^c}\sum_{i=1}^{3}\lambda_i^e \frac{1}{\lambda_i^e}\frac{\partial \psi_x^m}{\partial E_i^e}\boldsymbol{r}_i^e \otimes \boldsymbol{r}_i^e \\ =& \frac{1}{J^c}\sum_{i=1}^{3}\frac{\partial \psi_x^m\left(E_1, E_2, E_3, \xi, d\right)}{\partial E_i^e}\boldsymbol{r}_i^e \otimes \boldsymbol{r}_i^e\end{aligned} \tag{B.172}$$

When returning to the mechanical free energy function due to elastic deformations, the expression for it is decomposed into a positive part ψ_x^{m+} representing tension and a negative part ψ_x^{m-} representing compression.

$$\psi_x^m(\boldsymbol{E},\xi) = \psi_x^{m+}(\boldsymbol{E},\xi) + \psi_x^{m-}(\boldsymbol{E},\xi) \tag{B.173}$$

The positive and negative mechanical components of the free energy are separately characterized using the classical strain energy function of isotropic linear elasticity to model moderate large deformations, employing the logarithmic strain measure $\boldsymbol{E}^e$. The following equation expresses this relationship:

$$\left.\begin{aligned}
\psi_x^{m+}(\boldsymbol{E}^e,\xi) = \quad & J^c\left[G(\bar{\xi})\left(\left\langle E_1^e\right\rangle_+^2 + \left\langle E_2^e\right\rangle_+^2 + \left\langle E_3^e\right\rangle_+^2\right) + \right. \\
& \left.\tfrac{1}{2}\left(K(\bar{\xi}) - \tfrac{2}{3}G(\bar{\xi})\right)\left(\left\langle E_1^e + E_2^e + E_3^e\right\rangle_+\right)^2\right] \\
\psi_x^{m-}(\boldsymbol{E}^c,\xi) = \quad & J^c\left[G(\bar{\xi})\left(\left\langle E_1^e\right\rangle_-^2 + \left\langle E_2^e\right\rangle_-^2 + \left\langle E_3^e\right\rangle_-^2\right) + \right. \\
& \left.\tfrac{1}{2}\left(K(\bar{\xi}) - \tfrac{2}{3}G(\bar{\xi})\right)\left(\left\langle E_1^e + E_2^e + E_3^c\right\rangle_-\right)^2\right]
\end{aligned}\right\} \tag{B.174}$$

Where $G(\bar{\xi})$ and $k(\bar{\xi})$ are the reaction-dependent shear and bulk moduli respectively, and E_i^e denotes the principal elastic logarithmic strains. The clarity of Equation B.174 is improved by introducing the following expressions:

$$\left\langle E_i^e\right\rangle_+ = \begin{cases} E_i^e & \text{if } E_i^e > 0 \\ 0 & \text{otherwise} \end{cases} \tag{B.175}$$

$$\left\langle E_i^e\right\rangle_- = \begin{cases} E_i^e & \text{if } E_i^e < 0 \\ 0 & \text{otherwise} \end{cases} \tag{B.176}$$

As damage increases, the positive part of the free energy degrades, while the negative part remains unchanged. This phenomenon represents damage occurring under purely compressive stress. The split in free energy due to elastic deformations is necessary to maintain the material's resistance under compression.

The next contribution to changes in the free energy is the chemical free energy due to the mixing of ionic species with the solid host, denoted as $\psi_x^c(c)$. A regular solution model is employed for the chemical free energy, serving as a continuum approximation for mixing.

$$\psi_x^c(c) = \mu_0 c + R\theta c_{\max}(\bar{c}\ln|\bar{c}| + (1-\bar{c})\ln|1-\bar{c}|) \tag{B.177}$$

Here, $\bar{c}$ represents the normalized species concentration.

$$\bar{c} = \frac{c}{c_{\max}} \quad \bar{c} \in [0,1] \tag{B.178}$$

$c_{\max}$ represents the highest concentration of species in moles per unit reference volume when all available sites in the material are occupied. Moreover, μ_0 stands for the standard chemical potential of the diffusing species, R denotes the universal gas constant, and θ represents the absolute temperature.

$\psi_x^{\xi}(\xi)$ comprises an energy function linked to the energy barrier between phases (the energy difference needed for a substance to change from one phase to another). The remaining electrochemical energetic factors relate to the standard (reference) chemical state and the electrostatic potential of the electrodeposited lithium metal.

$$\psi_x^{\xi}(\xi) = W\bar{\xi}^2(1-\xi)^2 + \xi\mu_0^{\xi} + \xi F\phi_0 \tag{B.179}$$

The initial term controlled by W establishes the energy barrier height between phases in the continuum kinetics approach. The subsequent term defines the standard chemical potential of the electrodeposited species, while the third term denotes the energetic contribution linked to the electrostatic potential of the metal, ϕ_0.

$\psi_x^{\nabla 5}(|\nabla\xi|)$ is the interfacial free energy and is defined in the following way:

$$\psi_x^{\nabla\xi}(|\nabla\xi|) = \frac{1}{2}\lambda_\xi|\nabla\xi|^2 \tag{B.180}$$

$\psi_x^e($
$bmC^e, \xi, \boldsymbol{d})$ is the electrostatic energy and is defined in the current configuration as follows:

$$\psi^e = J\left(\frac{1}{2\varepsilon}\bar{\boldsymbol{d}}\cdot\bar{\boldsymbol{d}}\right) \tag{B.181}$$

Where $\varepsilon(\bar{\xi})$ denotes the reaction-dependent effective electrical permittivity. Electrical permittivity is a fundamental property of a material that describes how it responds to an electric field and measures how much an electric field can influence a material. When considering different materials, components of mixtures, or composites, effective electrical permittivity is used. This represents the observed permittivity for such materials, accounting for the interaction between different components or phases of the material.

Additionally, $\bar{\boldsymbol{d}}$ is the electric displacement in the current configuration. The electrostatic energy is isotropic in the deformed body because it only depends on the magnitude of $\bar{\boldsymbol{d}}$. The relation between the referential and current electric displacement is defined in the standard way:

$$\begin{aligned}\boldsymbol{d} =& y\boldsymbol{F}^{-1}\bar{\boldsymbol{d}}\\ \bar{\boldsymbol{d}} =& \frac{1}{J}\boldsymbol{F}\boldsymbol{d}\end{aligned} \tag{B.182}$$

Equation B.182 is substituted in Equation B.181 to obtain the referential electrostatic energy:

$$\begin{aligned}\psi^e &= J\left(\frac{1}{2\varepsilon}\bar{\boldsymbol{d}}\cdot\bar{\boldsymbol{d}}\right)\\ \psi_x^e &= J\left(\frac{1}{2\varepsilon}\left(\frac{1}{J}\boldsymbol{F}\boldsymbol{d}\right)\cdot\left(\frac{1}{J}\boldsymbol{F}\boldsymbol{d}\right)\right)\\ &= \frac{1}{J}\left(\frac{1}{2\varepsilon}\boldsymbol{F}\boldsymbol{d}\cdot\boldsymbol{F}\boldsymbol{d}\right)\\ &= \frac{1}{J}\left(\frac{1}{2\varepsilon}\boldsymbol{d}\cdot\boldsymbol{F}^T\boldsymbol{F}\boldsymbol{d}\right)\end{aligned} \tag{B.183}$$

The right Cauchy-Green strain tensor is introduced in Equation B.183 and subsequently substituted into this expression.

$$\begin{aligned}\psi_x^e(\boldsymbol{F}, \boldsymbol{d}, \xi) &= \frac{1}{J}\left(\frac{1}{2\varepsilon}\boldsymbol{d}\cdot\boldsymbol{F}^T\boldsymbol{F}\boldsymbol{d}\right)\\ \psi_x^e(\boldsymbol{C}^e, \boldsymbol{d}, \xi) &= \frac{1}{J}\left(\frac{1}{2\varepsilon}\boldsymbol{d}\cdot\boldsymbol{C}\boldsymbol{d}\right)\end{aligned} \tag{B.184}$$

Below is the expression for the reaction-dependent effective electrical permittivity given:

$$\varepsilon = \varepsilon_r\varepsilon_0 \tag{B.185}$$

Here, $\varepsilon_0 = 8.85\cdot10^{-12}$ F/m denotes the electrical permittivity of vacuum, and ε_r represents the reaction-dependent relative electrical permittivity of each material phase.

All the individual components of the free energy, as described in Equation B.173, Equation B.177, Equation B.179, Equation B.180, and Equation B.184, are substituted into the complete free energy function as given by Equation B.148.

$$\begin{aligned}\hat{\psi}_x\left(c^e, c, \xi, \nabla\xi, \boldsymbol{d}\right) =& \psi_x^m(\boldsymbol{C}^e, \xi) + \psi_x^c(c) + \psi_x^\xi(\xi) + \psi_x^{\nabla\xi}(|\nabla\xi|) + \psi_x^e\left(\boldsymbol{c}^e, \xi, \boldsymbol{d}\right)\\ =& \psi_x^{m+}(\boldsymbol{E}, \xi) + \psi_x^{m-}(\boldsymbol{E}, \xi) + \mu_0 c + R\theta c_{\max}(\bar{c}\ln|\bar{c}| + (1-\bar{c})\ln|1-\bar{c}|)\\ &+ W\bar{\xi}^2(1-\xi)^2 + \xi\mu_0^\xi + \xi F\phi_0 + \frac{1}{2}\lambda_\xi|\nabla\xi|^2 + \frac{1}{J}\left(\frac{1}{2\varepsilon}\boldsymbol{d}\cdot\boldsymbol{C}\boldsymbol{d}\right)\end{aligned} \tag{B.186}$$

B.5.3. Stress

The Mandel stress is defined earlier in Equation B.172 using the mechanical free energy. In Equation B.173, the mechanical free energy is split into positive and negative parts. This decomposition can also be applied to the Mandel stress because the same free energy is used, resulting in the following decomposition of the Mandel stress.

$$\boldsymbol{M} = \boldsymbol{M}^{e+} + \boldsymbol{M}^{e-} \tag{B.187}$$

Here, $\boldsymbol{M}^{e+}$ and $\boldsymbol{M}^{e-}$ are obtained by applying Equation B.174 to Equation B.172.

$$\begin{aligned}
\boldsymbol{M}^{e+} =& \frac{1}{J^c}\sum_{i=1}^{3}\frac{\partial \psi_x^{m+}(E_1,E_2,E_3,\xi,d)}{\partial E_i^e}\,\boldsymbol{r}_i^e\otimes\boldsymbol{r}_i^e \\
=& \frac{1}{J^c}\sum_{i=1}^{3}\frac{\partial}{\partial E_i}\left\{J^c\left[G(\bar{\xi})\left(\left\langle E_1^e\right\rangle_+^2+\left\langle E_2^e\right\rangle_+^2+\left\langle E_3^e\right\rangle_+^2\right)+\right.\right. \\
& \left.\left.\frac{1}{2}\left(K(\bar{\xi})-\frac{2}{3}G(\bar{\xi})\right)\left(\left\langle E_1^e+E_2^e+E_3^e\right\rangle_+\right)^2\right]\right\}\boldsymbol{r}_i^e\otimes\boldsymbol{r}_i^e \\
=& \frac{1}{J^c}\sum_{i=1}^{3}2J^cG(\bar{\xi})\left\langle E_i\right\rangle_+ + \left(k(\bar{\xi})-\frac{2}{3}G(\bar{\xi})\right)\left\langle E_1^e+E_2^e+E_3^e\right\rangle_+\,\boldsymbol{r}_i^e\otimes\boldsymbol{r}_i^e
\end{aligned} \tag{B.188}$$

$$\begin{aligned}
\boldsymbol{M}^{e-} =& \frac{1}{J^c}\sum_{i=1}^{3}\frac{\partial \psi_x^{m-}(E_1,E_2,E_3,\xi,d)}{\partial E_i^e}\,\boldsymbol{r}_i^e\otimes\boldsymbol{r}_i^e \\
=& \frac{1}{J^c}\sum_{i=1}^{3}\frac{\partial}{\partial E_i}\left\{y^c\left[G(\bar{\xi})\left(\left\langle E_1^e\right\rangle_-^2+\left\langle E_2^e\right\rangle_-^2+\left\langle E_3^e\right\rangle_-^2\right)+\right.\right. \\
& \left.\left.\frac{1}{2}\left(k(\bar{\xi})-\frac{2}{3}G(\bar{\xi})\right)\left(\left\langle E_1^e+E_2^e+E_3^e\right\rangle_-\right)^2\right]\right\}\boldsymbol{r}_i^e\otimes\boldsymbol{r}_i^e \\
=& \frac{1}{J^c}\sum_{i=1}^{3}2J^cG(\bar{\xi})\left\langle E_i\right\rangle_- + \left(k(\bar{\xi})-\frac{2}{3}G(\bar{\xi})\right)\left\langle E_1^e+E_2^e+E_3^e\right\rangle_-\,\boldsymbol{r}_i^e\otimes\boldsymbol{r}_i^e
\end{aligned} \tag{B.189}$$

The relationship between the Cauchy and Piola stress tensors and the Mandel stress is as follows:

$$\boldsymbol{T} = J^{e-1}\boldsymbol{R}^e M^e \boldsymbol{R}^{eT} \tag{B.190}$$

$$\boldsymbol{P} = J^c\left(\boldsymbol{R}^e M^e \boldsymbol{R}^{eT}\right)\boldsymbol{F}^{-T} \tag{B.191}$$

B.5.4. Electrochemical potential - Flux

The general expression of the electrochemical potential is defined earlier in Equation B.124 and is now specified by substituting Equation B.186 into this expression.

$$\begin{aligned}
\mu^e =& \frac{\partial\hat{\psi}_x}{\partial c}+F\phi \\
=& \mu_0 + R\theta c_{\max}\frac{\partial}{\partial\bar{c}}\left(\bar{c}\ln|\bar{c}|+(1-\bar{c})\ln|1-\bar{c}|\right)\frac{\partial\bar{c}}{\partial c}+F\phi
\end{aligned} \tag{B.192}$$

Substituting Equation B.178 in Equation B.192 gives:

$$\begin{aligned}
\mu^e =& \mu_0 + R\theta c_{\max}\frac{\partial}{\partial\bar{c}}\left(\bar{c}\ln|\bar{c}|+(1-\bar{c})\ln|1-\bar{c}|\right)\frac{\partial\bar{c}}{\partial c}+F\phi \\
=& \mu_0 + R\theta c_{\max}\frac{\partial}{\partial\bar{c}}\left(\bar{c}\ln|\bar{c}|+(1-\bar{c})\ln|1-\bar{c}|\right)\frac{\partial}{\partial c}\left(\frac{c}{c_{\max}}\right)+F\phi \\
=& \mu_0 + R\theta c_{\max}\left(\ln|\bar{c}|+\frac{\bar{c}}{\bar{c}}-\ln|1-\bar{c}|+(1-c)\frac{1}{1-c}(-1)\right)\frac{1}{c_{\max}}+F\phi \\
=& \mu_0 + R\theta\left(\ln\left|\frac{\bar{c}}{1-\bar{c}}\right|\right)+F\phi
\end{aligned} \tag{B.193}$$

The referential flux of the mobile ionic species is defined earlier with Fick's law and is repeated below:

$$\boldsymbol{h} = -\boldsymbol{M}_{mob}\nabla\mu^{e} \tag{B.194}$$

The mobility tensor is defined as a spherical tensor:

$$\boldsymbol{M}_{mob} = m\,(c)\,\boldsymbol{I} \tag{B.195}$$

Equation B.195 is substituted in Equation B.194:

$$\begin{aligned}\boldsymbol{h} =& -\boldsymbol{M}_{mob}\nabla\mu^{e}\\ =& -m\,(c)\,\boldsymbol{I}\nabla\mu^{e}\\ =& -m\,(c)\,\nabla\mu^{e}\end{aligned} \tag{B.196}$$

Here, m represents the effective mobility and is determined by the following expression:

$$m\,(c) = m_0 c\,(1-\bar{c}) \tag{B.197}$$

m_0 is decomposed into a solid electrolyte and electrodeposited lithium part:

$$m_0 = m_0^{SE} + m_0^{M} \tag{B.198}$$

m_0^{SE} and m_0^{M} are related to the diffusivity of each material phase through the standard relation:

$$\begin{aligned}m_0^{SE} =& \frac{D_0^{SE}}{R\theta}\\ m_0^{M} =& \frac{D_0^{M}}{R\theta}\end{aligned} \tag{B.199}$$

B.5.5. Reaction driving force - Electrodeposition Kinetics

The electrochemical potential of the electrodeposited species is defined earlier with Equation B.127. This expression is modified by substituting the microforce balance (Equation B.77).

$$\begin{aligned}\mu^{\xi} =& \frac{\partial\hat{\psi}_x}{\partial\xi} - E\\ =& \frac{\partial\hat{\psi}_x}{\partial\xi} - J^{c}\boldsymbol{M}^{e}\cdot\boldsymbol{N}^{r} + \operatorname{div}(\boldsymbol{g})\end{aligned} \tag{B.200}$$

The vector microstress $\boldsymbol{g}$ is defined earlier in Equation B.122 and is substituted into Equation B.200.

$$\begin{aligned}\mu^{\xi} =& \frac{\partial\hat{\psi}_x}{\partial\xi} - J^{c}\boldsymbol{M}^{e}\cdot\boldsymbol{N}^{r} + \operatorname{div}(\boldsymbol{g})\\ =& \frac{\partial\hat{\psi}_x}{\partial\xi} - J^{c}\boldsymbol{M}^{e}\cdot\boldsymbol{N}^{r} + \operatorname{div}\left(\frac{\partial\hat{\psi}_x}{\partial\nabla\hat{\xi}}\right)\end{aligned} \tag{B.201}$$

In Equation B.201, the expression of the free energy shown in Equation B.148 is now included.

$$\begin{aligned}\mu^{\xi} =& \frac{\partial\hat{\psi}_x}{\partial\xi} - J^{c}\boldsymbol{M}^{e}\cdot\boldsymbol{N}^{r} + \operatorname{div}\left(\frac{\partial\hat{\psi}_x}{\partial\nabla\hat{\xi}}\right)\\ =& \frac{\partial}{\partial\xi}\left(\psi_x^{m+}(\boldsymbol{E},\xi) + \psi_x^{m-}(\boldsymbol{E},\xi)\right) + \frac{\partial}{\partial\xi}\left(W\bar{\xi}^{2}(1-\xi)^{2}\right) + \mu_0^{\xi} + F\phi_0 - J^{c}\boldsymbol{M}^{\boldsymbol{e}}\cdot\boldsymbol{N} - \operatorname{div}(\lambda_{\xi}\nabla\xi)\end{aligned} \tag{B.202}$$

The partial derivatives of ξ with respect to the mechanical free energy are neglected due to their quadratic dependence on elastic strains, which are expected to be much smaller than other terms. As a result, these terms are omitted, simplifying Equation B.202.

$$\begin{aligned}\mu^{\xi} =& \frac{\partial}{\partial\xi}\left(\psi_x^{m+}(\boldsymbol{E},\xi) + \psi_x^{m-}(\boldsymbol{E},\xi)\right) + \frac{\partial}{\partial\xi}\left(W\bar{\xi}^{2}(1-\xi)^{2}\right) + \mu_0^{\xi} + F\phi_0 - J^{c}\boldsymbol{M}^{\boldsymbol{e}}\cdot\boldsymbol{N} - \operatorname{div}(\lambda_{\xi}\nabla\xi)\\ =& \frac{\partial}{\partial\xi}\left(W\bar{\xi}^{2}(1-\xi)^{2}\right) + \mu_0^{\xi} + F\phi_0 - J^{c}\boldsymbol{M}^{\boldsymbol{e}}\cdot\boldsymbol{N} - \operatorname{div}(\lambda_{\xi}\nabla\xi)\end{aligned} \tag{B.203}$$

The thermodynamic driving force $\mathcal{F}$ for electrodeposition is determined by substituting equations Equation B.193 and Equation B.203 into Equation B.129.

$$\begin{aligned}\mathcal{F} =& \mu^{\xi} - \mu^{e} \\ =& \frac{\partial}{\partial \xi}\left(W\bar{\xi}^2(1-\xi)^2\right) + \mu_0^{\xi} + F\phi_0 - J^c \boldsymbol{M}^{\boldsymbol{e}} \cdot \boldsymbol{N} - \operatorname{div}\left(\lambda_\xi \nabla \xi\right) - \mu_0 - R\theta\left(\ln\left|\frac{\bar{c}}{1-\bar{c}}\right|\right) - F\phi \\ =& \underbrace{\left(\mu_0^{\xi} - \mu_0\right)}_{\text{energetic}} \underbrace{- R\theta\left(\ln\left|\frac{\bar{c}}{1-\bar{c}}\right|\right)}_{\text{entropic}} + \underbrace{F\left(\phi_0 - \phi\right)}_{\text{electric}} + \underbrace{\frac{\partial}{\partial \xi}\left(W\bar{\xi}^2(1-\xi)^2\right)}_{\text{energetic barrier}} \underbrace{- J^c h(\bar{\xi}) \boldsymbol{M}^{e} \cdot \boldsymbol{N}^{r}}_{\text{Mechanical}} - \underbrace{\operatorname{div}\left(\lambda \xi \nabla \xi\right)}_{\substack{\text{Numerical} \\ \text{Regularization}}}\end{aligned} \tag{B.204}$$

The terms in Equation B.204 have the following meaning:

1. Energetic → It represents the difference in reference chemical potentials between species transported across the solid host and those within the electrodeposited metallic compound.
2. Entropic → This term captures the influence of configurational entropy. It is crucial to note that an increase in the concentration of ionic species at the reaction sites favors the electrodeposition of lithium, whereas a decrease in lithium concentration impedes electrodeposition.
3. Electric → This factor acts as an electric driving force for electrodeposition, arising from the difference in electric potential between the electrode and the solid conductor at the reaction site.
4. Energetic barrier → This term introduces a localized driving force to the reaction and is linked to the energy barrier between the phases, driving the reaction towards the two minima.
5. Mechanical → This factor accounts for the influence of mechanical stress on the driving force of the reaction. As discussed in subsection B.5.1, only the stress component perpendicular to the electrode-solid conductor interface affects the driving force for electrodeposition. This coupling contrasts with conventional diffusion-deformation theories, which assume an isotropic chemical distortion, where the reaction driving force interacts with mechanics through a compression term. Compressive stresses delay the electrodeposition of metallic compounds, while tensile stresses facilitate plating.

The next topic to discuss is the reaction kinetics equation. Consistent with electrokinetics, a Butler-Volmer non-linear reaction kinetics formulation is used for the evolution of electrodeposition $\bar{\xi}$.

$$\dot{\bar{\xi}} = \begin{cases} R_0\left(e^{\frac{-\alpha\mathcal{F}}{R\theta}} - e^{\frac{(1-\alpha)\mathcal{F}}{R\theta}}\right) & \text{if } 0 < \bar{\xi} < 1 \\ 0, & \text{if } \bar{\xi} = 1 \end{cases} \tag{B.205}$$

In this context, α represents a symmetry factor, indicating the proportion of the surface facilitating either anodic or cathodic reactions at the electrode interface. For single-electron transfer reactions, $\alpha = 0.5$ is commonly used. $R_0 > 0$ signifies a positive-valued reaction constant. It is important to note that Equation B.205 satisfies the dissipation inequality (Equation B.133), ensuring $-\mathcal{F}\dot{\bar{\xi}} \geq 0$. Electrodeposition occurs when $\bar{\xi} > 0$, implying a negative driving force $\mathcal{F} < 0$, which aligns with electrokinetics theory.

B.5.6. Electrostatics

Equation B.186 can also be substituted in Equation B.123:

$$\begin{aligned}\boldsymbol{e} =& \frac{\partial \hat{\psi}_x}{\partial \boldsymbol{d}} \\ =& \frac{1}{J}\frac{1}{2\varepsilon}\frac{\partial}{\partial \boldsymbol{d}}(\boldsymbol{d} \cdot \boldsymbol{C}\boldsymbol{d})\end{aligned} \tag{B.206}$$

The following relation is used to evaluate Equation B.206 further:

$$\nabla(\boldsymbol{u} \cdot \boldsymbol{v}) = (\nabla \boldsymbol{u})^T \boldsymbol{u} + (\nabla \boldsymbol{u})^T \boldsymbol{u} \tag{B.207}$$

Applying Equation B.207 on Equation B.206 gives:

$$\begin{aligned} \boldsymbol{e} =& \frac{1}{J}\frac{1}{2\varepsilon}\frac{\partial}{\partial \boldsymbol{d}}(\boldsymbol{d}\cdot\boldsymbol{C}\boldsymbol{d}) \\ =& \frac{1}{J}\frac{1}{2\varepsilon}\nabla_{\boldsymbol{d}}(\boldsymbol{d}\cdot\boldsymbol{C}\boldsymbol{d}) \\ =& \frac{1}{J}\frac{1}{2\varepsilon}\left((\nabla_{\boldsymbol{d}}\boldsymbol{d})^T\,\boldsymbol{C}\boldsymbol{d} + (\nabla_{\boldsymbol{d}}\boldsymbol{C}\boldsymbol{d})^T\,\boldsymbol{d}\right) \end{aligned} \tag{B.208}$$

The right Cauchy-Green strain tensor does not depend on the electric displacement, allowing it to be taken outside the gradient.

$$\begin{aligned} \boldsymbol{e} =& \frac{1}{J}\frac{1}{2\varepsilon}\left((\nabla_{\boldsymbol{d}}\boldsymbol{d})^T\,\boldsymbol{C}\boldsymbol{d} + (\boldsymbol{C}\nabla_{\boldsymbol{d}}\boldsymbol{d})^T\,\boldsymbol{d}\right) \\ =& \frac{1}{J}\frac{1}{2\varepsilon}\left((\nabla_{\boldsymbol{d}}\boldsymbol{d})^T\,\boldsymbol{C}\boldsymbol{d} + (\nabla_{\boldsymbol{d}}\boldsymbol{d})^T\,\boldsymbol{C}^T\boldsymbol{d}\right) \end{aligned} \tag{B.209}$$

The right Cauchy Green strain tensor is symmetric, and the gradient of the electric displacement is the identity tensor, resulting in the following simplification of Equation B.209:

$$\begin{aligned} \boldsymbol{e} =& \frac{1}{J}\frac{1}{2\varepsilon}\left((\nabla_{\boldsymbol{d}}\boldsymbol{d})^T\,\boldsymbol{C}\boldsymbol{d} + (\boldsymbol{C}\nabla_{\boldsymbol{d}}\boldsymbol{d})^T\,\boldsymbol{d}\right) \\ =& \frac{1}{J}\frac{1}{2\varepsilon}(\boldsymbol{I}\boldsymbol{C}\boldsymbol{d} + \boldsymbol{I}\boldsymbol{C}\boldsymbol{d}) \\ =& \frac{1}{J}\frac{1}{2\varepsilon}(\boldsymbol{C}\boldsymbol{d} + \boldsymbol{C}\boldsymbol{d}) \\ =& \frac{1}{J}\frac{1}{\varepsilon}\boldsymbol{C}\boldsymbol{d} \end{aligned} \tag{B.210}$$

B.6. Governing partial differential equations

The derivation discussed in this chapter resulted in the following set of governing equations:

1. Force balance defined in Equation B.62.

$$\operatorname{div}(\boldsymbol{P}) + \boldsymbol{f} = \boldsymbol{0} \tag{B.211}$$

   Where the first Piola stress tensor is given in Equation B.191.

2. The local balance for the ionic species is given by Equation B.212. In this expression, the flux (Equation B.196) is substituted:

$$\begin{aligned} \dot{c} =& -\operatorname{div}(\boldsymbol{h}) - \dot{\xi} \\ =& \operatorname{div}(m\nabla\mu^e) - \dot{\xi} \end{aligned} \tag{B.212}$$

3. The reaction kinetics shown in Equation B.205 is the governing PDE for the reaction coordinate:

$$\dot{\bar{\xi}} = \begin{cases} R_0\left(e^{\frac{-\alpha\mathcal{F}}{R\theta}} - e^{\frac{(1-\alpha)\mathcal{F}}{R\theta}}\right) & \text{if } 0 < \bar{\xi} < 1 \\ 0, & \text{if } \bar{\xi} = 1 \end{cases} \tag{B.213}$$

   Where the thermodynamic reaction driving force is defined in Equation B.204:

$$\begin{aligned} \mathcal{F} =& \left(\mu_0^{\xi} - \mu_0\right) R\theta\left(\ln\left|\frac{\bar{c}}{1-\bar{c}}\right|\right) + F\left(\phi_0 - \phi\right) + \frac{\partial}{\partial\xi}\left(W\bar{\xi}^2(1-\xi)^2\right) - J^c h(\bar{\xi})\boldsymbol{M}^e\cdot\boldsymbol{N}^r \\ & - \operatorname{div}(\lambda\xi\nabla\xi) \end{aligned} \tag{B.214}$$

4. The electric potential is governed by Gauss's law (Equation B.215), and the electric field. The expression of Gauss's law is finalized by substituting the net charge (Equation B.14) into this law.

$$\begin{aligned} \operatorname{div}(\boldsymbol{d}) &= q \\ &= F(c - c_0) \end{aligned} \tag{B.215}$$

Secondly, the electric field (Equation B.21) is substituted in the expression for the electric displacement (Equation B.210):

$$\begin{aligned} \frac{1}{J}\frac{1}{\varepsilon}\boldsymbol{C}\boldsymbol{d} &= \boldsymbol{e} \\ \boldsymbol{d} &= J\varepsilon\boldsymbol{C}^{-1}\boldsymbol{e} \\ \boldsymbol{d} &= -J\varepsilon\boldsymbol{C}^{-1}\nabla\phi \end{aligned} \tag{B.216}$$

Solving ϕ using Equation B.215 and Equation B.216 is inconvenient because it requires resolving a boundary layer in the range of a few nanometers, where electroneutral deviations occur. Therefore, in practice, electroneutrality is assumed to solve ϕ, ensuring that the net charge $q = F(c - c_0)$ equals zero. This assumption is used to rewrite Equation B.19.

$$\begin{aligned} \dot{q} &= -\operatorname{div}(\boldsymbol{i}) - F\dot{\xi} \\ 0 &= -\operatorname{div}(\boldsymbol{i}) - F\dot{\xi} \\ \operatorname{div}(\boldsymbol{i}) &= -F\dot{\xi} \end{aligned} \tag{B.217}$$

The referential current density, defined below with κ as the conductivity, is as follows:

$$\boldsymbol{i} = -\kappa\nabla\phi \tag{B.218}$$

Equation B.217 and Equation B.218 replaces Equation B.215 and Equation B.216.

C

Principle of virtual power

The derivation of the governing equation uses the principle of virtual power. In this appendix, the principle of virtual work is discussed following the derivations from Gurtin, Fried, and Anand[49].

C.1. Alternative formulation of force and moment balances

This section derives the force and moment balance using the generalized body force by applying different hypotheses. The first hypothesis to be ignored is the Cauchy relation $\boldsymbol{t}(\boldsymbol{n}) = \boldsymbol{T}\boldsymbol{n}$, resulting in the following definition of the generalized external power:

$$\mathcal{W}(\mathcal{R}_t) = \int_{\partial\mathcal{R}_t} \bar{\boldsymbol{t}}(\bar{\boldsymbol{n}}) \cdot \bar{\boldsymbol{v}}\, dA_y + \int_{\mathcal{R}_t} \boldsymbol{b} \cdot \bar{\boldsymbol{v}}\, dV_y \tag{C.1}$$

Now, the time will be fixed, indicating that the arbitrary spatial region no longer depends on time. Additionally, the velocity dependence of the generalized external power will be explicitly stated.

$$\mathcal{W}(\mathcal{R}, \bar{\boldsymbol{v}}) = \int_{\partial\mathcal{R}} \bar{\boldsymbol{t}}(\bar{\boldsymbol{n}}) \cdot \bar{\boldsymbol{v}}\, dA_y + \int_{\mathcal{R}} \boldsymbol{b} \cdot \bar{\boldsymbol{v}}\, dV_y \tag{C.2}$$

A new principle, called the change in frame, is introduced. A change in frame is a mapping of spatial point $\boldsymbol{y}$ to another spatial point $\boldsymbol{y}^*$ and is characterized by a rotation $\boldsymbol{Q}(t)$ and a translation $\boldsymbol{c}(t)$, as described by the expression below:

$$\boldsymbol{y}^* = \boldsymbol{Q}(t)(\boldsymbol{y} - \boldsymbol{0}) + \boldsymbol{c}(t) \tag{C.3}$$

The fixed spatial origin is denoted by $\boldsymbol{0}$. The frame dependence of the deformation gradient can be determined by taking the gradient of the deformation mapping:

$$\begin{aligned}
\boldsymbol{y}^* &= \boldsymbol{Q}(t)(\boldsymbol{y} - \boldsymbol{0}) + \boldsymbol{c}(t) \\
\hat{\boldsymbol{y}}^*(\boldsymbol{x}, t) &= \boldsymbol{Q}(t)(\hat{\boldsymbol{y}}(\boldsymbol{x}, t) - \boldsymbol{0}) + \boldsymbol{c}(t) \\
\nabla\hat{\boldsymbol{y}}^*(\boldsymbol{x}, t) &= \nabla(\boldsymbol{Q}(t)(\hat{\boldsymbol{y}}(\boldsymbol{x}, t) - \boldsymbol{0}) + \boldsymbol{c}(t)) \\
\nabla\hat{\boldsymbol{y}}^*(\boldsymbol{x}, t) &= \boldsymbol{Q}(t)\nabla\hat{\boldsymbol{y}}(\boldsymbol{x}, t) \\
\boldsymbol{F}^*(\boldsymbol{x}, t) &= \boldsymbol{Q}(t)\boldsymbol{F}(\boldsymbol{x}, t)
\end{aligned} \tag{C.4}$$

A variable is frame invariant when it remains unchanged during a change in frame. A vector is frame indifferent if it rotates with the same frame rotation.

The change in velocity due to a change in frame can be determined by taking the material time derivative of the frame change of the deformation mapping:

$$\begin{aligned}
\frac{\partial}{\partial t}(\hat{\boldsymbol{y}}^*(\boldsymbol{x}, t)) &= \frac{\partial}{\partial t}(\boldsymbol{Q}(t)(\hat{\boldsymbol{y}}(\boldsymbol{x}, t) - \boldsymbol{0}) + \boldsymbol{c}(t)) \\
\dot{\hat{\boldsymbol{y}}}^*(\boldsymbol{x}, t) &= \dot{\boldsymbol{Q}}(t)(\hat{\boldsymbol{y}}(\boldsymbol{x}, t) - \boldsymbol{0}) + \boldsymbol{Q}(t)\dot{\hat{\boldsymbol{y}}}(\boldsymbol{x}, t) + \dot{\boldsymbol{c}}(t) \\
\boldsymbol{v}^*(\boldsymbol{x}, t) &= \dot{\boldsymbol{Q}}(t)(\hat{\boldsymbol{y}}(\boldsymbol{x}, t) - \boldsymbol{0}) + \boldsymbol{Q}(t)\boldsymbol{v}(\boldsymbol{x}, t) + \dot{\boldsymbol{c}}(t)
\end{aligned} \tag{C.5}$$

The next step is also to define the frame transform of the velocity gradient:

$$\boldsymbol{L}^{*}\left(\boldsymbol{y}^{*},t\right)=\nabla_{y^{*}}\bar{\boldsymbol{v}}\left(\boldsymbol{y}^{*},t\right) \tag{C.6}$$

The gradient is rewritten using the chain rule:

$$\begin{aligned}\boldsymbol{L}^{*}\left(\boldsymbol{y}^{*},t\right)=&\nabla_{y^{*}}\bar{\boldsymbol{v}}\left(\boldsymbol{y}^{*},t\right)\\ =&\nabla_{y}\bar{\boldsymbol{v}}\left(\boldsymbol{y},t\right)\nabla_{y^{*}}\boldsymbol{y}\end{aligned} \tag{C.7}$$

Both gradient terms of Equation C.7 are separately evaluated further, beginning with $\nabla_{y}\bar{\boldsymbol{v}}$ by substituting Equation C.5 into this term:

$$\begin{aligned}\nabla_{y}\bar{\boldsymbol{v}}\left(\boldsymbol{y},t\right)=&\nabla_{y}\left(\dot{\boldsymbol{Q}}\left(t\right)\left(\hat{\boldsymbol{y}}\left(\boldsymbol{y},t\right)-\boldsymbol{0}\right)+\boldsymbol{Q}\left(t\right)\boldsymbol{v}\left(\boldsymbol{y},t\right)+\dot{\boldsymbol{c}}\left(t\right)\right)\\ =&\dot{\boldsymbol{Q}}\left(t\right)\nabla_{y}\boldsymbol{y}+\boldsymbol{Q}\nabla_{y}\boldsymbol{v}\left(\boldsymbol{y},t\right)\\ =&\dot{\boldsymbol{Q}}\left(t\right)+\boldsymbol{Q}\left(t\right)\boldsymbol{L}\left(\boldsymbol{y},t\right)\end{aligned} \tag{C.8}$$

To analyze the second gradient term of Equation C.7, $\boldsymbol{y}$ must first be written as function of $\boldsymbol{y}^{*}$. The spatial mapping function is used for this, exploiting the fact that $\boldsymbol{Q}$ is orthogonal so that $\boldsymbol{Q}\boldsymbol{Q}^{T}=\boldsymbol{I}$:

$$\begin{aligned}\boldsymbol{y}^{*}=&\boldsymbol{Q}\left(t\right)\left(\boldsymbol{y}-\boldsymbol{0}\right)+\boldsymbol{c}\left(t\right)\\ \boldsymbol{y}=&\boldsymbol{Q}^{T}\left(t\right)\left(\boldsymbol{y}^{*}-\boldsymbol{c}\left(t\right)\right)+\boldsymbol{0}\end{aligned} \tag{C.9}$$

The gradient can now be taken:

$$\nabla_{y^{*}}\boldsymbol{y}=\nabla_{y^{*}}\left(\boldsymbol{Q}^{T}\left(t\right)\left(\boldsymbol{y}^{*}-\boldsymbol{c}\left(t\right)\right)+\boldsymbol{0}\right)=\quad\boldsymbol{Q}^{T}\left(t\right) \tag{C.10}$$

Equation C.8 and Equation C.10 can be substituted into Equation C.7

$$\begin{aligned}\boldsymbol{L}^{*}\left(\boldsymbol{y}^{*},t\right)=&\nabla_{y}\bar{\boldsymbol{v}}\left(\boldsymbol{y},t\right)\nabla_{y^{*}}\boldsymbol{y}\\ =&\left(\dot{\boldsymbol{Q}}\left(t\right)+\boldsymbol{Q}\left(t\right)\boldsymbol{L}\left(\boldsymbol{y},t\right)\right)\boldsymbol{Q}^{T}\left(t\right)\\ =&\boldsymbol{Q}\left(t\right)\boldsymbol{L}\left(\boldsymbol{y},t\right)\boldsymbol{Q}^{T}\left(t\right)+\dot{\boldsymbol{Q}}\left(t\right)\boldsymbol{Q}^{T}\left(t\right)\end{aligned} \tag{C.11}$$

The spin tensor $\boldsymbol{\Omega}$ is introduced, which is defined below:

$$\boldsymbol{\Omega}=\dot{\boldsymbol{Q}}\left(t\right)\boldsymbol{Q}^{T}\left(t\right) \tag{C.12}$$

Equation C.12 is substituted into Equation C.11 to obtain the final expression for the frame change of the velocity gradient:

$$\begin{aligned}\boldsymbol{L}^{*}\left(\boldsymbol{y}^{*},t\right)=&\boldsymbol{Q}\left(t\right)\boldsymbol{L}\left(\boldsymbol{y},t\right)\boldsymbol{Q}^{T}\left(t\right)+\dot{\boldsymbol{Q}}\left(t\right)\boldsymbol{Q}^{T}\left(t\right)\\ =&\boldsymbol{Q}\left(t\right)\boldsymbol{L}\left(\boldsymbol{y},t\right)\boldsymbol{Q}^{T}\left(t\right)+\boldsymbol{\Omega}\end{aligned} \tag{C.13}$$

Returning to the generalized external power, we consider a new frame change from $\mathcal{F}$ to $\mathcal{F}^{*}$, assuming that the traction and body force are frame indifferent, as demonstrated by the following equations:

$$\begin{aligned}\bar{\boldsymbol{t}}^{*}\left(\boldsymbol{n}^{*}\right)&=\boldsymbol{Q}\bar{\boldsymbol{t}}\left(\bar{\boldsymbol{n}}\right)\\ \boldsymbol{b}^{*}&=\boldsymbol{Q}\boldsymbol{b}\end{aligned} \tag{C.14}$$

The power expression in the new frame is assumed to be as follows:

$$\mathcal{W}^{*}\left(\mathcal{R}^{*},\bar{\boldsymbol{v}}^{*}\right)=\int_{\partial\mathcal{R}^{*}}\bar{\boldsymbol{t}}^{*}\left(\bar{\boldsymbol{n}}^{*}\right)\cdot\bar{\boldsymbol{v}}^{*}\,dA_{y}+\int_{\mathcal{R}^{*}}\boldsymbol{b}^{*}\cdot\bar{\boldsymbol{v}}^{*}\,dV_{y} \tag{C.15}$$

First the integrand of the surface integral of Equation C.28 is considered. The earlier obtained expression for $\bar{\boldsymbol{v}}^{*}$ (Equation C.5) and $\bar{\boldsymbol{t}}^{*}$ (Equation C.14) can be substituted in this term:

$$\begin{aligned}\bar{\boldsymbol{t}}^{*}\left(\bar{\boldsymbol{n}}^{*}\right)\cdot\bar{\boldsymbol{v}}^{*}=&\boldsymbol{Q}\bar{\boldsymbol{t}}\left(\bar{\boldsymbol{n}}\right)\cdot\left(\dot{\boldsymbol{Q}}\left(\hat{\boldsymbol{y}}-\boldsymbol{0}\right)+\boldsymbol{Q}\bar{\boldsymbol{v}}+\dot{\boldsymbol{c}}\right)\\ =&\bar{\boldsymbol{t}}\left(\bar{\boldsymbol{n}}\right)\cdot\left(\boldsymbol{Q}^{T}\dot{\boldsymbol{Q}}\left(\hat{\boldsymbol{y}}-\boldsymbol{0}\right)+\boldsymbol{Q}^{T}\boldsymbol{Q}\bar{\boldsymbol{v}}+\boldsymbol{Q}^{T}\dot{\boldsymbol{c}}\right)\end{aligned} \tag{C.16}$$

Utilizing the fact that $\boldsymbol{Q}$ is an orthogonal tensor, the identity tensor can be obtained by multiplying it by its transpose:

$$\begin{aligned}\bar{\boldsymbol{t}}^{*}\left(\bar{\boldsymbol{n}}^{*}\right)\cdot\bar{\boldsymbol{v}}^{*} &= \bar{\boldsymbol{t}}\left(\bar{\boldsymbol{n}}\right)\cdot\left(\boldsymbol{Q}^{T}\dot{\boldsymbol{Q}}\left(\hat{\boldsymbol{y}}-\boldsymbol{0}\right)+\boldsymbol{Q}^{T}\boldsymbol{Q}\bar{\boldsymbol{v}}+\boldsymbol{Q}^{T}\dot{\boldsymbol{c}}\right)\\ &= \bar{\boldsymbol{t}}\left(\bar{\boldsymbol{n}}\right)\cdot\left(\boldsymbol{Q}^{T}\dot{\boldsymbol{Q}}\left(\hat{\boldsymbol{y}}-\boldsymbol{0}\right)+\bar{\boldsymbol{v}}+\boldsymbol{Q}^{T}\dot{\boldsymbol{c}}\right)\end{aligned} \tag{C.17}$$

A new vector $\boldsymbol{r}$ is introduced to simplify Equation C.16:

$$\boldsymbol{r}=\boldsymbol{y}-\boldsymbol{0} \tag{C.18}$$

This vector can now be substituted into Equation C.16:

$$\begin{aligned}\bar{\boldsymbol{t}}^{*}\left(\bar{\boldsymbol{n}}^{*}\right)\cdot\bar{\boldsymbol{v}}^{*} &= \bar{\boldsymbol{t}}\left(\bar{\boldsymbol{n}}\right)\cdot\left(\boldsymbol{Q}^{T}\dot{\boldsymbol{Q}}\left(\hat{\boldsymbol{y}}-\boldsymbol{0}\right)+\bar{\boldsymbol{v}}+\boldsymbol{Q}^{T}\dot{\boldsymbol{c}}\right)\\ &= \bar{\boldsymbol{t}}\left(\bar{\boldsymbol{n}}\right)\cdot\left(\boldsymbol{Q}^{T}\dot{\boldsymbol{Q}}\boldsymbol{r}+\bar{\boldsymbol{v}}+\boldsymbol{Q}^{T}\dot{\boldsymbol{c}}\right)\end{aligned} \tag{C.19}$$

Equation C.26 can be further simplified by introducing the following new vector:

$$\bar{\boldsymbol{w}}\left(\boldsymbol{y},t\right)=\boldsymbol{Q}^{T}\dot{\boldsymbol{c}}+\boldsymbol{Q}^{T}\dot{\boldsymbol{Q}}\boldsymbol{r} \tag{C.20}$$

The term $\boldsymbol{Q}^{T}\dot{\boldsymbol{Q}}$ is considered in more detail. This is facilitated by the orthogonality of $\boldsymbol{Q}$, which ensures the validity of the following relation:

$$\boldsymbol{Q}\boldsymbol{Q}^{T}=\boldsymbol{Q}^{T}\boldsymbol{Q}=I \tag{C.21}$$

The time derivative can be taken from the relation in Equation C.21:

$$\begin{aligned}\frac{\partial}{\partial t}\left(\boldsymbol{Q}^{T}\boldsymbol{Q}\right) &= \frac{\partial}{\partial t}\left(I\right)\\ \dot{\boldsymbol{Q}}^{T}\boldsymbol{Q}+\boldsymbol{Q}^{T}\dot{\boldsymbol{Q}} &= \boldsymbol{0}\\ \boldsymbol{Q}^{T}\dot{\boldsymbol{Q}} &= -\dot{\boldsymbol{Q}}^{T}\boldsymbol{Q}\\ \boldsymbol{Q}^{T}\dot{\boldsymbol{Q}} &= -\left(\boldsymbol{Q}^{T}\dot{\boldsymbol{Q}}\right)^{T}\end{aligned} \tag{C.22}$$

Equation C.22 shows that $\boldsymbol{Q}^{T}\dot{\boldsymbol{Q}}$ is equal to its negative transpose, indicating that this tensor is skew-symmetric. For every skew tensor, there exists an axial tensor $\boldsymbol{\lambda}$ such that the following expression is valid for every $\boldsymbol{r}$:

$$\boldsymbol{Q}^{T}\dot{\boldsymbol{Q}}\boldsymbol{r}=\boldsymbol{\lambda}\times\boldsymbol{r} \tag{C.23}$$

Finally, a new vector α is introduced, defined as follows:

$$\alpha=\boldsymbol{Q}^{T}\dot{\boldsymbol{c}} \tag{C.24}$$

Equation C.23 and Equation C.24 are now substituted in the vector $\bar{\boldsymbol{w}}$ (Equation C.20):

$$\bar{\boldsymbol{w}}\left(\boldsymbol{y},t\right)=\boldsymbol{Q}^{T}\dot{\boldsymbol{c}}+\boldsymbol{Q}^{T}\dot{\boldsymbol{Q}}\boldsymbol{r}=\quad\alpha+ \tag{C.25}$$

Equation C.25 is also known as the rigid velocity field, which can be used in the expression for $\bar{\boldsymbol{t}}^{*}\left(\bar{\boldsymbol{n}}^{*}\right)\cdot\bar{\boldsymbol{v}}^{*}$ Equation C.26:

$$\begin{aligned}\bar{\boldsymbol{t}}^{*}\left(\bar{\boldsymbol{n}}^{*}\right)\cdot\bar{\boldsymbol{v}}^{*} &= \bar{\boldsymbol{t}}\left(\bar{\boldsymbol{n}}\right)\cdot\left(\boldsymbol{Q}^{T}\dot{\boldsymbol{Q}}\boldsymbol{r}+\bar{\boldsymbol{v}}+\boldsymbol{Q}^{T}\dot{\boldsymbol{c}}\right)\\ &= \bar{\boldsymbol{t}}\left(\bar{\boldsymbol{n}}\right)\cdot\left(\bar{\boldsymbol{v}}+\bar{\boldsymbol{w}}\right)\end{aligned} \tag{C.26}$$

The same process is repeated for the second term of the power expression $\boldsymbol{b}^{*}\cdot\bar{\boldsymbol{v}}^{*}$:

$$\begin{aligned}\bar{\boldsymbol{b}}^{*}\cdot\bar{\boldsymbol{v}}^{*} &= \boldsymbol{Q}\bar{\boldsymbol{b}}\cdot\left(\dot{\boldsymbol{Q}}\left(\hat{\boldsymbol{y}}-\boldsymbol{0}\right)+\boldsymbol{Q}\bar{\boldsymbol{v}}+\dot{\boldsymbol{c}}\right)\\ &= \bar{\boldsymbol{b}}\cdot\left(\boldsymbol{Q}^{T}\dot{\boldsymbol{Q}}\boldsymbol{r}+\boldsymbol{Q}^{T}\boldsymbol{Q}\bar{\boldsymbol{v}}+\boldsymbol{Q}^{T}\dot{\boldsymbol{c}}\right)\\ &= \bar{\boldsymbol{b}}\cdot\left(\bar{\boldsymbol{v}}+\boldsymbol{Q}^{T}\dot{\boldsymbol{c}}+\boldsymbol{Q}^{T}\dot{\boldsymbol{Q}}\boldsymbol{r}\right)\\ &= \bar{\boldsymbol{b}}\cdot\left(\bar{\boldsymbol{v}}+\bar{\boldsymbol{w}}\right)\end{aligned} \tag{C.27}$$

The expressions for $\bar{\boldsymbol{t}}^* \cdot \bar{\boldsymbol{v}}^*$ (Equation C.26) and $\boldsymbol{b}^* \cdot \bar{\boldsymbol{v}}^*$ (Equation C.27) are substituted in the power expression of the new frame (Equation C.28):

$$\begin{aligned} \mathcal{W}^*\left(\mathcal{R}^*, \bar{\boldsymbol{v}}^*\right) &= \int_{\partial \mathcal{R}^*} \bar{\boldsymbol{t}}^*\left(\bar{\boldsymbol{n}}^*\right) \cdot \bar{\boldsymbol{v}}^* \, dA_{y^*} + \int_{\mathcal{R}^*} \boldsymbol{b}^* \cdot \bar{\boldsymbol{v}}^* \, dV_{y^*} \\ &= \int_{\partial \mathcal{R}^*} \bar{\boldsymbol{t}}\left(\bar{\boldsymbol{n}}\right) \cdot \left(\bar{\boldsymbol{v}} + \bar{\boldsymbol{w}}\right) \, dA_{y^*} + \int_{\mathcal{R}^*} \bar{\boldsymbol{b}} \cdot \left(\bar{\boldsymbol{v}} + \bar{\boldsymbol{w}}\right) \, dV_{y^*} \end{aligned} \tag{C.28}$$

The expression can be split into a velocity and rigid velocity field:

$$\begin{aligned} \mathcal{W}^*\left(\mathcal{R}^*, \bar{\boldsymbol{v}}^*\right) &= \int_{\partial \mathcal{R}^*} \bar{\boldsymbol{t}}^*\left(\bar{\boldsymbol{n}}^*\right) \cdot \bar{\boldsymbol{v}}^* \, dA_{y^*} + \int_{\mathcal{R}^*} \boldsymbol{b}^* \cdot \bar{\boldsymbol{v}}^* \, dV_{y^*} \\ &= \int_{\partial \mathcal{R}} \bar{\boldsymbol{t}}\left(\bar{\boldsymbol{n}}\right) \cdot \bar{\boldsymbol{v}} \, dA_y + \int_{\mathcal{R}} \bar{\boldsymbol{b}} \cdot \bar{\boldsymbol{v}} \, dV_y + \int_{\partial \mathcal{R}} \bar{\boldsymbol{t}}\left(\bar{\boldsymbol{n}}\right) \cdot \bar{\boldsymbol{w}} \, dA_y + \int_{\mathcal{R}} \bar{\boldsymbol{b}} \cdot \bar{\boldsymbol{w}} \, dV_y \\ &= \mathcal{W}\left(\mathcal{R}, \bar{\boldsymbol{v}}\right) + \mathcal{W}\left(\mathcal{R}, \bar{\boldsymbol{w}}\right) \end{aligned} \tag{C.29}$$

Where:

$$\mathcal{W}\left(\mathcal{R}, \bar{\boldsymbol{w}}\right) = \mathcal{W}_{rig}\left(\mathcal{R}, \bar{\boldsymbol{w}}\right) = \int_{\partial \mathcal{R}} \bar{\boldsymbol{t}}\left(\bar{\boldsymbol{n}}\right) \cdot \bar{\boldsymbol{w}} \, dA_y + \int_{\mathcal{R}} \bar{\boldsymbol{b}} \cdot \bar{\boldsymbol{w}} \, dV_y \tag{C.30}$$

This implies that $\mathcal{W}_{rig}\left(\mathcal{R}, \bar{\boldsymbol{w}}\right) = 0$ if and only if the power is frame indifferent:

$$\mathcal{W}^*\left(\mathcal{R}^*, \bar{\boldsymbol{v}}^*\right) = \mathcal{W}\left(\mathcal{R}, \bar{\boldsymbol{v}}\right) \tag{C.31}$$

So, it can be concluded that the generalized external power is frame-indifferent if and only if the force and moment balances are satisfied.

The generalized external power is introduced below, with the assumption that time remains fixed once again.

$$\int_{\partial \mathcal{R}} \bar{\boldsymbol{t}}\left(\bar{\boldsymbol{n}}\right) \cdot \bar{\boldsymbol{v}} \, dA_y + \int_{\mathcal{R}} \boldsymbol{b} \cdot \bar{\boldsymbol{v}} \, dV_y = \int_{\mathcal{R}} \boldsymbol{T} \cdot \nabla \bar{\boldsymbol{v}} \, dV_y \tag{C.32}$$

In Equation C.32, the left-hand side represents the external power $\mathcal{W}\left(\mathcal{R}\right)$, and the right-hand side represents the internal power $\mathcal{I}\left(\mathcal{R}\right)$. The power balance described above is analyzed with a virtual velocity field independent of the actual velocity field $\bar{\boldsymbol{v}}$. To clarify, the actual velocity $\bar{\boldsymbol{v}}$ is replaced by its virtual counterpart $\tilde{\boldsymbol{v}}$. The time remains fixed, allowing the virtual fields to be arbitrary functions $\tilde{\boldsymbol{v}}\left(\boldsymbol{y}\right)$. Furthermore, the spatial region $\mathcal{R}$ is a subregion of the deformed body $\mathcal{B}$, which also remains fixed in time. Consequently, the following expressions for virtual external and internal power are obtained:

$$\begin{aligned} \mathcal{W}\left(\mathcal{R}, \tilde{\boldsymbol{v}}\right) &= \int_{\partial \mathcal{R}} \bar{\boldsymbol{t}}\left(\bar{\boldsymbol{n}}\right) \cdot \tilde{\boldsymbol{v}} \, dA_y + \int_{\mathcal{R}} \boldsymbol{b} \cdot \tilde{\boldsymbol{v}} \, dV_y \\ \mathcal{I}\left(\mathcal{R}, \tilde{\boldsymbol{v}}\right) &= \int_{\mathcal{R}} \boldsymbol{T} \cdot \nabla \tilde{\boldsymbol{v}} \, dV_y \end{aligned} \tag{C.33}$$

Equalizing the virtual internal and external power gives the virtual power balance.

$$\begin{aligned} \mathcal{W}\left(\mathcal{R}, \tilde{\boldsymbol{v}}\right) &= \mathcal{I}\left(\mathcal{R}, \tilde{\boldsymbol{v}}\right) \\ \int_{\partial \mathcal{R}} \bar{\boldsymbol{t}}\left(\bar{\boldsymbol{n}}\right) \cdot \tilde{\boldsymbol{v}} \, dA_y + \int_{\mathcal{R}} \boldsymbol{b} \cdot \tilde{\boldsymbol{v}} \, dV_y &= \int_{\mathcal{R}} \boldsymbol{T} \cdot \nabla \tilde{\boldsymbol{v}} \, dV_y \end{aligned} \tag{C.34}$$

The next step is to demonstrate that the virtual power balance described in Equation C.34 encloses both the balance of linear momentum and Cauchy's relation. Establishing the following relation is necessary for this demonstration:

$$\begin{aligned} \operatorname{div}\left(\boldsymbol{A}^T \boldsymbol{u}\right) &= \boldsymbol{A} \cdot \nabla \boldsymbol{u} + \operatorname{div}\left(\boldsymbol{A}\right) \cdot \boldsymbol{u} \\ \boldsymbol{A} \cdot \nabla \boldsymbol{u} &= \operatorname{div}\left(\boldsymbol{A}^T \boldsymbol{u}\right) - \operatorname{div}\left(\boldsymbol{A}\right) \cdot \boldsymbol{u} \end{aligned} \tag{C.35}$$

Equation C.35 can be applied to the virtual internal energy:

$$\begin{aligned}\mathcal{I}(\mathcal{R},\tilde{\boldsymbol{v}}) &= \int_{\mathcal{R}} \boldsymbol{T}\cdot\nabla\tilde{\boldsymbol{v}}\, dV_y \\ &= \int_{\mathcal{R}} \operatorname{div}\left(\boldsymbol{T}^T\tilde{\boldsymbol{v}}\right)\, dV_y - \int_{\mathcal{R}} \operatorname{div}(\boldsymbol{T})\cdot\tilde{\boldsymbol{v}}\, dV_y\end{aligned} \tag{C.36}$$

The divergence rule for a vector can be applied to the first term.

$$\begin{aligned}\mathcal{I}(\mathcal{R},\tilde{\boldsymbol{v}}) &= \int_{\mathcal{R}} \operatorname{div}\left(\boldsymbol{T}^T\tilde{\boldsymbol{v}}\right)\, dV_y - \int_{\mathcal{R}} \operatorname{div}(\boldsymbol{T})\cdot\tilde{\boldsymbol{v}}\, dV_y \\ &= \int_{\mathcal{R}} \boldsymbol{T}^T\tilde{\boldsymbol{v}}\cdot\bar{\boldsymbol{n}}\, dA_y - \int_{\mathcal{R}} \operatorname{div}(\boldsymbol{T})\cdot\tilde{\boldsymbol{v}}\, dV_y \\ &= \int_{\mathcal{R}} \boldsymbol{T}\bar{\boldsymbol{n}}\cdot\tilde{\boldsymbol{v}}\, dA_y - \int_{\mathcal{R}} \operatorname{div}(\boldsymbol{T})\cdot\tilde{\boldsymbol{v}}\, dV_y\end{aligned} \tag{C.37}$$

The rewritten version of the internal energy is employed in the power balance equation (Equation C.35), and the expression is subsequently rearranged.

$$\begin{aligned}&\mathcal{W}(\mathcal{R},\tilde{\boldsymbol{v}}) = \mathcal{I}(\mathcal{R},\tilde{\boldsymbol{v}}) \\ &\int_{\partial\mathcal{R}} \bar{\boldsymbol{t}}(\bar{\boldsymbol{n}})\cdot\tilde{\boldsymbol{v}}\, dA_y + \int_{\mathcal{R}} \boldsymbol{b}\cdot\tilde{\boldsymbol{v}}\, dV_y = \int_{\mathcal{R}} \boldsymbol{T}\bar{\boldsymbol{n}}\cdot\tilde{\boldsymbol{v}}\, dA_y - \int_{\mathcal{R}} \operatorname{div}(\boldsymbol{T})\cdot\tilde{\boldsymbol{v}}\, dV_y \\ &\int_{\mathcal{R}} \operatorname{div}(\boldsymbol{T})\cdot\tilde{\boldsymbol{v}}\, dV_y + \int_{\mathcal{R}} \boldsymbol{b}\cdot\tilde{\boldsymbol{v}}\, dV_y + \int_{\partial\mathcal{R}} \bar{\boldsymbol{t}}(\bar{\boldsymbol{n}})\cdot\tilde{\boldsymbol{v}}\, dA_y - \int_{\mathcal{R}} \boldsymbol{T}\bar{\boldsymbol{n}}\cdot\tilde{\boldsymbol{v}}\, dA_y = 0 \\ &\int_{\mathcal{R}} (\operatorname{div}(\boldsymbol{T}) + \boldsymbol{b})\cdot\tilde{\boldsymbol{v}}\, dV_y + \int_{\partial\mathcal{R}} (\bar{\boldsymbol{t}}(\bar{\boldsymbol{n}}) - \boldsymbol{T}\bar{\boldsymbol{n}})\cdot\tilde{\boldsymbol{v}}\, dA_y = 0\end{aligned} \tag{C.38}$$

Now, the fundamental lemma of the calculus of variations is employed, which is stated as follows: Let $\boldsymbol{f}$ be a continuous vector field on $\mathcal{R}$, and let $\boldsymbol{h}$ be a continuous vector field on the smooth subsurface $\mathcal{S}$ of $\partial\mathcal{R}$, assuming that for all continuous vector fields, ϕ, on $\mathcal{R}$ that vanish on $\partial\mathcal{B}\setminus\mathcal{S}$.:

$$\int_{\mathcal{R}} \boldsymbol{f}\cdot\boldsymbol{\phi}\, dV + \int_{\mathcal{S}} \boldsymbol{h}\cdot\boldsymbol{\phi}\, dA = 0 \tag{C.39}$$

In that case:

$$\boldsymbol{f} \equiv \boldsymbol{0} \text{ in } \mathcal{R} \quad \text{and} \quad \boldsymbol{h} = \boldsymbol{0} \text{ on } \mathcal{S} \tag{C.40}$$

Applying this to the power balance, $\mathcal{S}$ becomes $\partial\mathcal{R}$, $\boldsymbol{\phi} = \tilde{\boldsymbol{v}}$, and the Lemma yields the following relations:

$$\begin{aligned}\operatorname{div}(\boldsymbol{T}) + \boldsymbol{b} &= \boldsymbol{0} \\ \bar{\boldsymbol{t}}(\bar{\boldsymbol{n}}) - \boldsymbol{T}\bar{\boldsymbol{n}} &= 0\end{aligned} \tag{C.41}$$

It is now important to demonstrate that the Cauchy stress tensor $\boldsymbol{T}$ is both symmetric and frame indifferent, ensuring that the virtual internal power $\mathcal{I}(\mathcal{R},\tilde{\boldsymbol{v}})$ remains invariant under changes of frame. This requires defining a mapping function $\boldsymbol{\phi}$ for arbitrary frame transformations while keeping time fixed.

$$\begin{aligned}\boldsymbol{\phi}(\boldsymbol{y}) &= \boldsymbol{y}^* \\ &= \boldsymbol{Q}(\boldsymbol{y}-\boldsymbol{0}) + \boldsymbol{c}\end{aligned} \tag{C.42}$$

To enhance clarity in the remaining discussion, the spatial arguments are no longer suppressed, resulting in the following expression for the internal power:

$$\mathcal{I}(\mathcal{R},\tilde{\boldsymbol{v}}) = \int_{\mathcal{R}} \boldsymbol{T}(\boldsymbol{y})\cdot\nabla_{\boldsymbol{y}}\tilde{\boldsymbol{v}}(\boldsymbol{y})\, dV_y \tag{C.43}$$

Introducing now the virtual velocity gradient:

$$\tilde{\boldsymbol{L}}(\boldsymbol{y}) = \nabla_{\boldsymbol{y}}\tilde{\boldsymbol{v}}(\boldsymbol{y}) \tag{C.44}$$

The transformed velocity gradient, previously defined by Equation C.13, can now be used in terms of the virtual velocity gradient.

$$\tilde{\boldsymbol{L}}^{*}\left(\boldsymbol{y}^{*}\right)=\boldsymbol{Q}\tilde{\boldsymbol{L}}\left(\boldsymbol{y}\right)\boldsymbol{Q}^{T}+\boldsymbol{\Omega} \tag{C.45}$$

With the introduction of the transformed velocity gradient, it becomes possible to demonstrate the frame-indifference of the internal energy. When the internal energy exhibits frame indifference, the following expression holds true:

$$\begin{aligned}\mathcal{I}\left(\mathcal{R}^{*},\tilde{\boldsymbol{v}}^{*}\right)=&\mathcal{I}\left(\mathcal{R},\tilde{\boldsymbol{v}}\right)\\ \int_{\mathcal{R}^{*}}\boldsymbol{T}^{*}\left(\boldsymbol{y}^{*}\right)\cdot\nabla_{\boldsymbol{y}^{*}}\tilde{\boldsymbol{v}}^{*}\left(\boldsymbol{y}^{*}\right)\,dV_{y^{*}}=&\int_{\mathcal{R}}\boldsymbol{T}\left(\boldsymbol{y}\right)\cdot\nabla_{\boldsymbol{y}}\tilde{\boldsymbol{v}}\left(\boldsymbol{y}\right)\,dV_{y}\\ \int_{\mathcal{R}^{*}}\boldsymbol{T}^{*}\left(\boldsymbol{y}^{*}\right)\cdot\tilde{\boldsymbol{L}}^{*}\left(\boldsymbol{y}^{*}\right)\,dV_{y^{*}}=&\int_{\mathcal{R}}\boldsymbol{T}\left(\boldsymbol{y}\right)\cdot\tilde{\boldsymbol{L}}\left(\boldsymbol{y}\right)\,dV_{y}\end{aligned} \tag{C.46}$$

A closer look will be given to the transformed internal energy, with the expression for the transformed velocity gradient substituted into this term.

$$\begin{aligned}\mathcal{I}\left(\mathcal{R}^{*},\tilde{\boldsymbol{v}}^{*}\right)&=\int_{\mathcal{R}^{*}}\boldsymbol{T}^{*}\left(\boldsymbol{y}^{*}\right)\cdot\tilde{\boldsymbol{L}}^{*}\left(\boldsymbol{y}^{*}\right)\,dV_{y^{*}}\\ &=\int_{\mathcal{R}^{*}}\boldsymbol{T}^{*}\left(\boldsymbol{y}^{*}\right)\cdot\left(\boldsymbol{Q}\tilde{\boldsymbol{L}}\left(\boldsymbol{\phi}^{-1}\left(\boldsymbol{y}^{*}\right)\right)\boldsymbol{Q}^{T}+\boldsymbol{\Omega}\right)\,dV_{y^{*}}\end{aligned} \tag{C.47}$$

To express $\mathcal{I}\left(\mathcal{R}^{*},\tilde{\boldsymbol{v}}^{*}\right)$ as a function of $\boldsymbol{y}$, it is necessary to transfer $dV_{y^{*}}$ to dV_{y}. The Jacobian is required for this transfer, as it represents the relationship between these two variables and can be obtained by calculating the determinant of the gradient of this deformation.

$$\begin{aligned}J=&\det\left(\nabla_{y}\phi\left(\boldsymbol{y}\right)\right)\\ =&\det\left(\nabla_{y}\left(\boldsymbol{Q}\left(\boldsymbol{y}-\boldsymbol{0}\right)+\boldsymbol{c}\right)\right)\\ =&\det\left(\boldsymbol{Q}\right)\end{aligned} \tag{C.48}$$

Orthogonal tensors, like $\boldsymbol{Q}$, have a determinant equal to 1. Consequently, the Jacobian becomes 1, indicating that $dV_{y^{*}}$ and dV_{y} are equal. This allows for the rewriting of $\mathcal{I}\left(\mathcal{R}^{*},\tilde{\boldsymbol{v}}^{*}\right)$ accordingly.

$$\begin{aligned}\mathcal{I}\left(\mathcal{R}^{*},\tilde{\boldsymbol{v}}^{*}\right)&=\int_{\mathcal{R}^{*}}\boldsymbol{T}^{*}\left(\boldsymbol{y}^{*}\right)\cdot\left(\boldsymbol{Q}\tilde{\boldsymbol{L}}\left(\boldsymbol{\phi}^{-1}\left(\boldsymbol{y}^{*}\right)\right)\boldsymbol{Q}^{T}+\boldsymbol{\Omega}\right)\,dV_{y^{*}}\\ &=\int_{\mathcal{R}^{*}}\boldsymbol{T}^{*}\left(\boldsymbol{\phi}\left(\boldsymbol{y}\right)\right)\cdot\left(\boldsymbol{Q}\tilde{\boldsymbol{L}}\left(\boldsymbol{y}\right)\boldsymbol{Q}^{T}+\boldsymbol{\Omega}\right)\,dV_{y}\end{aligned} \tag{C.49}$$

This expression is substituted into the frame indifference requirement of the internal energy.

$$\begin{aligned}\mathcal{I}\left(\mathcal{R}^{*},\tilde{\boldsymbol{v}}^{*}\right)=&\mathcal{I}\left(\mathcal{R},\tilde{\boldsymbol{v}}\right)\\ \int_{\mathcal{R}^{*}}\boldsymbol{T}^{*}\left(\boldsymbol{\phi}\left(\boldsymbol{y}\right)\right)\cdot\left(\boldsymbol{Q}\tilde{\boldsymbol{L}}\left(\boldsymbol{y}\right)\boldsymbol{Q}^{T}+\boldsymbol{\Omega}\right)\,dV_{y}=&\int_{\mathcal{R}}\boldsymbol{T}\left(\boldsymbol{y}\right)\cdot\tilde{\boldsymbol{L}}\left(\boldsymbol{y}\right)\,dV_{y}\end{aligned} \tag{C.50}$$

Equation C.50 is localized, and for clarity, the arguments of all the terms are suppressed again, as no transfers of domains are considered anymore.

$$\begin{aligned}\boldsymbol{T}\cdot\tilde{\boldsymbol{L}}=&\boldsymbol{T}^{*}\cdot\left(\boldsymbol{Q}\tilde{\boldsymbol{L}}\boldsymbol{Q}^{T}+\boldsymbol{\Omega}\right)\\ =&\boldsymbol{Q}^{T}\boldsymbol{T}^{*}\boldsymbol{Q}\cdot\tilde{\boldsymbol{L}}+\boldsymbol{T}^{*}\cdot\boldsymbol{\Omega}\end{aligned} \tag{C.51}$$

When considering a frame change with a constant $\boldsymbol{Q}$, $\boldsymbol{\Omega}$ becomes zero, simplifying Equation C.51 to the following expression:

$$\begin{aligned}\boldsymbol{T}\cdot\tilde{\boldsymbol{L}}=&\boldsymbol{Q}^{T}\boldsymbol{T}^{*}\boldsymbol{Q}\cdot\tilde{\boldsymbol{L}}+\boldsymbol{T}^{*}\cdot\boldsymbol{\Omega}\\ \left(\boldsymbol{T}-\boldsymbol{Q}^{T}\boldsymbol{T}^{*}\boldsymbol{Q}\right)\cdot\tilde{\boldsymbol{L}}=&0\end{aligned} \tag{C.52}$$

So, for arbitrary $\tilde{\boldsymbol{L}}$, the following applies:

$$\begin{aligned} \boldsymbol{T} - \boldsymbol{Q}^T \boldsymbol{T}^* \boldsymbol{Q} &= \boldsymbol{0} \\ \boldsymbol{T}^* &= \boldsymbol{Q} \boldsymbol{T} \boldsymbol{Q}^T \end{aligned} \tag{C.53}$$

Equation C.53 demonstrates that the Cauchy stress tensor is frame indifferent. This result can be substituted back into Equation C.51.

$$\begin{aligned} \boldsymbol{T} \cdot \tilde{\boldsymbol{L}} &= \boldsymbol{Q}^T \boldsymbol{T}^* \boldsymbol{Q} \cdot \tilde{\boldsymbol{L}} + \boldsymbol{T}^* \cdot \boldsymbol{\Omega} \\ \boldsymbol{T} \cdot \tilde{\boldsymbol{L}} &= \boldsymbol{Q}^T \boldsymbol{Q} \boldsymbol{T} \boldsymbol{Q}^T \boldsymbol{Q} \cdot \tilde{\boldsymbol{L}} + \boldsymbol{T}^* \cdot \boldsymbol{\Omega} \\ \boldsymbol{T} \cdot \tilde{\boldsymbol{L}} &= \boldsymbol{T} \cdot \tilde{\boldsymbol{L}} + \boldsymbol{T}^* \cdot \boldsymbol{\Omega} \\ \boldsymbol{T}^* \cdot \boldsymbol{\Omega} &= 0 \end{aligned} \tag{C.54}$$

The skew-symmetry of $\boldsymbol{\Omega}$ can be utilized to rewrite Equation C.54.

$$\begin{aligned} \boldsymbol{T}^* \cdot \boldsymbol{\Omega} &= 0 \\ \boldsymbol{T}^* \cdot \frac{1}{2} \left(\boldsymbol{\Omega} - \boldsymbol{\Omega}^T \right) &= 0 \\ \boldsymbol{T}^* \cdot \boldsymbol{\Omega} &= \boldsymbol{T}^* \cdot \boldsymbol{\Omega}^T \end{aligned} \tag{C.55}$$

The rules of the Tensor scalar product are used to rewrite Equation C.55 further:

$$\begin{aligned} \boldsymbol{T}^* \cdot \boldsymbol{\Omega} &= \boldsymbol{T}^* \cdot \boldsymbol{\Omega}^T \\ \boldsymbol{T}^* \cdot \boldsymbol{\Omega} &= \boldsymbol{T}^{*T} \cdot \boldsymbol{\Omega} \\ \boldsymbol{T}^* &= \boldsymbol{T}^{*T} \end{aligned} \tag{C.56}$$

So, Equation C.56 presents a different demonstration of the symmetry of the Cauchy stress tensor, assuming its frame indifference. This implies that the virtual power balance is fulfilled for any subregion $\mathcal{R}$ of the deformed body and for all choices of the virtual velocity $\tilde{\boldsymbol{v}}$. At all points of the deformed body, the following conditions apply:

- Stress $\boldsymbol{T}$ and traction $\bar{\boldsymbol{t}}\,(\bar{\boldsymbol{n}})$ are related by Cauchy's relation
$$\bar{\boldsymbol{t}}\,(\bar{\boldsymbol{n}}) = \boldsymbol{T}$$
- $\boldsymbol{T}$ and $\boldsymbol{b}$ satisfy the local balance of linear and angular momentum
$$\operatorname{div}(\boldsymbol{T}) + \boldsymbol{b} = \boldsymbol{0}$$
$$\boldsymbol{T} = \boldsymbol{T}^T$$
- $\boldsymbol{T}$ is frame indifferent under any frame change
$$\boldsymbol{T}^* = \boldsymbol{Q} \boldsymbol{T} \boldsymbol{Q}^T$$

C.2. Conventional theory based on the principle of virtual power

The previous section demonstrated that power expansion introduces stresses, body forces, and surface tractions, deriving unknown local force balances using virtual power. This section provides an example of deriving local force balances for plasticity. To achieve this, the decomposition of the deformation gradient into an elastic and plastic part, denoted respectively as $\boldsymbol{H}^e$ and $\boldsymbol{H}^p$ is initiated.

$$\nabla \boldsymbol{u} = \boldsymbol{H}^e + \boldsymbol{H}^p \tag{C.57}$$

The strain and rotation displacement are defined below:

$$\begin{aligned} \boldsymbol{E} &= \frac{1}{2} \left(\nabla \boldsymbol{u} + (\nabla \boldsymbol{u})^T \right) \\ \boldsymbol{W} &= \frac{1}{2} \left(\nabla \boldsymbol{u} - (\nabla \boldsymbol{u})^T \right) \end{aligned} \tag{C.58}$$

This means that the displacement gradient can also be written in the following way:

$$\nabla \boldsymbol{u} = \boldsymbol{E} + \boldsymbol{W} \tag{C.59}$$

This shows that the strain is the symmetric part of the displacement gradient, while the rotations are the skew-symmetric part. Therefore, the elastic and plastic strain and rotation can be obtained by respectively taking the symmetric and skew-symmetric parts of the elastic and plastic distortion.

$$\begin{aligned} \boldsymbol{E} &= \boldsymbol{E}^e + \boldsymbol{E}^p \\ \boldsymbol{W} &= \boldsymbol{W}^e + \boldsymbol{W}^p \end{aligned} \tag{C.60}$$

A final observation to note is that $\boldsymbol{H}^p$ is deviatoric, indicating that the plastic deformations do not lead to volume changes. This observation results in the following expression:

$$\operatorname{tr}(\boldsymbol{H}^p) = \operatorname{tr}(\boldsymbol{E}^p) = 0 \tag{C.61}$$

Now, returning to the virtual power formulation. This principle is based on the notion that each independent rate-like kinematic descriptor yields a power expansion, which can be described in terms of a corresponding force system consistent with its own balance. However, the fundamental "rate-like" descriptors, namely, velocity $\boldsymbol{v} = \dot{\boldsymbol{u}}$, and elastic and plastic distortions, $\dot{\boldsymbol{H}}^e$ and $\dot{\boldsymbol{H}}^p$, respectively, are not independent due to the constraints imposed by the following expressions:

$$\begin{aligned} \nabla \dot{\boldsymbol{u}} &= \dot{\boldsymbol{H}}^e + \dot{\boldsymbol{H}}^p \\ \operatorname{tr}\left(\dot{\boldsymbol{H}}^p\right) &= 0 \end{aligned} \tag{C.62}$$

The virtual power principle is based on the balance between internal and external power. In the previous section, internal power was described using the stress power $\boldsymbol{T} \cdot \nabla \dot{\boldsymbol{u}}$. However, now the kinematical processes are divided into elastic and plastic distortion rates, $\dot{\boldsymbol{H}}^e$ and $\dot{\boldsymbol{H}}^p$, respectively. The power conjugates of these tensors are the elastic stress tensor $\boldsymbol{T}^e$ and plastic stress tensor $\boldsymbol{T}^p$, resulting in the following internal power:

$$\mathcal{I}(\mathcal{R}_t) = \int_{\mathcal{R}_t} \boldsymbol{T}^e \cdot \dot{\boldsymbol{H}}^e + \boldsymbol{T}^p \cdot \dot{\boldsymbol{H}}^p \, dV_y \tag{C.63}$$

The external power remains unchanged from before and is shown in Equation C.1, leading to the following power balance:

$$\begin{gathered} \mathcal{W}(\mathcal{R}_t) = \mathcal{I}(\mathcal{R}_t) \\ \int_{\partial \mathcal{R}_t} \bar{\boldsymbol{t}}(\bar{\boldsymbol{n}}) \cdot \dot{\tilde{\boldsymbol{u}}} \, dA_y + \int_{\mathcal{R}_t} \boldsymbol{b} \cdot \dot{\tilde{\boldsymbol{u}}} \, dV_y = \int_{\mathcal{R}_t} \boldsymbol{T}^e \cdot \dot{\boldsymbol{H}}^e + \boldsymbol{T}^p \cdot \dot{\boldsymbol{H}}^p \, dV_y \end{gathered} \tag{C.64}$$

The fields $\dot{\tilde{\boldsymbol{u}}}$, $\dot{\boldsymbol{H}}^e$, and $\dot{\boldsymbol{H}}^p$ are considered at some arbitrary but fixed time, specified as virtual velocities in a consistent manner, meeting the constraints shown in Equation C.62. These virtual velocities are distinguished from the actual velocities by denoting these properties as $\tilde{\boldsymbol{u}}$, $\tilde{\boldsymbol{H}}^e$, and $\tilde{\boldsymbol{H}}^p$. The constraints can also be denoted using the virtual velocities:

$$\begin{aligned} \nabla \tilde{\boldsymbol{u}} &= \tilde{\boldsymbol{H}}^e + \tilde{\boldsymbol{H}}^p \\ \operatorname{tr}\left(\tilde{\boldsymbol{H}}^p\right) &= 0 \end{aligned} \tag{C.65}$$

A generalized virtual velocity is defined as a list comprising all the virtual velocities.

$$\mathcal{V} = \left(\tilde{\boldsymbol{u}}, \tilde{\boldsymbol{H}}^e, \tilde{\boldsymbol{H}}^p\right) \tag{C.66}$$

The virtual power balance is obtained by using the virtual velocities:

$$\begin{gathered} \mathcal{W}(\mathcal{R}) = \mathcal{I}(\mathcal{R}) \\ \int_{\partial \mathcal{R}} \bar{\boldsymbol{t}}(\bar{\boldsymbol{n}}) \cdot \tilde{\boldsymbol{u}} \, dA_y + \int_{\mathcal{R}} \boldsymbol{b} \cdot \tilde{\boldsymbol{u}} \, dV_y = \int_{\mathcal{R}} \boldsymbol{T}^e \cdot \tilde{\boldsymbol{H}}^e + \boldsymbol{T}^p \cdot \tilde{\boldsymbol{H}}^p \, dV_y \end{gathered} \tag{C.67}$$

The internal power must remain frame invariant under transformations of the form below:

$$\tilde{\boldsymbol{H}}^{e*} = \tilde{\boldsymbol{H}}^{e} + \boldsymbol{\Omega} \quad \text{and} \quad \tilde{\boldsymbol{H}}^{p*} = \tilde{\boldsymbol{H}}^{p} \tag{C.68}$$

It has been previously demonstrated that $\boldsymbol{T}$ is symmetric when $\boldsymbol{T} \cdot \boldsymbol{\Omega} = 0$. The same principle applies to $\boldsymbol{T}^e$, indicating that $\boldsymbol{T}^e$ is symmetric when $\boldsymbol{T}^e \cdot \boldsymbol{\Omega} = 0$. This condition has the following effect on the elastic part of the internal power:

$$\int_{\mathcal{R}} \boldsymbol{T}^e \cdot \left(\tilde{\boldsymbol{H}}^{e*} + \boldsymbol{\Omega}\right)\, dv_y = \int_{\mathcal{R}} \boldsymbol{T}^e \cdot \tilde{\boldsymbol{H}}^{e*}\, dv_y \tag{C.69}$$

When a tensor has a scalar tensor product with a symmetric tensor, only the symmetric part is used. The symmetric part of $\tilde{\boldsymbol{H}}^{e*}$ is as shown before, $\tilde{\boldsymbol{E}}^{e*}$. So, the integral becomes:

$$\int_{\mathcal{R}} \boldsymbol{T}^e \cdot \tilde{\boldsymbol{H}}^{e*}\, dv_y = \int_{\mathcal{R}} \boldsymbol{T}^e \cdot \tilde{\boldsymbol{E}}^{e*}\, dv_y \tag{C.70}$$

The next step is to determine the force balances implied by the virtual power. $\mathcal{V}$ can be chosen freely when applying the power balance as long as it remains consistent with the kinematic constraints. Therefore, a virtual velocity with arbitrary $\tilde{\boldsymbol{u}}$ is considered, with $\tilde{\boldsymbol{H}}^e = \nabla\tilde{\boldsymbol{u}}$. This implies that $\tilde{\boldsymbol{H}}^p$ becomes zero to satisfy the constraints shown in Equation C.65. The virtual power balance, subject to these constraints, reduces to the following expression:

$$\begin{aligned}
\int_{\partial\mathcal{R}} \bar{\boldsymbol{t}}\,(\bar{\boldsymbol{n}}) \cdot \tilde{\boldsymbol{u}}\, dA_y + \int_{\mathcal{R}} \boldsymbol{b} \cdot \tilde{\boldsymbol{u}}\, dV_y &= \int_{\mathcal{R}} \boldsymbol{T}^e \cdot \tilde{\boldsymbol{H}}^e + \boldsymbol{T}^p \cdot \tilde{\boldsymbol{H}}^p\, dV_y \\
\int_{\partial\mathcal{R}} \bar{\boldsymbol{t}}\,(\bar{\boldsymbol{n}}) \cdot \tilde{\boldsymbol{u}}\, dA_y + \int_{\mathcal{R}} \boldsymbol{b} \cdot \tilde{\boldsymbol{u}}\, dV_y &= \int_{\mathcal{R}} \boldsymbol{T}^e \cdot \tilde{\boldsymbol{H}}^e\, dV_y \\
\int_{\partial\mathcal{R}} \bar{\boldsymbol{t}}\,(\bar{\boldsymbol{n}}) \cdot \tilde{\boldsymbol{u}}\, dA_y + \int_{\mathcal{R}} \boldsymbol{b} \cdot \tilde{\boldsymbol{u}}\, dV_y &= \int_{\mathcal{R}} \boldsymbol{T}^e \cdot \nabla\tilde{\boldsymbol{u}}\, dV_y
\end{aligned} \tag{C.71}$$

Equation C.73 involves a single kinematic variable, which is the velocity $\tilde{\boldsymbol{u}}$ acting on the body. Therefore, this version of the virtual velocity is referred to as macroscopic.

The relation used previously, as shown in Equation C.35, is once again employed to rewrite the internal power in the same manner as demonstrated in Equation C.36 and Equation C.37, resulting in the following expression:

$$\int_{\mathcal{R}} \boldsymbol{T}^e \cdot \nabla\tilde{\boldsymbol{u}}\, dV_y = \int_{\mathcal{R}} \boldsymbol{T}^e\bar{\boldsymbol{n}} \cdot \tilde{\boldsymbol{u}}\, dA_y - \int_{\mathcal{R}} \operatorname{div}(\boldsymbol{T}^e) \cdot \tilde{\boldsymbol{u}}\, dV_y \tag{C.72}$$

This expression can be rewritten in the same way as shown in Equation C.38:

$$\begin{aligned}
\int_{\partial\mathcal{R}} \bar{\boldsymbol{t}}\,(\bar{\boldsymbol{n}}) \cdot \tilde{\boldsymbol{u}}\, dA_y + \int_{\mathcal{R}} \boldsymbol{b} \cdot \tilde{\boldsymbol{u}}\, dV_y &= \int_{\mathcal{R}} \boldsymbol{T}^e \cdot \nabla\tilde{\boldsymbol{u}}\, dV_y \\
\int_{\partial\mathcal{R}} \bar{\boldsymbol{t}}\,(\bar{\boldsymbol{n}}) \cdot \tilde{\boldsymbol{u}}\, dA_y + \int_{\mathcal{R}} \boldsymbol{b} \cdot \tilde{\boldsymbol{u}}\, dV_y &= \int_{\mathcal{R}} \boldsymbol{T}^e\bar{\boldsymbol{n}} \cdot \tilde{\boldsymbol{u}}\, dA_y - \int_{\mathcal{R}} \operatorname{div}(\boldsymbol{T}^e) \cdot \tilde{\boldsymbol{u}}\, dV_y \\
\int_{\mathcal{R}} (\operatorname{div}(\boldsymbol{T}^e) + \boldsymbol{b}) \cdot \tilde{\boldsymbol{u}}\, dV_y + \int_{\partial\mathcal{R}} (\bar{\boldsymbol{t}}\,(\bar{\boldsymbol{n}}) - \boldsymbol{T}^e\bar{\boldsymbol{n}}) \cdot \tilde{\boldsymbol{u}}\, dA_y &= 0
\end{aligned} \tag{C.73}$$

The fundamental lemma of the calculus of variations is employed to derive the traction condition and local force balance.

$$\begin{aligned}
\operatorname{div}(\boldsymbol{T}^e) + \boldsymbol{b} &= \boldsymbol{0} \\
\bar{\boldsymbol{t}}\,(\bar{\boldsymbol{n}}) - \boldsymbol{T}^e\bar{\boldsymbol{n}} &= 0
\end{aligned} \tag{C.74}$$

The traction condition, force balance, and symmetry condition are requirements met by the Cauchy stress tensor $\boldsymbol{T}$, indicating the validity of the following expression:

$$\boldsymbol{T} = \boldsymbol{T}^e \tag{C.75}$$

$\boldsymbol{T}$ can be regarded as the macroscopic stress and the force balance as the local macroscopic force balance.

An additional force balance is also associated with the plastic stress $\boldsymbol{T}^p$. To derive this force balance, a virtual velocity $\mathcal{V}$ with $\tilde{\boldsymbol{H}}^p$ is considered. Here, $\tilde{\boldsymbol{H}}^p$ is an arbitrary deviatoric tensor field. The relation between $\tilde{\boldsymbol{H}}^e$ and $\tilde{\boldsymbol{H}}^p$ is expressed as follows:

$$\tilde{\boldsymbol{H}}^e = \tilde{\boldsymbol{H}}^p \tag{C.76}$$

The kinematic constraints must still be satisfied, resulting in the following expression for the velocity:

$$\begin{aligned} \nabla\tilde{\boldsymbol{u}} &= \tilde{\boldsymbol{H}}^e + \tilde{\boldsymbol{H}}^p \\ &= -\tilde{\boldsymbol{H}}^p + \tilde{\boldsymbol{H}}^p \\ &= \boldsymbol{0} \end{aligned} \tag{C.77}$$

So, $\tilde{\boldsymbol{u}}$ becomes zero. This virtual velocity $\mathcal{V}$ is microscopic because no macroscopic motion is involved in any part of the body. Instead, only microscopic motions occur, inducing local changes in shape balanced by local stretch and rotation of the material structure. The virtual power balance for such a virtual velocity reduces to the following expression:

$$\begin{aligned} &\int_{\partial\mathcal{R}} \bar{\boldsymbol{t}}\,(\bar{\boldsymbol{n}}) \cdot \tilde{\boldsymbol{u}}\, dA_y + \int_{\mathcal{R}} \boldsymbol{b} \cdot \tilde{\boldsymbol{u}}\, dV_y = \int_{\mathcal{R}} \boldsymbol{T}^e \cdot \tilde{\boldsymbol{H}}^e + \boldsymbol{T}^p \cdot \tilde{\boldsymbol{H}}^p\, dV_y \\ &\int_{\mathcal{R}} -\boldsymbol{T}^e \cdot \tilde{\boldsymbol{H}}^p + \boldsymbol{T}^p \cdot \tilde{\boldsymbol{H}}^p\, dV_y = 0 \\ &\int_{\mathcal{R}} (\boldsymbol{T}^p - \boldsymbol{T}^e) \cdot \tilde{\boldsymbol{H}}^p\, dV_y = 0 \end{aligned} \tag{C.78}$$

As deriveved before, $\boldsymbol{T}^e$ is equal to $\boldsymbol{T}$:

$$\int_{\mathcal{R}} (\boldsymbol{T}^p - \boldsymbol{T}) \cdot \tilde{\boldsymbol{H}}^p\, dV_y = 0 \tag{C.79}$$

The deviatoric property is utilized to simplify the expression. A tensor $\boldsymbol{S}$ is considered deviatoric when its trace is equal to zero, as is the case for a skew tensor by definition. The deviatoric part of a tensor is denoted by appending a zero to the notation:

$$\boldsymbol{S}_0 = \mathrm{dev}\,(\boldsymbol{S}) \tag{C.80}$$

The deviatoric part of a tensor with three variables can be determined using the following expression:

$$\boldsymbol{S}_0 = S - \frac{1}{3}\mathrm{tr}\,(\boldsymbol{S})\,\boldsymbol{I} \tag{C.81}$$

next to discuss is the scalar tensor product of the deviatoric tensor $\boldsymbol{S}$ with the arbitrary tensor $\boldsymbol{T}$, as written below:

$$\boldsymbol{S} \cdot \boldsymbol{T} = S_{ij} T_{ji} \tag{C.82}$$

If only the deviatoric part of $\boldsymbol{T}$ is considered for the scalar tensor product, it can be expressed as follows:

$$\begin{aligned} \boldsymbol{T}_0 &= T_{ij} - \frac{1}{3} T_{kk} \delta_{ij} \\ \boldsymbol{S} \cdot \boldsymbol{T}_0 &= S_{ij} T_{ji} - \frac{1}{3} S_{ij} T_{kk} \delta_{ij} \end{aligned} \tag{C.83}$$

The second part of the expression above is expanded for three variables:

$$\begin{aligned} \frac{1}{3} S_{ij} T_{kk} \delta_{ij} &= \frac{1}{3} S_{11}\,(T_{11} + T_{22} + T_{33}) + \frac{1}{3} S_{22}\,(T_{11} + T_{22} + T_{33}) + \frac{1}{3} S_{33}\,(T_{11} + T_{22} + T_{33}) \\ &= \frac{1}{3}\,(S_{11} + S_{22} + S_{22})\,(T_{11} + T_{22} + T_{33}) \end{aligned} \tag{C.84}$$

The trace of the deviatoric tensor $\boldsymbol{S}$ and the arbitrary tensor $\boldsymbol{T}$ became visible in Equation C.85:

$$\begin{aligned}\frac{1}{3}S_{ij}T_{kk}\delta_{ij} =& \frac{1}{3}\left(S_{11}+S_{22}+S_{22}\right)\left(T_{11}+T_{22}+T_{33}\right)\\ =& \frac{1}{3}\mathrm{tr}\left(\boldsymbol{S}\right)\mathrm{tr}\left(\boldsymbol{T}\right)\end{aligned} \tag{C.85}$$

By definition, the trace of the deviatoric tensor is zero:

$$\frac{1}{3}S_{ij}T_{kk}\delta_{ij} = \frac{1}{3}\mathrm{tr}\left(\boldsymbol{S}\right)\mathrm{tr}\left(\boldsymbol{T}\right) = 0 \tag{C.86}$$

So, the scalar tensor product of a deviatoric tensor with the deviatoric part of an arbitrary tensor simplifies to the following expression:

$$\boldsymbol{S}\cdot\boldsymbol{T}_0 = S_{ij}T_{ji} - \frac{1}{3}S_{ij}T_{kk}\delta_{ij} = \quad S_{ij}T_{ji} \tag{C.87}$$

This implies that the scalar tensor product of a deviatoric tensor and an arbitrary tensor is equal to the scalar tensor product of a deviatoric tensor with the deviatoric part of the arbitrary tensor:

$$\boldsymbol{S}\cdot\boldsymbol{T} = \boldsymbol{S}\cdot\boldsymbol{T}_0 \tag{C.88}$$

The power balance discussed earlier is revisited with this understanding. In this expression, there is a scalar tensor product between the deviatoric tensor $\tilde{\boldsymbol{H}}^p$ and the arbitrary stress tensor $\boldsymbol{T}$. Hence, only the deviatoric part of the stress tensor $\boldsymbol{T}_0$ will be taken into account. Since $\boldsymbol{T}^p$ is already deviatoric, the remaining part of the expression remains unchanged:

$$\int_{\mathcal{R}}\left(\boldsymbol{T}^p-\boldsymbol{T}\right)\cdot\tilde{\boldsymbol{H}}^p\,dV_y = 0 \int_{\mathcal{R}}\left(\boldsymbol{T}^p-\boldsymbol{T}_0\right)\cdot\tilde{\boldsymbol{H}}^p\,dV_y \quad = 0 \tag{C.89}$$

This expression can be localized:

$$\left(\boldsymbol{T}^p-\boldsymbol{T}_0\right)\cdot\tilde{\boldsymbol{H}}^p = 0 \tag{C.90}$$

If $\tilde{\boldsymbol{H}}^p$ is considered to be an arbitrary skew tensor $\tilde{\boldsymbol{W}}^p$, it was also mentioned previously that $\boldsymbol{T}$ is symmetric, making $\boldsymbol{T}_0$ symmetric as well. The scalar tensor product of a symmetric and skew tensor is zero, so the localized power balance is simplified further:

$$\begin{aligned}\left(\boldsymbol{T}^p-\boldsymbol{T}_0\right)\cdot\tilde{\boldsymbol{H}}^p &= 0\\ \boldsymbol{T}^p\cdot\tilde{\boldsymbol{W}}^p-\boldsymbol{T}_0\cdot\tilde{\boldsymbol{W}}^p &= 0\\ \boldsymbol{T}^p\cdot\tilde{\boldsymbol{W}}^p &= 0\end{aligned} \tag{C.91}$$

The relation above is generally valid only when $\boldsymbol{T}^p$ is symmetric:

$$\boldsymbol{T}^p = \boldsymbol{T}^{pT} \tag{C.92}$$

Since $\tilde{\boldsymbol{H}}^p$ is an arbitrary deviatoric tensor field, the following relation can be derived for the general case:

$$\begin{aligned}\left(\boldsymbol{T}^p-\boldsymbol{T}_0\right)\cdot\tilde{\boldsymbol{H}}^p &= 0\\ \boldsymbol{T}^p-\boldsymbol{T}_0 &= 0\\ \boldsymbol{T}^p &= \boldsymbol{T}_0\end{aligned} \tag{C.93}$$

This expression is also referred to as the microscopic force balance because it is defined solely by microscopic virtual velocities.

D

Time derivative of a determinant

This appendix presents the derivation of the time derivative of the determinant of an arbitrary tensor $\Phi(t)$, which is used in deriving the governing equations. Let's consider a function $\phi(t)$ defined as follows:

$$\phi(t) = \det(\boldsymbol{\Phi}(t)) \tag{D.1}$$

ϕ is considered at a new timestep $t + \tau$:

$$\begin{aligned}\phi(t+\tau) &= \det(\boldsymbol{\Phi}(t+\tau)) \\ &= \det(\boldsymbol{\Phi}(t) + \boldsymbol{\Phi}(t+\tau) - \boldsymbol{\Phi}(t)) \\ &= \det\left(\boldsymbol{\Phi}(t)\left(\boldsymbol{I} + \boldsymbol{\Phi}^{-1}(t)\left(\boldsymbol{\Phi}(t+\tau) - \boldsymbol{\Phi}(t)\right)\right)\right)\end{aligned} \tag{D.2}$$

A new function $Q(t, \tau)$ is introduced below:

$$\boldsymbol{Q}(t,\tau) = \boldsymbol{\Phi}^{-1}(t)\left(\boldsymbol{\Phi}(t+\tau) - \boldsymbol{\Phi}(t)\right) \tag{D.3}$$

Equation D.3 is substituted in Equation D.2:

$$\begin{aligned}\phi(t+\tau) &= \det\left(\boldsymbol{\Phi}(t)\left(\boldsymbol{I} + \boldsymbol{\Phi}^{-1}(t)\left(\boldsymbol{\Phi}(t+\tau) - \boldsymbol{\Phi}(t)\right)\right)\right) \\ &= \det\left(\boldsymbol{\Phi}(t)\left(\boldsymbol{I} + \boldsymbol{Q}(t,\tau)\right)\right)\end{aligned} \tag{D.4}$$

$\det(\boldsymbol{AB})$ can be written as $\det(\boldsymbol{A})\det(\boldsymbol{B})$ and is used to rewrite Equation D.4:

$$\begin{aligned}\phi(t+\tau) &= \det\left(\boldsymbol{\Phi}(t)\left(\boldsymbol{I} + \boldsymbol{Q}(t+\tau)\right)\right) \\ &= \det(\boldsymbol{\Phi}(t))\det\left(\boldsymbol{I} + \boldsymbol{Q}(t+\tau)\right)\end{aligned} \tag{D.5}$$

Equation D.1 became visible in Equation D.5 and is used in this expression:

$$\begin{aligned}\phi(t+\tau) &= \det(\boldsymbol{\Phi}(t))\det\left(\boldsymbol{I} + \boldsymbol{Q}(t+\tau)\right) \\ &= \phi\left(t\right)\det\left(\boldsymbol{I} + \boldsymbol{Q}(t+\tau)\right)\end{aligned} \tag{D.6}$$

Both sides of Equation D.6 are subtracted by $\phi\left(t\right)$ and then divided by τ:

$$\begin{aligned}\phi(t+\tau) &= \phi\left(t\right)\det\left(\boldsymbol{I} + \boldsymbol{Q}(t+\tau)\right) \\ \frac{\phi(t+\tau) - \phi(t)}{\tau} &= \phi(t)\frac{\det(\boldsymbol{I} + \boldsymbol{Q}(t+\tau)) - 1}{\tau}\end{aligned} \tag{D.7}$$

Now the characteristic equation is introduced with ω as the eigenvalue and $\boldsymbol{A}$ as an arbitrary tensor:

$$\det(\boldsymbol{A} - \omega\boldsymbol{I}) = 0 \tag{D.8}$$

The characteristic equation can be rewritten by expanding the determinant:

$$-\det(\boldsymbol{A}-\omega\boldsymbol{I}) = \omega^3 - I_1(\boldsymbol{A})\omega^2 + I_2(\boldsymbol{A})\omega - I_3(\boldsymbol{A}) = 0 \tag{D.9}$$

Where I_1, I_2, and I_3 are the principal invariants, as given below:

$$\begin{aligned} I_1(\boldsymbol{A}) &= \mathrm{tr}(\boldsymbol{A}) \\ I_2(\boldsymbol{A}) &= \frac{1}{2}\left((\mathrm{tr}(\boldsymbol{A}))^2 - \mathrm{tr}\left(\boldsymbol{A}^2\right)\right) \\ I_3(\boldsymbol{A}) &= \det(\boldsymbol{A}) \end{aligned} \tag{D.10}$$

If $\boldsymbol{A}$ is replaced by $\boldsymbol{Q}(t,\tau)$, and ω is set to (-1), the determinant of $\boldsymbol{I}+\boldsymbol{Q}(t+\tau)$ is rewritten as shown in Equation D.9:

$$\det(\boldsymbol{I}+\boldsymbol{Q}(t+\tau)) = 1 + I_1(\boldsymbol{Q}(t,\tau)) + I_2(\boldsymbol{Q}(t,\tau)) + I_3(\boldsymbol{Q}(t,\tau)) \tag{D.11}$$

Equation D.10 is substituted in Equation D.11:

$$\begin{aligned} \det(\boldsymbol{I}+\boldsymbol{Q}(t+\tau)) =& 1 + I_1(\boldsymbol{Q}(t,\tau)) + I_2(\boldsymbol{Q}(t,\tau)) + I_3(\boldsymbol{Q}(t,\tau)) \\ =& 1 + \mathrm{tr}\left(\boldsymbol{Q}(t,\tau)\right) + \frac{1}{2}\left(\left(\mathrm{tr}\left(\boldsymbol{Q}(t,\tau)\right)\right)^2 - \mathrm{tr}\left(\boldsymbol{Q}(t,\tau)^2\right)\right) + \det(\boldsymbol{Q}(t,\tau)) \end{aligned} \tag{D.12}$$

The determinant of a tensor can also be written in terms of the trace:

$$\det \boldsymbol{A} = \frac{1}{6}\left(\left(\mathrm{tr}\left(\boldsymbol{A}\right)\right)^3 - 3\left(\mathrm{tr}\left(\boldsymbol{A}\right)\right)\left(\mathrm{tr}\left(\boldsymbol{A}^2\right)\right) + 2\cdot\mathrm{tr}\left(\boldsymbol{A}^3\right)\right) \tag{D.13}$$

Equation D.13 is substituted into Equation D.12 when $\boldsymbol{A}$ is replaced by $\boldsymbol{Q}(t,\tau)$.

$$\begin{aligned} \det(\boldsymbol{I}+\boldsymbol{Q}(t+\tau)) =& 1 + \mathrm{tr}\left(\boldsymbol{Q}(t,\tau)\right) + \frac{1}{2}\left(\left(\mathrm{tr}\left(\boldsymbol{Q}(t,\tau)\right)\right)^2 - \mathrm{tr}\left(\boldsymbol{Q}(t,\tau)^2\right)\right) + \det(\boldsymbol{Q}(t,\tau)) \\ =& 1 + \mathrm{tr}(\boldsymbol{Q}(t,\tau)) + \frac{1}{2}\left(\left(\mathrm{tr}(\boldsymbol{Q}(t,\tau))\right)^2 - \mathrm{tr}\left(\boldsymbol{Q}(t,\tau)^2\right)\right) + \\ & \frac{1}{6}\left(\left(\mathrm{tr}(\boldsymbol{Q}(t,\tau))\right)^3 - 3(\mathrm{tr}(\boldsymbol{Q}(t,\tau)))\left(\mathrm{tr}\left(\boldsymbol{Q}(t,\tau)^2\right)\right) + 2\left(\mathrm{tr}\left(\boldsymbol{Q}(t,\tau)^3\right)\right)\right) \end{aligned} \tag{D.14}$$

All higher order τ are truncated in Equation D.14:

$$\det(\boldsymbol{I}+\boldsymbol{Q}(t+\tau)) = 1 + \mathrm{tr}(\boldsymbol{Q}(t,\tau)) + \mathcal{O}\left(\tau^2\right) \tag{D.15}$$

Equation D.15 is divided by the timestep τ :

$$\begin{aligned} \frac{\det(\boldsymbol{I}+\boldsymbol{Q}(t+\tau)) - 1}{\tau} &= \frac{\mathrm{tr}(\boldsymbol{Q}(t,\tau))}{\tau} + \mathcal{O}(\tau) \\ &= \mathrm{tr}\left(\frac{\boldsymbol{Q}(t,\tau)}{\tau}\right) + \mathcal{O}(\tau) \end{aligned} \tag{D.16}$$

Equation D.16 is substituted in Equation D.7

$$\begin{aligned} \frac{\phi(t+\tau)-\phi(t)}{\tau} &= \phi(t)\frac{\det(\boldsymbol{I}+\boldsymbol{Q}(t+\tau)) - 1}{\tau} \\ &= \phi(t)\,\mathrm{tr}\left(\frac{\boldsymbol{Q}(t,\tau)}{\tau}\right) + \mathcal{O}(\tau) \end{aligned} \tag{D.17}$$

The expression for $\boldsymbol{Q}$ (Equation D.3) can now be substituted in Equation D.17:

$$\begin{aligned} \frac{\phi(t+\tau)-\phi(t)}{\tau} &= \phi(t)\,\mathrm{tr}\left(\frac{\boldsymbol{Q}(t,\tau)}{\tau}\right) + \mathcal{O}(\tau) \\ &= \phi(t)\,\mathrm{tr}\left(\boldsymbol{\Phi}^{-1}(t)\frac{\boldsymbol{\Phi}(t+\tau)-\boldsymbol{\Phi}(t)}{\tau}\right) + \mathcal{O}(\tau) \end{aligned} \tag{D.18}$$

The limit of τ goes to 0 is taken:

$$\begin{aligned} \lim_{\tau \to 0} \frac{\phi(t+\tau) - \phi(t)}{\tau} &= \lim_{\tau \to 0} \phi(t) \operatorname{tr}\left(\mathbf{\Phi}^{-1}(t) \frac{\mathbf{\Phi}(t+\tau) - \Phi(t)}{\tau}\right) + \lim_{\tau \to 0} \mathcal{O}(\tau) \\ \dot{\phi}(t) &= \phi(t) \operatorname{tr}\left(\mathbf{\Phi}^{-1}(t) \mathbf{\Phi}(t)\right) \end{aligned} \tag{D.19}$$

Equation D.1 is substituted in Equation D.19:

$$\begin{aligned} \dot{\phi}(t) &= \phi(t) \operatorname{tr}\left(\mathbf{\Phi}^{-1}(t) \mathbf{\Phi}(t)\right) \\ &= \det(\mathbf{\Phi}(t)) \operatorname{tr}\left(\mathbf{\Phi}^{-1}(t) \mathbf{\Phi}(t)\right) \end{aligned} \tag{D.20}$$

Equation D.20 is rewritten using the fact that $\operatorname{tr}(\boldsymbol{AB}) = \operatorname{tr}(\boldsymbol{BA})$.

$$\begin{aligned} \dot{\phi}(t) &= \det(\mathbf{\Phi}(t)) \operatorname{tr}\left(\mathbf{\Phi}^{-1}(t) \mathbf{\Phi}(t)\right) \\ &= \det(\mathbf{\Phi}(t)) \operatorname{tr}\left(\mathbf{\Phi}(t) \mathbf{\Phi}^{-1}(t)\right) \end{aligned} \tag{D.21}$$

E

Deriving the expression for the jump of multiple variables

The definitions of the jump and the average are previously provided and, for convenience, repeated below:

$$\begin{aligned} \{a\} =& \frac{a^+ - a^-}{2} \\ [\![a]\!] =& a^+ - a^- \end{aligned} \tag{E.1}$$

If the jump involves two variables, there is the possibility to express the expression in another convenient manner. This is achieved by employing the definition shown above, considering that one of the variables is a vector.

$$[\![a\boldsymbol{b}]\!] = a^+\boldsymbol{b}^+ - a^-\boldsymbol{b}^- \tag{E.2}$$

Equation E.2 is now rewritten by adding $\frac{a^+\boldsymbol{b}^-}{2}$ and $\frac{a^-\boldsymbol{b}^+}{2}$ to the expression. To maintain the expression's equivalence, these terms are also subtracted. Additionally, the existing terms are split into two parts.

$$\begin{aligned} [\![a\boldsymbol{b}]\!] =& a^+\boldsymbol{b}^+ - a^-\boldsymbol{b}^- \\ =& \frac{a^+\boldsymbol{b}^+}{2} + \frac{a^+\boldsymbol{b}^+}{2} - \frac{a^-\boldsymbol{b}^-}{2} - \frac{a^-\boldsymbol{b}^-}{2} - \frac{a^+\boldsymbol{b}^-}{2} + \frac{a^+\boldsymbol{b}^-}{2} + \frac{a^-\boldsymbol{b}^+}{2} - \frac{a^-\boldsymbol{b}^+}{2} \\ =& \frac{a^+}{2}\boldsymbol{b}^+ + a^+\frac{\boldsymbol{b}^+}{2} - \frac{a^-}{2}\boldsymbol{b}^- - a^-\frac{\boldsymbol{b}^-}{2} - \frac{a^+}{2}\boldsymbol{b}^- + a^+\frac{\boldsymbol{b}^-}{2} + \frac{a^-}{2}\boldsymbol{b}^+ - a^-\frac{\boldsymbol{b}^+}{2} \end{aligned} \tag{E.3}$$

Terms can now be combined to simplify the expression:

$$\begin{aligned} [\![a\boldsymbol{b}]\!] =& \frac{a^+}{2}\boldsymbol{b}^+ + a^+\frac{\boldsymbol{b}^+}{2} - \frac{a^-}{2}\boldsymbol{b}^- - a^-\frac{\boldsymbol{b}^-}{2} - \frac{a^+}{2}\boldsymbol{b}^- + a^+\frac{\boldsymbol{b}^-}{2} + \frac{a^-}{2}\boldsymbol{b}^+ - a^-\frac{\boldsymbol{b}^+}{2} \\ =& \frac{a^+}{2}\left(\boldsymbol{b}^+ - \boldsymbol{b}^-\right) + \left(a^+ - a^-\right)\frac{\boldsymbol{b}^+}{2} + \frac{a^-}{2}\left(\boldsymbol{b}^+ - \boldsymbol{b}^-\right) + \left(a^+ - a^-\right)\frac{\boldsymbol{b}^-}{2} \\ =& \frac{a^+ + a^-}{2}\left(\boldsymbol{b}^+ - \boldsymbol{b}^-\right) + \left(a^+ - a^-\right)\frac{\boldsymbol{b}^+ + \boldsymbol{b}^-}{2} \end{aligned} \tag{E.4}$$

The definition of the jump and the average, as presented in Equation E.4, can be simplified by substituting their definitions into this expression.

$$\begin{aligned} [\![a\boldsymbol{b}]\!] =& \frac{a^+ + a^-}{2}\left(\boldsymbol{b}^+ - \boldsymbol{b}^-\right) + \left(a^+ - a^-\right)\frac{\boldsymbol{b}^+ + \boldsymbol{b}^-}{2} \\ =& \{a\}\,[\![\boldsymbol{b}]\!] + [\![a]\!]\,\{\boldsymbol{b}\} \end{aligned} \tag{E.5}$$